Trinity College Dublin
Coláiste na Tríonóide, Baile Átha Cliath
The University of Dublin

Computational and Experimental Study of Optical properties of TiO_2 Arrays Fabricated via Soft Nanoimprint Lithography

Jorge Alberto Garcia Coindreau

A thesis presented for the degree of

Doctor in Philosophy

School of Physics

Trinity College Dublin

February, 2021

Declaration

I declare that this thesis has not been submitted as an exercise for a degree at this or any other university and it is entirely my own work.

I was involved in several collaborations, and where appropriate my collaborators are acknowledged for their contributions.

I agree to deposit this thesis in the University's open access institutional repository or allow the Library to do so on my behalf, subject to Irish Copyright Legislation and Trinity College Library conditions of use and acknowledgement.

Acknowledgments

Firstly, I would like to thank my supervisor Prof. Louise Bradley for her constant guidance and support throughout my research. It has been a great opportunity and joy to be part of her research group.

Secondly, I would also like to thank Dr. Calin Hrelescu for his generous involvement in my project and research. His assistance, insights, and friendship had great impact in my research. I would also like to thank Dr. Xia Zhang whom I collaborated with in my research and who offered me a lot of help. I really enjoyed working with both.

Moreover, I would like to thank Dr. Brian Jennings for being a great friend. He was always being there to help and advise me during my research. I would like to thank everyone in Louise Bradley Group and the Photonics team in Trinity for making my time during the PhD enjoyable. I would also like to thank the previous group members: Dr. Luke Higgins, Dr. Vasilios Karanikolas, Dr. Esteban Pedrueza, Dr. Graham Murphy, Dr. John Gough and Dr. Katarzyna Siewierska for their help and support in my path towards the completion of the PhD.

I would also like to offer my thanks to Dermot and Eoin in the Advanced Microscopy Lab for their technical support and assistance. I would also like to thank Ken Concannon and Alan O'Meary for their help in assisting with computer problems and issues that arose in the labs.

I am grateful for all the great friendships I developed during my stay in Dublin: Brian, Michael, Gaurav, Frank, Subhayan, Calin, Dovydas, Chuan, Romina, Alessandro, Mario, Emmanuele, Stella, Colm, Sylvia, Matteo, Xia, Mike, Michelangelo, Sabine, Frank and Kata.

I would also like to thank my family from back home who supported me greatly during this time. I would like to thank my good friends from Mexico, especially, Eduardo, Mauricio, Fernando, Mauricio, Mauricio, and Esteban who made many stressful time times in my PhD less stressful.

Lastly, I would like to thank my girlfriend Anais for all her patience and support shown even while working on her own PhD. She helped me a lot in my PhD and took very good care of me in the last steps. I would not have been able to complete my thesis if it were not for her.

Abstract

In this thesis the optical properties of large 1 mm^2 titanium oxide (TiO_2) nanoarrays and the interactions with Rhodamine 6G are studied computationally and experimentally. Three TiO_2 arrays with different particle size and periodicity are studied, which are labelled A600, A550 and A480. The arrays used in this work were fabricated by the group of Marco Abbarchi from Aix-Marseille Université, Marseille, France using soft-nano imprint lithography, a novel fabrication method for TiO_2 that allows for the fast large area arrays to be fabricated. A residual TiO_2 layer is left underneath the array from the fabrication process, allowing for the possibility of quasi-guided modes (QGMs) to supported by the array. The conditions of the layer and manipulation of the QGMs are studied finite-difference time domain (FDTD) simulations. QGMs require a layer that is sufficiently optically and physically thick and are coupled to the Rayleigh anomalies. QGMs wavelength is controlled by the properties of the substrate and residual layer. The properties of the individual pillars of the arrays have little to no effect on the QGMs. TiO_2 arrays were experimentally characterized and the effect of varying concentrations of Rhodamine 6G (R6G) on the optical properties of the arrays is reported. Normal transmission and reflection measurements of the three arrays show no signs of QGMs. The arrays were not able to support QGMs because of the low refractive index of the residual. The low refractive index of the residual layer is due to discontinuities and porosity of the layer lowering the effective refractive index. QGMs were observed on the arrays as sharp features in the reflection and transmission measurements after the addition of R6G. R6G increased the effective refractive index of the layer. The addition of R6G also significantly changes the darkfield scattering spectra of the arrays as a function of the concentration. These results make it clear that it is possible to modify the properties of the layer by introducing different materials. The modification of the photoluminescence (PL) of R6G coupled to the TiO_2 arrays was investigated. The emission of R6G on the arrays and off the arrays is measured using three different focused laser excitations at 375 nm, 405 nm, and 466 nm. The A600 showed a modification of R6G photoluminescence with excitation of the 375 and 405 nm lasers, while the other arrays showed non. Time-resolved photoluminescence spectroscopy, photobleaching, power dependence measurements and FDTD simulations were performed to identify the mechanism responsible for this modification. These measurements point toward excitation enhancement of R6G on the A600 array 405 nm and 375 nm excitation due to higher electric fields regions, although these results are not conclusive.

List of publications and conference contributions

***Article*:** Gough, J. J., McEvoy, N., O'Brien, M., McManus, J., **Garcia-Coindreau, J.,** Bell, A. P., ... & Bradley, A. L. (2019). Dependence of Photocurrent Enhancements in Hybrid Quantum Dot-MoS_2 Devices on Quantum Dot Emission Wavelength. ACS Photonics, 6(4), 976-984.

Article: Murphy, G. P., Gough, J. J., Higgins, L. J., Karanikolas, V. D., Wilson, K. M., **Coindreau, J. A. G**., ... & Bradley, A. L. (2017). Ag colloids and arrays for plasmonic non-radiative energy transfer from quantum dots to a quantum well. Nanotechnology, 28(11), 115401.

Conference Paper: Higgins, L. J., Marocico, C. A., **Coindreau, J. G**., Karanikolas, V. D., Bell, A. P., Gough, J. J., ... & Bradley, A. L. (2017, July). Influence of plasmonic array geometry on non-radiative energy transfer from a quantum well to a quantum dot layer. In 2017 19th International Conference on Transparent Optical Networks (ICTON) (pp. 1-4). IEEE.

Poster Presentation: "Power dependence on non-radiative energy transfer from CdSe quantum dots to InGaN/GaN", Photonics Ireland, 2017, Galway, Ireland.

Poster Presentation: "Power dependence on non-radiative energy transfer from CdSe quantum dots to InGaN/GaN", Bad Honnef Physics School on Exciting nanostructures, 2017, Physikzentrum Bad Honnef, Germany.

Table of Contents

Declaration i

Acknowledgments ii

Abstract ii

List of publications and conference contributions iv

1 Introduction 1

1.1 Thesis Structure 7

2 Theory 9

2.1 Scattering Properties of Dielectric Resonators 9

2.2 Collective Resonances of Dielectric Arrays 16

3 Materials and Methods 22

3.1 Material: Titanium Oxide Arrays 22

3.2 Sample Preparation: R6G on TiO_2 Arrays 26

3.3 Experimental Methods: Normal reflection, Normal transmission and Darkfield measurements 27

3.4 Experimental Methods: Time Resolved Photoluminescence and Photoluminescence Measurements 29

3.5 Computational Methods: Finite Difference Time Domain Simulations 30

3.6 Multipole Decomposition of Extinction 36

4 Computational Study of TiO_2 Arrays Fabricated via Soft-NIL 44

4.1 Single Pillars and Arrays with no Substrate 46

4.2 Single Pillars and Arrays on a Substrate and TiO2 Layer 58

4.3 Conclusion 73

5 Experimental Analysis of TiO2 arrays 75

5.1 Experimental normal incidence zero-order reflection and transmission for the A600, A550 and A480 76

5.2 Effects of increasing R6G concentration on the zero-order reflection and transmission for the A600, A550 and A480 arrays 86

5.3 Effects of increasing R6G concentration on the back scattering of light under dark field illumination for the A600, A550 and A480 arrays. 96

5.4 Conclusion 100

6 TiO2 Arrays Influence on Rhodamine 6G Photoluminescence and Time-Resolved Photoluminescence 102

6.1 Photoluminescence of R6G on TiO_2 arrays 103

6.2 Time Resolved Photoluminescence of R6G on TiO_2 arrays 109

6.3 Power Dependence of Time Resolved Photoluminescence of R6G on the A600 ... 111

6.4 Photobleaching of R6G on TiO_2 arrays 114

6.5 FDTD study and Discussion on Array properties on the enhanced R6G emission observed on the A600 array at 375 and 405 nm. 117

6.6 Conclusion 125

7 Conclusion and Future Work 127

8 References 130

1 Introduction

Manipulation of light at its beginning concentrated on enhancing what the eye could see, for example: eyeglasses to correct vision, telescopes allowing to look at far away objects, and microscopes allowing the study of what was too small to observe with the bare eye. Manipulation of light has expanded greatly from using spatially resolved images as means to enhance what can be seen by the eyes. Newton's experiments on the refraction of white light through a prism that separated it into colours, led to an understanding that spectral information of light can also be analysed. The development of the electromagnetic theory by Maxwell led to the understanding that light was an electromagnetic wave and that visible light was only a small part of the electromagnetic spectrum. The photoelectric effect gave great insights into light-matter interaction and led to the concept of light being quantized in energy packets, i.e. photons[1]. Light has been crucial to the understanding of the fundamental properties of the universe, such as the Michelson–Morley experiment[2] that disproved the existence of ether as a medium for light propagation and eventually led to the formulation of special relativity.

In a similar trend to electronics, light manipulation has been pushed to smaller and smaller sizes. The downscaling of light matter interactions into optical subwavelength scales has been for the most part focused on metallic nanostructures and exploiting surface plasmons. Surface plasmons are collective oscillations of the free electrons that occur at the boundary between a metal and a dielectric and generate very strong localized fields at subwavelengths scales near the surface of the metal. Pioneering work was performed by R. Ritchie[3] on plasma losses by fast electrons in thin metal made surface plasmons[4]. Raman spectroscopy is a powerful optical technique that gives information on the material properties through inelastic scattering of light caused by the excitation of molecular vibrational modes. This process, however, is very inefficient, as approximately one in a million photons is inelastically scattered. In the late 1970-1980s, surface plasmons were used to increase the Raman signal dramatically and led to surface enhanced Raman spectroscopy. The success of surface plasmons in surface enhanced Raman spectroscopy and the creation of new reliable fabrication methods sparked the interest in plasmonics for a great variety of applications[4,5]. Such applications are also based on localized surface plasmons (LSPs), which like surface plasmons, are the collective resonant oscillations of the free electrons in small metallic nanoparticles and have strong localized electric fields.

LSPs can be tuned by the material properties and size of the particle and are sensitive to changes in the refractive index of the environment. Applications of plasmonics include, but are not exclusive to: surface enhanced Raman spectroscopy[6–9] , photovoltaic devices[10–12], LEDs[13–15], and biosensing[16]. Gold and silver nanoparticles have been the most dominantly used metals in plasmonics. Gold supports plasmon resonance greater than 550 nm and silver supports resonances down to 350 nm[17]. Silver, however, has a significant drawback. Its rapid oxidation degrades significantly its plasmonic properties and limits its reliability for applications[17]. Other plasmonic materials such as aluminium support resonances across the UV-visible range and has a self-insulating thin optically inert oxide layer that has a small effect on the plasmonic properties[17]. However, gold, silver and aluminium suffer from high ohmic losses in the visible light range which limits their applications[18,19]. Consequently, the quality factor of the LSPs in single metallic nanoparticles is limited predominantly by the refractive index of the material, with the environment, size, and shape playing a smaller role[20,21]. Dielectric nanostructures, so-called "Mie resonators" or "dielectric resonators", are an exciting alternative to the metal nanoparticles due to their low ohmic losses in the visible range[22–24].

Unlike metal nanoparticles, in which LSPs govern light matter interactions, dielectric resonators trap light inside them, forming electric and magnetic resonant modes. These modes eventually leak out leading to significant scattering[25]. Dielectric particles need a high refractive index in contrast to their environment to support electric and magnetic resonances. The nature of the resonances in dielectric resonators is described by Mie theory[26]. They support electric and magnetic dipoles, quadrupoles and higher order terms. The frequencies of these resonances, like metallic nanoparticles, depend on the size, shape and refractive index. The wavelength of the lowest energy resonance of a dielectric resonator in air, the magnetic dipole, can be estimated by the $diameter \times refractive\ index$ of the particle[25]. Dielectric resonators supporting magnetic resonances in the visible range were investigated theoretically in the work of Andrey B. Evlyukhin et al.[27] in mid-2010. Silicon was used due to its low losses in the visible light range (>450 nm) and high refractive index. A silicon sphere with a 65 nm radius has a magnetic dipole resonance roughly at 550 nm[25,27]. In 2012, Andrey B. Evlyukhin et al. first demonstrated the electric and magnetic resonances of single silicon nanoparticles in the visible light range[25]. Two silicon spheres were measured with radii of 104 nm and 132 nm, with two prominent peaks and other smaller peaks in the scattering spectra. The scattering spectra of the silicon particles were compared to Mie theory, the two prominent peaks corresponded to the magnetic and electric dipoles and the smaller peaks to the higher order electric and magnetic

quadrupole. The magnetic dipoles observed for these silicon particles were at around 900 nm and 730 nm, respectively. Soon after, Arseniy I. Kuznetsov et al. showed the magnetic dipole response across a larger size range of silicon particles[28]. This showed that silicon nanoparticles can achieve magnetic responses across most of the visible light range (~475-900 nm).

Optical metasurfaces are two-dimensional (2D) ordered structures with metal/dielectric materials with dimensions in the order of the wavelength of light. as building blocks. Optical metasurfaces are particularly exciting because of their optical properties that do not occur naturally in materials[29], such as negative index metamaterials[30] and optical cloaking[31]. Optical metasurfaces, such as 2D arrays of plasmonic resonators have been extensively researched[21]. As mentioned before, metal nanoparticles have high ohmic losses in the visible range and the quality factor of the LSPs is limited by the material properties. This inspired the search for low-loss plasmonic resonances in plasmonic metasurfaces. With ordered arrays of metallic nanoparticles, it is possible to have resonances with very high quality factors when the period is roughly the wavelength of the incident light[21]. This is achieved by the collective resonances of plasmonic arrays, for which the LSPs of the nanoparticles couple to the Rayleigh anomalies (RAs). These resonances are referred to as surface lattice resonances (SLRs)[21]. SLRs are redshifted from the RA, the linewidth and redshift are determined by the coupling strength between the individual particle resonances and the RA[32]. SLRs have been extensively studied due to their low-losses and high-quality Q-factors. RAs are in-plane diffraction orders that are also known as Wood's anomalies. They were first discovered by Wood's in early 20th century while working with gratings[33]. They are sharp features in the reflection or transmission spectra from gratings that arise from the grating orders[34]. Theoretical works by S. Zhou et al.[21,35] showed how to obtain these very sharp collective resonances, but early works on SLRs did not achieve the narrow resonances promised by theory due to unreliable fabrication techniques and non-ideal experimental set-ups[21]. The first observation of very sharp SLRs was observed in a gold nanoparticle array by Kravets et al[36]. Due to the high Q-factors and sensitivity to the environment of SLRs[37], they have been considered for applications in enhancing the emission of dyes[38,39], LEDs[40], non-linear optics[41,42] , lasing[43,44], biosensing[45], photovoltaics[46].

Naturally, with the more recent focus on dielectric nanostructures, there was interest in SLRs in dielectric arrays in the visible light range. Andrey B. Evlyukhin et al. studied in 2010 the optical properties of 2D silicon arrays by using the coupled dipole equations[27]. Lattice resonances with Fano-like sharp features were obtained in reflection and transmission when the periodicity of the array was larger than the resonant wavelengths of the silicon sphere for infinite

arrays[27]. However, the physical realization of these structure did not come until later due to the difficulties in fabricating silicon arrays at the nanoscale[23,47]. SLRs in dielectric nano arrays can be used for high quality mirrors[48], the Kerker effect[49], electromagnetic induced transparency[50], enhanced light emssion[51,52], and colour generation surfaces[53,54]. Very similar to SLRs, and often undistinguished in literature[32], the individual pillar resonances in the arrays can couple into guided modes if the array is encased by a waveguide[32,51] or on top of a waveguide[50]. These modes are called quasi-guided modes (QGMs) as they are eventually scattered out by the particles[42,55].

Material	Spectral Range, μm	Refractive Index, n	Extinction Coefficient, k	Band Gap Type	Band Gap Energy, eV	Referen
c-Si	0.50–1.45	4.293–3.486	0.045–0.001	indirect	1.12	[68]
	1.45–2.40	3.484–3.437	~0			[69]
a-Si	0.50–1.00	4.47–3.61	1.12–0.01	indirect	1.50	[70]
GaAs	0.50–0.80	4.037–3.679	0.376–0.089	direct	1.46	[71]
GaP	0.50–0.80	3.590–3.197	~0	indirect	2.26	[71]
InP	0.50–0.80	3.456–3.818	0.203–0.511	direct	1.27	[72]
TiO_2	0.50–1.00	2.715–2.483	~0	indirect	3.05	[73]
Ge	0.50–0.60	4.460–5.811	2.366–1.389	indirect	0.67	[71]
	0.60–0.80	5.811–4.699	1.389–0.3			
	0.80–1.90	4.684–4.129	0.3–0.001			[74]
	1.90–2.40	4.111–4.069	~0			[69]
GaSb	1.00–2.40	4.140–3.846	0.225–0.001	direct	0.69	[75]
Te	4.00–14.0	4.929–4.785	~0	indirect	0.34	[76]
PbTe	4.10–12.5	5.975–5.609	~0	direct	0.31	[77]
GeTe[a]	6.20–11.8	7.3–7.278	~0	direct	0.2	[78]
SiC	11.0–15.0	~20	~15	—	—	[79]

[a]Theoretical values of the refractive index are quoted for GeTe.

Figure 1-1 Table showing the properties of different high index materials proposed for dielectric resonators, taken from Ref[23].

Silicon is widely used as a dielectric material due to its low ohmic losses in the visible range[23]. However, the performance of silicon as a dielectric resonator reduces in the blue and near-UV region due to the increase in ohmic losses[23,56]. Silicon is not the only dielectric material suitable for use in the visible range, and other materials have been proposed[21] as shown in **Figure 1-1**. A particularly interesting material is titanium dioxide (TiO_2), as it exhibits near to zero losses in the blue and near UV-range and it has a relatively high refractive index[23,57,58]. TiO_2 is a widely used material in many applications, from photocatalysis[59–62] to cosmetics[63]. Furthermore, TiO_2 is used in the photodegradation of organic dyes[55,67,69–71] as it increases the degradation rate[64–66]. Apart from its optical properties, TiO_2 is a material that is highly stable, light-weight, abundant, and safe for humans[67], making it a very appealing material for applications. Recently, fabrication techniques of TiO_2 nanostructures have improved using soft nano-imprint lithography, which led to the fabrication of very large area (>1mm^2) arrays with very good fidelity of particles and periodicity in the nanometer range[68,69]. Furthermore, this technique is compatible with many different substrates and devices as the maximum

temperature does not have to exceed 350 °C during fabrication, as this temperature is enough to crystallize and stabilize the TiO_2 into anatase structure[68,69]. This is a cost-effective and scalable method for fabricating TiO_2 metasurface. For all these reasons, TiO_2 is a very promising material for dielectric resonators. Although, Mie resonances in TiO_2 nanostructures have already been reported in the visible range in several studies[54,68–73], the potential of TiO_2-based metasurfaces has not be fully explored yet.

This thesis considers TiO_2 arrays fabricated via soft nano-imprint lithography by the group of Marco Abbarchi from Aix-Marseille Université, Marseille, France, according to the method described in references[68,69]. The particles of these arrays are nanopillars and have Mie resonances in the visible range. The square 2D arrays have an area of 1 mm^2 and vary in nanopillar dimension and periodicity. The periodicity of the arrays allows for SLRs to exist; however, the arrays are constructed on a glass substrate and due to the index mismatch between the super substrate (air), the SLRs cannot propagate. Due to the fabrication process of soft nano-imprint lithography, a residual TiO_2 layer is sandwiched between the pillars and the glass substate, allowing for the propagation of QGMs.

The aim of this thesis is to investigate the potential for these arrays to support high Q factors resonances such as QGMs. If the arrays can support QGMs this will make them very appealing to use in many applications such as high-quality mirrors, the Kerker effect, electromagnetic induced transparency, sensing, enhanced light emission, and colour generation surfaces. This high appeal comes from the arrays not needing any additional fabrication steps to support QGMs while already using a cheap and fast method capable of producing large area arrays on many different types of substrates. The thesis will aim at studying the behavior of these both optically and experimentally in order give insights on what is required for the arrays to be able to support QGMs. Furthermore, this thesis will also aim to explore the interaction of the arrays with R6G, this is done to demonstrate the potential for enhanced light emission applications as well how the incorporation of materials onto the array changes its optical properties demonstrating is potential for sensing applications. This thesis will give a clear idea of the behavior of QGMs and what parameters are important in order to fabricate QGM ready arrays and as well what properties of the arrays are beneficial to be used in applications.

1.1 State of the Art

There has been plenty of computational work on collective resonances and QGMs in dielectric metasurfaces. Collective resonances in dielectric structures have been studied computationally significantly, the effects of the size of the arrays were extensively studied by V. I. Zakomirnyi et al.[74] showing arrays need to be sufficiently large to support high Q-factor resonances. .The effects of randomness in different array properties have also been studied extensively by V. I. Zakomirnyi et al[75] showing how much uniformity is needed in the arrays to support QGMs. QGMs in silicon hexagonal arrays have been studied in P. Ding. et al.[51], in this computational study he showed the potential for a silicon array built on top of a waveguide to be used for light emission enhancement. Similarly in study on silicon hexagonal arrays embedded in a waveguide by Gabriel W. Castellanos et al. [32], he studies computational the field enhancement of the electric field profile as a function of distance from the substrate. Computational studies on the suitability of QGMs on dielectric metasurfaces have been explored also other applications such as electromagnetic induced tranparency[50]. Computational studies on QGMs on 2-D metasurfaces, to the best of my knowledge do not report on higher order QGMs could to higher order RAs, as well as an incomplete analysis of the of what happens to the multipole resonances of the individual pillars when they light couple into QGMs. This thesis will computationally explore the properties of the arrays by looking at QGMs coupled to higher order RAs. The thesis will also study the multipole resonances of the individual pillars by performing multipole decomposition of the spectra in cartesian coordinates developed by Evlyukhin et al[76].

High Q-factor resonances of ~298 have been experimentally observed for SLRs in silicon array. However, when it comes to experimental studies of TiO_2 based metasurfaces most of them are focused on colour generation surfaces[54,68–73.] Where they study the effects of the different lattice and pillar dimensions. Philipp Gutruf et al. demonstrated the effect on the colour generation by the SLRs by changing the periodicity of the arrays both computationally and experimentally, achieving a Q-factor of ~30. However, the study of QGMs in TiO_2 structures are few[77,78], in 3-D structure for increase absorption in solar cells and in 1D structure of a polymer grating covered with TiO_2 for sensing. To the best of my knowledge there is a lack of experimental demonstration of QGMs in dielectric arrays specifically TiO_2 based arrays. Furthermore, there are only two studies done on arrays fabricated by soft nano-imprint lithography [68,69] from people who fabricated the arrays used in this thesis. These works are

focused on the fabrication of the arrays and on their scattering properties for colour generation surfaces and sensing by using the arrays porosity to change the optical properties of the arrays by introducing humidity. However, the full potential of these arrays to support QGMs, the possibility to alter the QGMs by the porosity of the array, and the possible use of these arrays in emission enhancement remains unexplored and it is studied in this thesis.

1.2 Thesis Structure

The structure of the thesis will now be discussed. The next section, chapter 2, contains theory on dielectric resonators, the basis of Mie theory and multipole expansion of the scattering properties are presented. This section also discusses in detail the behaviour of the collective resonances of 2-D arrays for different configurations with examples from literature. Chapter 3 describes the materials and methods used in this thesis. The dimensions and properties of the arrays, sample preparation, and experimental setups are presented in this chapter. This section also includes the theory and set-up for the finite difference time domain simulation, and the theory and application of cartesian multipole decomposition of the spectra.

Chapter 4 focuses on the detailed investigation of the optical properties of TiO_2 arrays using finite difference time domain numerical simulation method and by performing multipole decomposition of the pillars in cartesian coordinates[76]. The effects the residual TiO_2 layer has on the different multipole resonances of the individual pillars is studied. This chapter also focuses on the multipole interactions with RAs for TiO_2 arrays in air, on a glass substrate and on a residual TiO_2 layer. The conditions for the existence of the QGMs in term of the properties of the TiO_2 layer and the sensitivity to the layer are explored. Chapter 5 focuses on the experimental properties of fabricated TiO_2 arrays and the influence of Rhodamine 6G on the reflection, transmission, and darkfield scattering properties of the arrays. Sharp QGMs are observed in the transmission and reflection only after the addition of high concentrations of Rhodamine 6G. Finite difference time domain simulations are performed to demonstrate the effects of surface roughness and discontinuities in the residual layer on the optical properties, as well as to prove the ability of the arrays to support QGMs. Finite difference time domain simulations are also performed to show the nature of the observed QGMs in experiments. Chapter 6 chapter focuses on the photoluminescence modification of Rhodamine 6G on the arrays under focused laser excitation. The emission is characterised by time resolved and

frequency resolved photoluminescence, photobleaching, and power dependent emission measurements. The geometry of the arrays is seen to modify the emission of Rhodamine 6G significantly. Finally, in chapter 7 conclusions are drawn and some comments on future work are presented.

2 Theory

In this section the theory behind the basic elements and behaviours present in this thesis will be reviewed. This thesis focuses on the properties TiO_2 arrays, the basic element of these arrays is the TiO_2 pillars. The TiO_2 pillars can be considered as a dielectric material in the visible light range and the TiO_2 has almost zero absorption for wavelengths >350 nm. Therefore, the scattering properties of dielectric resonators and the multipole role in the scattering will be discussed. The TiO_2 arrays used in this thesis are 2-D periodic nanopillar square arrays on top of a residual TiO_2 layer built on a glass substrate. The properties of the collective resonances of dielectric arrays will also be discussed in this section.

2.1 Scattering Properties of Dielectric Resonators

Analytical solutions of the scattering properties of particles of subwavelength scale only exist for two geometries, a sphere and infinite cylinder in a homogeneous medium. The scattering properties for a sphere can be obtained by Mie theory. Mie theory was developed in the early 1900s and it is named after Gustav Mie, a main contributor who wrote the key paper in 1908[79]. The basis of Mie theory is given below, for a complete derivation and further information refer to Ref[26]. Maxwell's curl equations in Gaussian units, with fields with a time dependence of $e^{i\omega t}$, no charges, and setting the magnetic permeability to 1, can be simplified to

$$\begin{aligned} \boldsymbol{\nabla} \times \vec{\boldsymbol{H}} &= \mathrm{i}km^2\vec{\boldsymbol{E}} \qquad (\boldsymbol{a}) \\ \boldsymbol{\nabla} \times \vec{\boldsymbol{E}} &= -ik\vec{\boldsymbol{H}} \qquad (\boldsymbol{b}) \end{aligned} \qquad \text{2-1}$$

where $\vec{\boldsymbol{E}}$ is the electric field, $\vec{\boldsymbol{H}}$ is the magnetic field, k is the wavenumber in vacuum and m is the complex refractive index. Taking the divergence on both equations, using the identity $\boldsymbol{\nabla} \cdot \left(\boldsymbol{\nabla} \times \vec{\boldsymbol{A}}\right) = 0$, considering a homogenous medium with constant refractive index m, and a charge density of zero, Maxwell's divergence equations can be expressed as

$$\nabla \cdot \vec{E} = 0 \qquad (a)$$
$$\nabla \cdot \vec{H} = 0 \qquad (b) \qquad \text{2-2}$$

Under these conditions the electric and magnetic fields satisfy the scalar wave equation

$$\Delta \cdot \psi + k^2 m^2 \psi = 0 \qquad \text{2-3}$$

A simple solution to this equation is a plane wave propagating in the z direction

$$\psi = e^{ikmz - i\omega t} \qquad \text{2-4}$$

The scalar wave equation is separable under spherical coordinates

$$(x, y, z) \rightarrow (r\cos\varphi \sin\theta\,, r\sin\varphi\sin\theta\,, r\cos\theta) \qquad \text{2-5}$$

and in these coordinates, it has solutions of the form:

$$\psi_{ln} = \left.\begin{matrix}\cos l\varphi \\ \sin l\varphi\end{matrix}\right\} P_n^l(\cos\theta) z_n(mkr) \qquad \text{2-6}$$

where n and l are integers and $n \geq l \geq 0$, the first factor is either a cosine or a sine, $\boldsymbol{P_n^l}(x)$ are Legendre polynomials and $\boldsymbol{z_n}(x)$ is any spherical Bessel function. If function $\boldsymbol{\psi}$ satisfies the wave equation, vectors $\vec{M}_\psi$ and $\vec{N}_\psi$ are defined by

$$\vec{M}_\psi = \nabla \times (r\psi) \qquad (a)$$
$$mk\vec{N}_\psi = \nabla \times \vec{M}_\psi \qquad (b) \qquad \text{2-7}$$

They satisfy the wave vector equation and are related by

$$mk\vec{M}_\psi = \nabla \times \vec{N}_\psi \qquad (b) \qquad \text{2-8}$$

If u and v are two solutions to the scalar wave equation and $\vec{M}_u$, $\vec{N}_u$, $\vec{M}_v$, $\vec{N}_v$ are derived vectors, Maxwell's equations (**2-1 a,b**) are satisfied if

$$\vec{E} = \vec{M}_v + i\vec{N}_u \qquad (a)$$
$$\vec{H} = -m\left(\vec{M}_u + i\vec{N}_v\right) \qquad (b) \qquad \text{2-9}$$

The components of the vectors $\vec{M}_\psi = \left(M_r, M_\theta, M_\varphi\right)$ and $\vec{N}_\psi = \left(N_r, N_\theta, N_\varphi\right)$ are

$$M_r = 0 \qquad (a)$$
$$M_\theta = \frac{1}{r\sin\theta}\frac{\partial(r\psi)}{\partial\varphi} \qquad (b)$$
$$M_\varphi = -\frac{1}{r}\frac{\partial(r\psi)}{\partial\theta} \qquad (c) \qquad \text{2-10}$$
$$mkN_r = \frac{\partial^2(r\psi)}{\partial r^2} + m^2k^2r\psi \qquad (d)$$

$$mkN_\theta = \frac{1}{r}\frac{\partial^2(r\psi)}{\partial r \partial \theta} \qquad (\boldsymbol{e})$$

$$mkN_\varphi = \frac{1}{r\sin\theta}\frac{\partial^2(r\psi)}{\partial r \partial \varphi} \qquad (\boldsymbol{f})$$

For the scattering of a homogenous sphere of radius a and refractive index m at the origin of the coordinate system, in vacuum ($m_2 = 1$) and incident electric field polarized along the x axis and traveling in the z direction is described by

$$\vec{\boldsymbol{E}} = \hat{\boldsymbol{e}}_{\boldsymbol{x}} e^{-ikmz+i\omega t} \qquad (\boldsymbol{a})$$

$$\vec{\boldsymbol{H}} = \hat{\boldsymbol{e}}_{\boldsymbol{y}} e^{-ikmz+i\omega t} \qquad (\boldsymbol{b}) \qquad \text{2-11}$$

The incident fields, the scattered fields and the internal fields of the sphere can be written from two solutions to the scalar wave equation in spherical coordinates, as shown above. The equations for the internal and incident fields will not be shown here, for the complete derivation refer to Ref[26]. The scattered fields can be expressed by the following two solutions to the scalar wave equation be taking into consideration the infinity conditions

$$u = e^{i\omega t}\cos\varphi \sum_{n=1}^{\infty} -a_n (-i)^n \frac{2n+1}{n(n+1)} P_n^1(\cos\theta) h_n^2(kr) \qquad (\boldsymbol{a})$$

$$v = e^{i\omega t}\sin\varphi \sum_{n=1}^{\infty} -b_n (-i)^n \frac{2n+1}{n(n+1)} P_n^1(\cos\theta) h_n^2(kr) \qquad (\boldsymbol{b}) \qquad \text{2-12}$$

$h_n^2(kr)$ are the spherical Hankel functions of the second kind, due to their asymptotic behaviour at infinity. Only the scattering coefficients a_n and b_n need to be derived to solve for the scattered fields. The scattering coefficients are derived by applying boundary conditions at the boundary of the sphere to the field components. The solutions for these coefficients are expressed by Ricatti-Bessel function with the wave vector and radius of the sphere as arguments and they can be calculated by computational scripts. The scattering coefficients depend on the radius (a) and refractive index of the sphere m, and the refractive inside of the environment (m_2). Once these coefficients are calculated the extinction and scattering efficiencies can be calculated by

$$Q_{ext} = \frac{2}{x^2}\sum_{n=1}^{\infty}(2n+1)\,Re(a_n + b_n)$$

$$Q_{sca} = \frac{2}{x^2}\sum_{n=1}^{\infty}(2n+1)\,Re(|a_n|^2 + |b_n|^2) \qquad \text{2-13}$$

where $x = ka$. These infinite series can be terminated early after n_{max} iterations, the value for n_{max} was proposed by Bohren and Huffman (1983) as[80]

$$n_{max} = x + 4x^{1/3} + 2 \qquad 2\text{-}14$$

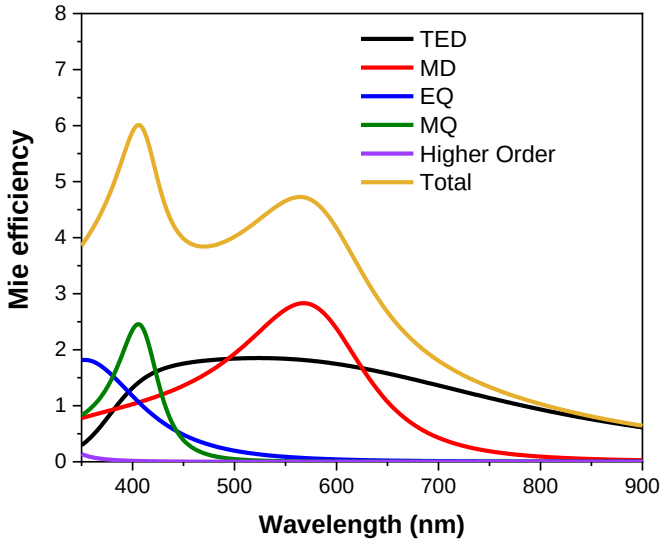

Figure 2-1 Scattering efficiency and the multipole contributions (electric dipole (TED), magnetic dipole (MD), electric quadropole (EQ), magnetic quadropole (MQ) and higher order terms) to the scattering for a dielectric sphere with refractive index = 2.1 and 130 nm radius in vacuum calculated from a Mie MATLAB script from Ref[80].

The multipole contributions of the scattering and extinction can be calculated by only taking the contributions from a_1 for the electric dipole (ED), b_1 for the magnetic dipole (MD) contributions[27,81] and a_2 for the electric quadrupole (EQ) and b_2 for the magnetic quadrupole (MQ). An example of the scattering and the multipole contributions of a sphere is shown in **Figure 2-1**. The positions of the multipole contributions can change by shifts in the refractive index of the sphere and radius. The shape of the scattering spectra can be changed by varying the refractive index and radius of the sphere. As seen in **Figure 2-2 a-d**, the multipoles become sharper with increasing refractive index, this is due to the increase in confinement of the resonance in the sphere with increasing refractive index. The multipoles also have different sensitivities to changes in the refractive index, the quadrupoles peak position does not increase as much as the dipoles with increasing refractive index, also the sensitivities are different for the magnetic and electric multipoles. The wavelengths of the multipoles in the scattering spectra can also be altered by the radius of the sphere as seen in **Figure 2-3 a-d**. As seen for changes in refractive index, the multipoles have different sensitivities to the radius of the sphere. The

quadrupoles are less sensitive to the radius of the sphere compared to the dipole moments and the electric and magnetic multipoles also exhibit different sensitivity to the radius. With increasing radius, the intensity of the peaks decreases. Multipole decomposition by Mie theory is only applicable for spheres.

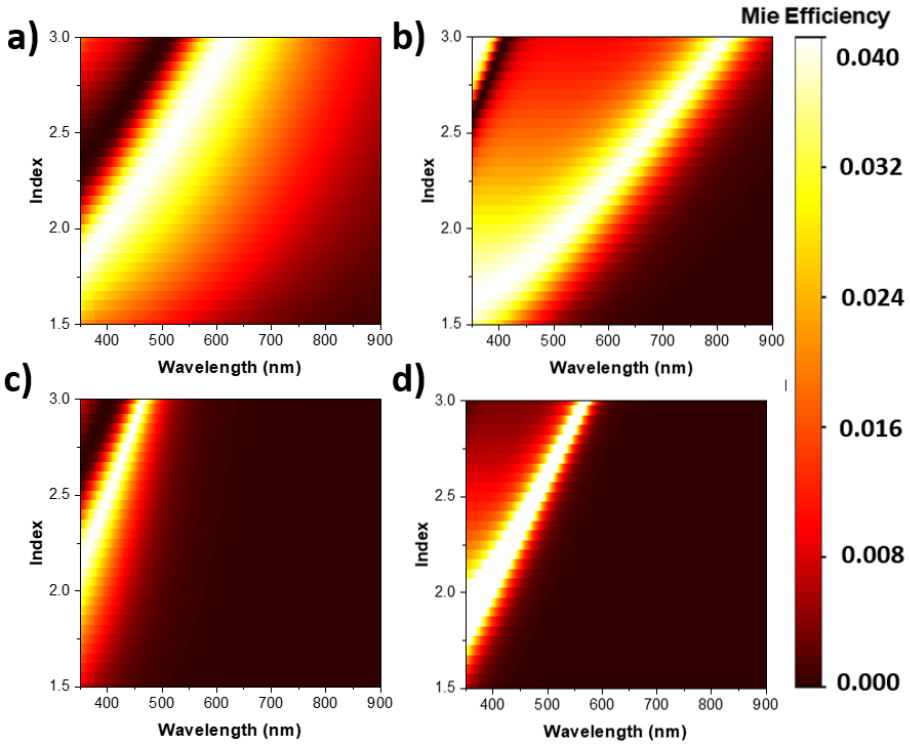

Figure 2-2 Scattering efficiency of the multipole contributions for a dielectric sphere with 130 nm radius in vacuum for different refractive index calculated from a Mie MATLAB script from Ref[80]. a) electric dipole, b) magnetic dipole, c) electric quadrupole, and d) magnetic quadrupole.

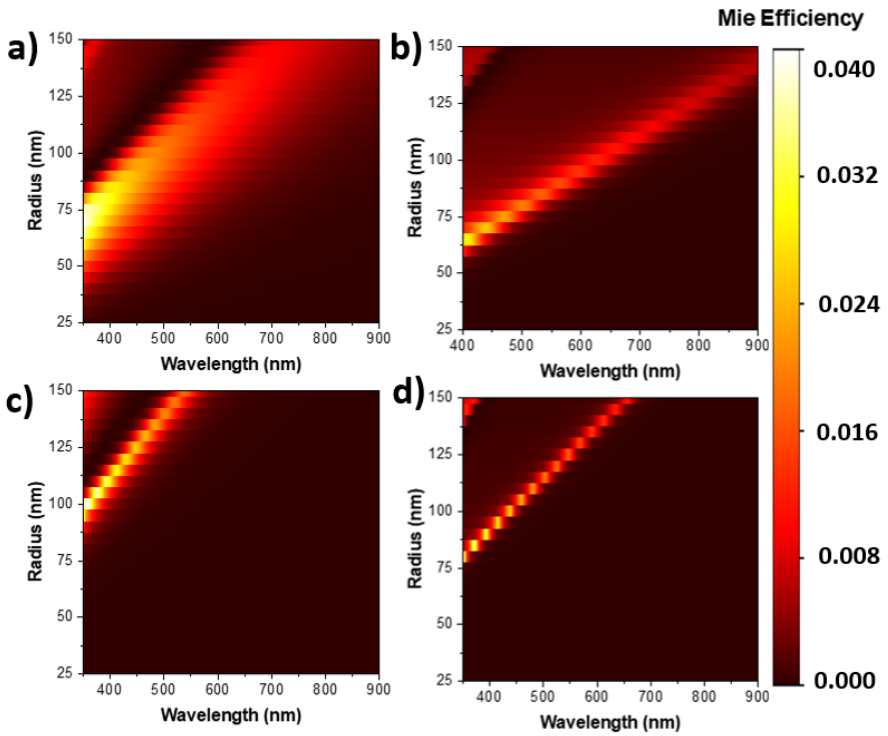

Figure 2-3 Scattering efficiency of the multipole contributions for a dielectric sphere with refractive index of 3 in vacuum for different radii, calculated from a Mie MATLAB script from Ref[80]. a) electric dipole, b) magnetic dipole, c) electric quadrupole, and d) magnetic quadrupole.

The shape of the scattering spectrum changes with refractive index (**Figure 2-4 a**), particle size (**Figure 2-4 b**) and particle shape (**Figure 2-4 c**). **Figure 2-4 c** shows the scattering spectra of the differently shaped particles calculated by finite difference time domain simulations. Mie theory is only applicable on spheres, to calculate the scattering spectra of arbitrarily shaped particle numerical methods must be used. The scattering spectra are normalized to the incident wave intensity. The scattering spectra changes significantly by going from a sphere to a square to a cylinder with the same size of diameter as the sphere. A drastic change is observed when reducing the height of the cylinder by half, the magnetic dipole of a particle requires field retardation for a displacement current loop, if the particle is too shallow the magnetic dipole is supressed while the electric dipole can still exist if the magnetic permeability is 1 inside and outside the particle as the magnetic current caused by the electric dipole can exist outside the particle[82]. The magnetic and electric dipole can be made to overlap by changing the aspect ratio of the particle[54]. Another interesting property of dielectric nanoparticles is that they can exhibit nonradiating anapoles which are formed by the destructive interference between the toroidal dipole and the electric dipole, resulting in a zero contribution to the far-field[22]. Anapoles in the optical range have been observed in silicon disks[83]. Dielectric nanoparticles are affected by their supporting substrate supporting, however in contrast to their

plasmonic counterparts the effects of the substrate on the scattering are reduced as the fields in dielectric particles are more concentrated inside the nanoparticle[82]. The dipole resonances broaden and increase in scattering efficiency with increasing refractive index of the susbtrate[82].

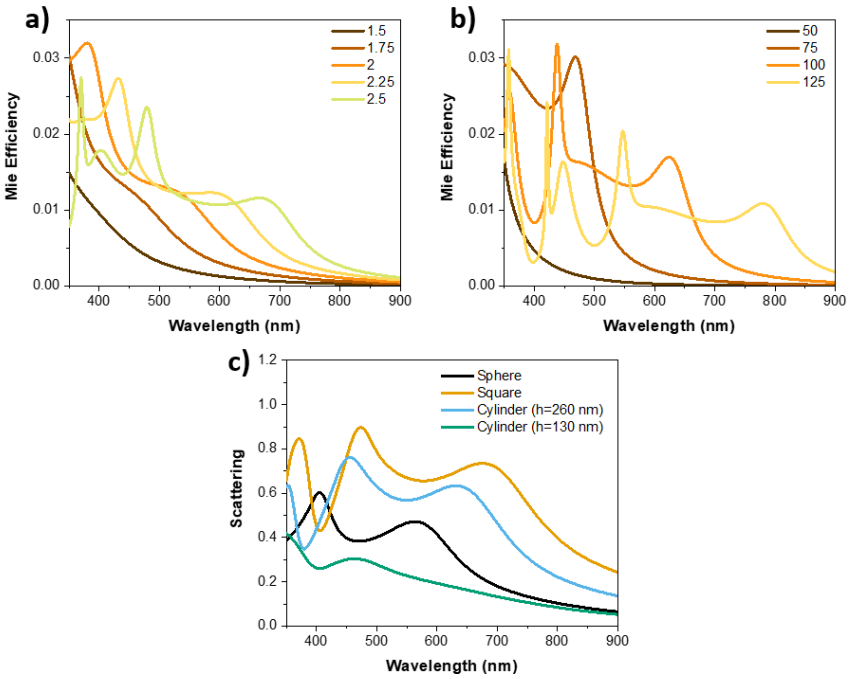

Figure 2-4 a) Total scattering efficiency for a dielectric sphere with radius of 130 nm over a range of refractive indices b) Total scattering efficiency for a dielectric sphere with refractive index =3 radii varying from 50 to 125 nm. Calculated from a Mie MATLAB script from Ref[80]. c) Scattering spectra normalized to the source intensity calculated by FDTD simulations for different shapes: sphere with diameter of 260 nm. square with lengths of 260 nm, and two cylinders with diameter of 260 nm and heights of 260 nm and 130 nm, respectively. All with refractive index of 2.1.

2.2 TiO_2 Arrays: Photonic Crystal or Metasurface?

In this section the literature is reviewed on what type of structure the TiO_2 arrays in this thesis are. These TiO_2 arrays have Mie resonators as building blocks with resonances in the visible and have a periodicity in the order of the wavelength of visible light. Photonic crystals (PC) are spatial ordered materials with a periodically varying refractive index, the periodicity is in the order of the wavelength of light, for visible light it means a periodicity of 100-1000 nm[84]. Photonic crystals due to the destructive interference of light by the periodicity of the refractive index have photonics gap, i.e., certain in-plane light wavevectors cannot propagate in the crystal. Dielectric metasurfaces are described in literature as ordered lattices of

nanoparticles that alter light at subwavelengths scales[85] and also as "two-dimensional structure enabling complete control on light amplitude, phase, and polarization" with strong light-matter interaction on a subwavelength scale[86]. 2-D dielectric arrays with periodicities in the order of the wavelength of light are described in literature as and with Dielectric metasurfaces[32,50,52,54,54,69,71,75,85]. However, there is also in literature 2-D arrays of dielectric nanoparticles with dielectric nanoparticle and periodicity in the order of the wavelengths and similar geometries being referred to 2-D photonic crystals[87–89]. However, photonic crystals do not require for the nanoparticles to support resonances in wavelengths relevant to the diffraction orders and the focus is usually on the photonic bandgap effects, whereas in a metasurface the interesting effect is in the collective resonances of the particles in the arrays. Since these arrays have Mie resonators as building blocks, they are considered metasurfaces.

2.3 Collective Resonances and Quasi-Guided Modes in Dielectric Arrays

Dielectric arrays allow the light to be controlled not only by the particle's resonances but also by the structure of the array. Ordered structures have interesting properties that arise from the lattice order such as Rayleigh anomalies (RAs). Collective resonances that appear due to the RAs in dielectric arrays are called surface lattice resonances (SLRs) [32,36]. The spectral positions of the RAs are calculated using the grating equation[32]

$$\vec{k}_{\parallel d} = \vec{k}_{\parallel \mathrm{i}} + \vec{G} \qquad 2\text{-}15$$

$\vec{k}_{\parallel d}$ is the wave vector for the in plane diffraction orders which are the Rayleigh anomalies, $\vec{k}_{\parallel i}$ is the in plane projection of the incident wave vector, and $\vec{G}$ is the reciprocal lattice vector of the dielectric array. For normal incidence ($\vec{k}_{\parallel i} = 0$) and a rectangular lattice the wavelength of the RAs can be calculated by[85]

$$\lambda_{RA} = \frac{n}{\sqrt{\left(\frac{m_x}{a_x}\right)^2 + \left(\frac{m_y}{a_y}\right)^2}} \qquad 2\text{-}16$$

where a_x and a_y are the lattice constants in the x and y direction. m_x and m_y are the positive integers, and n is the refractive index of the environment. The different order of RAs are

described by the two integers (m_x, m_y), first order (1,0) and (0,1), mixed first order RA (1,1), second order RA (2,0) and (0,2) and so on.

Arrays embedded in a homogenous environment can exhibit sharp scattering features when the individual particles resonances (ED, MD) couple to the RAs of the array structure. Work done on hexagonal silicon disk array embedded in a homogenous environment by Castellanos et al.[32] on the finite difference time domain calculated extinction spectra in **Figure 2-5 c** (schematics in **Figure 2-5 a**) showed that both the ED and MD can couple to RAs to form SLRs. As seen in **Figure 2-5 c** for the disk with diameter of 110 nm the larger sharp peak at 627 nm is due to the ED coupling to the first order RA at 613 nm and the smaller peak at 617 nm is the MD coupled to the first order RA ($m_x + m_y = 1$). They refer to these sharp features as ED-SLR and MD-SLR. The positions of this resonances can be controlled by the shape of the particle as seen in **Figure 2-5 c**, the resonances blue shift with decreasing diameter. Another interesting feature of these coupled resonances is that there is a strong electric field enhancement outside the particle. However, if the array is not embedded in a homogenous medium, SLRs cannot couple due to phase mismatching between RAs in the substrate and supersubstrate[32].

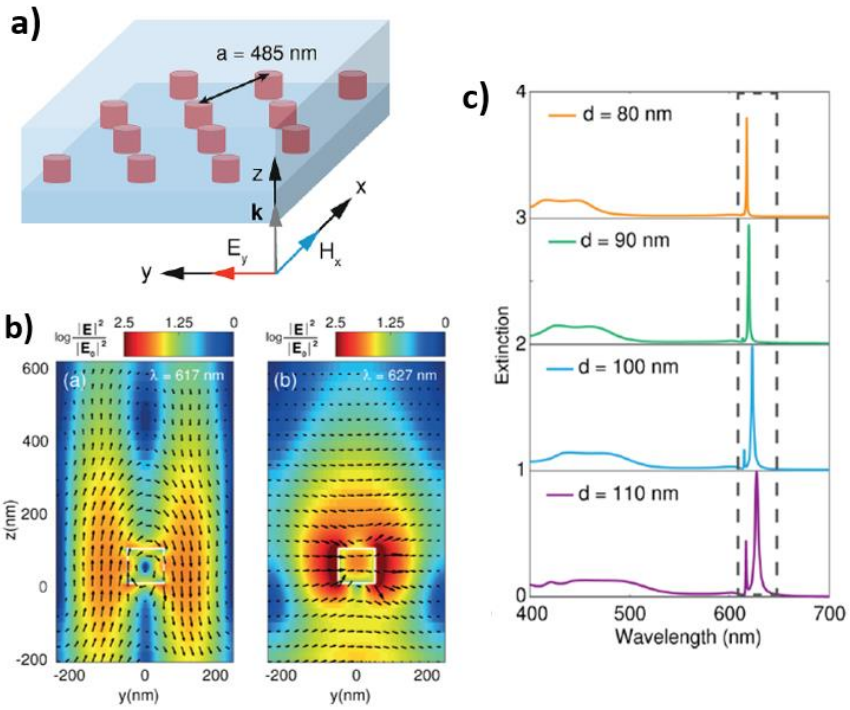

Figure 2-5 a) Schematic of a silicon disk hexagonal array embedded in a homogenous environment with refractive index of n=1.46. b) spatial distribution of the electric field intensity profile at the wavelengths corresponding to the ED-SLR (right) and MD-SLR (right). c) Extinction spectra for silicon disk hexagonal arrays with different silicon disks diameters, d. Results obtained using FDTD simulations. All images were taken from Ref[32]

Arrays are usually built on substrates this will limit the potential for SLRs to propagate, as the in plane-coupling strength of the particles can reduce due to surface mismatch between the substrate and supersubstrate in-plane diffraction orders[32]. However, if the arrays are coated with a thin layer of a dielectric material with higher refractive index than the substate, the array the layer can act as an optical wave guide and arrays can couple light as a diffractive grating into optically guided modes in the layer. These are known as quasi guided modes (QGMs) since the array particles eventually scatter these modes out of the waveguide[32,51,91]. The QGMs have been discussed in 1-D photonic crystal slabs in the early 2000s were they observed strong interaction between the plasmonic resonances of the 1-D grating and QGMs[91]. QGMs are also referred to in literature as guided modes resonances, in Ref[92] uses a 1-D grating very similar in geometry to Ref[91] and refers to the same phenomena observed as guided mode resonances. In this work they referred to this interaction as a waveguide-plasmon polariton as the plasmon transmute into the waveguide mode and vice-versa[93], however in other works involving dielectric material the coupling of QGMs being done by the array acting as a grating[32]. **Figure 2-6 a** show the schematics of such an array from Ref [51], like the SLRs coupled to the particle's resonance, the QGM produce sharp features in the extinction (**Figure 2-6 b)** and yield high intensity electric field in the layer guiding the QGM (**Figure 2-6 c)**. Another configuration for dielectric nanoparticle arrays to allow QGMs to propagate is by placing the array on top of a waveguide **Figure 2-7 a** (images of **Figure 2-7** taken from Ref[50]), like the previous configuration these QGMs exhibit strong sharp extinction resonances seen as the sharp dips in transmission in **Figure 2-7 b** and generate strong electric field intensities confined in the waveguide **Figure 2-7 c**.

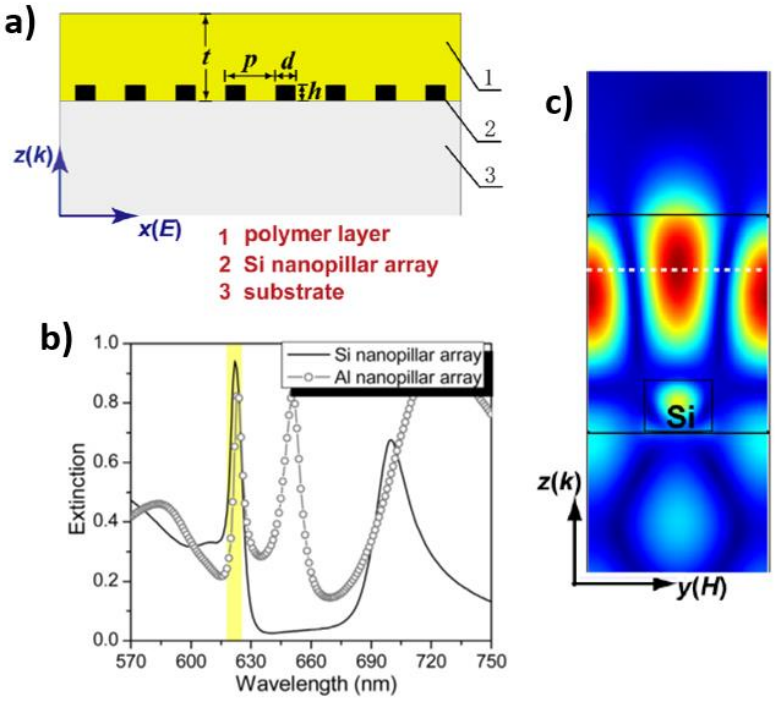

Figure 2-6 a) Schematic of a silicon disk square array on glass embedded in a 525 nm thick polymer waveguide with refractive index of n=1.59. b) Extinction spectra for silicon disk square array embedded in a 525 nm thick polymer waveguide with refractive index of n=1.59, c) Spatial distribution of the electric field intensity at the wavelength of the peak highlighted in yellow in b). Results obtained from computer simulations. Images taken from reference [51].

The positions of the QGMs can be varied by changing the periodicity of the structure **Figure 2-7 b**, the thickness of the layer[50,51], and the refractive index of the layer. However, they are not very sensitive to changes in the size and shape of the nano particle but the intensity of the QGMs will vary by changing the aspect ratio[51]. Since the QGMs are heavily influenced by the periodicity of the array, they are clearly coupled to the RAs. An interesting phenomenon arising from these structures is the electromagnetically induced transparency (EIT) -like effect. This occurs from the destructive interference between the QGMs and the magnetic dipole and requires overlap between them[50].This is observed in the near one transmission band appearing in the transmission spectra in **Figure 2-7 b** and the near zero extinction band in **Figure 2-6 b**. When fabricating arrays, the size of these arrays will not be infinite, the size of the array matters, and results will be different in finite arrays compared to the infinite arrays generally used in theoretical works[74]. Arrays need to be significantly larger than 100 by 100 units to converge to the infinite array, even so weak collective resonances are observed for small arrays (15 x 15) that get stronger with increasing array size[74]. The fidelity of the array elements is also important when fabricating arrays, collective resonances are still present, although weak, with 51% of the

particles missing, however positional and size disorders can drastically suppress the collective resonances[75].

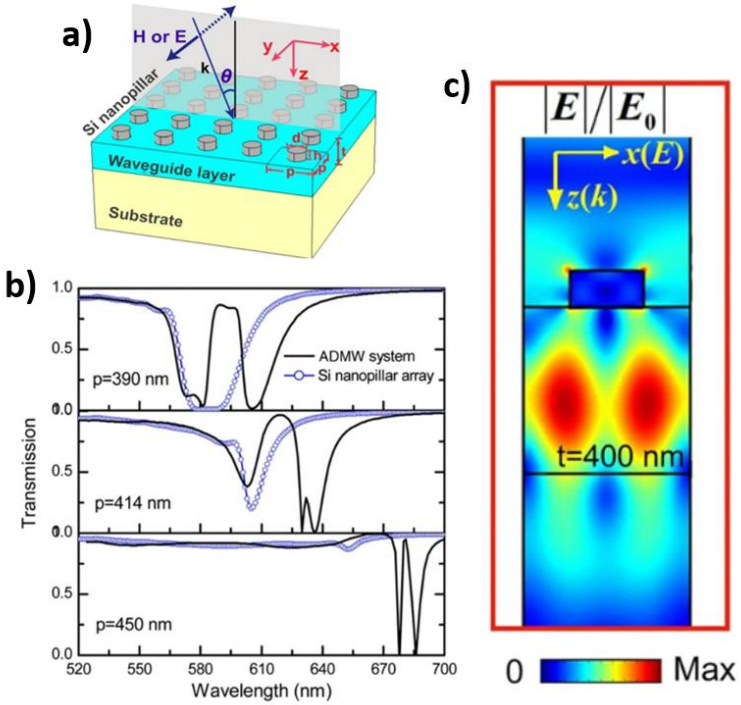

Figure 2-7 a) Schematic of a silicon disk square array on a polystyrene, n=1.59, 400 nm thick waveguide layer on a glass substrate. b) Transmission spectra for array depicted in a) for different periodicities, p, and c) spatial distribution electric field intensity. Results obtained from computer simulations. Images taken from Ref[50].

2.4 Conclusion

In this chapter the theory and properties of dielectric "Mie" resonators was discussed, giving the foundation into the behaviour of the TiO_2 pillars present in the arrays. The TiO_2 pillars have multipole scattering resonances (TED, MD, EQ, MQ) that will vary in shape and wavelength when the dimensions of the pillar change. As discussed, these arrays will likely not be able to support SLRs due to phase mismatching between the substrate and super substrate RAs. However, these arrays have the possibility to support electric and magnetic QGMs propagate in the residual layer underneath and generate high E-fields in the layer. The positions of the QGMs is mainly determined by the RAs and layer properties.

3 Materials and Methods

This chapter focuses on the materials and methods relevant for this thesis. Firstly, the physical properties of the arrays will be discussed, followed by an overview of the fabrication method of the arrays, the soft-nanoimprint lithography. This section will compare this method to others and state its benefits from other fabrication methods. The numerical method used to calculate the optical properties of the arrays is Finite Difference time domain method for computational electrodynamics. The basic theory behind the method and the simulation parameters will also be discussed. Finally, the method used for the decomposition of the scattering spectra into its multipole components for arbitrarily shaped objects will be presented.

3.1 Material: Titanium Oxide Arrays

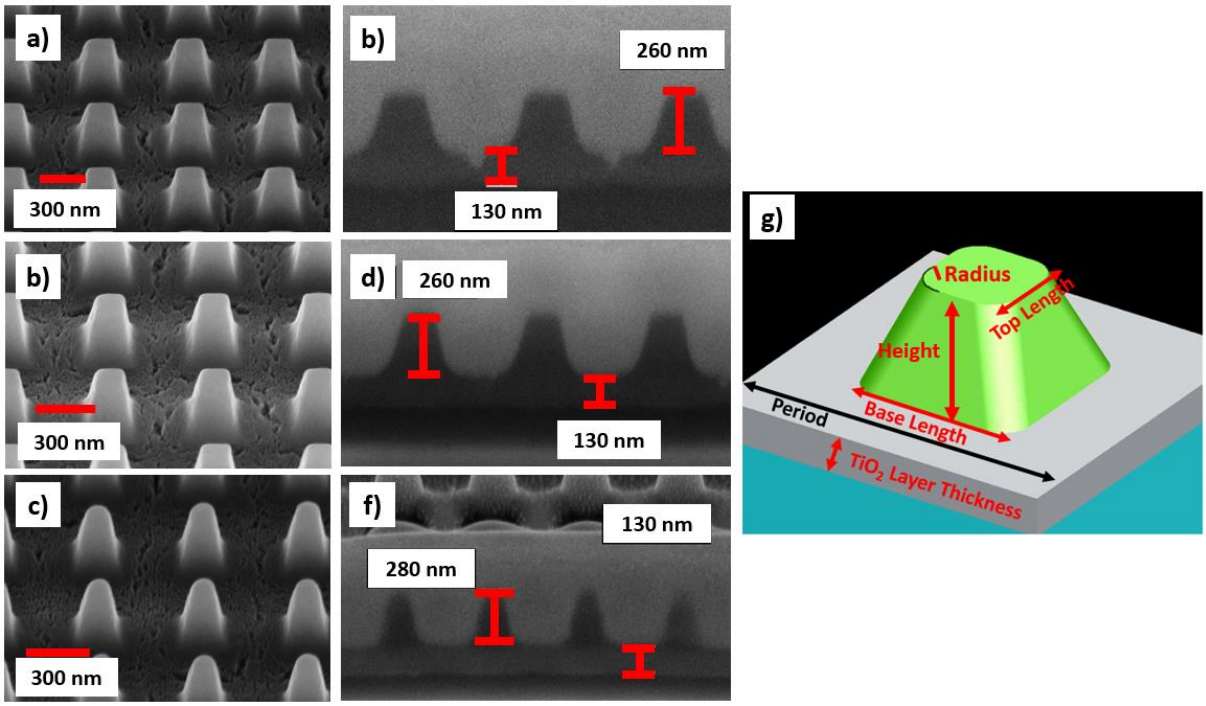

Figure 3-1 (a,c,e) Tilted scanning electron miscroscope (SEM) images of the A600, A550 and A480 arrays, respectively. (b,d,f) SEM images of array crossections of the A600, A550 and A480 respectivley. The cuts were performed by coating the arrays with platinum and then cutting with a focused ion beam. (g) diagram of geometric properties of the TiO_2 arrays.

The focus of this thesis are TiO_2 arrays fabricated *via* soft nano imprint lithography (soft-NIL method), as described used in these works[68,69]. They were fabricated by the group of

Marco Abbarchi from Aix-Marseille Université, Marseille, France. Three arrays are investigated in this work, and are labelled A600, A550, and A480. Each array covers an area of 1mm^2. These arrays were all fabricated on the same glass substrate and are different from each other by the periodicity and the pillar dimensions. Scanning electron microscope (SEM) images of the arrays are shown in **Figure 3-1**. The pillars in the arrays have the shape of a truncated square pyramid and are characterized by the dimensions shown in **Figure 3-1 g**. These are the length of the base (base length), the length of the top surface (top length) and the height of the pillar and the roundness if the corners (radius). The properties of the arrays are given in **Table 3-1,** the dimensions were obtained by measuring SEM imaging of the TiO_2 arrays cross-section cut by a focused-ion beam**.** Due to the nature of the fabrication method of the arrays, soft-nanoimprint lithography, a thin TiO_2 layer is left behind underneath the pillars. In **Figure 3-1 b, d** and **f** the thickness of the residual layer is measured to be roughly 130 ± 10 nm. The TiO_2 on this residual layer, as seen in **Figure 3-1 a, c** and **e** and **Figure 3-2 a,** is much rougher and porous compared to the TiO_2 of the pillar. This is likely caused by the removal of the silicon mould during fabrication as the pillars probably slightly stick to the mould resulting in a pull on this residual layer until the pilar is eventually released from the mould. The holes in the residual layer observed between the pillars can be up to 80 nm deep, **Figure 3-2 c** shows a closeup of the cross section of a hole (highlighted in red). The residual layer off the arrays, on the glass substrate a residual TiO_2 layer is also present on the glass substrate besides the arrays, is flat (much less rough) **Figure 3-2 b**. The TiO_2 layer off the array is thicker than on the arrays at ~180 nm. However, observations on the roughness are only made based on the images. Atomic force microscope measurements could have been used to confirm the surface roughness of the layers. This residual layer off the arrays has no effects on the measurement properties of the arrays as long as measurements are performed far from the edges of the arrays.The roughness is only observed on the arrays and not on the flat TiO_2 layer adjacent to the arrays in **Figure 3-2 b**. The TiO_2 layer off the array is thicker than on the arrays at ~180 nm.

Table 3-1 Dimensions of the A600, A550 and A460 arrays. The uncertainty in these measurements is ±10%. All arrays have the same area of 1 mm^2, A600 having the least amount of pillar density and the A480 the highest.

Array	Period	Base Length	Top Length	TiO_2 Layer Thickness	Height
A600	600 nm	320 nm	170 nm	~130 nm	260 nm
A550	550 nm	280 nm	150 nm	~130 nm	260 nm
A480	480 nm	185 nm	75 nm	~130 nm	280 nm

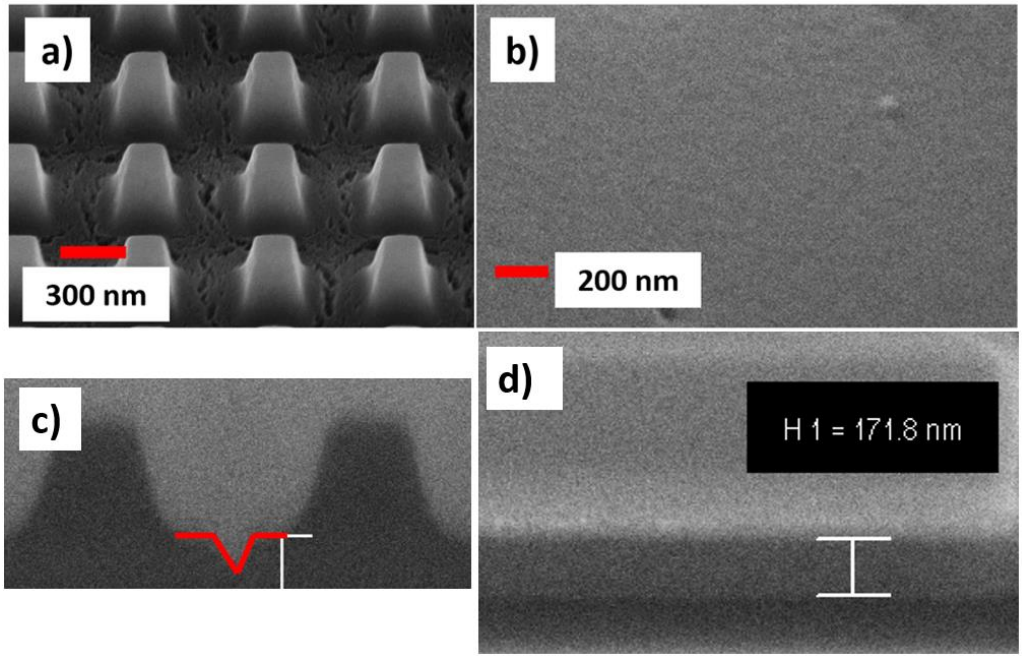

Figure 3-2 a) SEM image of the A600 array. The layer between the pillars is very rough and porous. b) SEM image of the TiO_2 layer next to the arrays. It is very smooth compared to the layer between the pillars. c) Close up of cross-section of the A600 array, focusing on the trenches that formed between the pillars. The trench is highlighted in red and is 70 nm deep. d) SEM image of the cross section of the TiO_2 layer next to the arrays, the layer has a thickness of 170 nm.

3.2 Soft Nano Imprint Lithography

Fabrication methods for dielectric metasurfaces is generally done by using lithographic, chemical, dewetting and laser assisted methods[94]. Lithographic methods, such as electron beam lithography, and reactive ion beam etching, are multistep fabrication processes. They offer high reproducibility, complex shapes and, high resolution however they require costly equipment, and they are slow multistep methods is therefore impractical for large scale fabrication of nanostructures[94]. Chemical methods such as chemical vapor deposition, chemical etching sometimes used in conjunction with other fabrication methods, have the disadvantage of producing a lot of toxic waste, possible contamination of the nanostructures and require additional steps in the fabrication process making these methods impractical for large scale[94]. Solid state dewetting is a method that can be used for large scale fabrications, however this method requires high annealing temperatures of greater than 750 degrees[68]. These high temperatures pose a problem as this makes the method incompatible for building surfaces of

various kinds of substrate and devices. This method is simple and has high yield but it does not offer a lot of control on the arrangements of nanoparticles[94].

Fabrication of TiO_2 metasurfaces by soft-nanoimprint lithography (soft-NIL) is proposed as an ideal method, due to its low annealing temperatures of 350°C (max), the patterning process does not damage the substrate, it is fast and cost effective. Fabrication of TiO_2 metasurfaces by soft-NIL involves three steps as outlined **Figure 3-3 a**, involving TiO_2 xerogel dip-coating, nanoimprinting, and finally thermal annealing, as explained in Ref[68]. This method also requires a silicon master mould with the desired pattern. The silicon master mould is fabricated by other fabrication methods which offer high accuracy and reproducibility. The use of this master is what makes this method highly accurate while being cheap and fast. Below is a rough description of the steps in soft-NIL, for more details on the fabrication method of these arrays see Ref[68].

1. A glass or silicon substrate is immersed by dipping into a $TiCl_4$: EtOH: PEO-PPO-PEO Pluronic F127 (Aldrich): H_2O solution. This step covers the substrate with TiO_2 xerogel. The thickness of the xerogel layer is controlled by the withdrawal speed.
2. PDMS mould fabricated from the silicon master is placed on top of the TiO_2 xerogel surface. They are placed in a cold heat plate for 10 minutes in a primary vacuum.
3. Annealing for 3 minutes at 120°C
4. The PDMS mould is then removed.
5. Annealing for 10 min at 350 °C for 10 min. This is necessary to remove of the F127 polymer and for the TiO_2 xerogel to condensate and crystallize into anatase.

The pillars fabricated by Soft-NIL will have smaller features than the silicon master as seen in **Figure 3-3 c** and **d**, this is due to the removal of the solution components and the condensation of the xero gel during the annealing processes. The result of using this fabrication method by using a silicon master with square pillars are truncated pyramids as seen in **Figure 3-3 a** and **e**. A residual layer of TiO_2 left behind from the pressing of the mold as the mold never penetrates the xerogel all the way to the substrate.

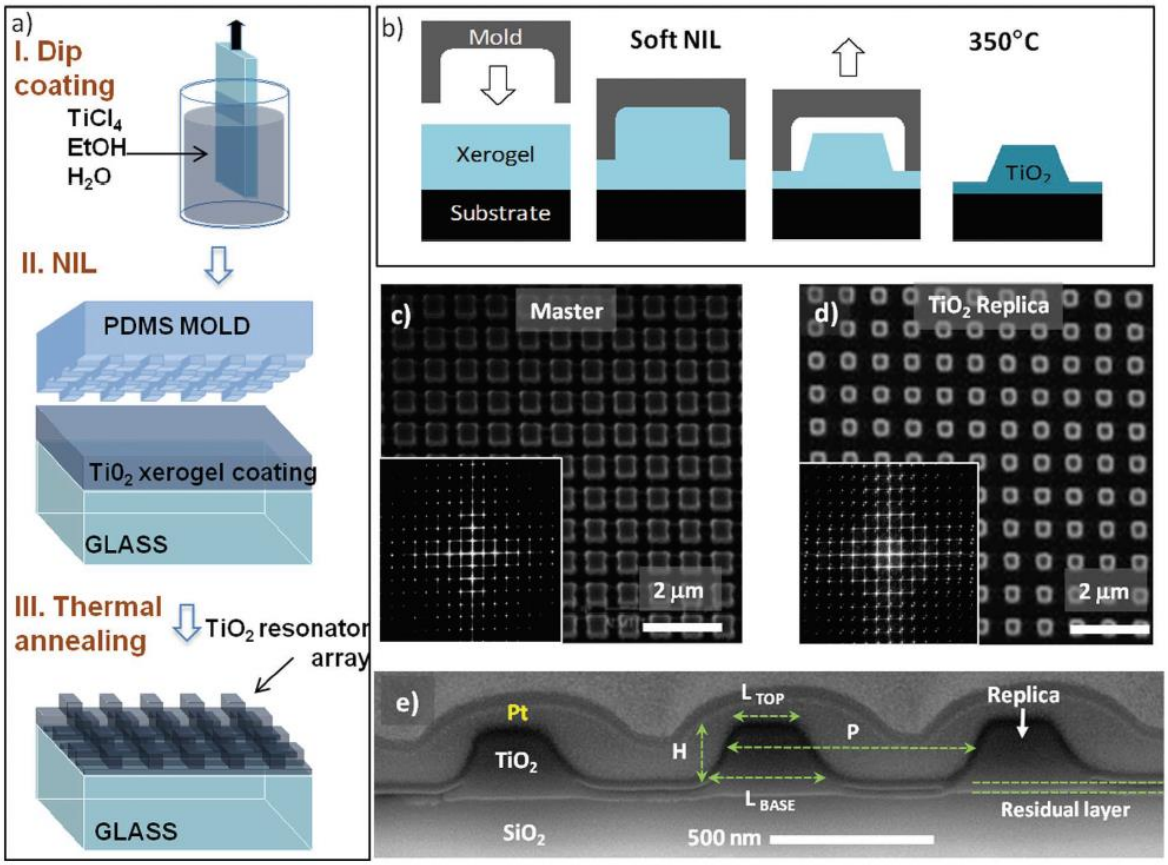

Figure 3-3 a) Flow diagram illustrating the three successive steps applied to elaborate the arrays from sol–gel/NIL process. b) Detail of the NIL process (steps II and III in panel (a)). c) HR-SEM images of the silicon master. d) Same as (c) for the corresponding TiO_2 pillars arrays replica on a glass. The Fourier transforms of the corresponding HR-SEM image are given in the bottom left inset. e) HR-SEM image of the pattern profile (from a similar sample of that shown in panels (c) and (d). The horizontal dashed lines represent the residual TiO_2 layer. The sample was prepared via LMIS-FIB milling. From the top to the bottom of the image are highlighted the protective platinum layer (Pt, deposited for enhancing the contrast with the TiO_2), the TiO_2 MR, the residual 2D TiO_2 layer, and finally, the underlying SiO_2 substrate. The relevant parameters of the pillars (height, *H*, base size, L_{BASE},top size, L_{TOP}) and of the pattern periodicity (P) are highlighted. (caption and image taken from Ref[68].

3.3 Sample Preparation: R6G on TiO_2 Arrays

Chapters 5 and 6 focus on the interactions between R6G and TiO_2 arrays. R6G was added on the TiO_2 arrays by spin coating a solution of R6G in ethanol. The R6G solution in ethanol has its photoluminescence peak at 560 nm. Before R6G is added, the arrays were bathed in acetic acid for 10 minutes, afterwards bathed for 10 minutes in acetone, then rinsed in IPA and dried before spinning coating. 125 µL of the R6G in ethanol solution were dropped with a pipette onto the arrays and left to rest for 30 seconds before spin coating. To spin a new solution of R6G on the arrays, they are rinsed with acetic acid to remove most of the R6G, then cleaned by the method described previously before spin coating the new solution. The arrays were

checked after cleaning to confirm that their optical properties were of were the same as before R6G was added.

3.4 Experimental Methods: Normal reflection, Normal transmission and Darkfield measurements

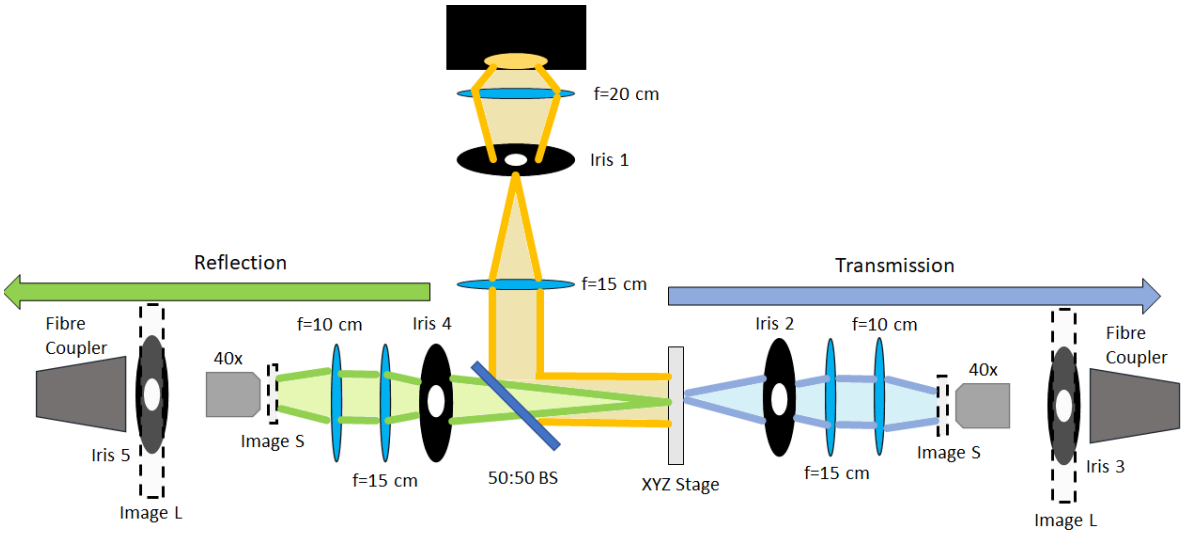

Figure 3-4 Shematics for the normal reflection and tranmission measurements set-up. The light source is a Xenon lamp.

The custom-built experimental set-up shown in **Figure 3-4** was used for the normal incidence and collection reflection and transmission measurements. Normal incidence light was used so the in-plane diffraction orders (RAs) do not depend on the incident light wavelength and consequently numerical simulations of the arrays are faster and simpler to perform using normal incidence light. This set-up allows for collection of light reflected and transmitted from a sample area of ~200 μm^2, this was done by Iris 3 and 5 cropping the expanded image of the arrays (Image L). A Xenon lamp was used as an illumination source, the filament of the source was imaged on Iris 1 and a bright uniform area of the filament was let through. A lens with f = 15 cm was placed 15 cm away from the Iris 1 to form an image at infinity. A very good collimated white light beam for the length of the set-up was formed. A 50:50 beam splitter (BS) was used as shown in the diagram above to direct the collimated white light beam toward the

sample and to allow the collection of the reflected light. The sample is mounted on an x,y,z stage which can be tilted on two different axes to adjust for tilt. The reflection and transmission segments are mirror images of each other, and both use the optics in the same manner. Light that gets transmitted from the sample is collected by a 15 cm focal length 2.54 cm diameter lens. Iris 2 has a 0.5 cm opening, and it is placed 12.5 cm away from the sample to reduce the collection angle, this yields a collection angle of 1.2°. The 2.54 cm diameter f = 10 cm lens placed directly behind the f = 15 cm lens forms an image ~10 cm away from the lens. A 40x objective collects the light from this image to form a magnified image on Iris 3, by moving the sample and closing or opening the iris an area can be selected. The light passing through Iris 3 goes into a fibre via a fibre coupler. The fibre directs the transmitted light into an Andor 230i spectrometer with an Andor CCD camera.

To obtain the percent of the light reflected the following equation was used:

$$R = \frac{R_s - Dark}{\frac{R_g}{0.08} - Dark} \qquad 3\text{-}1$$

$\boldsymbol{R_s}$ is the reflected light from the sample, $\boldsymbol{R_g}$ is the reflected light from a clean glass slide, this is used since glass reflection from a glass slide is ~8% across the visible spectra and can be divided by 8% to obtain the light source reference spectra. $\boldsymbol{Dark}$ is the background light collected with the white light beam blocked and also contains the dark counts of the spectrometer. The background light is unwanted stray light from computer monitors, light source reflections, etc. To obtain the percent of transmitted light through the array the following equation was used,

$$T = \frac{T_s - Dark}{T_{ns} - Dark} \qquad 3\text{-}2$$

$\boldsymbol{T_s}$ is the transmitted light from the sample, T_{ns} is the transmitted light when no sample is present. The extinction spectra can be calculated by:

$$Ext = 100\% - R - T \qquad 3\text{-}3$$

where *R* and *T* are the percentage of reflected and transmitted light collected from the arrays.

Darkfield scattering measurements of the arrays were obtained by using a darkfield microscope with 20x and 50x objectives. A darkfield microscope illuminates the sample with a cone of light and collects the reflected light within the cone that is not the 0-order reflection.

The scattered spectra were measured by an Andor 230i spectrometer coupled to an Andor CCD camera. To obtain the scattering spectra shown in Chapter 5.3, the raw measured scattering spectra from the sample were treated in the following way:

$$S^* = \frac{S - Glare}{Ref. - Glare} \qquad 3\text{-}4$$

where S^* is the treated scattering data, S is the untreated scattering data, *Glare* is the spectra when there is no sample in placed, and *Ref.* is the reference spectra of the white light obtained from a dark area on a glass diffuser.

3.5 Experimental Methods: Time Resolved Photoluminescence and Photoluminescence Measurements

The effects of the TiO_2 arrays on R6G emission were investigated in both the frequency and time domains. The photoluminescence spectroscopy in frequency and time domains was performed simultaneously using a PicoQuant Microtime 200 confocal microscope. Three different pulsed lasers were used to excite the R6G molecules in reflection geometry, using a 40x objective with NA of 0.6. The excitation wavelengths used were 375 nm, 405 nm and 466 nm. The photoluminescence (PL) emission from R6G was directed by a 50:50 beam splitter to an avalanche photodiode for time-resolved photoluminescence (TRPL) measurements and through a multimode fiber to a Czerny-Turner spectrometer (HORIBA Jobin Yvon TRIAX 190) equipped with a CCD camera (Symphony II) for recording the PL spectra. The instrument response function is approximately 150 ps in the TRPL experiments. In the measurements, the PL and TRPL were recorded by scanning an area of 80 x 80 μm^2 for 3 minutes with a step size of 280 nm and dwell time of 8 ms. PL was collected over the first 10 seconds of the scan of the 80 x 80 μm^2 scan meaning only 5.6% of the area of the scan was used to collect PL. Several different areas on the arrays and on the TiO_2 layer were recorded and averaged.

For analysis of the time decay of the photoluminescence, the decays were fitted by a tri-exponential as R6G lifetime on TiO_2 has a multi-exponential decay[95]. The PL decays were fitted by:

$$I(t) = A_1 e^{t/\tau_1} + A_2 e^{t/\tau_2} + A_3 e^{t/\tau_3} \qquad 3\text{-}5$$

From the fit, the intensity weighted average lifetime can be calculated by:

$$\tau_{avg} = \frac{A_1^2\tau_1^2 + A_2^2\tau_2^2 + A_3^2\tau_3^2}{A_1\tau_1 + A_2\tau_2 + A_3\tau_3} \quad 3\text{-}6$$

The PL decays were normalized to the maximum value of the PL decay. Time was shifted to have time=0 at the maximum of the PL decay, this facilitates the analysis of the data. The tri-exponential fits were done on the first 8 ns of the after the maximum of the PL decay.

3.6 Computational Methods: Finite Difference Time Domain Simulations

Numerical simulation of the properties of the TiO_2 array was performed using a finite difference time domain (FDTD) method for computational electrodynamics. This method is a numerical approach to solving Maxwell's equations in the time domain. The basic theory behind FDTD is the solving of the Maxwell's curl equations as shown below,

$$\nabla \times \vec{H} = \frac{\partial \vec{D}}{\partial t} + \vec{J} \quad (a)$$
$$\nabla \times \vec{E} = -\frac{\partial \vec{B}}{\partial t} + \vec{M} \quad (b) \quad 3\text{-}7$$

where $\vec{E}$ is the electric field strength vector, $\vec{H}$ is the magnetic field strength vector, $\vec{D}$ is the electric displacement vector, $\vec{B}$ is the magnetic density flux density vector, $\vec{J}$ is the electric current density vector and $\vec{M}$ is the magnetic current density vector. The derivation of the basic theory FDTD presented here very closely follows Ref [96]. Then equation 3-7 can be rewritten as

$$\nabla \times \vec{H} = \varepsilon \frac{\partial \vec{E}}{\partial t} + \sigma^e \vec{E} + \vec{J}_i \quad (a)$$
$$\nabla \times \vec{E} = \varepsilon \frac{\partial \vec{H}}{\partial t} + \vec{H} + \vec{M}_i \quad (b) \quad 3\text{-}8$$

by using the constitutive relations for linear isotropic and dispersive media,

$$\vec{\boldsymbol{D}} = \varepsilon \vec{\boldsymbol{E}} \quad (\boldsymbol{a})$$

$$\vec{\boldsymbol{B}} = \mu \vec{\boldsymbol{H}} \quad (\boldsymbol{b})$$

3-9

where ε is the permittivity and μ the permeability of the material, respectively. Also by substituting the electric current density $\vec{\boldsymbol{J}} = \vec{\boldsymbol{J}}_{\boldsymbol{c}} + \vec{\boldsymbol{J}}_{\boldsymbol{i}}$ as the sum of the conduction current density $\vec{\boldsymbol{J}}_{\boldsymbol{c}} = \sigma^e \vec{\boldsymbol{E}}$ (σ^e is the electric conductivity) and is the external current source $\vec{\boldsymbol{J}}_{\boldsymbol{i}}$ and the magnetic current density $\vec{\boldsymbol{M}} = \vec{\boldsymbol{M}}_{\boldsymbol{c}} + \vec{\boldsymbol{M}}_{\boldsymbol{i}}$ where $\vec{\boldsymbol{M}}_{\boldsymbol{c}} = \sigma^m \vec{\boldsymbol{H}}$ (σ^m is the magnetic conductivity). Then equations **3-8 a** and **b**, can be expanded into their 6 scalar components in 3-D cartesian coordinates

$$\frac{\partial E_x}{\partial t} = \frac{1}{\varepsilon}\left(\frac{\partial H_z}{\partial y} - \frac{\partial H_y}{\partial z} - \sigma^e E_x - J_{ix}\right) \quad (\boldsymbol{a})$$

$$\frac{\partial E_y}{\partial t} = \frac{1}{\varepsilon}\left(\frac{\partial H_x}{\partial z} - \frac{\partial H_z}{\partial x} - \sigma^e E_y - J_{iy}\right) \quad (\boldsymbol{b})$$

$$\frac{\partial E_z}{\partial t} = \frac{1}{\varepsilon}\left(\frac{\partial H_x}{\partial y} - \frac{\partial H_y}{\partial x} - \sigma^e E_z - J_{iz}\right) \quad (\boldsymbol{c})$$

$$\frac{\partial H_x}{\partial t} = \frac{1}{\mu}\left(\frac{\partial E_y}{\partial z} - \frac{\partial E_z}{\partial y} - \sigma^e H_x - M_{ix}\right) \quad (\boldsymbol{d})$$

$$\frac{\partial H_y}{\partial t} = \frac{1}{\mu}\left(\frac{\partial E_z}{\partial x} - \frac{\partial E_x}{\partial z} - \sigma^e H_y - M_{iy}\right) \quad (\boldsymbol{e})$$

$$\frac{\partial H_z}{\partial t} = \frac{1}{\mu}\left(\frac{\partial E_x}{\partial y} - \frac{\partial E_y}{\partial x} - \sigma^e H_z - M_{iz}\right) \quad (\boldsymbol{f})$$

3-10

From these equations if the material properties and the initial field conditions are known only the derivatives are needed to solve the equations. FDTD method is discrete in both space and time and therefore the FDTD simulation space is a discrete grid, the unit cell of this grid is called a Yee cell, named after Yee who derived the finite difference equation for Maxwell's curl equations in 1966[96]. Since both time and space are discrete in FDTD simulations, the derivatives are approximated by finite differences. The derivative of an arbitrary function $f(x)$ is,

$$f'(x) = \lim_{\Delta x \to 0} \frac{f(x + \Delta x) - f(x)}{\Delta x} \qquad 3\text{-}11$$

In the FDTD method Δx does not go to zero so the derivative can be approximated in the finite difference method by

$$f'(x) \approx \frac{f(x + \Delta x) - f(x)}{\Delta x} \qquad 3\text{-}12$$

This is the forward difference approximation and has an error of $O(\Delta x)$. The error can be further reduced to $O((\Delta x)^2)$ by approximating the derivative by the central difference

$$f'(x) \approx \frac{f(x + \Delta x) - f(x - \Delta x)}{\Delta x} \qquad 3\text{-}13$$

The error in the finite difference approximation can be further reduced by expanding and approximating to higher order derivatives. In FDTD simulations time advances in steps of Δt, however the electric and magnetic field components are sampled at different time instants. Electric field components are sampled at integers of Δt (0, Δt, $2\Delta t$…) and the magnetic field components are sampled at half integer times of Δt ($0.5\Delta t$, $1.5\Delta t$, $2.5\Delta t$…). Therefore, by implementing the central difference method to the spatial derivatives in equation **3-10 a** one arrives at the following equation

$$\begin{aligned} &\frac{E_x^{n+1}(n_x, n_y, n_z) - E_x^n(n_x, n_y, n_z)}{\Delta t} \\ &= \frac{1}{\varepsilon(i,j,k)} \frac{H_z^{n+\frac{1}{2}}(i,j,k) - H_z^{n+\frac{1}{2}}(i,j-1,k)}{\Delta y} \\ &- \frac{1}{\varepsilon(i,j,k)} \frac{H_y^{n+\frac{1}{2}}(i,j,k) - H_y^{n+\frac{1}{2}}(i,j,k-1)}{\Delta z} \\ &- \frac{\sigma^e(i,j,k)}{\varepsilon(i,j,k)} E_x^{n+\frac{1}{2}}(i,j,k) - \frac{1}{\varepsilon(i,j,k)} J_x^{n+\frac{1}{2}}(i,j,k) \end{aligned} \qquad 3\text{-}14$$

The superscript n is an integer number for the time step, indices i, j, k, are integers for movement between Yee cells of size ($\Delta x \times \Delta y \times \Delta z$) in the x, y and z direction, respectively. As mentioned before the electric and magnetic fields are sampled at different time instants in FDTD calculations, so there is no $E_x^{n+\frac{1}{2}}(i,j,k)$. $E_x^{n+\frac{1}{2}}(i,j,k)$ is substituted by the average between time instants $(n+1)\Delta t$ and $n\Delta t$:

$$E_x^{n+\frac{1}{2}}(i,j,k) = \frac{E_x^{n+1}(i,j,k) - E_x^n(i,j,k)}{2} \qquad 3\text{-}15$$

By solving for $E_x^{n+1}(i,j,k)$ in equation **3-14** by substituting in equation **3-15** the following equation is derived

$$\begin{aligned} E_x^{n+1}(i,j,k) = {} & \frac{2\varepsilon(i,j,k) - \Delta t\sigma^e(i,j,k)}{2\varepsilon(i,j,k) + \Delta t\sigma^e(i,j,k)} E_x^n(i,j,k) \\ & + \frac{2\Delta t}{\big(2\varepsilon(i,j,k) + \Delta t\sigma^e(i,j,k)\big)\Delta y}\Bigg(H_z^{n+\frac{1}{2}}(i,j,k) \\ & - H_z^{n+\frac{1}{2}}(i,j-1,k)\Bigg) \\ & - \frac{2\Delta t}{\big(2\varepsilon(i,j,k) + \Delta t\sigma^e(i,j,k)\big)\Delta z}\Bigg(H_y^{n+\frac{1}{2}}(i,j,k) \\ & - H_y^{n+\frac{1}{2}}(i,j,k-1)\Bigg) - \frac{2\Delta t}{2\varepsilon(i,j,k) + \Delta t\sigma^e(i,j,k)} J_x^{n+\frac{1}{2}}(i,j,k) \end{aligned} \qquad 3\text{-}16$$

The same process can be done to all the rest of the equations **3-10 (b-f)**, and with these equations the fields everywhere on the simulation grid can be propagated through time if the initial field conditions and material properties ε, σ^e, μ and σ^m are known.

In this thesis FDTD simulations are done with Lumerical, commercially available FDTD software. Lumerical was chosen due to the large library of built-in materials, user friendly graphical interface, simulation of a wide range of optical systems, and its use in numerous publications across many scientific fields. The results for the electromagnetic fields and power in Lumerical are in the frequency domain are normalized by the continuous wave (CW) normalization state that removes any frequency dependence to the finite pulse length. To obtain the electric field results in the frequency domain a Fourier transform is performed on the time domain:

$$\vec{\boldsymbol{E}}(\boldsymbol{\omega}) = \int e^{i\omega t}\, \vec{\boldsymbol{E}}(\boldsymbol{t})\, dt \qquad 3\text{-}17$$

In CW normalization the electric field is divided by the source signal in the frequency domain:

$$\vec{\boldsymbol{E}}_{\boldsymbol{cw}}(\boldsymbol{\omega}) = \frac{\vec{\boldsymbol{E}}(\boldsymbol{\omega})}{s(\omega)} \qquad 3\text{-}18$$

where

$$s(\omega) = \int e^{i\omega t}\, s(t)\, dt \qquad 3\text{-}19$$

$s(t)$ is the time dependence of the source. Similarly, for the magnetic field we have

$$\vec{\boldsymbol{H}}_{\boldsymbol{cw}}(\boldsymbol{\omega}) = \frac{\vec{\boldsymbol{H}}(\boldsymbol{\omega})}{s(\omega)} \qquad 3\text{-}20$$

and for the Poynting vector

$$\vec{\boldsymbol{P}}_{\boldsymbol{cw}}(\boldsymbol{\omega}) = \frac{\vec{\boldsymbol{E}}(\boldsymbol{\omega}) \times \vec{\boldsymbol{H}}^{*}(\boldsymbol{\omega})}{|s(\omega)|^2} \qquad 3\text{-}21$$

3.6.1 FDTD simulation set-up

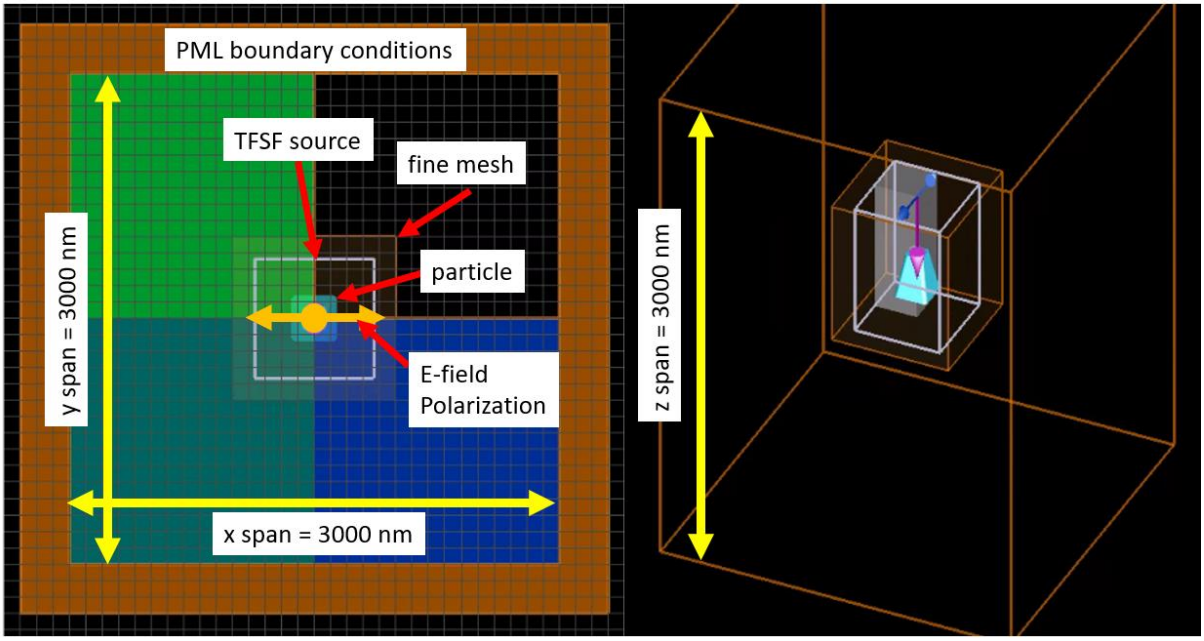

Figure 3-5 Schematics for single particle simulations in the Chapter 4, x, y view on the left and 3-D view on the right.

Schematics of the single particle simulations are shown in **Figure 3-5**. For the single particle simulation perfectly matched layer (PML) boundary conditions were used for the x, y and z boundaries. Since it is not possible to simulate infinite spaces PML boundary conditions are used to absorbed incident electromagnetic fields with near to no reflections that allow the

FDTD simulation to converge. A broadband (350-900 nm) Total-Field Scattered-Field (TFSF) source with the electric field polarized in the x direction propagating in the backwards z direction was used. A TFSF source is a planewave source that separates the simulation in two regions. One region inside the grey box shown in **Figure 3-5** that includes the incident field and the scattered field. The other region is outside the grey box, that only includes the scattered field. The TSFS source allows to obtain the scattering spectra easily by collecting the light leaving the TFSF region inside the grey box. A simulation span of 3 µm by 3 µm by 3 µm was used and the fine mesh had a step size of 5 nm in each direction. All the structures used in this thesis are symmetric in the x and y direction, therefore, to reduce computation time, the simulation space was reduced by 4 by applying symmetry boundary conditions in addition to the PML boundary conditions. Antisymmetric boundary conditions were used in the x axis since the electric field is polarized in the x axis. Symmetric boundary conditions were used for the y axis.

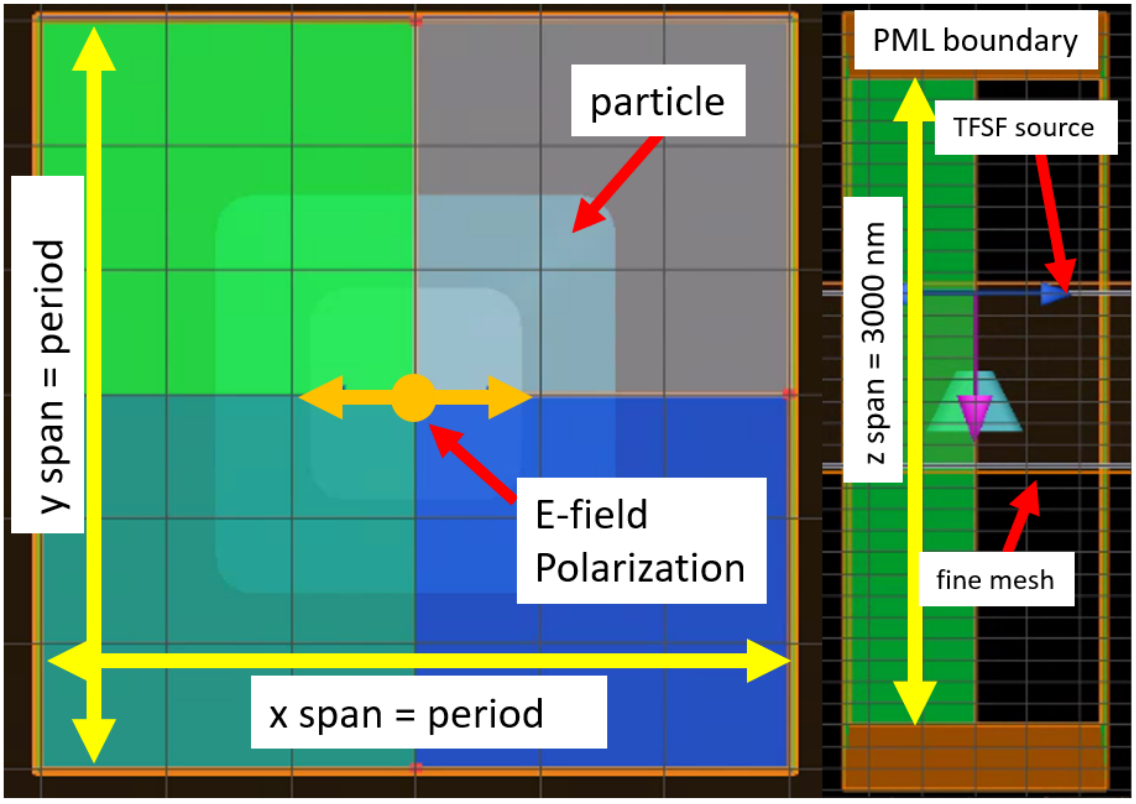

Figure 3-6 Schematics for array simulations in the Chapter 4, x-y view in the left and x-z view to the right.

Schematics of the single particle simulations are shown in **Figure 3-5**. The simulation conditions for the array simulations are nearly identical to the single particle simulations. Instead of having PML boundary conditions at the x and y boundary, period boundary

conditions are used. The x and y span of the single particle simulation are the periodicity of the array. Simulations of the arrays will be done by taking the shape of the pillars to be that of a rounded truncated pyramid. The pillar shape used in the simulation is of a rounded square truncated pyramid (**Figure 3-7 a**). The pillars have the following properties, base length, top length, height, roundness, and refractive index. For the base length, top length and height unless otherwise specified, the dimension for these properties for the A600, A550 and A480 pillar are the same as in **Table 3-1**. A radius of 30 nm for the roundness of the corners was used for all the pillars as this gives a good resemblance to the pillars in the SEM images, however this feature has little to no influence on the properties of the arrays. The glass substrate is used in the simulations unless otherwise specified. They are modelled as dielectrics with refractive index of 1.5 and extends to the edge of the simulation region. The refractive index used for the pillars and the TiO_2 layer are specified in each of the results chapters. The TiO_2 layer thickness is 130 nm for all the arrays unless specified.

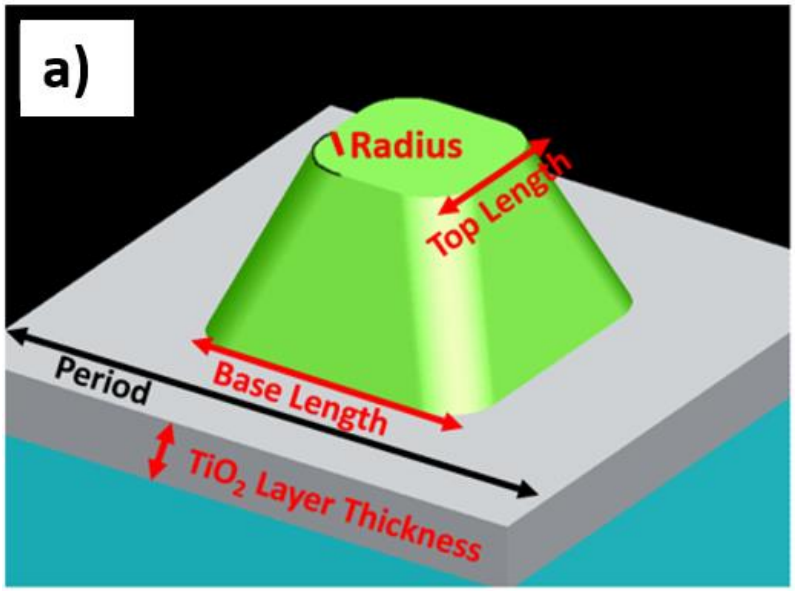

Figure 3-7 Diagram of geometric array properties used in FDTD simulations

3.7 Multipole Decomposition of the Extinction

To gain insight on how the resonances of the induvial particles are affected by the different properties of the arrays and how they couple into collective resonances, the multipole contributions must be extracted. Calculating the scattering and extinction spectra analytically

for arbitrarily shaped particles is not a trivial matter. Mie theory can solve analytically for spheres. For irregular shaped objects numerical calculations such as Discrete Dipole Approximation (DDA), Finite difference time domain method (FDTD) and finite element modelling are the most used. However, multipole decomposition of the extinction spectra cannot be obtained directly by these methods alone. In the next section, multipole decomposition of the extinction in cartesian coordinates for arbitrarily shaped particles is described by using as a reference the work done by Evlyukhin et al[76]. From electric field **E(r)** inside the particle the polarization is obtained from

$$\boldsymbol{P}(\boldsymbol{r}) = \varepsilon_0\big(\varepsilon_p - \varepsilon_d\big)E(\boldsymbol{r}) \qquad 3\text{-}22$$

where ε_0 is the vacuum dielectric constant, ε_p is the relative dielectric permittivity of the particle and ε_d is the relative permittivity of the environment. For this derivation of multipoles in cartesian coordinates, the origin of the coordinate system is located at the centre of mass of the particle because if the particle is homogenous the number of multipole terms in the expansion is minimum[97].

To obtain the multipole decomposition of the light induced polarization, the polarization can be written by using a property of the Dirac-delta function as,

$$\boldsymbol{P}(\boldsymbol{r}) = \int \boldsymbol{P}(\boldsymbol{r}')\boldsymbol{\delta}(\boldsymbol{r} - \boldsymbol{r}')\boldsymbol{dr}' \qquad 3\text{-}23$$

where $\delta(r - r')$ is the Dirac-delta function. It is expanded with respect to r' around the origin in a Taylor series and using the definitions for the multipole moments. The induced polarization is expressed as

$$\begin{aligned}\boldsymbol{P}(\boldsymbol{r}) \approx \boldsymbol{p}\boldsymbol{\delta}(\boldsymbol{r}) - \frac{1}{6}\widehat{\boldsymbol{Q}}'\boldsymbol{\nabla}\boldsymbol{\delta}(\boldsymbol{r}) + \frac{i}{\omega}[\boldsymbol{\nabla}\times\mathbf{m}\boldsymbol{\delta}(\boldsymbol{r})] + \frac{1}{6}\widehat{\boldsymbol{O}}'[\boldsymbol{\nabla}\otimes\boldsymbol{\nabla}\boldsymbol{\delta}(\mathbf{r})] \\ - \frac{i}{2\omega}\big[\boldsymbol{\nabla}\times\widehat{\boldsymbol{M}}'\boldsymbol{\nabla}\boldsymbol{\delta}(\boldsymbol{r})\big]\end{aligned} \qquad 3\text{-}24$$

In this expression

$$\boldsymbol{p} = \int \boldsymbol{P}(\boldsymbol{r}')\boldsymbol{dr}' \qquad 3\text{-}25$$

is the electric dipole moment,

$$\boldsymbol{m} = -\frac{i\omega}{2}\int [\mathbf{r}' \times \boldsymbol{P}(\boldsymbol{r}')]\boldsymbol{dr}' \qquad 3\text{-}26$$

is the magnetic dipole moment,

$$\widehat{\boldsymbol{O}}' = \int [\boldsymbol{P}(\boldsymbol{r}') \otimes \boldsymbol{r}' \otimes \boldsymbol{r}' + \boldsymbol{r}' \otimes \boldsymbol{P}(\boldsymbol{r}') \otimes \boldsymbol{r}' + \boldsymbol{r}' \otimes \boldsymbol{r}' \otimes \boldsymbol{P}(\boldsymbol{r}')]\boldsymbol{dr}' \qquad 3\text{-}27$$

is the electric octupole tensor,

$$\widehat{\boldsymbol{Q}}' = 3\int [\boldsymbol{r}' \otimes \boldsymbol{P}(\boldsymbol{r}') + \boldsymbol{P}(\boldsymbol{r}') \otimes \boldsymbol{r}']\boldsymbol{dr}' \qquad 3\text{-}28$$

is the electric quadrupole tensor and

$$\widehat{\boldsymbol{M}}' = -\frac{2i\omega}{3}\int \{[\mathbf{r}' \times \boldsymbol{P}(\boldsymbol{r}')] \otimes \boldsymbol{r}'\}\boldsymbol{dr}' \qquad 3\text{-}29$$

is the magnetic quadrupole tensor, the integrals are over the volume of the particle, $\otimes$ is the tensor product. The electric quadrupole tensor, magnetic quadrupole tensor and electric octupole tensor are not in irreducible representation. The electric quadrupole and octupole tensors are symmetric but not traceless and the magnetic quadrupole tensor is traceless but not symmetric. The contributions from the toroidal dipole moment term in the multipole decomposition appear in the framework of the irreducible representation of the cartesian multipole moments[76,98,99]. The irreducible electric quadrupole tensor is:

$$\widehat{\boldsymbol{Q}} = \widehat{\boldsymbol{Q}}' - 2\int [\boldsymbol{r}' \cdot \boldsymbol{P}(\boldsymbol{r}')]\widehat{\boldsymbol{U}}\,\boldsymbol{dr}' \qquad 3\text{-}30$$

$\widehat{\boldsymbol{U}}$ is the 3x3 unit tensor. The electric octupole in irreducible representation is

$$\widehat{\boldsymbol{O}} = \widehat{\boldsymbol{O}}' - \widehat{\boldsymbol{O}}'' \qquad 3\text{-}31$$

where the tensor $\widehat{\boldsymbol{O}}''$ is

$$O''_{\beta\gamma\tau} = \delta_{\beta\gamma}V_\tau + \delta_{\beta\tau}V_\gamma + \delta_{\gamma\tau}V_\beta \qquad 3\text{-}32$$

where $\beta = x, y, z,\ \gamma = x, y, z,\ \tau = x, y, z, \delta_{\beta\gamma}$ is the Kronecker delta function and vector $\boldsymbol{V}$ is

$$\boldsymbol{V} = \frac{1}{5}\int \{2[\boldsymbol{r}' \cdot \boldsymbol{P}(\boldsymbol{r}')]\boldsymbol{r}' + \boldsymbol{r}'^{\boldsymbol{2}} \cdot \boldsymbol{P}(\boldsymbol{r}')\}\, \boldsymbol{dr}' \qquad 3\text{-}33$$

Lastly the irreducible magnetic quadrupole tensor is

$$\widehat{\boldsymbol{M}} = \widehat{\boldsymbol{M}}' - \widehat{\boldsymbol{M}}'' \qquad 3\text{-}34$$

where $\widehat{\boldsymbol{M}}''$ is an asymmetric tensor:

$$M''_{\beta\gamma} = \frac{1}{2}\sum_{\tau} \epsilon_{\beta\gamma\tau} W_{\tau} \qquad 3\text{-}35$$

where $\epsilon_{\beta\gamma\tau}$ is the Levi-Civita tensor and vector $\boldsymbol{W}$ is:

$$\boldsymbol{W} = \frac{2\omega}{3i}\int \{-[\boldsymbol{r}' \cdot \boldsymbol{P}(\boldsymbol{r}')]\boldsymbol{r}' + \boldsymbol{r}'^{\boldsymbol{2}} \cdot \boldsymbol{P}(\boldsymbol{r}')\}\, \boldsymbol{dr}' \qquad 3\text{-}36$$

The irreducible tensors $\widehat{\boldsymbol{Q}}$, $\widehat{\boldsymbol{O}}$ and $\widehat{\boldsymbol{M}}$ can then be substituted in equation **3-24**. After some rearrangements, the following expression is obtained for the induced polarization.

$$\begin{aligned}\boldsymbol{P}(\boldsymbol{r}) \approx \boldsymbol{p}\boldsymbol{\delta}(\boldsymbol{r}) &- \frac{1}{6}\widehat{\boldsymbol{Q}}\boldsymbol{\nabla}\boldsymbol{\delta}(\boldsymbol{r}) + \frac{i}{\omega}[\boldsymbol{\nabla} \times \boldsymbol{m}\boldsymbol{\delta}(\boldsymbol{r})] + \frac{1}{6}\widehat{\boldsymbol{O}}[\boldsymbol{\nabla} \otimes \boldsymbol{\nabla}\boldsymbol{\delta}(\boldsymbol{r})] \\ &- \frac{i}{2\omega}\left[\boldsymbol{\nabla} \times \widehat{\boldsymbol{M}}\boldsymbol{\nabla}\boldsymbol{\delta}(\boldsymbol{r})\right] - \frac{i}{\omega}\boldsymbol{T}\boldsymbol{\Delta}\boldsymbol{\delta}(\boldsymbol{r}) - \frac{q}{6}\boldsymbol{\nabla}\boldsymbol{\delta}(\boldsymbol{r}) \\ &+ [\boldsymbol{\nabla} \otimes \boldsymbol{\nabla}\boldsymbol{\delta}(\boldsymbol{r})]\boldsymbol{L}\end{aligned} \qquad 3\text{-}37$$

Where ∇ is the Laplace operator, $\boldsymbol{T}$ is the toroidial dipole as

$$\boldsymbol{T} = \frac{i\omega}{6}\boldsymbol{V} - \frac{1}{4}\boldsymbol{W} \qquad 3\text{-}38$$

vector $\boldsymbol{L}$ as

$$\boldsymbol{L} = \frac{1}{3}\boldsymbol{V} - \frac{i}{4\omega}\boldsymbol{W} \qquad 3\text{-}39$$

and the scalar q as

$$\boldsymbol{q} = 2\int [\boldsymbol{r}' \cdot \boldsymbol{P}(\boldsymbol{r}')]\, \boldsymbol{dr}' \qquad 3\text{-}40$$

The extinction power of the particle is determined by:

$$P_{ext} = \frac{\omega}{2}\mathbf{Im}\int [\boldsymbol{E}^*_{\boldsymbol{inc}} \cdot \boldsymbol{P}(\boldsymbol{r})]\, \boldsymbol{dr} \qquad 3\text{-}41$$

Substituting in expression **3-37** for the induced polarization into the extinction power yields

$$P_{ext} = \frac{\omega}{2}\mathbf{Im}\left\{\boldsymbol{E}^*_{\boldsymbol{inc}} \cdot\left(\boldsymbol{p} + \frac{ik_d}{v_d}\boldsymbol{T} - \frac{ik_d}{6}\widehat{\boldsymbol{Q}} + \frac{1}{v_d}[\mathbf{m}\times\boldsymbol{n}_{\boldsymbol{inc}}] + \frac{ik_d^2}{6}\widehat{\boldsymbol{O}}(\boldsymbol{n}_{\boldsymbol{inc}}\boldsymbol{n}_{\boldsymbol{inc}}) - \frac{ik_d}{2v_d}\left[\boldsymbol{\nabla}\times(\widehat{\boldsymbol{M}}n_{inc})\right]\right)\right\} \qquad 3\text{-}42$$

where $v_d = \sqrt{c/\varepsilon_d}$, k_d is the wavenumber in the surrounding media, $n_{inc} = k_d/k_d$ is the unit vector along the incident direction. For the case where the incident plane wave is linearly polarized in the x axis and propagating in the z direction the extinction cross section is obtained by

$$\sigma_{ext} = \frac{k_d}{\varepsilon_0\varepsilon_d|E^*_{0x}|^2}\mathrm{Im}\left\{E^*_{0x}\left(p_x + \frac{ik_d}{v_d}T_x + \frac{1}{v_d}m_{yz} - \frac{ik_d}{6}Q_{xz} - \frac{ik_d^2}{6}O_{xzz} - \frac{ik_d}{2v_d}M_{yz}\right)\right\} \qquad 3\text{-}43$$

where $\boldsymbol{E}_{0x}$ is the electric field amplitude of the incident wave in the x direction. If the particle is on a substrate then $\boldsymbol{E_{0x}}$ is the superposition incident wave and the light reflected by the substrate when no particle is present[100]. Infinite arrays are treated the same as single particle. For the arrays the only fields from a particle in one unit cell of the array are considered. Small negative contribution from the higher order multipoles (quadropoles and higher order multipoles) can be obtained from this method due to the discrete approximation of the particle and they are considered artifacts of the numerical calculations[100]. Larger significant negative contributions from the multipoles can appear from interaction between different multipoles emerging from asymmetric environments[100–102] (i.e. particle on a substrate in air).

In this thesis FDTD simulations were used to obtain the electric field distributions. Since FDTD is a discrete method in space, the integration over the particle volume for the multipole contributions in discrete space are approximated by

$$f = \int F(r')dr' \approx \sum_i \sum_j \sum_k F(i,j,k)\Delta x \Delta y \Delta z \qquad 3\text{-}44$$

where i, j, k are indices of the position in the FDTD grid inside the particle in the x y and z direction respectively, $\Delta x, \Delta y, \Delta z$ are the cell size in their respective dimensions and for the work in this thesis they are all 5 nm. All the electric field components inside the particle and the incoming wave can be easily obtained by using the FDTD method. After extracting the data, the multipole components in the extinction were calculated using a MATLAB script. In this work the incident planewave was polarized in the x direction and propagating in the negative z direction. In this work the electric dipole contribution (ED) to the extinction cross section is presented as the total electric dipole contribution (TED) which is the electric dipole and toroidal dipole contributions added together

$$\sigma_{ext}^{TED} = \frac{k_d}{\varepsilon_0 \varepsilon_d |E_{0x}^*|^2} \mathrm{Im}\left\{E_{0x}^* \left(p_x + \frac{ik_d}{v_d} T_x\right)\right\} \qquad 3\text{-}45$$

The magnetic dipole contribution (MD) to the extinction is,

$$\sigma_{ext}^{MD} = -\frac{k_d}{\varepsilon_0 \varepsilon_d |E_{0x}^*|^2} \mathrm{Im}\left\{\frac{1}{v_d} E_{0x}^* m_y\right\} \qquad 3\text{-}46$$

the electric quadrupole contribution is,

$$\sigma_{ext}^{EQ} = \frac{k_d}{\varepsilon_0 \varepsilon_d |E_{0x}^*|^2} \mathrm{Im}\left\{\frac{ik_d}{6} E_{0x}^* Q_{xz}\right\} \qquad 3\text{-}47$$

the magnetic quadrupole contribution is,

$$\sigma_{ext}^{MQ} = -\frac{k_d}{\varepsilon_0 \varepsilon_d |E_{0x}^*|^2} \mathrm{Im}\left\{\frac{ik_d}{2v_d} E_{0x}^* M_{yz}\right\} \qquad 3\text{-}48$$

for the electric octupole,

$$\sigma_{ext}^{EOC} = -\frac{k_d}{\varepsilon_0 \varepsilon_d |E_{0x}^*|^2} \mathrm{Im}\left\{\frac{k_d^2}{6} E_{0x}^* O_{xzz}\right\} \qquad 3\text{-}49$$

and the total extinction

$$\sigma_{ext}^{Total} = \sigma_{ext}^{TED} + \sigma_{ext}^{MD} + \sigma_{ext}^{EQ} + \sigma_{ext}^{MQ} + \sigma_{ext}^{EOC} \qquad 3\text{-}50$$

To be certain that the extinction contributions are calculated correctly, and FDTD simulation was done on a 130 nm radius dielectric sphere with refractive index of 2.1 and compared with Mie theory. The extinction coefficients calculated from the FDTD calculation by the described method above were divided by the cross-sectional area of the sphere πr^2 to obtain the Mie efficiencies. The comparison between Mie theory and FDTD simulation results on the decomposition is shown in **Figure 3-8**. The values calculated from the FDTD decomposition are nearly identical in shape and position to the Mie theory contributions. The FDTD values are slightly larger than Mie theory at the shorter wavelengths, however the differences are like each other enough and in this work the focus will be in the position and shape of the multipoles.

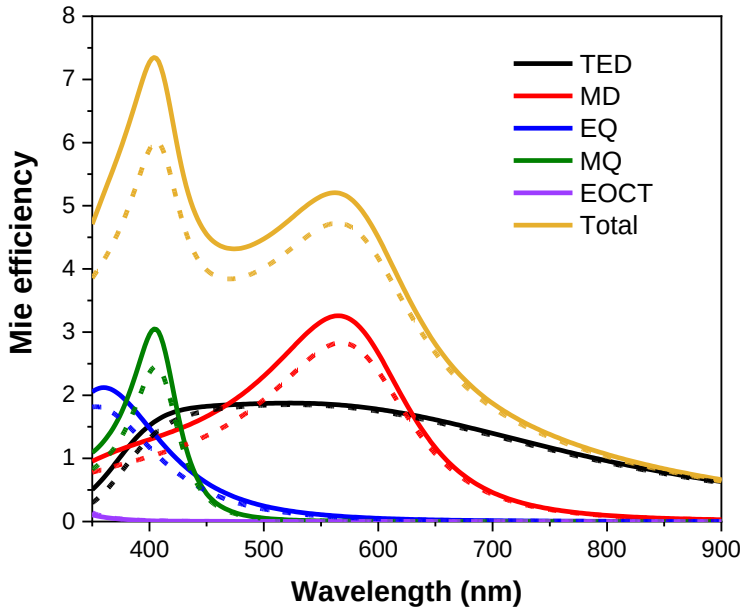

Figure 3-8 Mie efficiency comprarison of a r=130 nm dielectric sphere of refractive index of 2.1. Solid lines are the results obtained from the cartesian multipole expansion of the fields obtained from FDTD simulations. Dashed lines are the Mie thoery solutions.

3.8 Conclusion

IN conclusion, this chapter provides the information needed to understand the expected properties of the TiO_2 arrays and on their fabrication method. The three arrays have pillars with Mie resonances in the visible and with periodicity in the order of the wavelength of visible light. Therefore, these arrays will be also diffracting light. These arrays were fabricated using soft-

nanoimprint lithography a cheap and fast method which leaves behind a residual layer underneath the array. The properties of this layer are especially important to study as this layer will determine if the array supports QGMs or not. This chapter also covered the experimental preparation of the arrays for measurements as well as the experimental techniques used to detect QGMs presence in the arrays and investigate the effect of R6G emission caused by the arrays. FDTD method is reviewed, as this method will be used to study the behaviour of QGMs on ideal arrays and determine the properties the array need to support QGMs. Lastly, multipole decomposition of the extinction for arbitrarily shaped particles is discussed, this method will be used to provide more information of what is happening to the resonances of the individual pillars when places in an array.

4 Computational Study of TiO_2 Arrays Fabricated via Soft-NIL

This chapter is focused on understanding the properties of TiO_2 arrays fabricated *via* soft-nano imprint lithography (soft-NIL method) as described in the works of Bottein et al.[31] and Checcucci et al.[32]. Due to the nature of this process, the TiO_2 arrays produced *via* this method leave behind a TiO_2 layer on top of which the TiO_2 pillars are resting (**Figure 4-1 g**). In this chapter, the effects the different elements and properties of the array have on the multipole resonances of the dielectric pillars and QGMs are discussed. Three arrays are investigated in this work: the A600, A550, and A480. These arrays were all fabricated on the same substrate and are different from each other by the periodicity and dimensions of the TiO_2 pillar. The dimensions of the arrays were obtained using Scanning Electron Microscope (SEM) on Focused Ion Beam (FIB) cut images seen in **Figure 4-1 a-f**. It is very important to note that the thickness of the residual TiO_2 observed in **Figure 4-1 b,d,f** was measured to be roughly 130 nm in these arrays. Upon closer examination of **Figure 4-1 a,c,e**, one can see that the layer of TiO_2 looks quite porous. In **Figure 4-1 b,d,f**, there is contrast between the pillars and the layer (the layer is lighter in shade than the pillars). From these images, if you look close enough, it is seen that the layer has a slightly lighter colour than the pillar, which points towards the layer having a lower effective refractive index than the more compact pillars.

Table 4-1 Dimensions of the three arrays used in the FDTD simulations unless stated otherwise.

Array	Period	Base Length	Top Length	TiO_2 Layer Thickness	Height
A600	600 nm	320 nm	170 nm	130 nm	260 nm
A550	550 nm	280 nm	150 nm	130 nm	260 nm
A480	480 nm	185 nm	75 nm	130 nm	280 nm

Simulations of these arrays are done using finite difference time domain (FDTD) method, described in more detail in section 3.5.1. The shape of the pillars to be that of a rounded truncated pyramid. These arrays have the following properties: the period, base length, top length, height, roundness, TiO_2 layer thickness, refractive index of the TiO_2 pillar, refractive

index of the TiO_2 layer thickness, and the refractive index of the substrate. Most of these properties used for the simulations are listed in **Table 4-1** for the three arrays and shown in the schematics of the arrays **Figure 4-1 g**. The roundness of the corners of the pillar is approximated to be roughly 30 nm for all arrays from the SEM images, however this property has little to no effect on the optical properties of the array. The refractive index of bulk anatase TiO_2 is roughly 2.54 at 550 nm, however the TiO_2 in these arrays is porous, due to them being fabricated by soft-nano imprint lithography. So the TiO_2 on the arrays will have a smaller refractive index than bulk TiO_2[68]. Therefore, due to TiO_2 having near to no losses in the visible range (400-900 nm) in this simulation the TiO_2 pillars, TiO_2 layer, and substrate are simulated as a dielectric. The pillars with refractive index of 2.1, unless otherwise mentioned. The refractive index of the pillar was chosen as 2.1 as this is a good approximate static value to the results obtained on the titania coatings for Soft-NIL fabrication[68] and since the layer is more porous and rough, a slightly lower value are chosen. The simulations will be performed under normal incidence, which match the experimental set-up that will be used to measure the arrays, of the electric field oriented along the x-axis and propagating along the z-axis, coming from the airside of the array, and going into the substrate as shown in **Figure 4-2 a**.

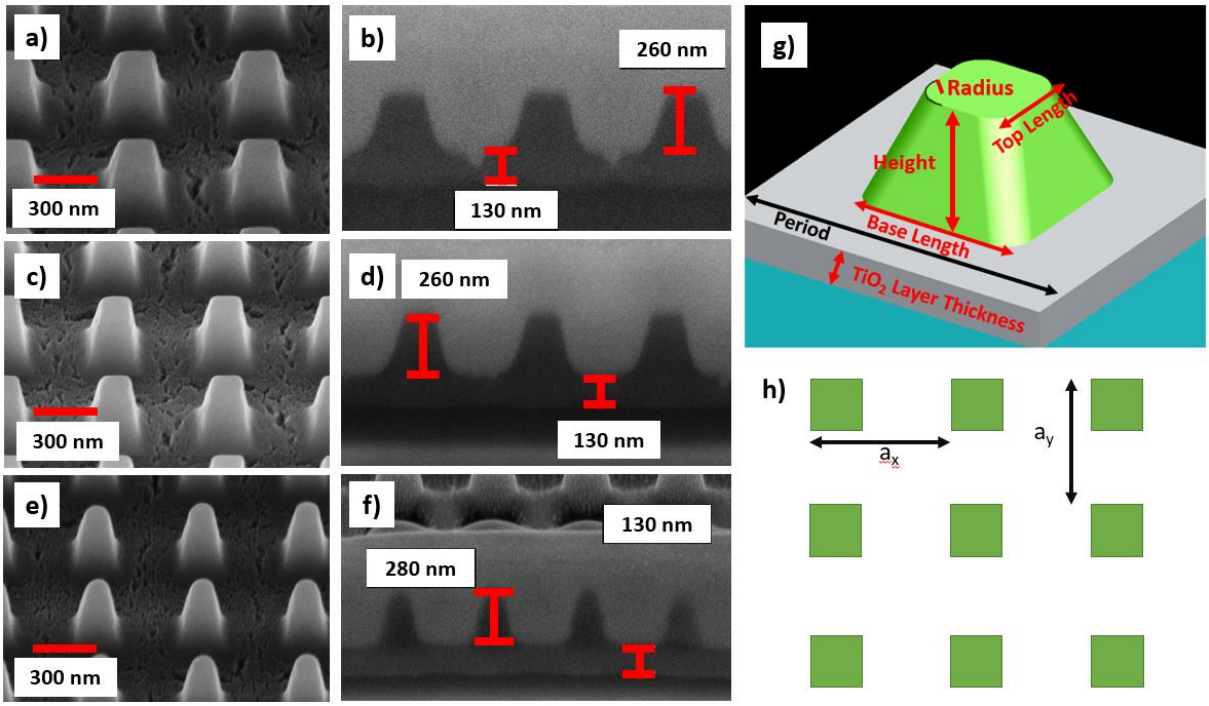

Figure 4-1 a) SEM image of the A600 array, b) cross-section of the A600 array coated in platinum layer only for focusing ion beam cutting, c) SEM Image of the A550 array, d) cross-section of the A550 array coated in platinum layer only for focusing ion beam cutting, e) SEM image of the A480 array, f) cross-section of the A480 array coated in platinum layer only for focusing ion beam cutting, and g) top-down view of array layout, where a_x and a_y are the lattice constants in the x and y directions, respectively (in the case of these arrays, a_x=a_y).

4.1 Single Pillars and Arrays without Substrate

Firstly, the properties of the individual pillars in air will be examined and then the arrays will be considered. In **Figure 4-2 b** the extinction spectra obtained from FDTD simulations of the three arrays are shown. The three pillars have different extinction spectra. The A600 and A550 are very similar in their physical shape (the ratio between their top and bottom lengths and height are very similar (0.535 vs. 0.536). This causes the extinction spectra of the A600 and A550 to be similar in shape. However, the A480 is taller by 20 nm and has a different ratio (0.405) between the top and bottom lengths than the A600 and A550, yielding an extinction spectrum with a different shape. Changing just the size of particle will just shift the scattering spectra, to change the shape of the scattering spectra the shape of the particle needs to be changed. In order to better understand the properties of the individual pillars, a Cartesian multipole decomposition of the extinction spectra is performed using the formulation which is described in detail in section 2.2 and is based on the method presented by Evlyukhin et al[76]. As described earlier in section 3.3, the application of this method was first confirmed on a sphere and compared with the results from Mie theory. The shape and position of the decomposition matched very well with Mie theory. By performing multipole decomposition using the E-field distribution obtained from the FDTD simulation, the following multipoles contributions are extracted: the total electric dipole moment (TED) which contains the electric dipole moment and the toroidal dipole moment, the magnetic dipole (MD), the electric quadrupole (EQ), the magnetic quadropole (MQ) and the electric octupole (EOCT). The EOCT contribution is negligible compared with the TED, MD, EQ and MQ contributions for wavelengths greater than 450 nm (purple line in **Figure 4-2 c-e**). EOCT is not considered any further in the discussions as the RAs positions would be far from the where the EOCT becomes relevant.

The multipole decomposition on the A600 pillar is shown in **Figure 4-2 c**. It is observed that the MD and TED are overlapping and that the TED is quite broad. The broadness and overlap of the TED is due to poor confinement as a consequence of the not so high refractive index of TiO_2[82] and higher refractive index leads to greater confinements and longer live ED resonances. The broad peaks of the MD and ED of the A600 pillar are roughly at 650 nm and 665 nm, respectively. The EQ peak is at 450 nm and the MQ peak is at 466 nm. For the A550 pillar in **Figure 4-2 d**, the relative positions and shape of the multipole moments is very similar to A600, due to their similar shape as discussed before. Its MD peak is at 600 nm, the TED peak at 590 nm, the centre of the EQ is at 422 nm, and the MQ is at 425 nm. The EQ for

the A600 and A550 has two maxima in the extinction close to each other, this is probably due to the difference in length between the top and bottom lengths of the pillars. Finally, for the A480 pillar in **Figure 4-2 e**, the MD peak is at 446 nm, TED at 375 nm, EQ at 352 nm and the MQ moment peak is at a wavelength lower than 350 nm, outside the simulation range of 350-900 nm. This range was chosen because this is the detection limit of the experimental set-up used to measure the arrays in later chapters.

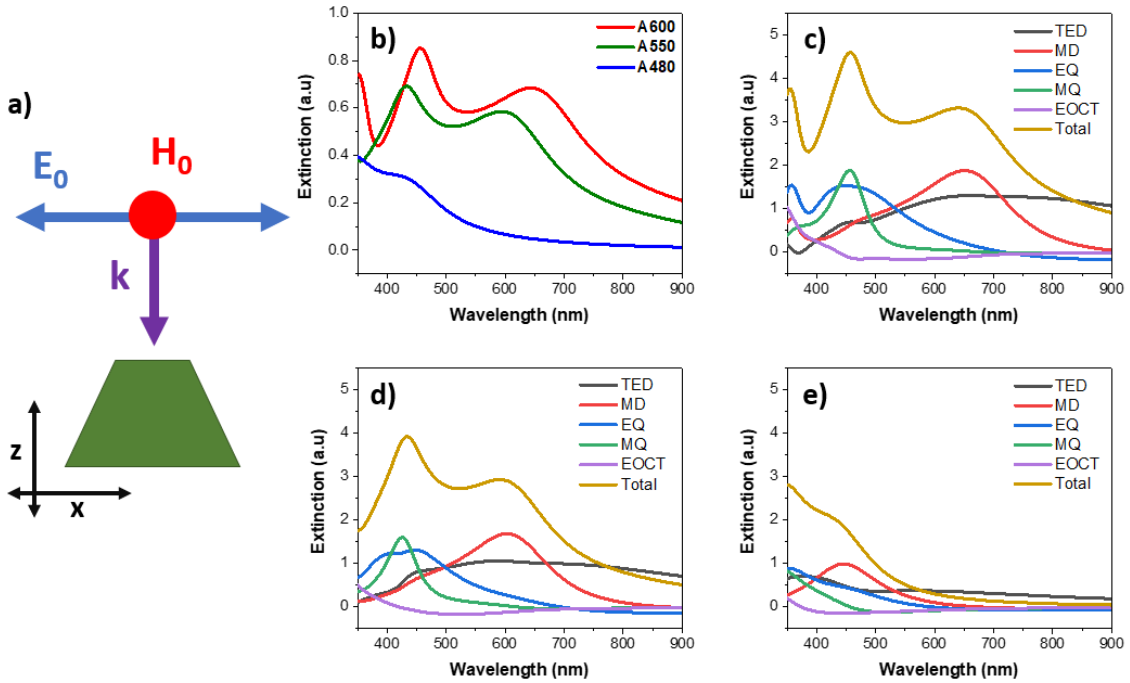

Figure 4-2 Extinction spectra of the single pillars in air. a) schematics of pillar and incident electric field (with amplitude E_0) and magnetic field (with amplitude H_0) used for simulations, b) extinction spectra obtained from FDTD simulations for the three pillars, the spectra are normalized to the source intensity. Multipole decomposition of the extinction cross section for the c) A600, d) A550 and e) A480 pillars.

FDTD simulations were performed on the A550 pillar with different refractive indices 1.9, 2.1, and 2.4. This range was chosen since it gives a good idea of how variations on the refractive index of the pillar will affect the resonances. This range of values is possible from the fabrication process. After performing multipole decompositions on the results, it can be seen in **Figure 4-3** that by increasing the refractive index of the A550 pillars, the resonances red shift with increasing refractive index, as expected, and become narrower due to the increased confinement of the light. The EQ (**Figure 4-3 c)**, and MQ (**Figure 4-3 d)**, change in position very similarly and continue to overlap with increasing refractive index. The TED and MD are becoming more distinct from each other as they both narrow with the increasing index. In this

section, the positions of the multipoles of the individual pillars in air have been determined and it is observed how pillar refractive index affects their position and shapes.

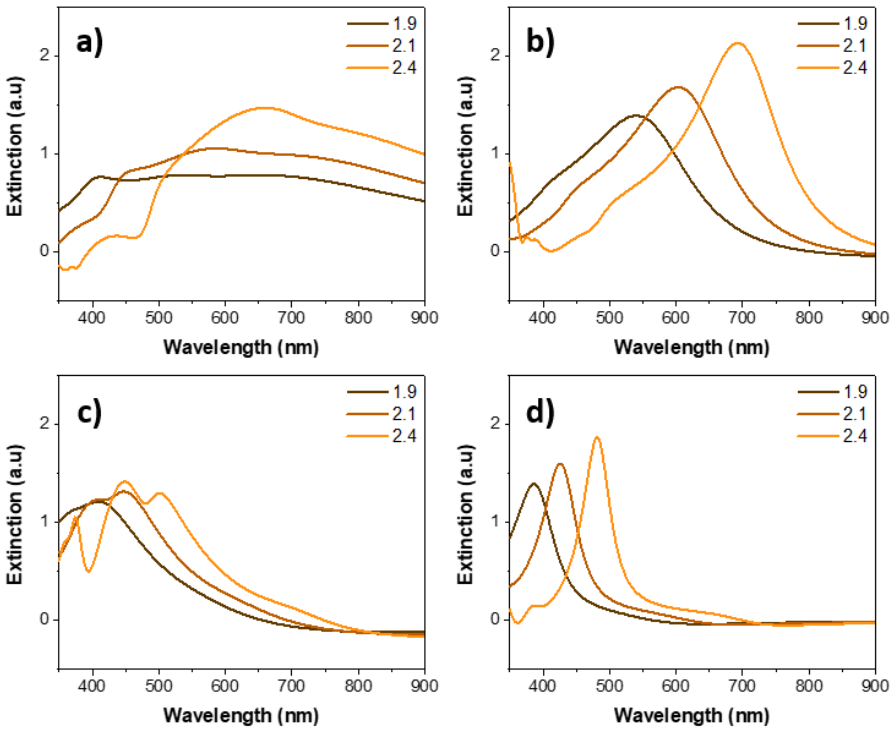

Figure 4-3 Multipole moments of the A550 pillar with increasing refractive index (1.9, 2.1, 2.4), a) electric dipole (TED), b) magnetic dipole (MD), c) electric quadrupole (EQ) and d) the magnetic quadrupole.

Now that the positions of the multipoles in the single pillars in air are known, the effect of a square array structure on the multipoles will be investigated. Dielectric structures in arrays can have their electric and magnetic resonances couple collectively to RAs of the array[27,32,75]. The wavelength of the RAs for rectangular arrays with normal incidence are calculated by the following equation[90],

$$\lambda_{RA} = \frac{n}{\sqrt{\left(\frac{m_x}{a_x}\right)^2 + \left(\frac{m_y}{a_y}\right)^2}} \qquad 4\text{-}1$$

where a_x and a_y are the lattice constants in the x and y direction. m_x and m_y are the positive integers, and n is the refractive index of the environment. In the case of the arrays in this study, $a_x = a_y = a$ and the previous equation becomes:

$$\lambda_{RA} = \frac{a \cdot n}{\sqrt{(m_x)^2 + (m_y)^2}} \qquad 4\text{-}2$$

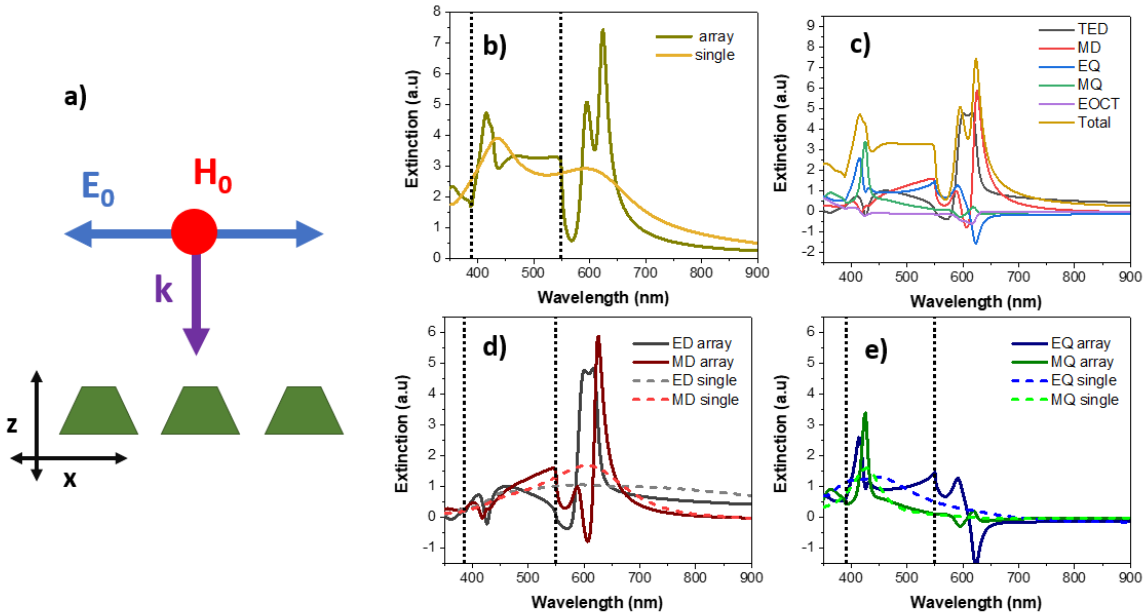

Figure 4-4 Extinction spectra of the A550 array in air, a) schematics of array and incident electric field (with amplitude E_0) and magnetic field (with amplitude H_0) used for simulations, b) comparison of extinction spectra obtained from FDTD simulations between single pillar and array, dashed black lines show first and second order RAs wavelength, c) decomposed extinction spectra the array, d) comparison between TED and MD in an array and a single pillar, e) comparison between EQ and MQ in an array and a single pillar.

Next, the FDTD simulation results for the extinction spectra of the array structure in air are presented. Firstly, the A550 array with a 550 nm period and pillars with a refractive index of 2.1, is shown in **Figure 4-4 b.** It can be immediately seen that the spectrum has changed significantly from the single pillar. This is due to the significant interaction of the pillar's multipoles with the RAs. **Figure 4-4 c** shows the decomposed spectra of the A550 array. The first order RA $\left[(m_x, m_y) = (1,0)\ or\ (0,1)\right]$ and the second order $\left[(m_x, m_y) = (1,1)\right]$ for the A550 are at 550 nm and 388.9 nm, respectively. The sharp double peak observed at 596 nm and 624 nm is predominantly due to the TED (centred at 608 nm) and MD (at 624 nm) coupling with the first order RA at 550 nm. Both the TED and MD of the single pillar are slightly detuned from the RA with their peaks at 590 nm and 600 nm (**Figure 4-4 d)**. The MD and TED resonances on the arrays are much sharper and slightly red shifted, they exhibit an asymmetric Fano-type resonance due to the coupling of the very sharp lattice modes with the broad resonances of the single pillars.

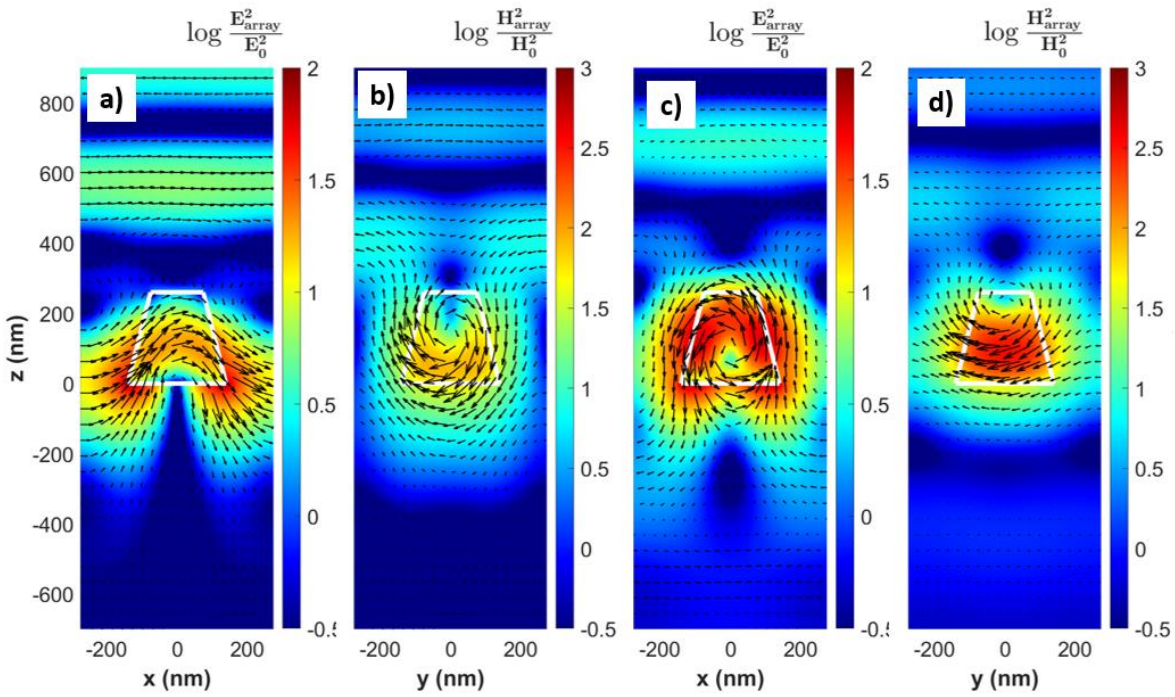

Figure 4-5 Electric and Magnetic field intensity distributions for the A550 array with no substrate, normalized to the incident field intensity. The colour represents the relative intensity to the incident field on a logarithmic scale and the black arrows represent the real part of the vector electric/magnetic field in the xz and yz planes. a) The electric field intensity distribution at wavelength 608 nm, b) The magnetic field intensity distribution at wavelength 608 nm, c) The electric field intensity distribution at wavelength 626 nm, d) The magnetic field intensity distribution at wavelength 626 nm.

To confirm the results from the multipole decomposition, the electric and magnetic field intensity distribution of the A550 array with the position of the TED at 608 nm, is examined in **Figure 4-5 b**. It is observed that the real part of the vectorial magnetic field indicated by the black arrows in **Figure 4-5 b**, curls around the pillar. In the case of the electric field intensity distribution (**Figure 4-5 a)**, two lobes of high e-field intensity can be seen. These field profiles are signatures of the electric dipole. It is also observed that the real part of the vectorial electric field is oriented predominantly in the x axis and the real part of the vectorial magnetic field has strong z components. From this, it is determined that the TED coupled to the first order RA $(m_x, m_y) = (0,1)$, which is propagating along the y axis of the array plane. Very similarly, an examination of the fields of the MD (624 nm) shows that the vectorial e-field is curling around the pillar and that there is a single high magnetic field intensity lobe inside the pillar, both signatures of the MD. The real part of the electric field vector around the pillar is nearly parallel to the z axis and the real part of the magnetic field vector is strongly oriented along the x axis. Therefore, the MD is coupled to the first order RA $(m_x, m_y) = (1,0)$ that is propagating along the x axis of the array plane.

Looking next at the second extinction peak in the array spectrum, in **Figure 4-4 c**, it can be observed that this peak is directly related to the EQ and MQ. They are most likely interacting with the second order lattice mode at 388.9 nm. In **Figure 4-4 e**, the EQ and MQ of the array and single pillar are plotted together. As it can be seen, the EQ and MQ resonances sharpen, the MQ peak position does not shift, while the EQ resonance is blue shifted by ~10 nm from the single pillar EQ peak position. It is observed that the EQ is interacting with the first order RA at 550 nm, the EQ peak as seen in **Figure 4-2 d** still has significant contributions to the extinction spectra at 550 nm. The field intensity and vectorial components of the electric and magnetic field for the EQ at 414 nm are shown in **Figure 4-6 a,b** respectively, and for the MQ at 426 nm in **Figure 4-6 c,d**. For the EQ, four high e-field intensity regions are evident, this field profile is signature of the electric dipole. The MQ also shows 4 high intensity lobes in inside the pillar.

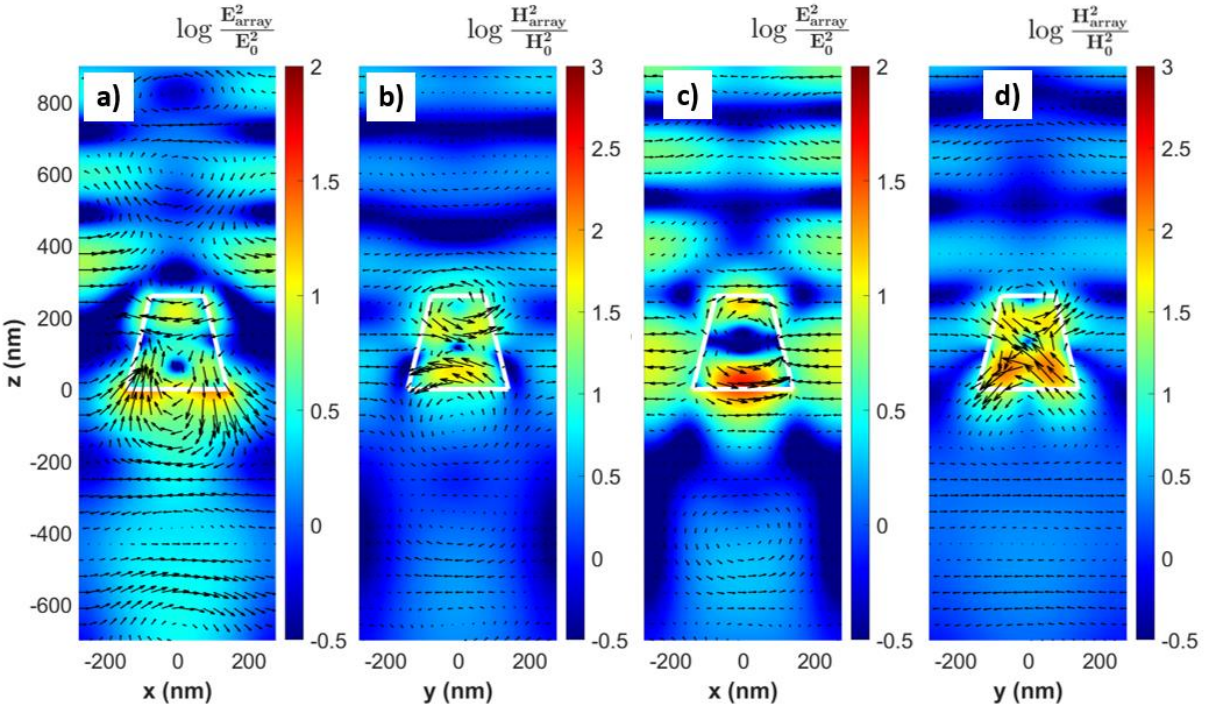

Figure 4-6 Electric and Magnetic field intensity distributions for the A550 array in air, normalized to the incident field intensity. The colour represents the intensity on a logarithmic scale and the black arrows represent the real part of the vector electric/magnetic field on the xz/yz plane. Here the following is shown: a) the electric field intensity distribution at wavelength 414 nm, b) the magnetic field intensity distribution at wavelength 414 nm, c) the electric field intensity distribution at wavelength 426 nm, d) the magnetic field intensity distribution at wavelength 426 nm.

To confirm that these TED and MD resonances are coupling to the first order RA and EQ and MQ are coupled to the second order RA, FDTD simulations are performed where the periodicity of the lattice is varied only in one dimension at the time. Firstly, the lattice constant

in the y direction a_y was varied to 500 nm, 550 nm, 600 nm, and 750 nm, **Figure 4-7 a** shows the total extinction spectra for the A550 array for the different a_y. It is observed that both the dipole and quadrupole features shifting with a_y. By performing the multipole decomposition on the extinction spectra, the TED is shifting considerably with a_y in **Figure 4-7 b.** On the other hand, the MD position remains relatively constant in **Figure 4-7 c**, although it does change in intensity, sharpness and blue shifts a little bit with increasing a_y. This is likely due to the pillars having weaker interactions between the electric and magnetic fields of neighbouring pillars as they move away from each other. This confirms that the TED is traveling in the *y* direction and is coupled to the $(m_x, m_y) = (0,1)$ RA, and the MD is travelling in the *x* direction and is coupled to the (m_x, m_y) =RA(1,0). The $(m_x, m_y) = (1,1)$ RA for the new arrays with a_y=500 nm, 550 nm, 600 nm and 750 nm are at 369.9 nm, 388.9 nm, 405.4 nm and 443.5 nm. Looking closely at the quadrupoles peak in **Figure 4-7 d**, red shifting of the peak is observed with increasing period. The kinks observed in the spectra (shown by the arrays) correspond to $(m_x, m_y) = (1,1)$ RA. The EQ position in **Figure 4-7 e** varies with increasing a_y and varies with the second order RA, providing evidence to support the assumption that the EQ is coupled to the second order RA in an infinite array in air. The other two features of the EQ appear to be coupled with both first order lattice modes as one feature remains static and the other shifts with increasing a_y**.** The MQ position in **Figure 4-7 f** also varies with increasing a_y and moves with the second order RA. Similarly, to the EQ, the MQ is coupled to the second order RA.

We will now focus on the effects that the refractive index of the pillar has on the arrays. As was seen in **Figure 4-3 (a-d),** the positions of the different multipoles of a single pillar change with the refractive index of the pillar. In **Figure 4-8 a**, the FDTD simulated extinction spectra of the A550 array with different refractive index in the pillar is shown. The resonances of the single pillar red shift with increasing index, and a similar effect is observed in the array structures where the dipole and multipole features are red shifting with increasing index. However, as opposed to the single pillars where the resonances sharpen with increasing index due to increased confinement, the RAs coupled resonances broaden with increasing index. The increase in refractive index of the pillar increases and redshift its scattering cross section as seen in **Figure 4-3** (extinction equals scattering when there is no absorption), corresponding to shorter-lived SLRs as they are scattered out faster by the pillars. This was also confirmed by the simulation time as the simulation needed less iterations to converge, meaning that SLRs took more time to get scattered out of the arrays.

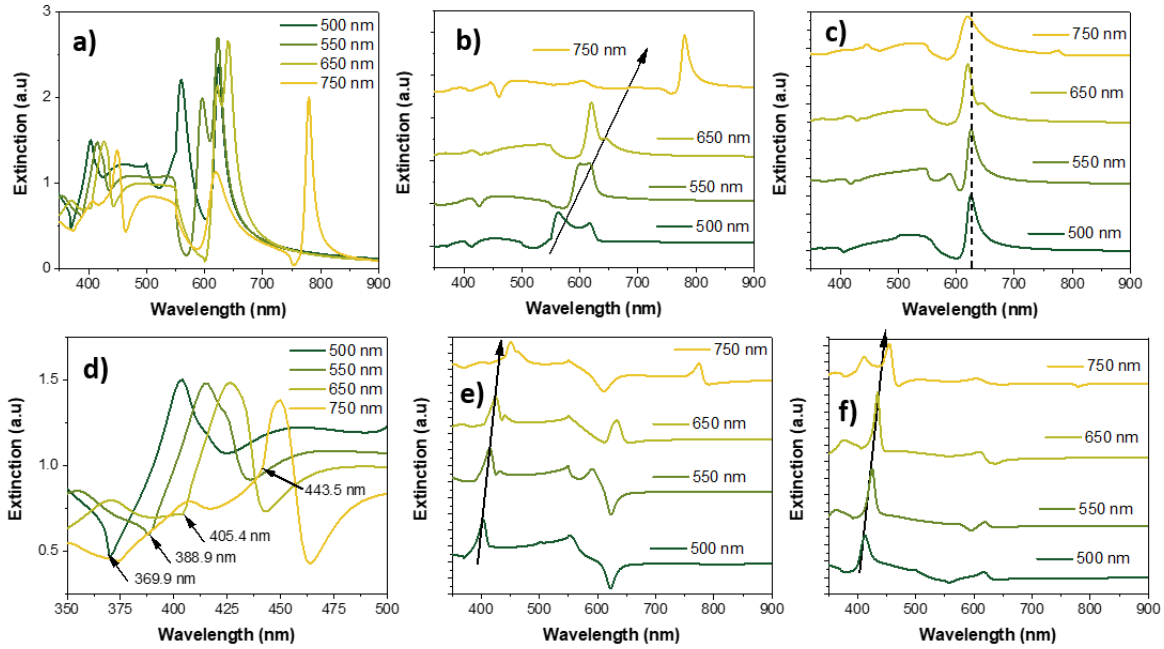

Figure 4-7 Extinction spectra and multipole decomposition of the A550 array for different values of a_y (500, 550, 600, 650 and 750 nm), a) Extinction spectra of the arrays, b) TED obtained from multipole decomposition, c) MD from the multipole decomposition, d) close-up of the extinction spectra in the region of the second order RAs, e) EQ from the multipole decomposition, f) MQ from the multipole decomposition.

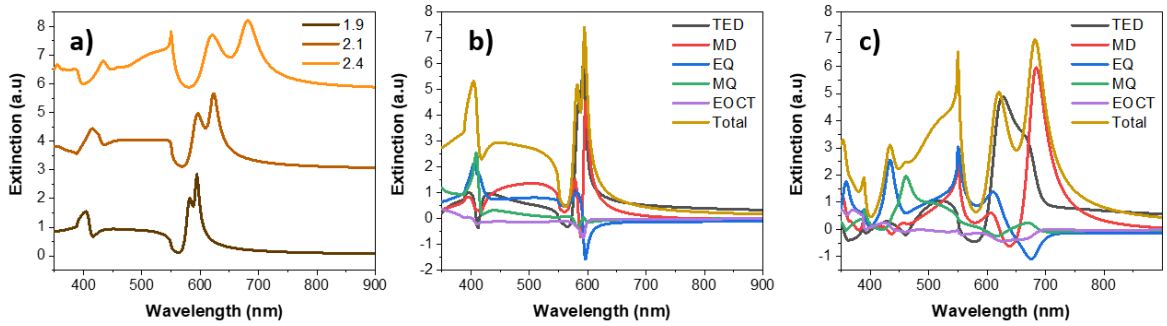

Figure 4-8 Array extinction spectra dependence on the refractive index of the pillar for the A550 array in air shows a) the total extinction spectra obtained from FDTD simulations, b) the decomposed extinction spectra for an array with pillars with index of 1.9, c) the decomposed extinction spectra for an array with pillars with index of 2.4.

The other most prominent change happens right at the first order RA (550 nm), with the 2.4 index, where a sharp increase in the extinction spectrum is observed. After performing the multipole decomposition on the array with index 2.4 in **Figure 4-8 c**, it is observed that the MD and the EQ are responsible for this feature. The electric and magnetic field intensity and vector maps at the wavelength of the first order RA (550 nm) are shown in **Figure 4-9 a-f**. The

magnetic field intensity and vector images for refractive indices 1.9, 2.1 and 2.4 respectively, in **Figure 4-9 b,d,f**, have virtually the same features just with varying intensity. However, where things differ is at the e-field intensity and vector images in **Figure 4-9 a,c,e** for refractive indices 1.9, 2.1 and 2.4, respectively. One can see that for 1.9 and 2.1, the images are virtually the same. One can observe the quadrupole moment in both, and the vectorial part of the fields look very similar. However, in the case of the 2.4 refractive index array, despite the field intensity shape looking very similar to the other two arrays, the e-field vector lines change entirely. This difference could arise due to the EQ and MD constructively interfering with first order RA, also seen as the sharp peak in 550 nm in **Figure 4-8 c**.

One can now extend the discussion to the extinction spectra for the A600 and the A480. In **Figure 4-10 a**, the extinction spectra of the three arrays in air (A600, A550 and A480) from the FDTD simulations are shown. For the A600 the first order RA is at 600 nm and the second order RA is at 424 nm. One observes, similarly to the A550, the TED and MD couple dominantly to the first order RA, and the EQ and MQ couple to the second order RA (**Figure 4-10 b**). The A550 and A600 arrays extinction spectra have very similar shape and features, just slightly shifted from each other. This is because of the very similar aspect ratios in pillar size (**Figure 4-2 c, d**) and the relative positions of the resonances to the RAs. The A480 array extinction spectra (**Figure 4-10 c**) is different from the other two. The coupling to the second order RA is not observed as it is at 339 nm below the FDTD simulation range (350-900 nm) and the coupling of the MD and TED to the first order RA at 480 nm has a much smaller full width half maximum. That is due to the A480 pillar having much smaller extinction than the A550 and A600 at the positions of their SLRs. The A480 array also shows the EQ is coupling with the first order RA and contributes significantly to the peak observed in **Figure 4-10 c**.

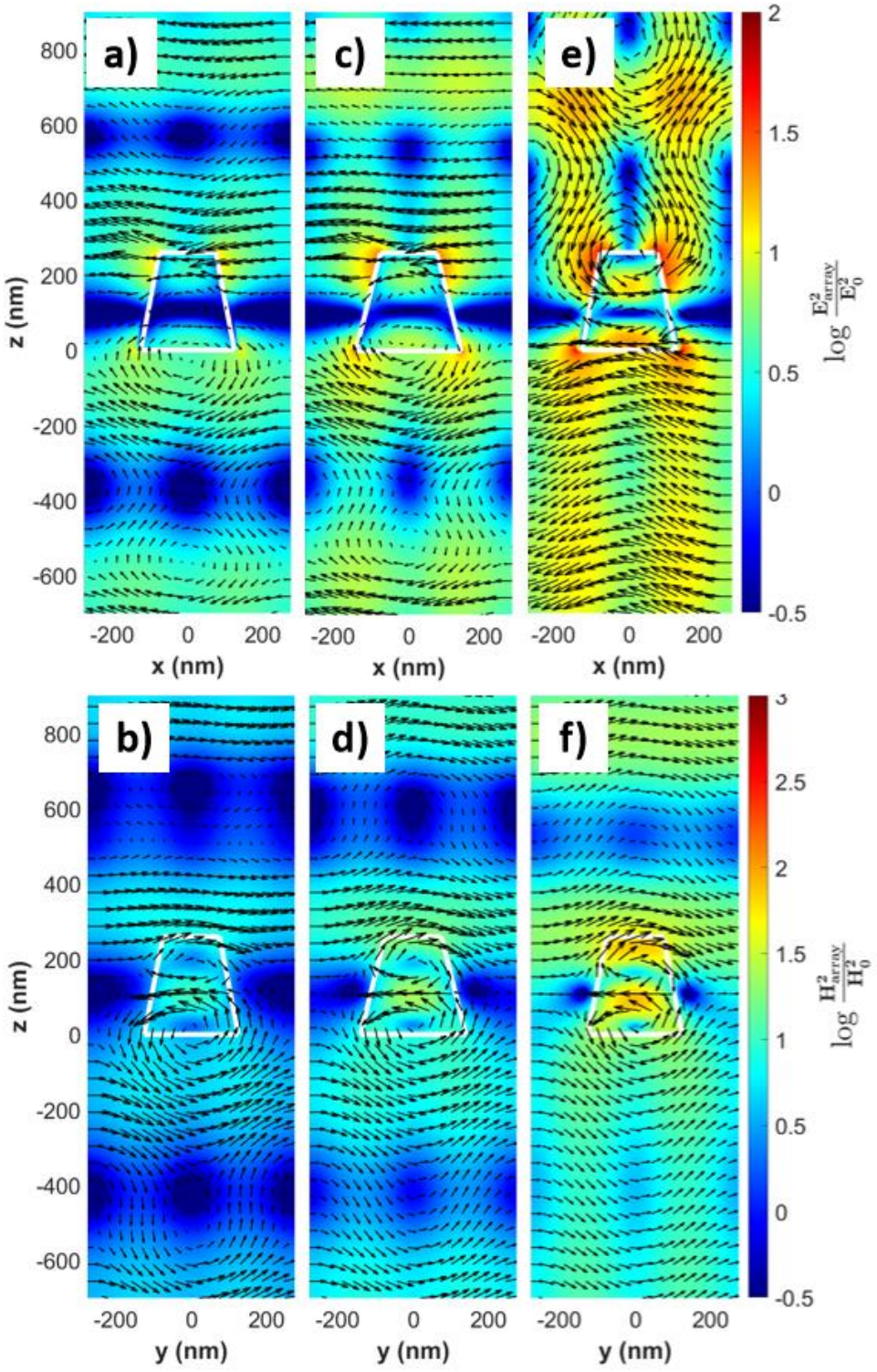

Figure 4-9 Electric and magnetic field intensity distributions normalized to the incident field intensity for the first order RA at 550 nm for the A550 array in air for different pillar refractive indices. The colour represents the intensity on a logarithmic scale and the black arrows represent the real part of the vector electric/magnetic field on the xz/yz plane. Specifically, here is shown a) the electric field intensity distribution for pillar with index of 1.9, b) the magnetic field intensity distribution for pillar with index of 1.9, c) the electric field intensity distribution for pillar with index of 2.1, d) the magnetic field intensity distribution for pillar with index of 2.1, e) the electric field intensity distribution for pillar with index of 2.4, f) the magnetic field intensity distribution for pillar with index of 2.4.

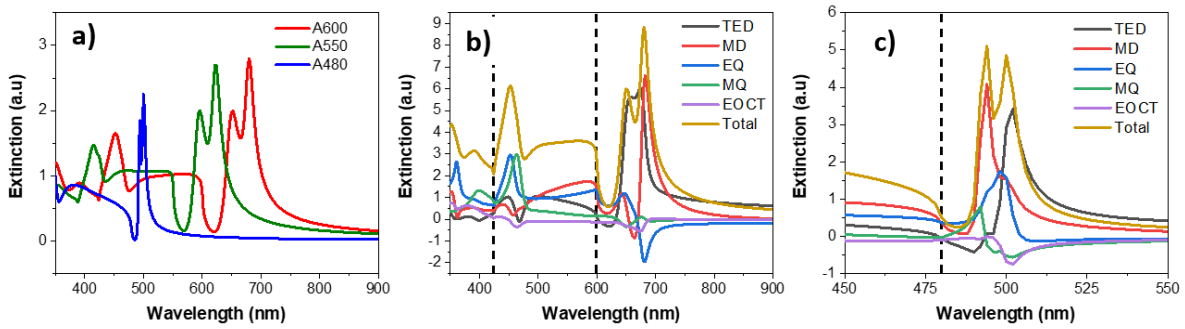

Figure 4-10 a) FDTD extinction spectra for the three arrays on air, b) decomposed extinction spectra for A600, c) decomposed extinction spectra for A480. First and second order RAs marked by the black dashed lines.

We will now look at the reflection and transmission spectra of these arrays obtained from the FDTD simulations in **Figure 4-11.** The reflection and transmission spectra have been normalized to the source power. A very interesting feature observed for all these arrays is the sharp near unity band in reflection caused by the dipole coupling to the first order RA. Another useful property of the RA coupled modes (SLRs) is that they generate a high electric field intensity regions between the pillars which can be used to modify emitters by modifying radiative rate or increasing the excitation [32]. A significant increase in reflection is also observed by the second order RA-quadrupole feature in the A600 and A550 arrays. However, as will be seen in the next section, these features resulting from the coupling of pillar's resonances with the RA will be lost as soon as the substrate is added.

SLRs were observed for all three arrays in air (A600, A550 and A480). For the three arrays, a SLRs was observed were predominantly the TED and MD coupled to the first order RA. For the A550 and A600 a smaller peak in the extinction was observed to, this was due to the EQ and MQ coupling to the second order RA. The overlap between the RAs and the pillar's multipole resonances does influence the position and Q-factor of the SLRs, therefore it is possible to manipulate the SLRs by changing the dimensions and refractive index of the pillar.

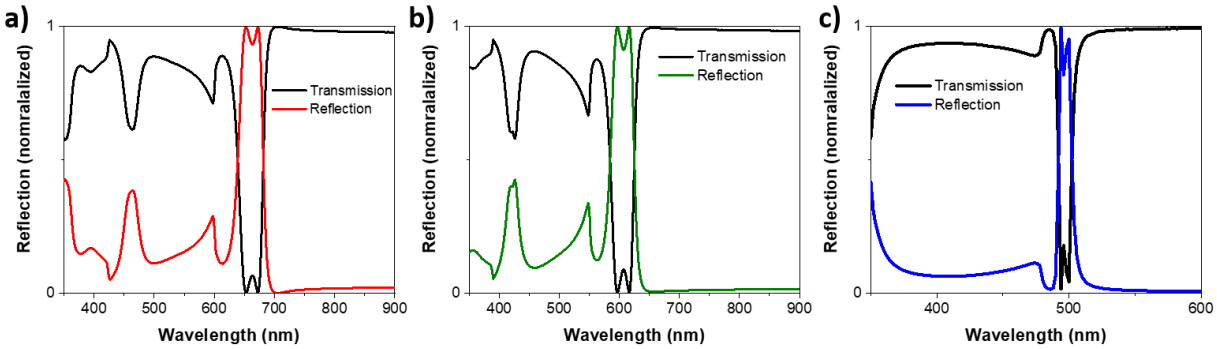

Figure 4-11 FDTD Reflection and Transmission spectra normalized to the source power for the arrays in air, a) A600, b) A550 and c) A480. Obtained from FDTD calculations.

4.2 Single Pillars and Arrays on a Substrate and TiO_2 Layer

This section is dedicated to the effects the substrate has on the single pillars and on the array structure and move on towards adding the TiO_2 layer underneath the pillar. Next, the effects of the substrate with different refractive indices close to glass (n=1.5) are investigated. The substrate in the simulations extends to the edge of the simulation region. The extinction results of the FDTD simulations on the single particle on a substrate (**Figure 4-12 a**) with a refractive index of 1.5 are shown in **Figure 4-12 b.** Upon a first look into the extinction spectra of the pillars on a substrate in **Figure 4-12 b**, one sees that the multipole resonances of the pillars have broadened and shifted, especially the A600 (**Figure 4-12 c)** and the A550 (**Figure 4-12 d).** The positions of the resonances with and without substrate can be seen in **Table 4-2** below.

Table 4-2 Wavelength (nm) of the single pillar multipole resonances with and without substrate. For the pillars of the A600, A550 and A480 arrays

	TED		**MD**		**EQ**		**MQ**	
	air	**substrate**	**air**	**substrate**	**air**	**substrate**	**air**	**substrate**
A600	650	700	665	610	450	470	466	488
A550	590	640	600	456	422	455	425	~425
A480	375	380	444	412	352	364	350<	350<

For the A600, the most notable change is the MD, which broadens significantly with the addition of the substrate: the peak blueshifts to 610 nm (55 nm change), and it develops a broad shoulder on the blue side. The TED redshifts to 700 nm and becomes more prominent in the spectra. The shifting of the resonances is likely due to nearfield effects the refractive index of the substrate has on the resonances[82]. The broadening observed is due to the increase in light out coupling into the substrate due to the fields of the multipoles extending into the substrate[82]. The broadening and shifts of the multipoles will become more pronounced with increasing refractive index of the layer[82]. The EQ broadens and redshifts slightly (20 nm), and lastly the MQ redshifts even less (12 nm), broadens and reduces significantly in intensity with increasing substrate index. The A550 multipoles show very similar changes to that of the A600. The TED redshifts by 50 nm to 640 nm, the MD peak blueshifts 44 nm similarly to A600 nm, the

broadening on the blue side is also present, the EQ broadens slightly and redshifts by 32 nm and, lastly, the MQ position does not have any noticeable change, but it is significantly broader and less intense. For the A480, things are a bit different: the TED is broader and slightly redshifted (5 nm), the MD is broader, has relatively the same intensity, and has blue shifted by 22 nm. With the addition of the substrate, the resonances change both in position and sharpness, but the overall shapes and positions do not change significantly since for Mie resonators, the resonances are mainly confined inside the particle[82].

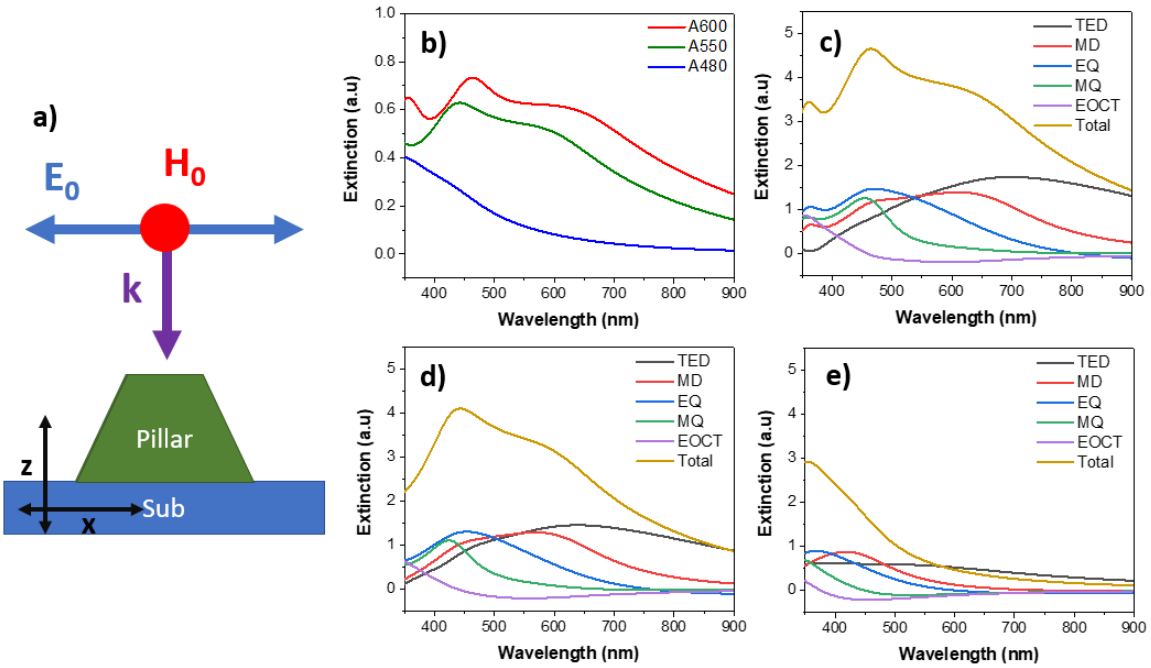

Figure 4-12 Extinction spectra of the single pillars on a substrate, a) schematics of pillar on substrate and incident electric (E_0) and magnetic field (H_0) used for simulations, b) extinction spectra obtained from FDTD simulations for the three arrays normalized to the source intensity. Decomposed extinction spectra for the c) A600, d) A550 and e) A480.

In **Figure 4-13**, the refractive index is varied from 1.4 to 1.7 of the substrate in order to observe the effects on different multipoles of the A550. The TED **(Figure 4-13 a)** intensity is increased with larger refractive index but does not shift significantly. A more interesting behaviour is observed in the MD **(Figure 4-13 b)**, where one sees that with increasing index, it continues to blueshift and the overall intensity seems to remain the same. The EQ **(Figure 4-13 c)** redshifts very slightly and broadens with increasing index. The MQ **(Figure 4-13 d)** blueshifts slightly and continues to broaden and quenches as the refractive index of the substrate increases. Lastly, in the total extinction spectra **(Figure 4-13 d)**, one can observe how the spectrum changes from two distinct peaks with no substrate to slowly losing its definition as the index of the substrate increases.

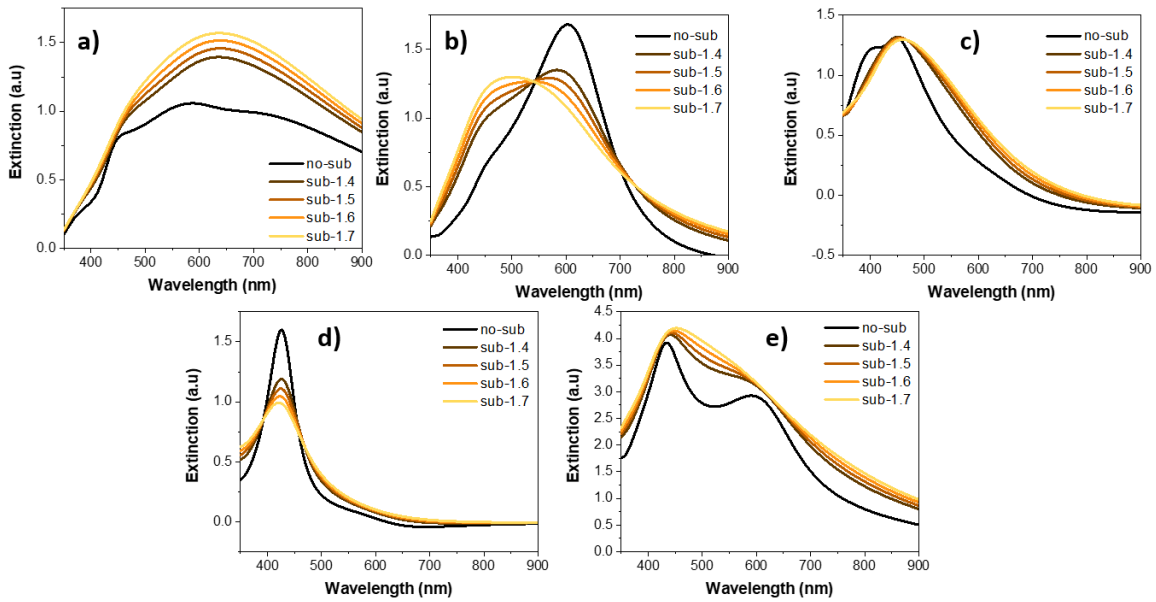

Figure 4-13 Multipole moments of the A550 pillar on a substrate with increasing substrate refractive index (1.4-1.7), a) electric dipole (ED) spectra, b) magnetic dipole (MD) spectra, c) electric quadrupole (EQ) spectra and d) the magnetic quadrupole (MQ) spectra and e) the total extinction spectra.

As it can be seen, although altered by the substrate, the position of the resonances and the overall shape of the extinction spectra do not change drastically compared with the case where there is no substrate. With the addition of the substrate, the array now has two sets of RAs, from the substrate side (glass) and from the super substrate side (air). The positions of the RAs from the glass side are 1.5 times larger than from the air side (from **Equation 4-2**). For example, the RA (2,0) for the A550 on the substrate side is at 450 nm. In contrast, in an array structure, the addition of the substrate underneath the pillars can cause the SLRs not to couple due phase mismatching between the RAs in the substrate and supersubstrate[32]. FDTD simulations were performed for the A600, A550 and A480 arrays with a substrate with refractive index of 1.5. It is observed in **Figure 4-14 b** that there is no significant coupling of the arrays' multipoles with the RAs when the substrate is added. One can also notice that more kinks in the extinction spectra of the arrays appear, which correspond to the RAs from the substrate's side. Performing multipole decomposition on the A600, the extinction spectrum in **Figure 4-14 c** lets us observe that there is very little change in the multipole spectra of the single pillar (dotted lines) and of the array (solid line). The changes observed in the spectra happen only at the RAs of both the substrate and air. The positions of the RAs are denoted by the horizontal lines in the graphs. The multipole decomposition of the A550 in **Figure 4-14 d** and

the A480 in **Figure 4-14 e** show the same results as the A600, no significant coupling is observed between the lattice modes and the multipoles.

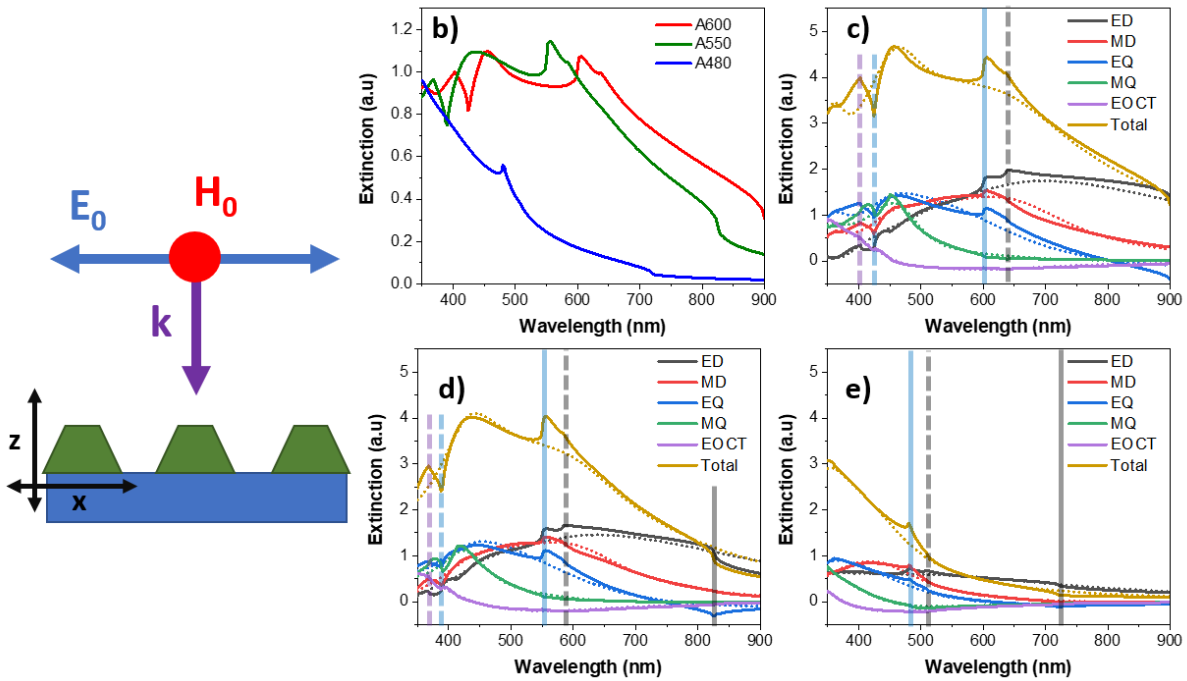

Figure 4-14 Extinction spectra of the arrays on a substrate, a) schematics of pillar on substrate and incident electric (E_0) and magnetic field (H_0) used for simulations, b) extinction spectra obtained from FDTD simulations for the three arrays. Decomposed extinction spectra for the c) A600, d) A550 and e) A480. (The dotted lines show the spectra for the single pillar on a substrate). The horizontal lines the graphs are the positions of RAs. Grey solid line first order RA from the substrate side. Blue solid line first order RA from the air side. Grey dashed line second order RA from the substrate side. Blue dashed line second order RA from the air side. Purple dashed line is a higher order RA(2,1) from the substrate side.

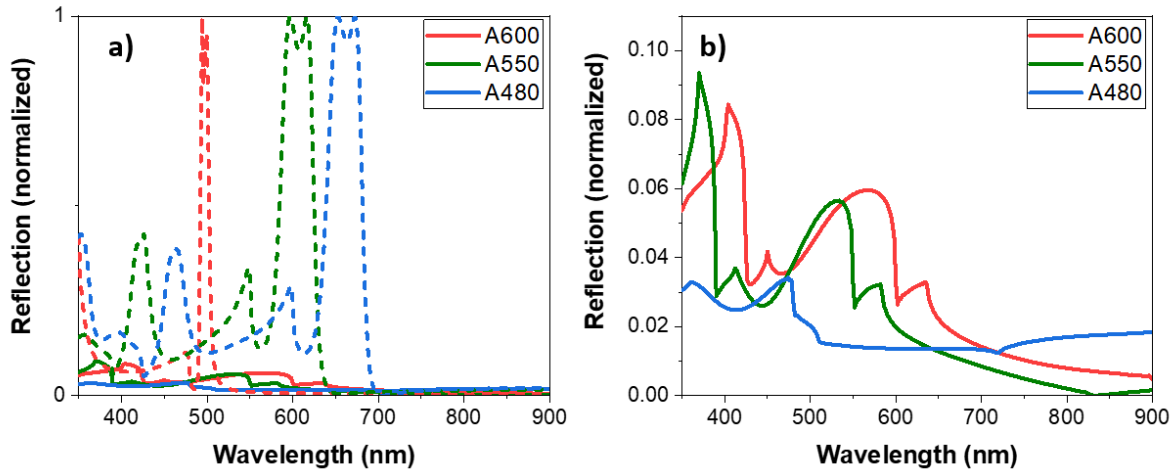

Figure 4-15 Reflection spectra for the three arrays on a substrate. a) comparison of the reflection spectra of the arrays in air (dashed lines) and with substrate (solid lines), b) close-up of the reflection spectra of the three arrays on a substrate.

The reflection spectra for the array with a substrate is substantially different from the array with no substrate. A comparison between the two is shown in **Figure 4-15 a**. As expected, the near unity reflection due to the SLRs is lost as there is no more coupling, and much less reflection is observed overall. Upon closer inspection of the reflection spectra in **Figure 4-15 b**, one observes that the RAs of the substrate and air side are responsible for the shape of the reflection spectra as it was seen in the extinction spectra.

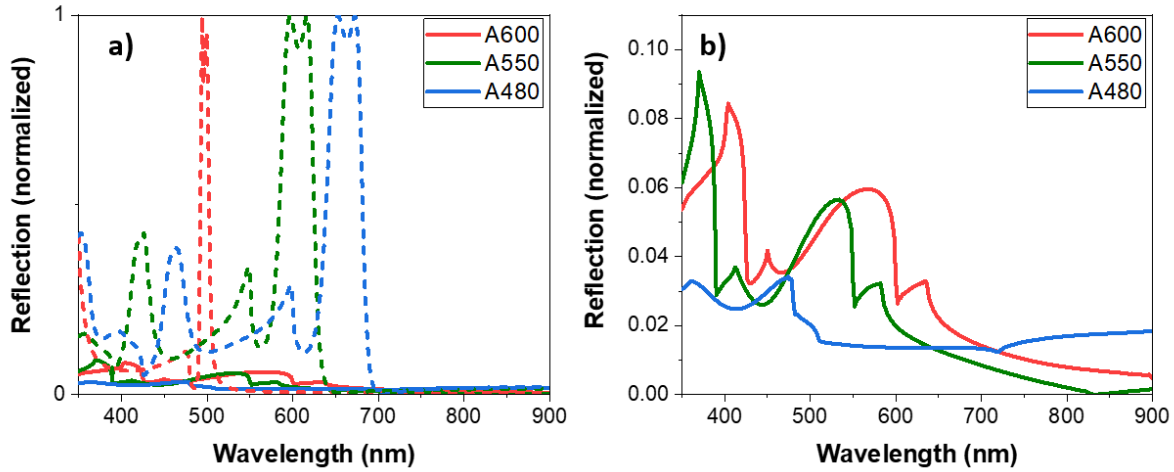

Figure 4-16 Reflection spectra for the three arrays on a substrate. a) comparison of the reflection spectra of the arrays in air (dashed lines) and with substrate (solid lines), b) close-up of the reflection spectra of the three arrays on a substrate.

There is one element missing from the complete array structure, namely the TiO_2 layer. This layer is in-between the pillars and the substrate (**Figure 4-17 a**). The refractive index of this layer will be varied from 1.5-1.9, this range will cover values lower than the substrate and close to pillar's refractive index. We will begin by looking at the effects the TiO_2 layer has on the resonances of the single pillar. The extinction spectra for the A550 pillar on a substrate with a refractive index of 1.6 is shown in **Figure 4-17 b**, with different layer refractive indices (1.5 and 1.9). As mentioned earlier, for these arrays, the layer underneath the pillar has a lower index than the pillar. The differences between the pillar on a substrate of 1.5 and on a layer of 1.5 are very small as seen in **Figure 4-17 b,** they are slightly different due to the refractive index of the substrate being 1.6. In **Figure 4-17 c**, one sees the decomposed spectra for the layer with refractive index of 1.5. One observes the same trend for the 1.5 layer with the introduction of a substrate: the TED redshifts, MD blueshifts and broadens, and the EQ and MQ behave as in the case of just the substrate. No major changes are observed by introducing the 130 nm thick TiO_2

layer with refractive index of 1.5. A similar trend is seen for the layer with refractive index of 1.9 in **Figure 4-17 d**, but with more pronounced changes. There is a greater redshift for the TED, greater blueshift for the MD but less broad than for the layer with index of 1.5. In **Figure 4-18** the effects that the layer's refractive index has on the different multipoles across a larger range are presented. **Figure 4-18 a** presents the TED exhibiting a very similar trend to what was observed for the substrate dependence on refractive index, except for 1.3 (significantly lower than the substrates index of 1.6), where the TED is broader and shows a prominent peak on its blue side. In **Figure 4-18 b** it can be observed how the MD blueshifts and becomes less broad as the refractive index of the layer increases, forming a sharper peak. The EQ behaviour in **Figure 4-18 c** is relatively constant with increasing layer index. The MQ however exhibits quenching and broadening with increasing layer index, up to 1.9, where it increases.

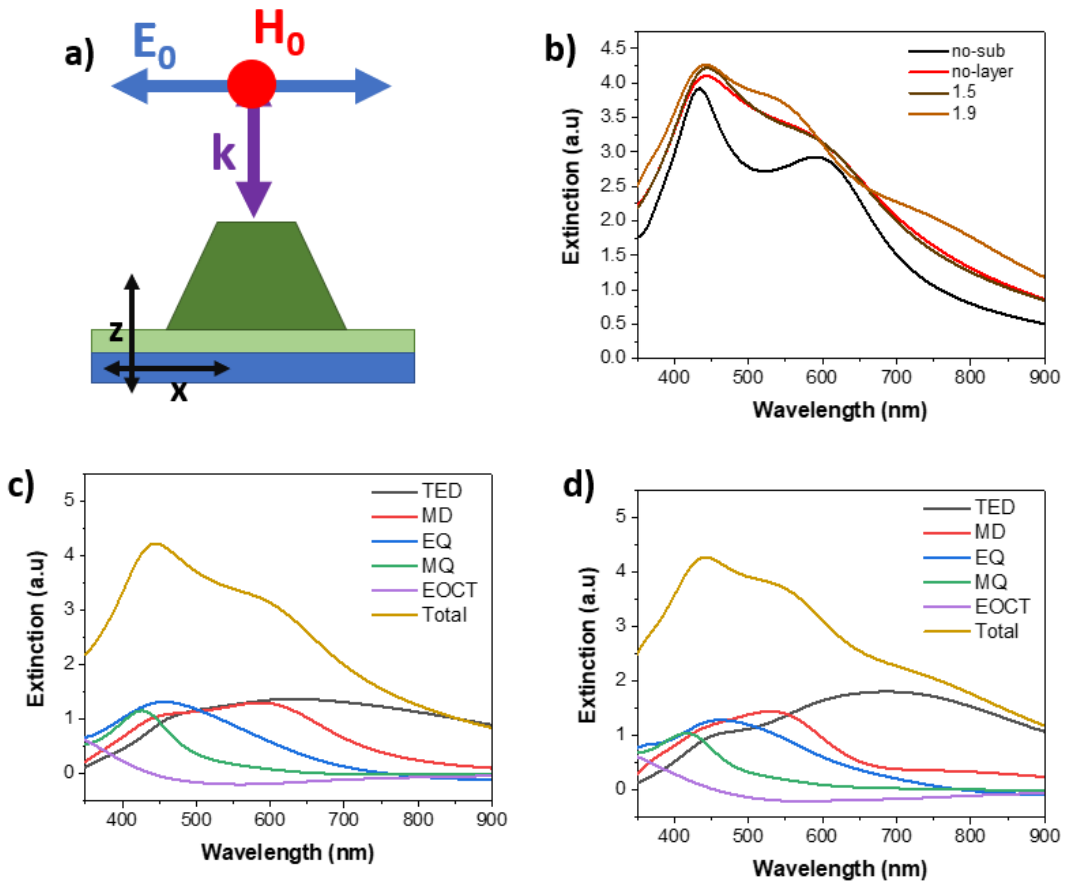

Figure 4-17 Extinction spectra of the A550 pillar on a substrate with refractive index of 1.6 with a TiO_2 layer underneath the pillar, a) schematics of pillar on substrate with layer and incident electric (E_0) and magnetic field (H_0) used for simulations, b) extinction spectra obtained from FDTD simulations for the A550 pillar, the black line is the extinction spectrum with no substrate and the red line is with just the substrate. The brown and orange lines correspond to the inclusion of a 130 nm thick TiO_2 layer with refractive indices of 1.5 and 1.9, respectively. Decomposed extinction spectra for the A550 with a TiO_2 layer with refractive index of c) 1.5 and d) 1.9.

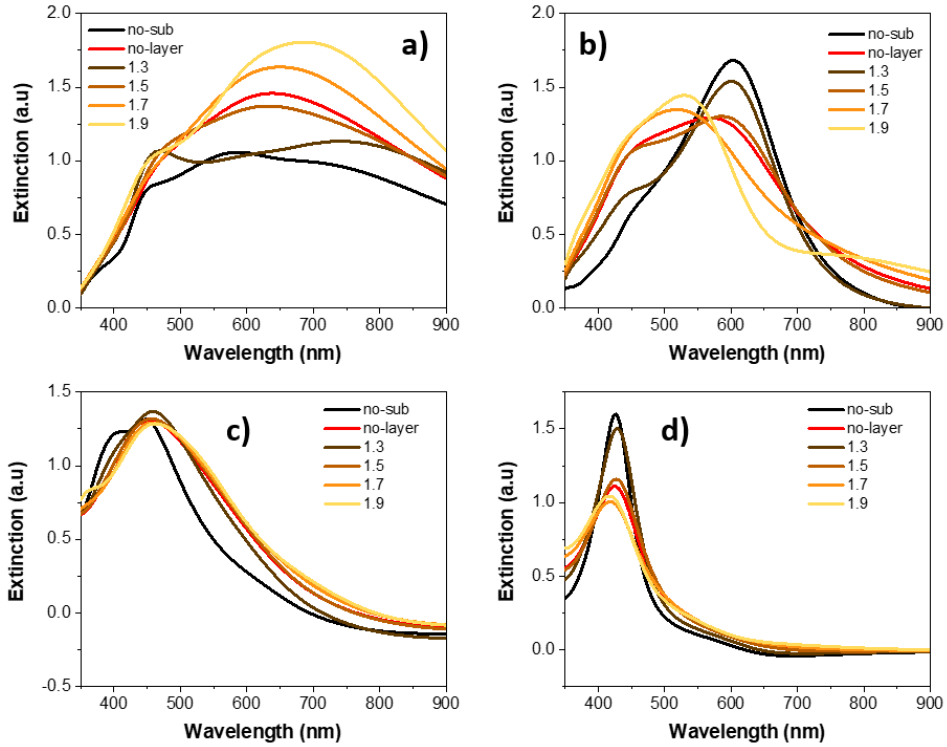

Figure 4-18 Multipole moments of the A550 pillar on a substrate with an intermediate TiO_2 layer of varying refractive index, a) total electric dipole (TED), b) magnetic dipole (MD), c) electric quadrupole (EQ) and d) the magnetic quadrupole (MQ) (The black line in the graphs corresponds to the pillar on air and the red line to the pillar on a substrate with refractive index of 1.5).

The changes in the resonances of the single pillar on the TiO_2 layer are not vastly different from the single particle in free space and nearly identical to the particle on a substrate. However, **Figure 4-19 a-c** shows the multipole decomposition of A600, A550 and A480 arrays, respectively, with a TiO_2 layer with refractive index of 1.4. In **Figure 4-19 d-e**, the multipole decomposition of the arrays A600, A550 and A480, respectively, with a TiO_2 layer with refractive index of 1.9, are shown. It is obvious from the differences in the graphs that the index of the layer plays a big role in the behaviour of the array. For the case where the refractive index is 1.4, one observes a situation very similar to that of an array with just the substrate. The layer with refractive index of 1.9 shows very sharp features in the spectra, the A480 shows a very sharp TED resonance at 776 nm which appears to be coupling with the first order lattice mode of the substrate at 768 nm. The sharp features in the middle at 548 nm and 564 nm appear to be the TED, MD and EQ coupling with the second order RA from the substate at 543 nm. It is also observed that now the electric octupole (EOCT) is showing interactions with the lattice modes. For the A550 array, one observes very similar behaviour as the large sharp resonance of A480

at 886 nm appears to be coupled with the first order RA from the substrate at 880 nm and it is predominantly a TED resonance. The second largest sharp peak observed at 642 nm appears to be coupled with the second order RA of the substate at 622 nm. In the region inside the red square, it appears that all the multipoles are contributing to the features observed. This region appears in-between the first and second order lattice mode of the air side of the array. For the A600 array, due to the range of the simulation, the coupling of the first order lattice mode from the substrate at 960 nm is not observed. However, all the other features are very similar to those observed on the A550. The new sharp features seen in the extinction spectra are responsible for very sharp and strong reflection peaks for the three arrays as shown in **Figure 4-20 a-c**.

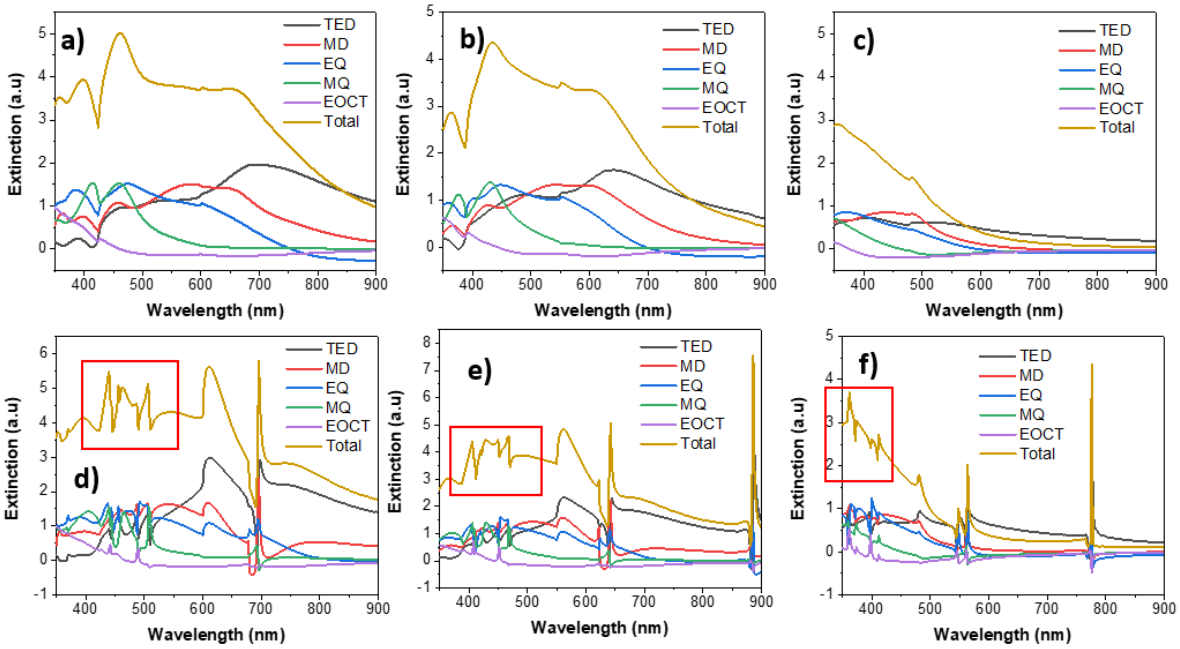

Figure 4-19 Multipole decomposition for the three arrays with different layer refractive index, a) A600 array with layer index of 1.4, b) A550 array with layer index of 1.4, c) A480 array with layer index of 1.4, d) A600 array with layer index of 1.9, e) A550 array with layer index of 1.9, f) A480 array with layer index of 1.9. Substrate index of 1.6 for all arrays.

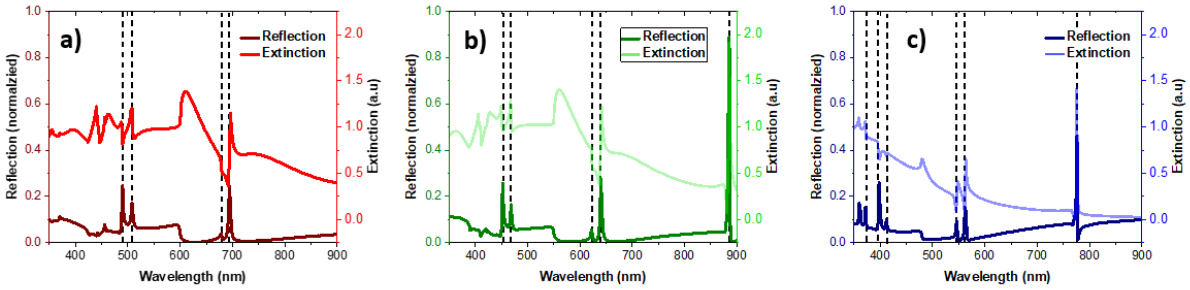

Figure 4-20 FDTD results of the reflection and extinction spectra for arrays with a TiO_2 layer with index of 1.9 for the a) A600, b) A550, and A480 arrays.

In **Figure 4-21 a**, the decomposed extinction spectra of the A550 array with a layer with a refractive index of 1.9 and substrate with refractive index of 1.5, is shown. These parameters were chosen because they resemble what it can be expected in experiments and the extinction spectra shows a lot of features (sharp peaks) in the range from 350-900 nm. In **Figure 4-21 b** the reflection spectrum for this array is shown, the new peak observed at 826 nm in the extinction spectra is present as a sharp peak in the reflection. By taking a close look at the extinction decomposition, one can see that the sharp peaks (826 and 856 nm) observed in the grey area, are mainly due to the TED and some contribution from the EQ. These two peaks occur after the first order RA from the substrate at 825 nm and are the strongest peaks in reflection. The second set of peaks in the red area are due mostly to the MD and a small contribution from the EQ. This second set of peaks (592 and 628 nm) are the second strongest reflection peaks and occur after the second order RA from the substrate at 583 nm. The third set of peaks and the third strongest reflection peaks are in the green area and occur between the first and second order RA from the air side (389 and 550 nm). We will now look at the field intensity maps of each of these peaks to gain more insight.

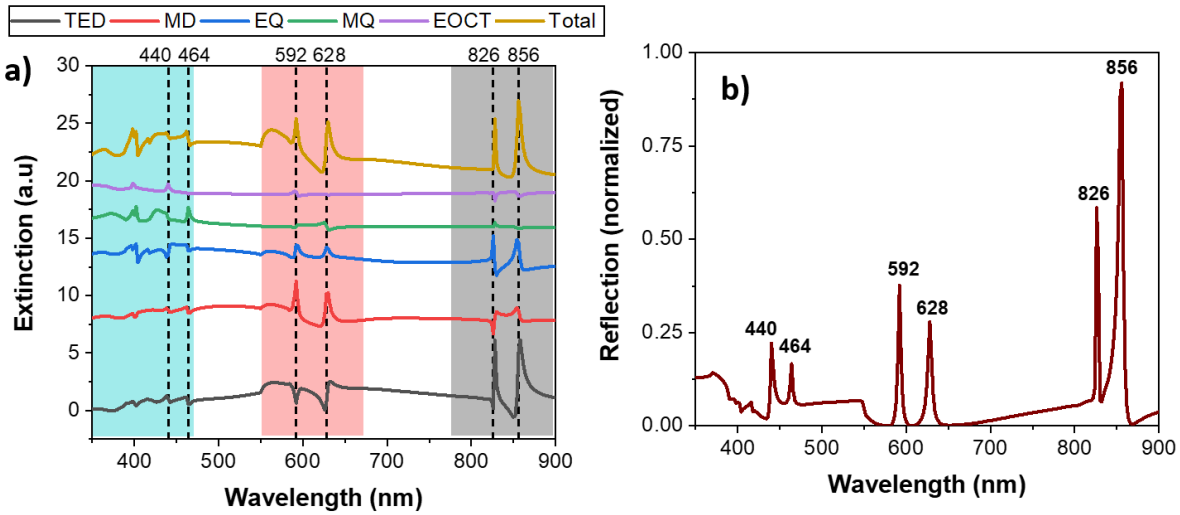

Figure 4-21 a) Decomposed extinction spectra and b) reflection spectra from FDTD simulation of the A550 array on substrate of refractive index of 1.5 and layer index of 1.9. The sharp peaks of the reflection spectra are marked by the dashed lines on the extinction spectra.

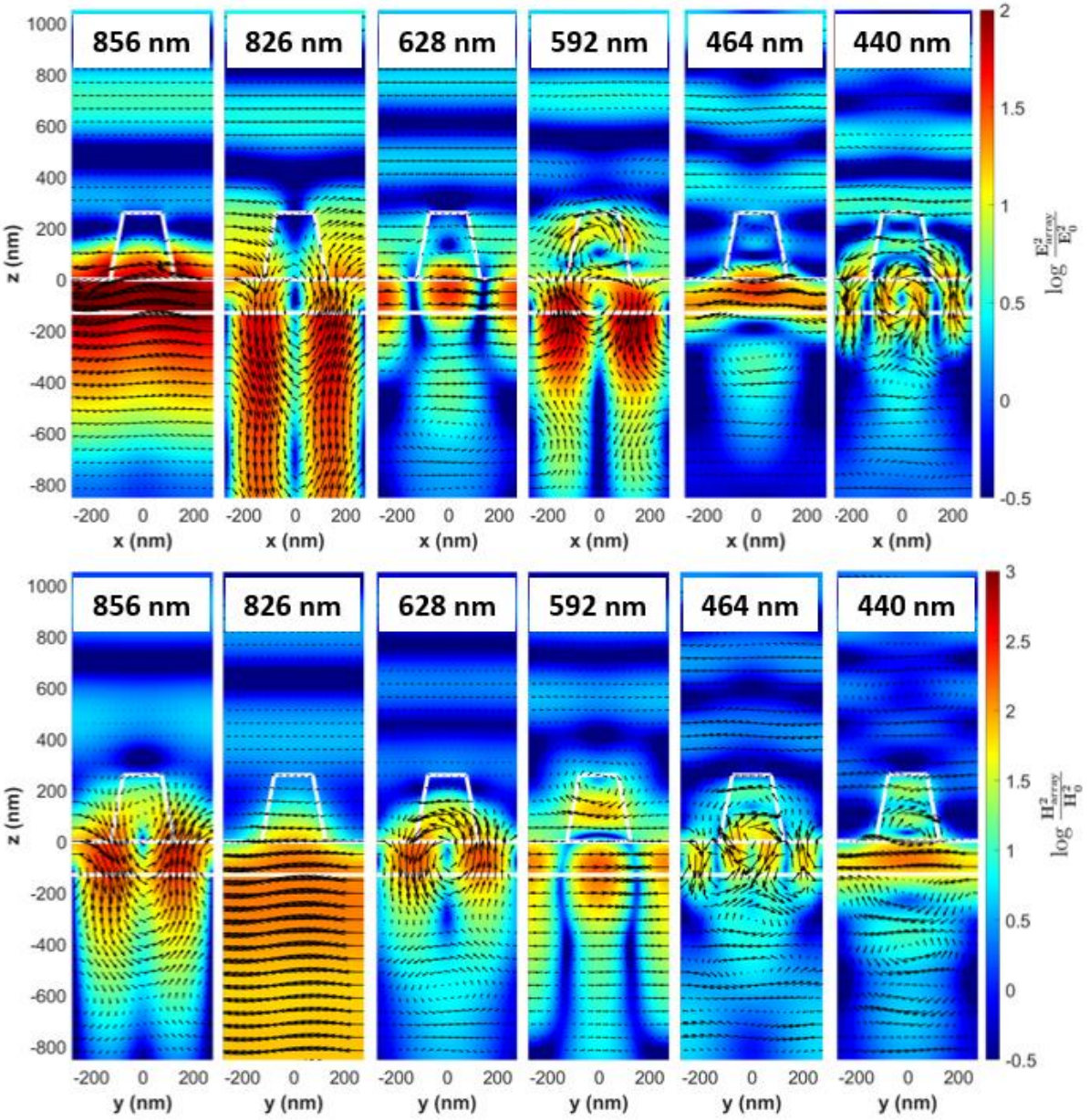

Figure 4-22 Electric and Magnetic field intensity distributions normalized to the incident field intensity for the A550 array on substrate of refractive index of 1.5 and TiO_2 layer of refractive index of 1.9. The colour represents the intensity on a logarithmic scale and the black arrows represent the real part of the vector electric/magnetic field on the xz/yz plane. Top row: electric fields distributions, Bottom row: magnetic field distributions for the positions of the sharp peaks shown in **Figure 4-21 b**.

The electric and magnetic field intensity distributions for the sharp reflection peak at 856 nm are shown in **Figure 4-22**. The electric field intensity distribution shows very intense fields, mainly confined in the layer. There is also significant spreading into the substrate and pillar. The magnetic field is mainly confined in the layer and circulating, a signature of electric modes. By looking at the electric and magnetic field orientation it can be concluded that this is an electric quasi-guided mode (QGM) that is mostly confined in the layer and it is propagating along the y axis of the layer. This peak will be referred to as E-QGM1. The electric and magnetic

fields of the peak at 826 nm are shown in **Figure 4-22**. The electric field of this peak has a very similar profile to the magnetic field profile at 856 nm. One observes a circulating electric field that is not confined in the layer as it penetrates significantly into the substrate. The magnetic field intensity at 826 nm has a very similar shape to the electric field at 856 nm, the orientation of the field is predominantly along the y axis and it is not confined in the layer since it spreads into the substrate. This peak is consequently a magnetic mode coupled to a RA of the substrate that is propagating along the x direction. However, it is not clear if this mode is a QGM or a lattice mode because even though it is mostly propagating through the substrate, this mode is still propagating in the layer and it is not observed without the layer. We will refer to this mode as M-QGM1. The second set of peaks observed in the reflection show field intensity maps as depicted in **Figure 4-22** that are significantly different from the E-QGM1 and M-QGM1. For the electric and magnetic field intensity distributions for the reflection peak at 628 nm in **Figure 4-22**, it is observed that both the electric and magnetic fields are confined predominantly in the layer and since the magnetic field forms a loop around the layer, this indicates that the peak at 628 nm is an electric QGM traveling along the y axis of the layer. Three lobes of intense electric field in the layer can be observed, one directly underneath the pillar and two between the pillars, with electric fields oriented 180 degrees from their neighbours. This means there are three propagating electric fields travelling in the y axis, in opposite direction from their neighbours. From this, it is concluded that this QGM is very likely coupled to the second order (1,1) RA from the substrate side, since it will be affected by a_y because its propagating in the y direction and it will also be affected by a_x because the lobes in the electric field form a "standing wave" in the x axis. This mode will be referred to as E-QGM2. For the peak at 592 nm, by looking at the electric and magnetic field distributions in **Figure 4-22** and following the same analysis done on the fields for E-QGM2, this is a magnetic QGM that is very likely coupled to the second order (1,1) RA from the substrate side. This mode is penetrating more into the substrate than the E-QGM2. This mode will be referred to as M-QGM2. We will now look at the electric and magnetic field intensities for the peak at 464 nm in **Figure 4-22**. The electric field is mainly oriented along the x axis and is confined in the layer. The magnetic field is looping around the layer clearly pointing to an electric QGM propagating along the x axis. It is not very clear from the fields if this QGM is coupled to a_x, though it is possible due to the multiple magnetic loops around the layer and due to the electric field being the most intense directly underneath the pillar. This mode will be referred to as E-QGM3. Lastly, by looking at the electric and magnetic field distribution in **Figure 4-22** for the peak at 440 nm and performing the same analysis on the electric and magnetic fields, one can arrive to the same conclusion as for E-QGM3, but for

a magnetic QGM propagating along the x axis. This mode will be referred to as M-QGM3. The next section will examine the RA these modes are coupled to and their dependence to different array parameters. Below is a table that summarizes how the QGMs from the peaks observed in reflection are referred as.

Table 4-3 Summary of how the QGMs from the peaks observed in reflection are referred as.

Type of QGM	E-QGM1	M-QGM1	E-QGM2	M-QGM2	E-QGM3	M-QGM3
Peak Positions	856 nm	826 nm	628 nm	592 nm	464 nm	440 nm

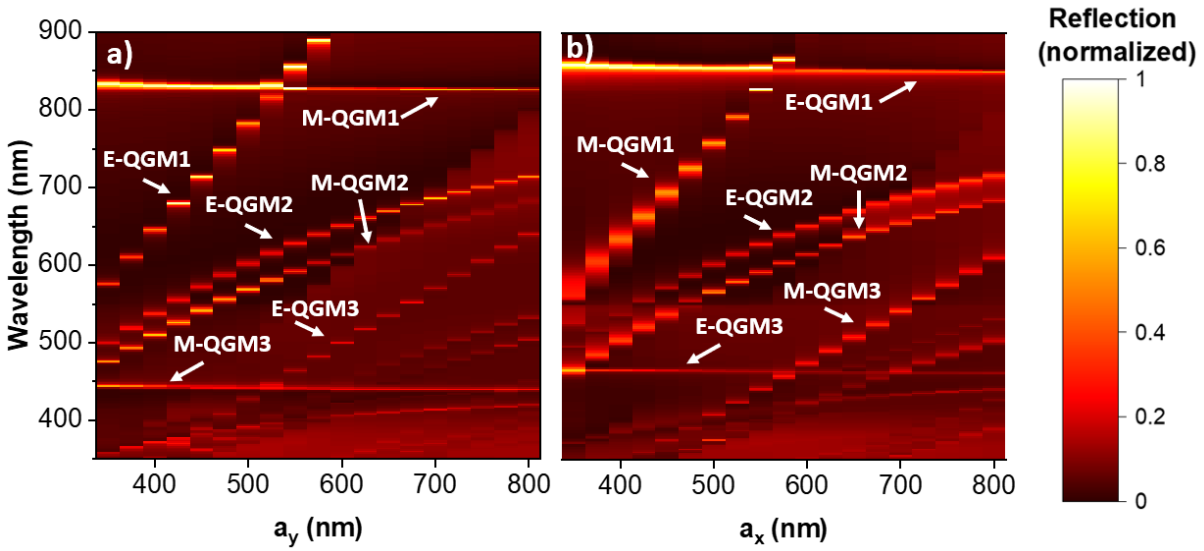

Figure 4-23 FDTD Reflection spectra of the A550 array (same material parameters as array in in **Figure 4-21)** dependence on the lattice constants a) a_y and b) a_x. The static lattice constant is 550 nm in both cases.

In **Figure 4-23 a** and **b** one sees the dependence of the reflection spectra on the lattice constants a_y and a_x of the array from **Figure 4-21**. One observes that E-QGM1 varies linearly with the change of the lattice constant a_y, while the M-QGM1 is independent of a_y. On the other hand, by varying a_x, one sees that the M-QGM1 is now varying linearly and E-QGM1 is constant. It is clear now that the E-QGM1 is propagating along the y axis and is coupled to the $(0,1)$ RA from the substrate side (825 nm at a_y=550 nm) and M-QGM1 is propagating along the x axis and is coupled to the $(1,0)$ RA from the substrate side (825 nm at a_y=550 nm). For the second set of peaks, E-QGM2 and M-QGM2, it is observed that both are varying when either a_x or a_y are varied. Furthermore, their dependence on the lattice constants is not linear,

but rather has a $1/\sqrt{c+1/x^2}$ dependence. Due to the nonlinear dependence on the lattice constant and their proximity to RA (1,1) from the substrate, the E-QGM2 and M-QGM2 are clearly coupled with the (1,1) RA from the substrate side at 583 nm at a_x=a_y=550 nm. For the last set of peaks, E-QGM3 and M-QGM3, one observes a very similar behaviour to the first set of peaks: E-QGM3 is linearly dependent on a_y, while independent of a_x and M-QGM3 is linearly dependent on a_x while independent of a_y. The only RA close to these resonances that would explain this behaviour is the second order (2,0) RA and (0,2) RA from the substrate for a_x=a_y=550 nm at 412.5 nm. Therefore, E-QGM3 is coupled to the (0,2) RA from the substrate and propagating along the y direction and M-QGM3 is coupled to the (2,0) RA from the substrate and propagating along the x direction. One also observes reflection peaks coupled to higher order terms appearing in the reflection spectra as the lattice constants increase.

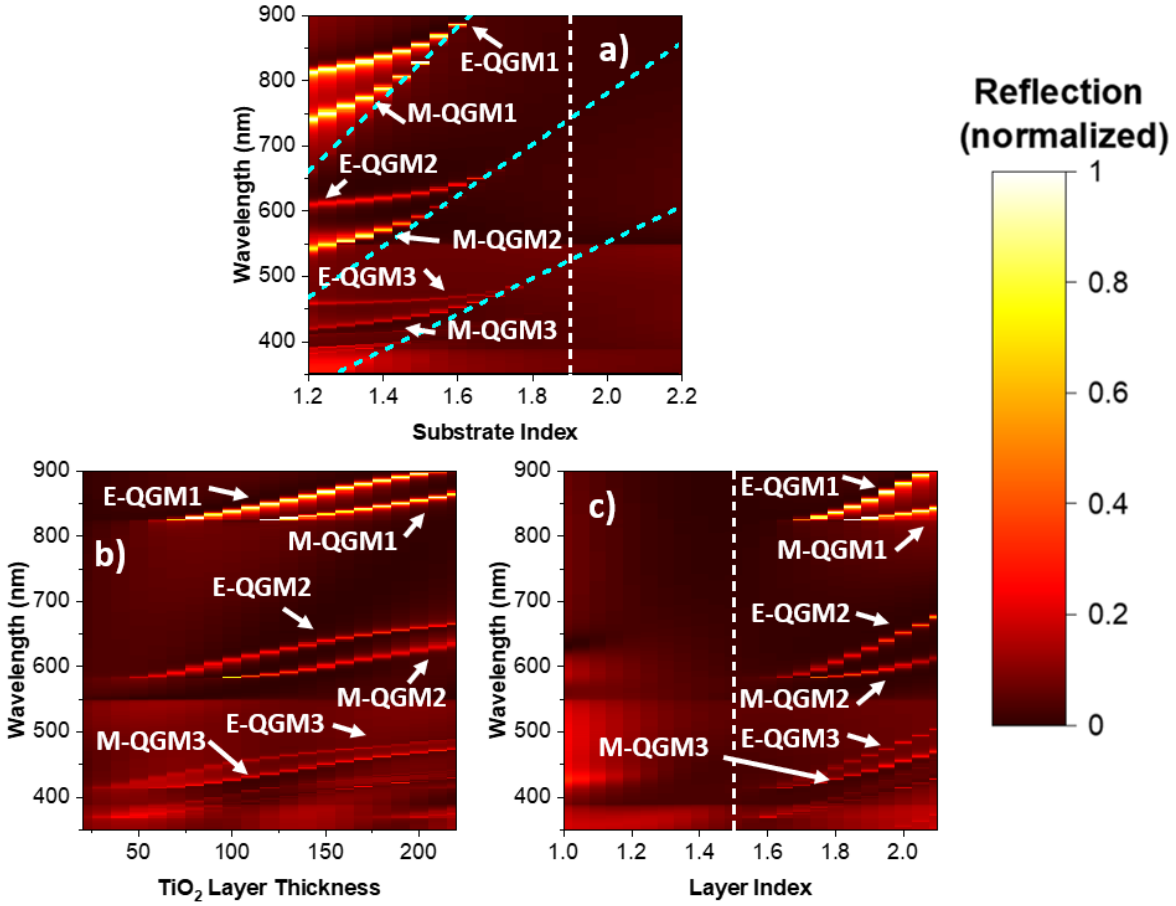

Figure 4-24 FDTD Reflection spectra for the A550 array**.** Dependence on a) the substrate's refractive index (white dashed line shows the index of the TiO_2 layer), the first (top to bottom) light blue dashed line represents the (0,1) and (1,0) RA from the substrate, the second represents the (1,1) RA from the substrate and the third line is the (0,2) and (2,0) RA from the substrate side, b) the layer thickness and c) the layer refractive index (white dashed line is at the refractive index of the substrate).

Now the dependence of the reflection spectra on the properties of the substrate and layer is presented. In **Figure 4-24 a**, the dependence of the reflection spectra on the substrate's refractive index is shown. It can be observed that all the peaks vary with the refractive index. However, the E-QGMs vary less due to the E-QGMs being more confined in the layer as seen in **Figure 4-22**. It can also be observed that E-QGM1 varies more than E-QGM2, which in turn varies more than E-QGM3. The same is observed for the M-QGMs. This is due to the field becoming more confined in the layers. Also, asymptotic behaviour is observed for all the QGMs as they approach their coupled RA, further confirming their coupling. The sharp peaks vanish as the index of the substrate approaches the index of the layer at 1.9 since modes can no longer exist in the layer. In **Figure 4-24 c** one sees the impact of the refractive index of the layer on the reflection spectra. The E-QGMs are more sensitive to changes in refractive index than the M-QGMs and the QGM1s show the least dependence. This behaviour is the exact opposite from the one observed in the index dependence of the substrate, but it is not surprising as the modes that are affected the most are the modes most confined in the layer. One can also observe that the index of the layer must be larger than that of the substrates, also expected as otherwise the layer would not support guided modes. Next, the dependence of the positions of the QGMs on the thickness of the layer will be observed in **Figure 4-24 b**. The layer must be thick enough to support the QGMs.

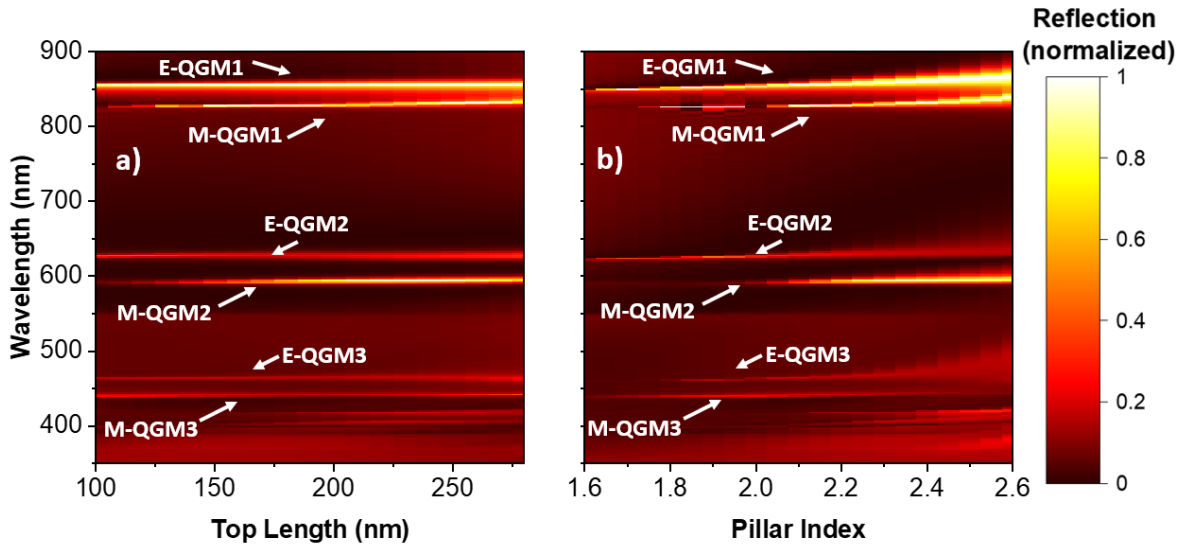

Figure 4-25 FDTD Reflection spectra of the A550 array in **Figure 4-21** showing the dependence on the a) the top length of the pillar and b) the refractive index of the pillar.

The dependence of the QGMs on the shape of the pillar was also explored in **Figure 4-25 a.** The top length of the pillar was varied from 100 nm to 250 nm (until the pillar was a

cube). One observes virtually no variance in the position of the QGMs, however the M-QGM2 does get significantly more intense as the shape approaches a square. Very similarly, when the refractive index of the pillar is varied from 1.6 to 2.6, very little to no change is observed in the positions of the QGMs, though again the M-QGM2 does get significantly more intense as the index increases. One also observes some broadening of the resonances with increasing index, which is not surprising as more optically dense materials scatter the light stronger. It can be concluded that the wavelength of the QGMs does not depend on the particle properties but rather on the properties of the layer and substrate.

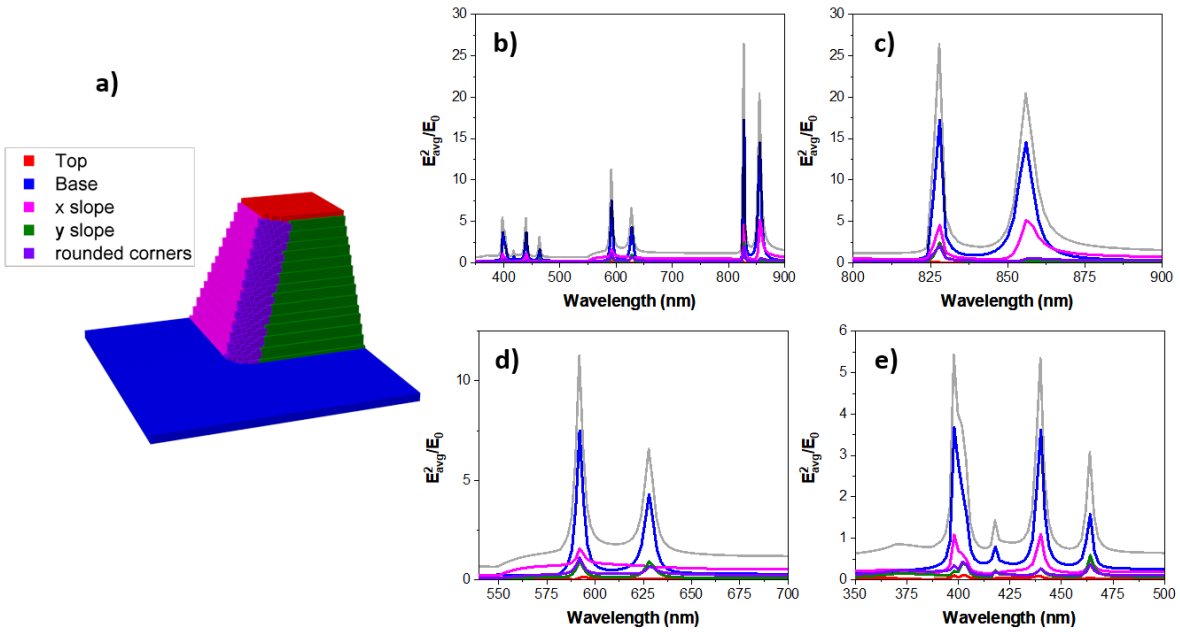

Figure 4-26 a) Division of array into 5 different areas, top, base, x-slope, and the rounded corners. Average electric field intensity across a 5 nm layer above the surface of the A550 array on a substrate of refractive index of 1.5 and layer index of 1.9 for the different areas of the array represented as the grey line, the contributions from each area are represented by the different colour lines, b) entire spectra, c) close-up from 800-900 nm, d) close-up from 525-700 nm, e) close-up from 350-500 nms.

Further on, the average electric field intensity normalized to the incident field across a 5 nm layer over the surface of the array will be looked at. The unit cell of the array is divided into 5 different areas (top, base, x slope, y slope and rounded corners) as seen in **Figure 4-26 a**. This is done to see the contributions from each area to the average electric field intensity. In **Figure 4-26 b** the average electric field intensity for the A550 array with a TiO_2 layer with an index of 1.9 is shown. It can immediately be seen that the reflection peaks observed produce high electric field intensities of up to ~20 larger than the incident field for the QGM1s. Looking closely at **Figure 4-26 c**, it is seen that the base is responsible for most of the prominent peaks in electric field enhancement, which is to be expected because QGMs are bound in the layer.

For the QGM2s (**Figure 4-26 d**), electric field enhancements of up to ~10x are seen and again, most of this enhancement comes from the base. Lastly, the QGM3s (**Figure 4-26 e**) show electric field enhancements of roughly 5x and most of the contributions to the enhancement again come from the base. One also sees a new peak appearing at 400 nm, which is not observed in the reflection spectra, but it is observed in the extinction spectra, in **Figure 4-27 a**. Upon inspection of the electric and magnetic field intensity distributions of the peak at 400 nm in **Figure 4-27 b** and **c**, profiles very similar to the QGM2s are observed, which indicates that this mode might be arising from a higher order (1,2) RA as the electric field is very similar to H-QGM3 and the magnetic field is very similar to H-QGM2. It is also interesting that the field intensity seems to halve progressively from region to region. There will be a more detailed examination of the electric field enhancements in the following chapters.

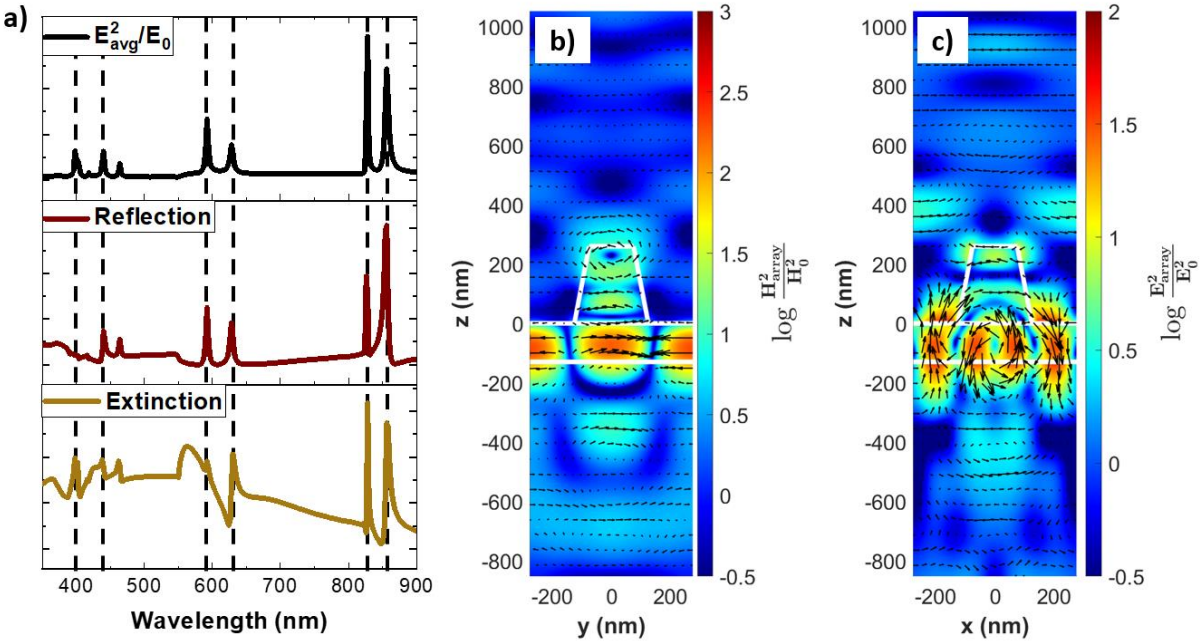

Figure 4-27 a) Comparison of the reflection, extinction and the average electric field intensity across a 5 nm layer above the surface of the array. The black dashed lines overlap with the peaks observed in the electric field intensity enhancement. The Electric and Magnetic field intensity distributions were normalized to the incident field intensity for the A550 array on a substrate of refractive index of 1.5 and layer index of 1.9. The colour represents the intensity on a logarithmic scale and the black arrows represent the real part of the vector electric/magnetic field on the xz/yz plane. Presented are the electric **a)** and magnetic field intensity distribution **b)** at 400 nm.

4.3 Conclusion

In conclusion, in this chapter it has been demonstrated that the resonances of the single TiO_2 pillar are broadened and shifted by the addition of a substrate and the TiO_2 layer. The

magnitude of the broadening and shifting can be controlled by changing the refractive index of the layer or substrate. In the case of the arrays in air, the coupling of the TED and MD with the first order RA was observed as a large double peak in reflection and extinction. A smaller peak in the extinction related to the coupling for the EQ and MQ to the second order RA was also observed. The positions of the SLRs of arrays in air can be manipulated in position and width by the optical and physical properties of the pillars. The addition of the substrate to the array, caused the SLRs to no propagate in the arrays. The addition of the residual layer allowed QGMs to propagate in the arrays when the refractive index of the layer is larger than the refractive index of the substrate. QGMs were observed as six sharp strong peaks in the reflection spectrum in three sets. The first set E-QGM1 and M-QGM1 were coupled to the first order RA from the substrate side. The second set E-QGM2 and M-QGM2 were coupled to the second order RA from the substrate side. The third set E-QGM3 and M-QGM3 were coupled to the third order RA from the substrate side. The position of the QGMs can be varied by changing the properties of the layer and substrate, changing the properties of the pillar does not change the position of the QGMs, only reduces the Q-factor of the resonances when the refractive index or size of the pillar is increased. Therefore, the most important properties to control to eb able to support QGMs are the thickness and refractive index of the layer and the substrate on which the arrays are built.

5 Experimental Analysis of TiO2 arrays

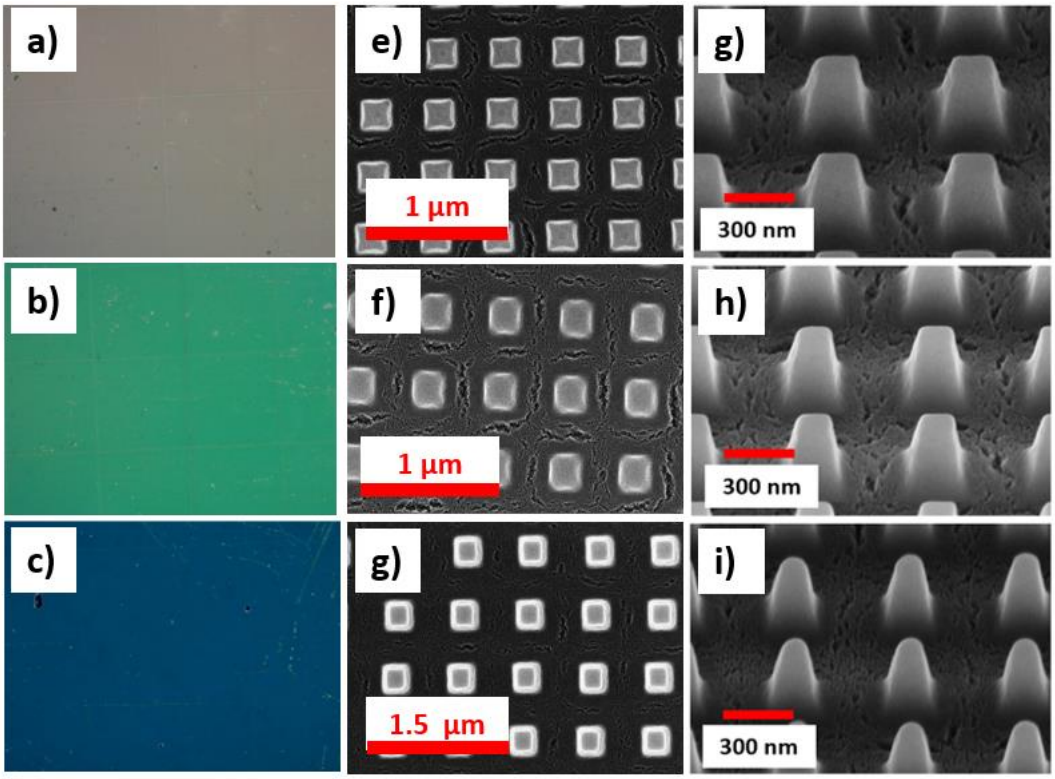

Figure 5-1 Darkfield scattering images captured with a 20x objective under darkfield illumination for the a) A600, b) A550 and c) A480 arrays. SEM images of the d) A600, e) A550 and f) A480 arrays. Angled SEM images of the g) A600, h) A550 and i) A480 arrays.

In the previous chapter, the properties of the arrays using FDTD numerical simulations were investigated in-depth. This chapter will focus on the properties of the physical arrays and on the modification of them with R6G using both experimental measurements and simulations. As mentioned previously, the TiO_2 arrays were fabricated by the group of Marco Abbarchi from Aix-Marseille Université, Marseille, France using soft nano-imprint lithography. Due to the nature of this fabrication method, a residual layer of TiO_2 is left behind. As explored in the previous chapter, the thickness and refractive index of this layer is very important. The refractive index and thickness of the residual layer controls the positions in the QGMs. In the case of these arrays, the layer is roughly 130 nm, thick enough to support QGMs if the refractive index is higher than 1.5 (refractive index of the glass substrate). Specific to these arrays is the fact that the layer between the pillars is quite porous and rough, which lowers the effective refractive index and reduces the ability of the array to support QGMs. The effect of the porosity and irregularities of the residual layer on the transmission and reflection spectra will be looked

at through FDTD simulations and the results will be compared with the experimental measurements. The high porosity of the residual layer makes it possible to absorb other materials and change the optical properties of the layer. The consequences R6G has on the experimental transmission, reflection and darkfield scattering of the A600, A550 and A480 for several concentrations will be investigated. The same dimensions and simulation set-up discussed in Chapter 4 will be used.

5.1 Experimental normal incidence reflection and transmission for the A600, A550 and A480

In this section, the normal reflection and transmission using the set-up described in the section 3.3 are discussed. By using this set-up, light transmitted and reflected out of the array is collected only in a cone with half angle of approximately 1.2° from a normal incidence beam, allowing one to collect light that has not been scattered at high angles. To obtain the percent of the total light reflected, the reflected light from the arrays was normalized to the reflection of a clean microscope glass slide, then multiplied by the reflection of glass at normal incidence which is approximately 8%, accounting for both sides of the glass slide. To obtain the percent of transmitted light through the array, the reflected light was normalized to the transmission when no sample was present.

Table 5-1 RA positions the A600, A550, and A480 arrays.

	RA(1,0)$_a$	**RA(1,1)$_a$**	**RA(1,0)$_s$**	**RA(1,1)$_s$**	**RA(2,0)$_s$**	**RA(2,1)$_s$**
A600	600	424.3	900	636.4	450	402.5
A550	550	388.9	825	583.4	412.5	369.0
A480	480	339.4	720	509.1	360	322.0

The extinction spectra are then calculated by $Ext = 100\% - R - T$ where R and T are the percentages of reflected and transmitted light collected from the arrays. **Figure 5-2 a** shows the normal reflection spectra of the arrays. There are no strong reflection features for any of the three arrays from QGMs coupled to lattice order RAs, however an RA feature in the reflection spectra is observed shown in **Figure 5-2 a.** In this chapter the 1st order RA from the air side will be referred as RA (1)$_a$ = RA (0,1)$_a$=RA (1,0)$_a$ and 1st order RA from the substrate side as RA

$(1)_s$ = RA $(0,1)_s$=RA $(1,0)_s$, the higher order RA will be referred to in a similar manner (see **Table 5-1)** . By using **equation 4-2** the lattice order RAs are calculated for the different arrays at normal incidence. **Table 5-1** contains the positions of the RAs for all three arrays.

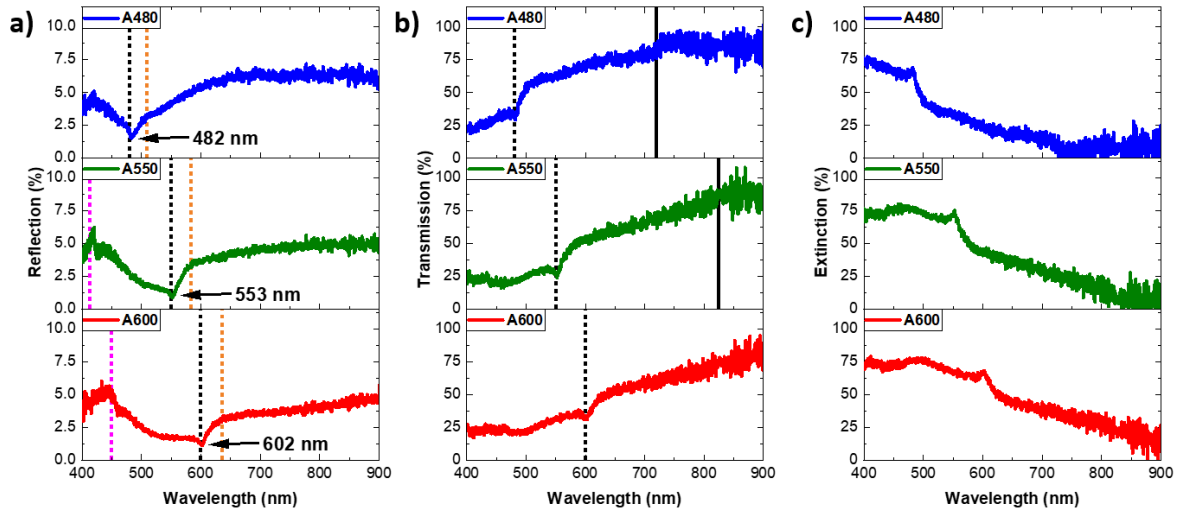

Figure 5-2 Experimental results for the a) normal reflection (pink dashed line at RA$(2)_s$, black dashed line at RA$(1)_a$, orange dashed line at RA$(1,1)_s$), b) normal transmission (black dashed line at RA$(1)_a$, , black solid line at RA$(1)_s$) and c) the extinction spectra for the A600, A550 and A480 arrays.

The normal reflection spectra for the three arrays are very similar to each other. All of them show at RA $(1)_a$, a sharp dip in reflection and at RA $(1,1)_s$, one sees a sudden change in slope for all arrays. For the A550 and A600 at RA $(2)_s$, one notices a sharp change in slope. In the transmission spectra in **Figure 5-2 b**, there is a sharp dip in transmission at RA $(1)_a$ (black dashed line) for the three arrays. At RA $(1,1)_s$, one observes a sudden change in slope for all arrays. For the A550 and A600 at RA $(2)_s$ there is a change in slope, but also at RA $(1)_s$ for the A550 at 825 nm and A480 at 720 nm. One does not observe this feature for the A600 because the RA $(1)_s$ is at 900 nm, which is the limit of the collection range. Finally, in **Figure 5-2 c,** the extinction is shown**.** The extinction spectra of the three arrays does not show any strong sharp intense features that one would see if there were any coupling QGMs to RAs. The transmission, reflection or extinction do not show any signs of QGMs coupling to RA. This could be due to two things: either due to the refractive index of the layer not being larger than the refractive of glass (1.5) due to the high porosity or it may also be due to the surface roughness of the TiO_2 layer. In **Figure 5-1 d-i** one can appreciate the roughness and porosity of the TiO_2 layer.

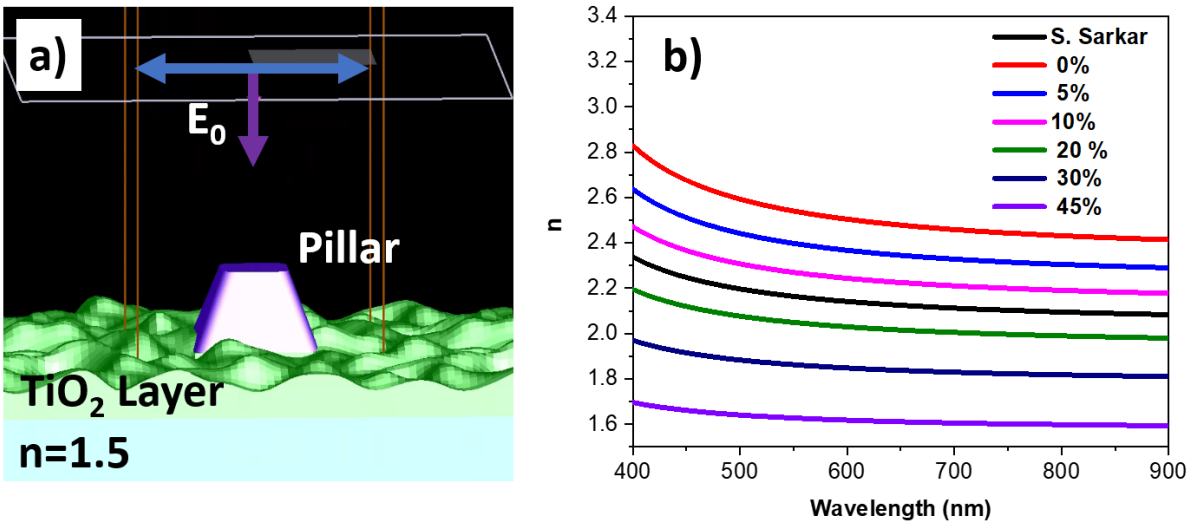

Figure 5-3 a) schematic of the FDTD simulation for the arrays, E_0 is the incident electric field, purple arrow is the propagation direction (z axis), the blue arrow is the electric field polarization (x-axis), and the orange lines are the limits of the unit cell (the period of the array). b) Refractive index of TiO_2 for different porosities used in the FDTD simulations.

The following investigation will focus on the way in which TiO_2 layers with different porosities and roughness affect the obtained reflection and transmission spectra measured by performing FDTD simulations. For these FDTD simulations, the same set-up as in the previous chapter is used, as shown in the schematic in **Figure 5-3 a**. However, instead of using a TFSF source, a plane wave source is implemented. Also, the TiO_2 layer is modelled by a rough surface. The root mean square (RMS) of the surface is increased to observe the resulting effects on the spectra. Experimentally obtained data of the refractive index on a thin TiO_2 layer is used from S. Sarkar et al[58]. Then by using the Maxwell-Garnett equation, one can calculate the refractive index of TiO_2 for different porosities[103]:

$$\frac{n^2-1}{n^2+2}=\left(1-\frac{P}{100\%}\right)\frac{n_d^2-1}{n_d^2+2}$$

where n is the refractive index, n_d is the refractive index of bulk TiO_2 (roughly 2.54 at 550 nm) and P is the porosity. Now, the refractive index for different porosities can be calculated by using the TiO_2 refractive index on a thin layer from S. Sarkar et al[58]. The refractive index for different porosities is shown in **Figure 5-3 b**. In this work, the arrays are gratings, the experimental set-up only allows for the zero-order reflection and transmission from the arrays to be collected. One can obtain the zero-order reflection and transmission of the FDTD simulation of the TiO_2 using a built-in function from the FDTD software (Lumerical). In **Figure 5-4 a,b**, the zero-order FDTD reflection and transmission for the A550 array are shown with the total reflection obtained.

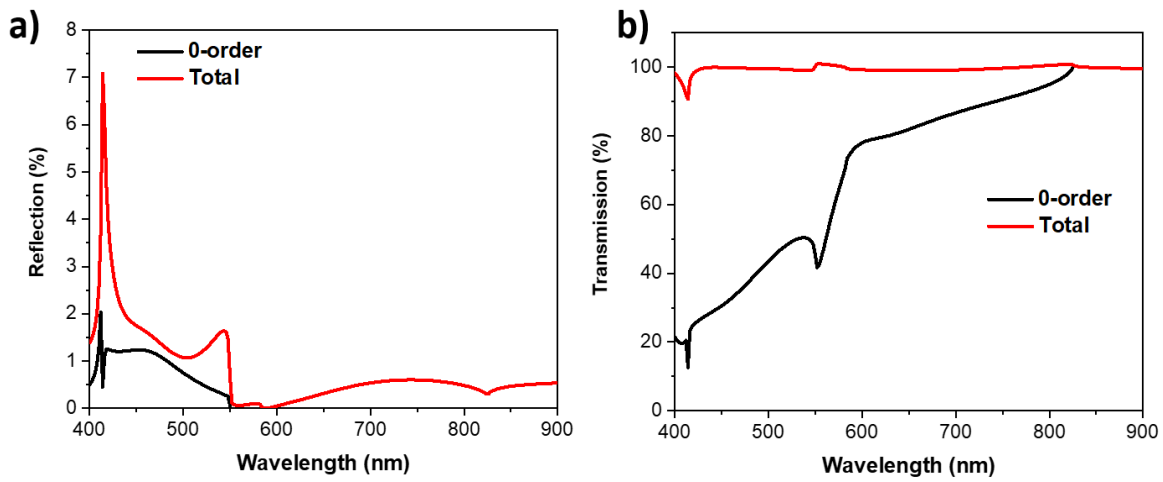

Figure 5-4 Comparison of the zero-order a) reflection and b) transmission for the A550 array with 30% porosity pillar and 45% porosity layer.

To properly calculate the experimental reflection and transmission spectra from FDTD simulation, one must consider the back reflections from the glass substrate (n=1.5), namely of 4%. Two simulations are needed: one simulation where the incoming beam comes from the air side of the array and another from the substrate side, as shown in **Figure 5-5 b**. Simulations do not account for the back reflection of the substrate since they consider the substrate as infinitely thick. Back reflections from the substrate are significant to the reflection spectra in the experiments as ~4% of the light is back reflected. From the simulation from the air side, one can obtain the 0-order reflection R and transmission T as shown in **Figure 5-5 a**. From the simulation from the substrate side, one obtains the 0-order reflection R^* and transmission T^* as depicted in **Figure 5-5 b**. From these, one can now calculate to total reflection R_T shown in **Figure 5-5 c**:

$$R_T = R + 0.04TT^*$$

and the total transmission T_T shown in **Figure 5-5 c**:

$$T_T = 0.96T(1 + 0.04R^*)$$

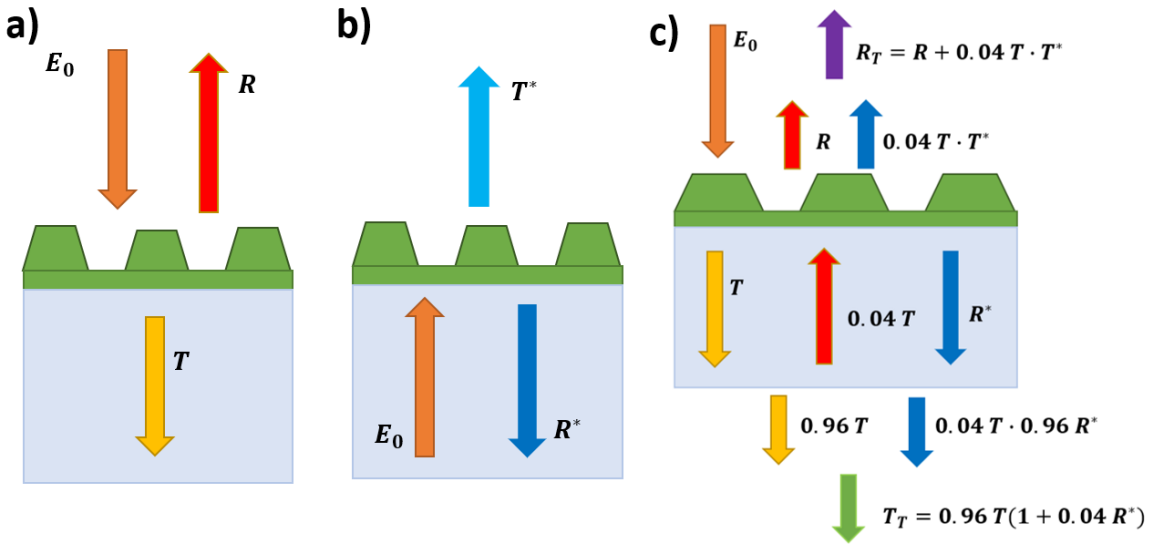

Figure 5-5 a) Diagram showing the reflection R and transmission T obtained from FDTD simulation with incident field E_0 from the air side, b) diagram showing the reflection R^* and transmission T^* obtained from FDTD simulation with incident field E_0 from the substrate side. c) diagram showing the different contributions to the total reflection R_T and total transmission T_T.

Figure 5-6 shows as an example, the contribution of the back reflection to the total transmission R_T and total transmission T_T for the A550 array with 30% porosity for the pillar and 35% porosity for a flat layer. The back reflection plays a significant role in the total reflection. The sharp features from RA coupling into QGMs come from the first reflection, while the back reflection from the substrate's side is very similar in shape to the transmission spectra. The back reflection has negligible contribution to the total transmission (T_T).

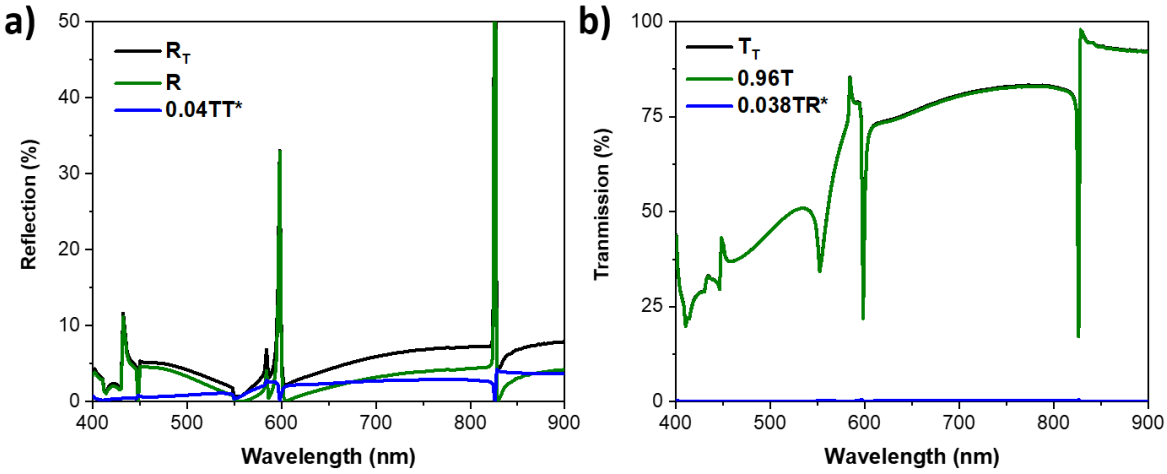

Figure 5-6 a) Contributions of the back reflection ($0.04TT^*$) and first reflection (R) to the total reflection spectra (R_T), b) contributions of the back reflection ($0.038TR^*$) and transmission ($0.96T$) to the total transmission spectra (T_T), from FDTD simulations on the A550 with a 30% porosity pillar and 35% porosity layer with no roughness.

Several simulations were performed for the A550 array with different porosities for the pillar and a 45% porosity layer with no roughness to determine which would better match with experimental results. In **Figure 5-7 a**, one can observe the FDTD zero-order reflection spectra dependence on different porosities of the pillar. The spectrum does not change significantly with increasing porosity. The features of the reflection spectra become less prominent, and the reflection overall reduces. The best match to experiment is 30% porosity, since higher porosities, despite having a shape more like experiment, show much lower reflection. **Figure 5-7 b** shows the FDTD zero-order reflection spectra of the A550 array with a 30% porosity pillar and with varying layer porosity. The position of the RA $(2)_s$ is marked by the orange dashed line and the best match with the experimental position is with a 45% porosity layer. Also, this layer does not support the QGMs for the lower order RAs, unlike layers with porosities smaller than 40%. Therefore, 30% porosity for the pillar and 45% porosity for the layer provide the best match with experimental data. For a layer with 35% porosity, one observes RA-QGM coupling (marked by the black dashed lines in **Figure 5-7 a**) and that the strongest peak at 826nm corresponds to an electric QGM coupled to the RA $(1)_s$ (E-QGM1) at 825nm. The RA-coupled QGMs come in electric and magnetic pairs, the electric QGMs are redshifted compared to magnetic QGMs and appear before the magnetic QGMs. The second strongest peaks at 598 nm corresponds to the electric QGM coupled to the RA $(1,1)_s$ (E-QGM2) and the smaller peak at 584 nm is the magnetic QGM coupled to the RA $(1,1)_s$ (M-QGM2). A sharp peak at 432 nm near RA$(2)_s$ is very likely an electric QGM (E-QGM3).

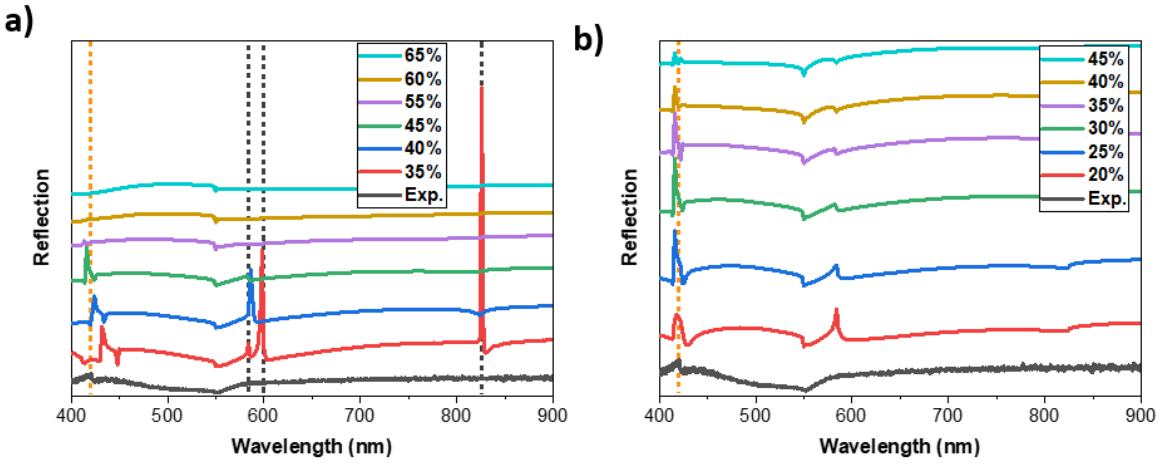

Figure 5-7 0-order reflection spectra obtained from FDTD simulation on the A550 array with a flat layer. a) zero-order reflection dependence on the porosity of the layer with a 30% porosity pillar (black dashed lines show the positions of the sharp peaks at 35% porosity), b) zero-order reflection dependence on the porosity of the pillar with a 45% porosity layer (orange dashed line is at RA$(2)_s$).

From the SEM images in Error! Reference source not found. of the arrays, one observes that the pillars are smooth and identical to each other, while the layer is not. A rough surface was used as the TiO_2 layer and the RMS of the surface was varied to simulate the randomness of the layer. Work done about how randomness in the different array properties affect the coupling of RA with the particle resonances have been conducted by Zakomirnyi et al [75]. The randomness in the different properties of the array elements (period, size, discontinuities) weakens the collective resonances in the arrays, so one expects to observe similar behaviour for RA-coupled QGMs when randomness is introduced in the layer. However, what is done in these simulations is not a true treatment of randomness since there is a pattern that repeats in every unit cell. Nevertheless, this will still give an insight into the effects of small irregularities on the reflection and transmission spectra. **Figure 5-8 a** shows the FDTD results for the total reflection for the A550 array with a 30% porosity pillar and a 35% porosity layer for increasing surface roughness. The QGM coupled to $RA(1,1)_s$ disappears with increasing roughness, as well as the magnetic QGMs coupled to $RA(1,1)_s$. Also, the electric QGM blueshifts towards $RA(1,1)_s$. Similarly, the QGM coupled to $RA(2)_s$ blueshifts and increases in intensity as it approaches $RA(2)_s$ at 412.5 nm. The $RA(1)_a$ dip in reflection does not change considerably with increasing roughness. The behaviour of these peaks with increasing roughness is very similar to decreasing the thickness or refractive index of the layer. In **Figure 5-8 b** the reflection spectra dependence on surface roughness of the A550 array with a 30% porosity pillar and a 45% porosity layer is shown. The sharp features from RAs from the substrate side disappear with increasing roughness. Also, the QGM coupled with the $RA(2)_s$ at 412.5 nm reduces in intensity as the roughness increases, matching well with the experimental reflection at roughness larger than 30nm. **Figure 5-8 c** shows the transmission for the same array. Like in the case of reflection, features that appear due to the RAs from the substrate become less prominent with increasing roughness and the $RA(1,1)_s$ dip is now a discontinuity in the slope. The transmission spectra at roughness larger than 30 nm matches quite well with the experimental transmission. The extinction spectra for the same array are shown in **Figure 5-8 d**. As it can be seen, it matches quite well in shape with the experimental one, for most of the spectral range (except between 400-500 nm) is not as flat as the measured extinction.

Next, the effect the gaps (see Error! Reference source not found. **b)** in the layer between the pillars have on the reflection and transmission spectra will be investigated. These gaps are created during the fabrication probably from an overstretch of the layer when the silicon master is removed. In Error! Reference source not found. the gaps between the arrays can be

appreciated. They are random in size and shape, and they are usually between 50-100 nm wide. Error! Reference source not found. **b** shows a cross section of one of the gaps (highlighted in red) which is roughly 80 nm deep. For the FDTD simulations, a model of a 3x3 unit cell was implemented with randomly placed gaps between the arrays, roughly 80 nm deep and 70-100 nm wide as shown in Error! Reference source not found. **c**. The 3x3 cell was used to increase the randomness of the gaps. However, this section is replicated for all the arrays and because of this, some features related to high order RAs from the gaps with periodicity of 1650 nm could be introduced.

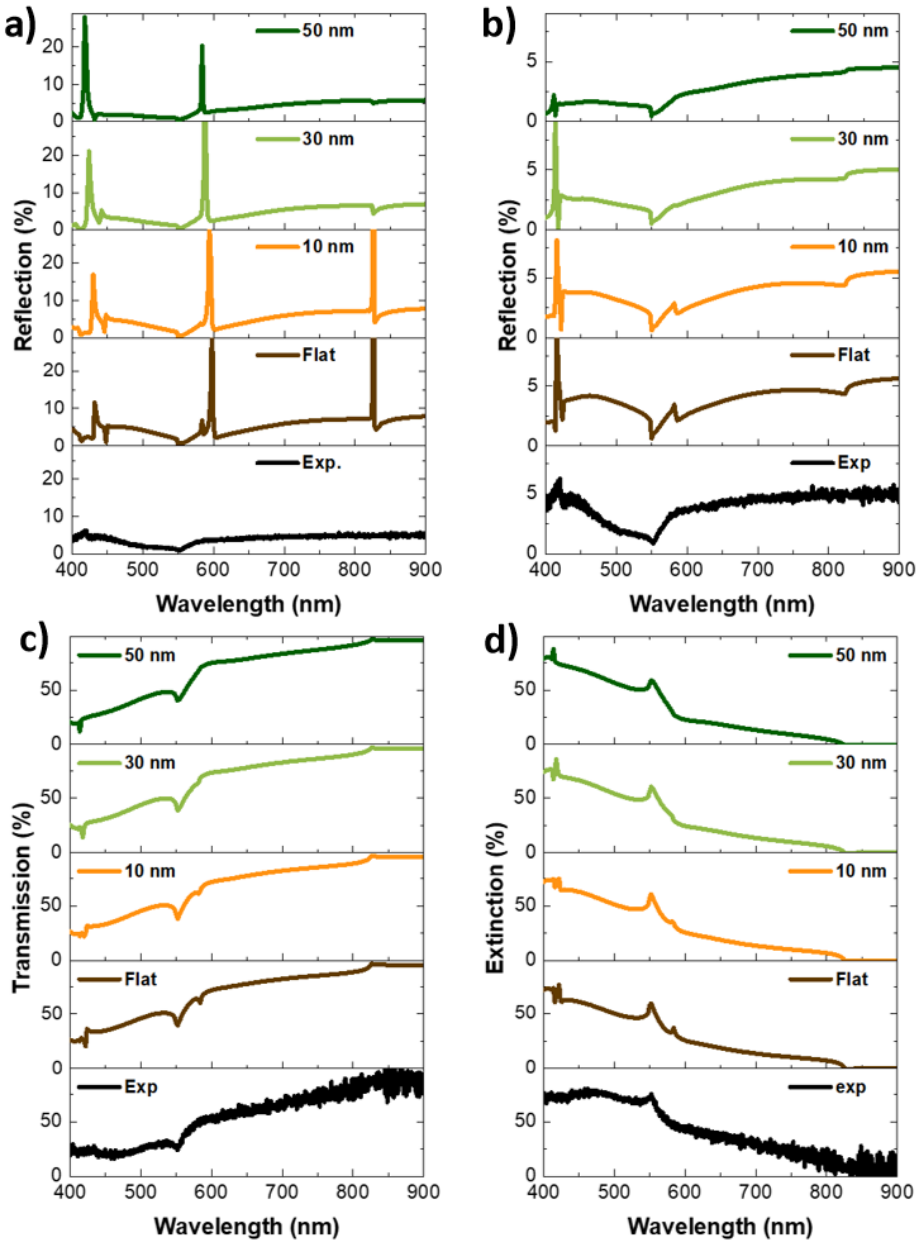

Figure 5-8 Effects of increasing porosity on the a) 0-order reflection spectra for the A550 array with 30% porosity pillar and 35% porosity layer. b) zero-order reflection spectra, c) zero order transmission

and d) extinction spectra for the A550 array with 30% porosity pillar and 45% porosity layer.

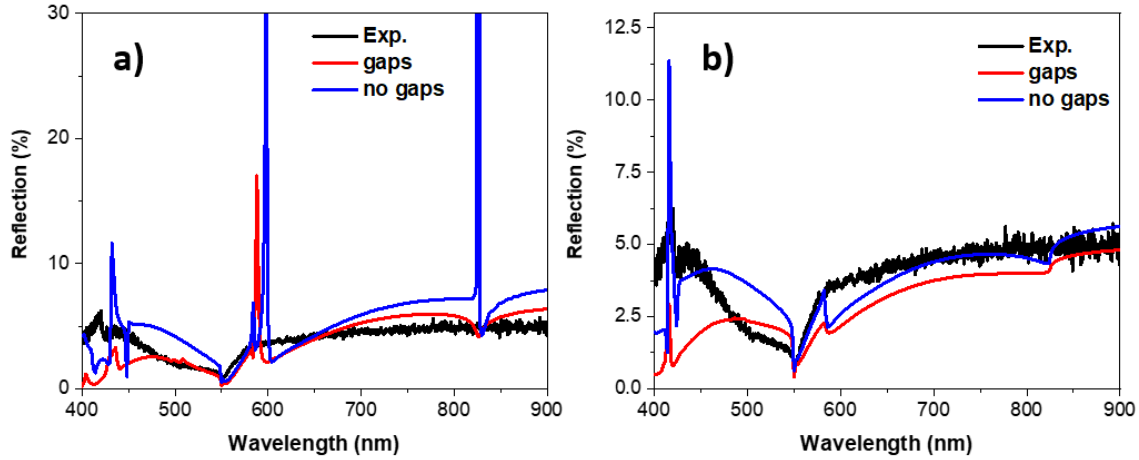

Figure 5-9 Influence of gaps in the TiO_2 layer on the reflection spectra of the A550 array with 30% porosity pillar and a layer of a) 35% porosity and b) 45% porosity.

In **Figure 5-9 a,** one can see the effect the gaps have on the reflection spectra for the A550 array with a pillar with 30% porosity and a layer with 35% porosity. E-QGM1 disappears and E-QGM3 blueshift towards the RA and decreases in intensity. **Figure 5-9 b** shows the effect the gaps have on the A550 array with a pillar of 30% porosity and a layer with 45 % porosity. The dips in reflection caused by the $RA(1)_s$ and $RA(1,1)_s$ become less pronounced and E-QGM3 decreases in intensity and blueshifts slightly. There is no significant difference between the effects the roughness and gaps have on the reflection spectra. Extra roughness and gaps in the layer essentially act towards limiting the capacity of the layer to support QGMs in the same way as decreasing the refractive index or reducing the thickness.

The comparison of the best fit simulation spectra to the experimental results for the A600, A550 and A480 arrays in **Figure 5-2** are shown in **Figure 5-10**. The best fit parameters for the simulations that recreated the experimental spectra in the most accurately are 30% porosity for the pillar and 45% porosity for the layer with 50 nm roughness. The shape of the FDTD transmission spectra in **Figure 5-10 a** is nearly identical to the experimental transmission for all the arrays. The FDTD transmission is slightly higher than the experimental one, which is likely caused by scratches and imperfections on the backside of the glass and unaccounted effects of the imperfections of the TiO_2 layer and array. The FDTD reflection spectra above 500 nm in **Figure 5-10 b** matches well in shape and intensity with the experiments for all the arrays.

From 400-500 nm, the FDTD results do not have the increase visible at lower wavelengths; this feature is missing in the three arrays. This feature was not reproduced by any combination of refractive index for the pillar and layer. It is possible that it is an artefact from higher order transmission that reflects from the substrate, and it is detected within the collection angle in the experimental set-up.

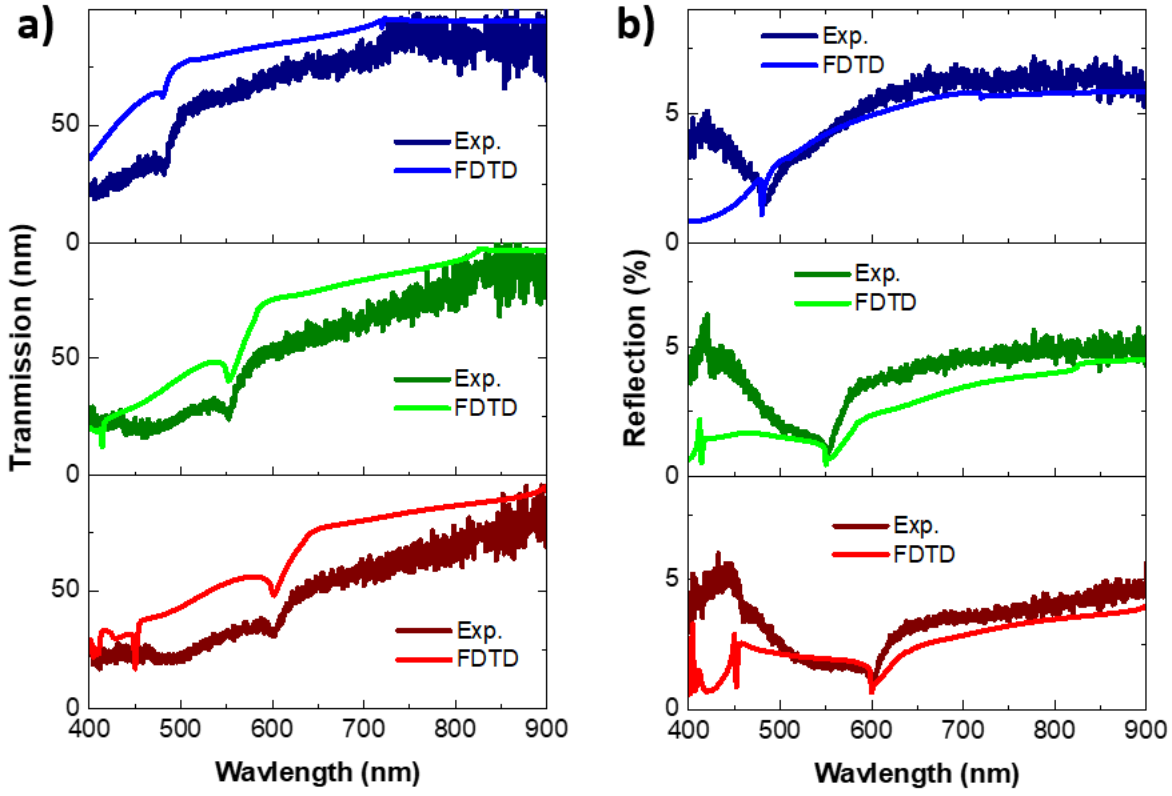

Figure 5-10 Comparison of the experimental and computational a) zero-order reflection and b) zero-order transmission spectra for the A600, A550 and A480 arrays.

5.2 Effects of increasing R6G concentration on the zero-order reflection and transmission for the A600, A550 and A480 arrays

In this section the effects of Rhodamine 6G (R6G) on the arrays will be discussed. Four solutions of different concentrations of R6G in ethanol were prepared: 0.25 mM, 0.50 mM, 1.00 mM and 2.00 mM. R6G was added to the arrays by dropping 125 µL of the solution onto the arrays and let to rest for 30 seconds before spin coating. The arrays were cleaned in acetic acid for 10 minutes, then for 10 minutes with acetone, then rinsed in IPA and dried before spinning at a higher concentration again. Despite our best efforts, the R6G did not spread evenly across the arrays at the higher concentration (see images on **Figures Figure** 5-19, **Figure** 5-20, and **Figure** 5-22 at 1.00 mM), different areas within the array have different concentrations this affects the optical properties of the arrays as two different areas within the same array might have different reflection or transmission spectra. It was also observed by eye that the R6G was more concentrated on the arrays, probably due to the high porosity of the layer within the array compared to the layer of the array.

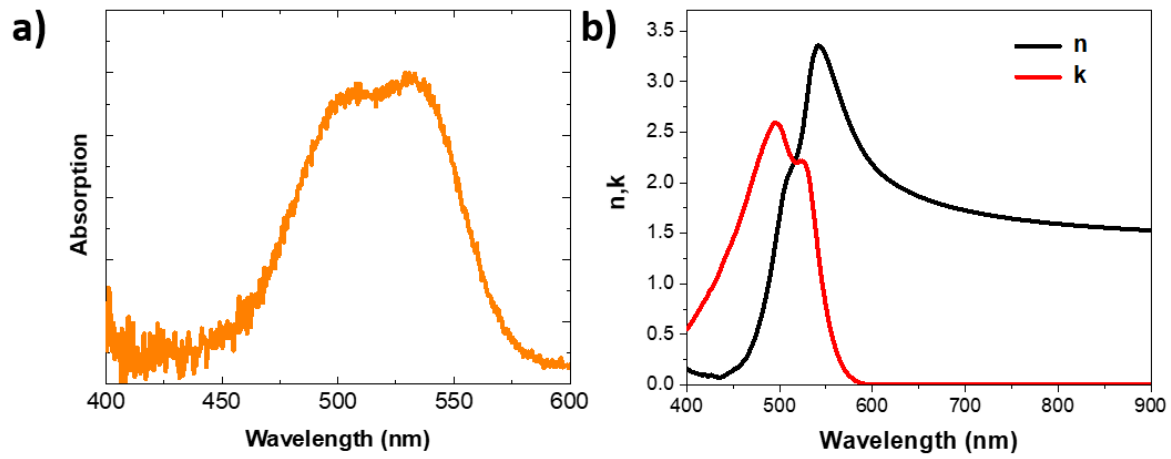

Figure 5-11 a) Experimental absorption of R6G on a section of flat TiO_2 layer next to the arrays. The monomer and h-dimer absorption peaks can be observed at 530 and 500 nm, respectively. b) real (n) and imaginary (k) refractive index calculated with the experimental data in a) using a MATLAB code from Djorovic et al[104] that takes the experimental absorption cross section and calculates the polarizability by performing a Kramers-Kronig transformation.

The absorption spectrum of R6G on the TiO_2 layer next to an array is shown in **Figure 5-11 a.** It is not trivial to measure the absorption of dye on the arrays since the changes in refractive index in the array caused by the dye also affect the reflection and transmission spectra

in the range of the R6G absorption. One observes two peaks in the absorption: at 530 nm and 500 nm. The peak at 530 nm corresponds to the R6G monomer and the peak at 500 nm is due to R6G H-aggregates[105,106]. A MATLAB code was used from Djorovic et al.[104] that takes the experimental absorption cross section and calculates the polarizability from it by performing a Kramers-Kronig transformation. Then one can convert to the complex refractive index from the polarizability by:

$$n = \sqrt{1 + \alpha/\epsilon_0}$$

where α is the polarizability obtained from the code and ϵ_0 is the vacuum permittivity. **Figure 5-11 b** shows the real n and imaginary k parts of the refractive index calculated from the absorption in **Figure 5-11 a.** The high porosity of the TiO_2 layer allows for R6G to be absorbed into the layer. If the R6G concentration is high enough this could allow for QGMs too. The effects of R6G on the A550 array will be studied next, which has $RA(1)_s$ and $RA(1,1)_s$ >580 nm and $RA(2)_s$ within the experimental spectral range. The first two concentrations (0.25 and 0.50 mM) of R6G on the A550 array yielded virtually no changes in the reflection spectra as seen in **Figure 5-12 a,b**. For the higher concentrations, one can observe a very strong reflection peak at 835 nm very near $RA(1)_s$ at 820 nm (black dashed line in **Figure 5-12 a**). This peak is from an electric QGM coupled $RA(1)_s$ (E-QGM1). Two peaks at 594 and 626 nm appear at high concentrations. They are not nearly as strong in reflection as the E-QGM1 peak, i.e. less than 10%. In simulation, they are usually roughly half of the intensity of the E-QGM1. From the Fano-shape of these peaks and their close position to the $RA(1,1)_s$ (orange short dashed line in **Figure 5-12 b),** these are likely from the electric and magnetic QGM coupled $RA(1,1)_s$ i.e. E-QGM2, M-QGM2, with E-QGM2 at 626 nm and M-QGM2 at 594 nm. The $RA(1)_a$ feature at 550 nm is present for all concentrations and does not change in position. This correlates to the R6G being present mostly in the layer and possibly forming a thin layer on top. If the layer is too thick, the $RA(1)_a$ is lost and a new RA(1) related to the refractive index for the thick layer would appear. One observes how the small feature related to $RA(2)_s$ becomes slightly more prominent and how it redshifts. The redshift is caused mainly by an increasing refractive index in the layer but can also occur by increasing the layer thickness.

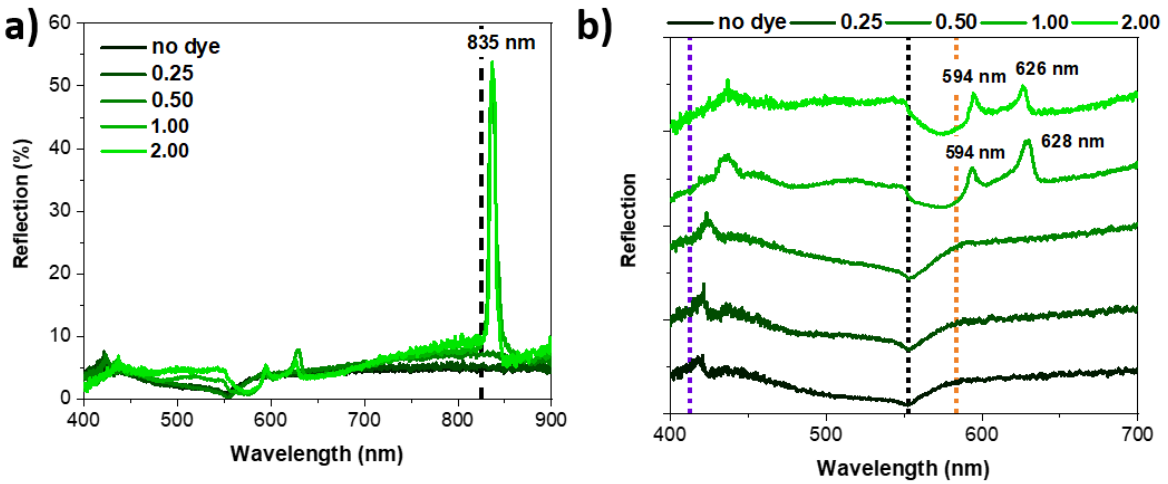

Figure 5-12 a), b) Two different views of the effect of increasing R6G concentration on the experimental zero-order reflection for the A550 (purple short dashed line at $RA(2)_s$, black short dashed line at $RA(1)_a$, orange short dashed line at $RA(1,1)_s$), black dashed line at $RA(1)_s$).

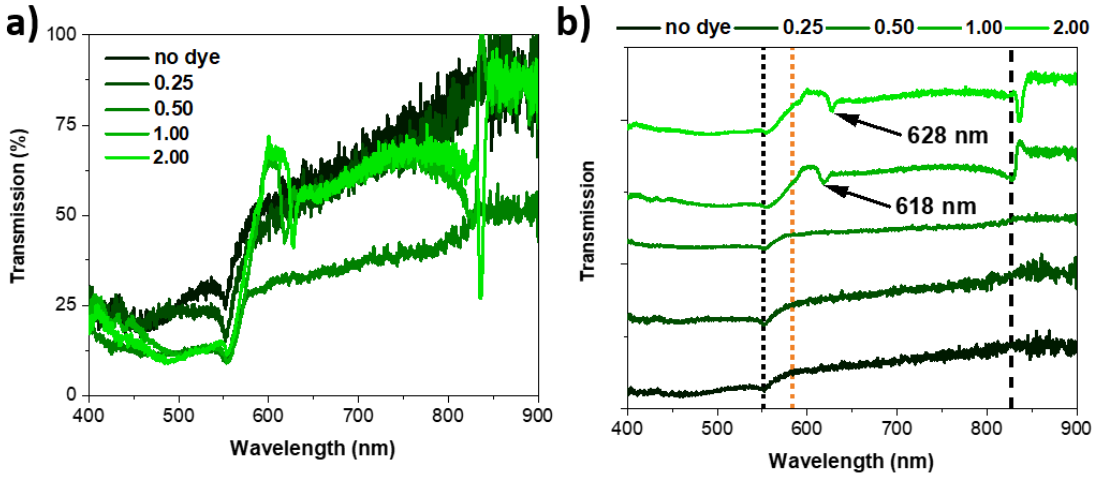

Figure 5-13 Two different views of the effects that increasing the R6G concentration has on the experimental 0-order transmission for the A550, (black short dashed line at $RA(1)_a$, orange short dashed line at $RA(1,1)_s$), black dashed line at $RA(1)_s$).

Figure 5-13 a,b shows the transmission spectra of the A550 array with increasing concentration of R6G. Again, significant changes in transmission are observed at the higher concentrations of 1.00 mM and 2.00 mM. For 2.00 mM, one observes a dip in transmission at 628 nm corresponding to the E-QGM2 peak observed in reflection. A dip in transmission is also observed for the E-QGM1. Lastly, the region between 450-550 nm is lower due to the absorption of the R6G. For the 1.00 mM, the transmission spectra does not correspond well with the reflection spectra. For the 1 mM concentration, the R6G dried the most unevenly across the arrays (see images in **Figure 5-19**). Despite this, the spectrum is quite interesting as one sees that the region measured has a slightly lower concentration of R6G. The effects of a

layer with a lower refractive index are seen by the E-QGM2 blueshifts and, similarly, the E-QGM1 is not nearly as strong and is blue shifted to the RA.

The relation of these peaks to the QGMs will be verified by FDTD simulations. In the previous chapter it was observed that the QGMs are dependant mostly on the properties of the layer and the substrate. For the simulation, one assumes that the R6G is only affecting the layer and that it penetrates the layer uniformly. This assumption was done since as seen in Chapter 4 the properties of the pillars have very little to no effect on the QGMs. To obtain the refractive index of the layer, the R6G and TiO_2 were mixed and the effective refractive index was calculated by using the Maxwell-Garnett equation.

$$\frac{n_{eff}^2 - n_{TiO2}^2}{n_{eff}^2 + 2\,n_{TiO2}^2} = \delta\left(\frac{n_{r6g}^2 - n_{TiO2}^2}{n_{r6g}^2 + 2\,n_{TiO2}^2}\right)$$

where n_{eff} is the effective refractive index, n_{R6G} is the refractive index of R6G, n_{TiO2} is the refractive index of TiO_2 with 0% porosity (**Figure 5-3 b)** and δ is the volume fraction of R6G.

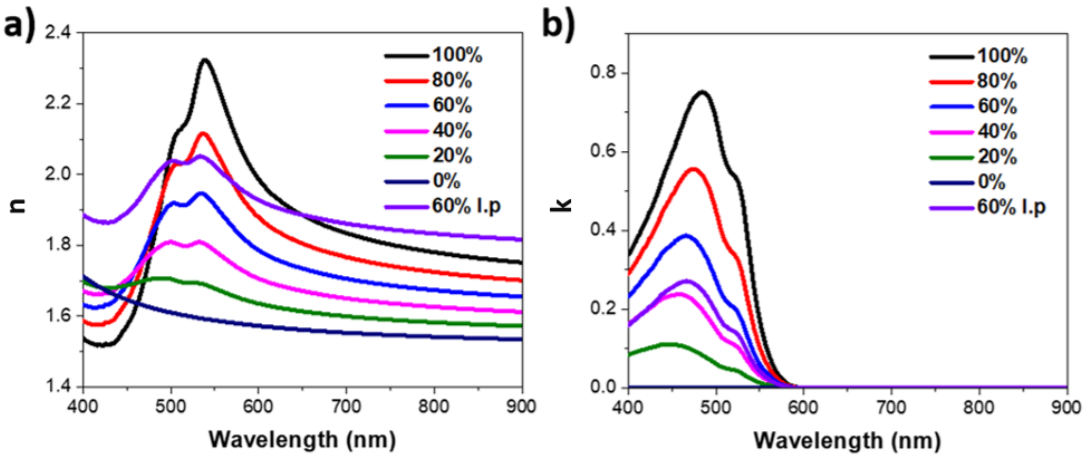

Figure 5-14 a) Real part and b) imaginary part of the effective refractive index from the TiO_2 mix for increasing R6G concentration (0-100%) of the R6G refractive index in **Figure 5-11 b** for a volume fraction 0.55. The label "60% l.p" refers to 60% concentration R6G for a volume fraction of 0.45.

The R6G refractive index is shown in **Figure 5-11 b** and the percent of R6G filling the volume fraction was varied from 0 to 100%, where 100% is the refractive index shown in figure **Figure 5-11 b.** The real parts of the effective refractive indices are shown in **Figure 5-14 a** and their imaginary counterparts are shown in **Figure 5-14 b**. The TiO_2/R6G mix labelled as "60% l.p" mixed material has a volume inclusion fraction of 45% and has 60% of the inclusion filled with R6G. The FDTD reflection spectra obtained with this index matches quite well with the 2.00 mM spectra. **Figure** 5-15 **a,b** shows the FDTD zero-order reflection and transmission

spectra with increasing R6G content. The QGM related to $RA(2)_s$ disappears with the addition of R6G and no QGMs can be observed in reflection related to $RA(2)_s$ with increasing R6G concentration. This is due to the non-zero absorption of R6G in the range between 400-580 nm. The higher R6G concentrations correspond well to the experimental spectra. Let us look now at the M-QGM2, the E-QGM2, and the E-QGM1. In the transmission spectra, one sees how the dips in reflection are directly related to the QGMs. **Figure** 5-15 **c** shows the comparison between the experimental reflection for the 2.00 mM A550 array and the FDTD zero-order reflection spectra using the 60% l.p and 100% refractive indices for the layer. The FDTD position of the peaks matches very well with the experimental position in both cases although the "60% l.p" mixed layer has better match in the sharp peaks positions even better in position. It is noted that the E-QGM1 at 626 nm is much larger than in the experimental spectrum. This could be due to a higher concentration of R6G being present or due to the tail of the R6G absorption on the arrays being slightly longer due to formation of j-aggregates on the arrays. The peak of the j-aggregate absorption is roughly at 550 nm[106]. The features of the sharp dips in the transmission spectra shown in **Figure** 5-15 **d** also agree well with the experimental results and the overall spectral shape matches very well with the experimental results, except in the region between 450-550 nm. The shape of this region in experiment is mainly caused by the absorption of R6G in this region. The 100% R6G concentration layer matches with this section better as it has a higher R6G concentration than the 60% l.p layer. These relative ratios of TiO_2 to R6G give the good correspondence with the experimental data. However, it is also possible to obtain a similar refractive index using a higher concentration of R6G. As mentioned previously, the transmission spectra for the A550 1.00 mM does not match with the reflection spectra. The FDTD transmission spectra for a layer with 80% of the porosity filled with R6G is compared to the experimental 1.00 mM data in **Figure** 5-15 **e**. One observes a very good match in shape and position, but one can also see that for this concentration E-QGM1 is not fully supported. Lastly, one can confirm that the sharp peaks observed in the reflection in the FDTD simulations are QGMs by looking at the field profiles of the array with a layer 60% l.p. The electric and magnetic field intensity distributions for the M-QGM2 at 594 nm are shown in **Figure 5-16 a** and **b,** respectively. The electric field forms a loop around the layer and substrate, which confirms that this is a magnetic QGM traveling along the y axis. The three lobes of the magnetic field in the layer indicate that this is a M-QGM coupled to $RA(1,1)_s$. Similarly, for the E-QGM2 at 624 nm, the magnetic field forms a loop around the layer in **Figure 5-16 d** and there are three intense electric field lobes confined mostly in the layer in **Figure 5-16 c**, confirming that this is an electric QGM propagating along the x axis which is coupled to $RA(1,1)_s$. The electric and

magnetic field profiles for the E-QGM1 at 835 nm are shown in **Figure 5-16 e** and **f**, respectively. A magnetic loop and high electric field intensity in the layer show that this is an electric QGM traveling in the y direction which is coupled to $RA(1)_s$. The sharp reflection peaks and transmission dips observed with the addition of R6G in the experiments are directly related to QGMs coupled to RAs. However, no higher order QGMs are observed for $RA(2)_s$ due to high losses by R6G absorption in the layer in the range from 400-580 nm.

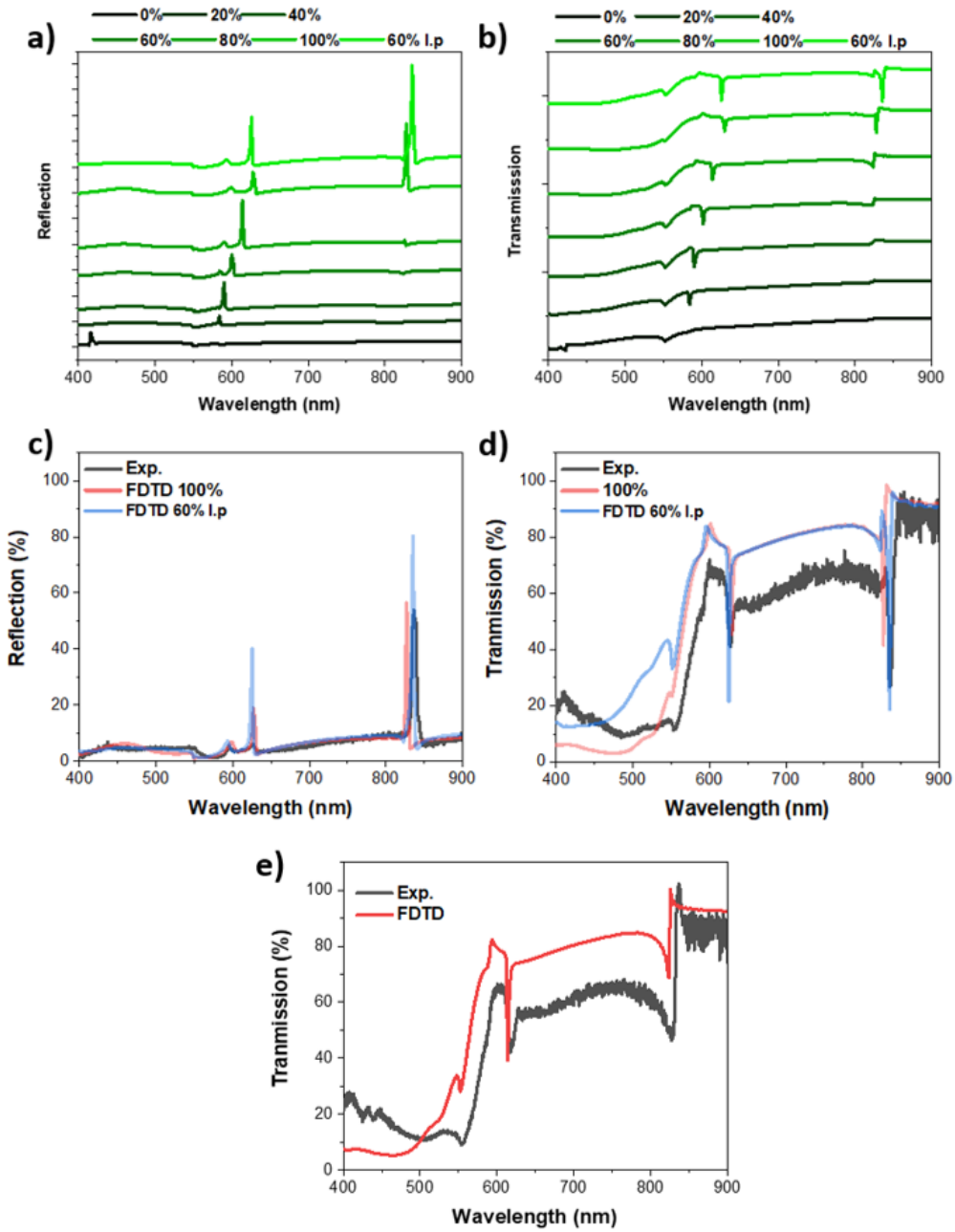

Figure 5-15 FDTD results for the zero-order a) reflection and b) transmission spectra for the A550 array with a 30% porosity pillar and increasing R6G concentration in the layer. A550 array comparisons: Experimental reflection spectra for the 2.00 mM with FDTD zero-order reflection and FDTD simulation reflection spectra for different TiO_2/R6G combinations, c) reflection and d) tranmission, e) experimental transmission spectra for the 1.00 mM with FDTD 0-order transmission and FDTD transmission spectra for 80% R6G concentration

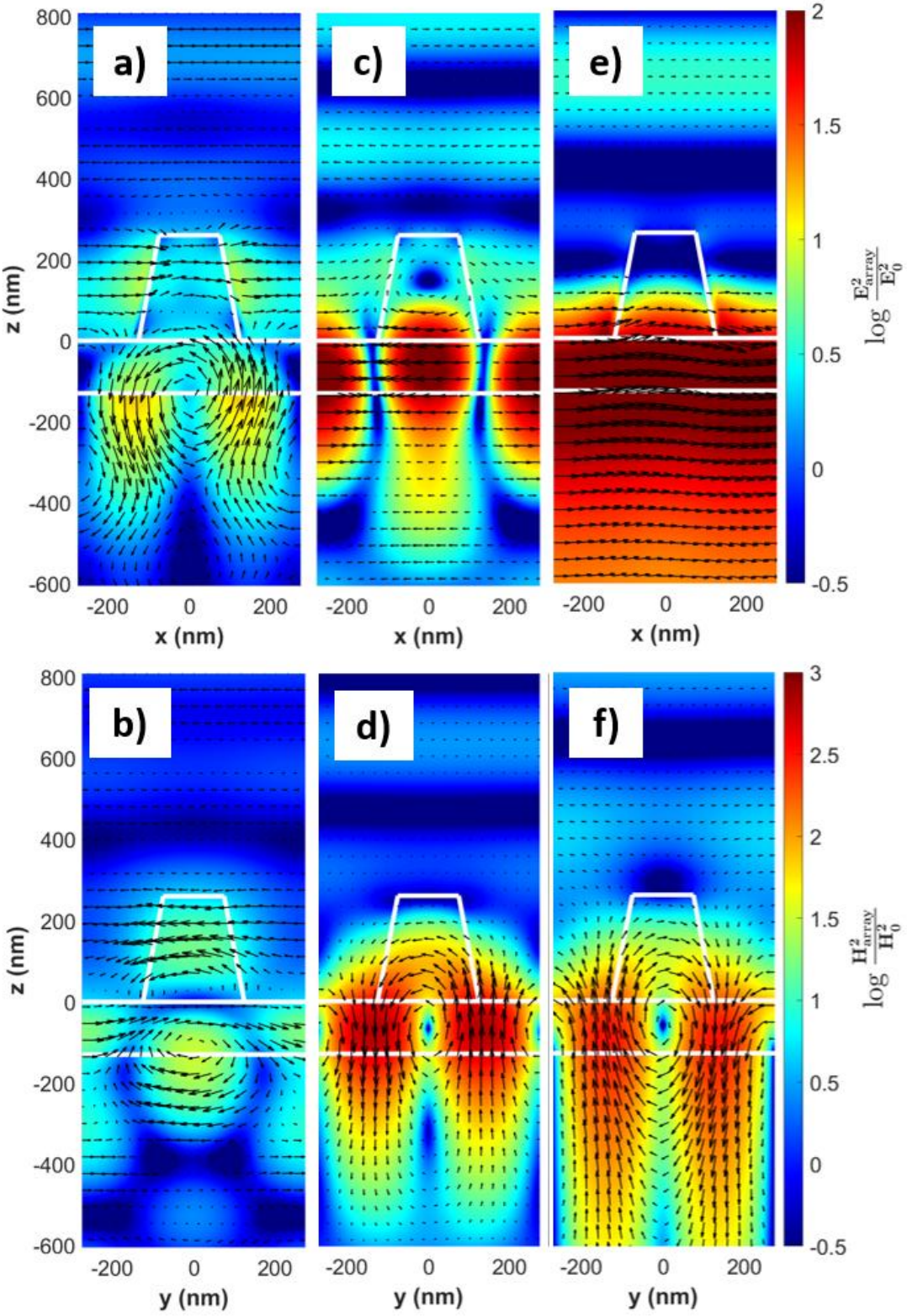

Figure 5-16 Electric and Magnetic field intensity distributions normalized to the incident field intensity for an A550 array with TiO_2 layer (60% l.p). The colour represents the intensity on a logarithmic scale and the black arrows represent the real part of the vectorial electric/magnetic field on the xz/yz plane. a) shows the electric field intensity distribution and b) magnetic field distribution for M-QGM2 at 594 nm. c) shows the electric field intensity distribution and d) magnetic field distribution for E-QGM2 at 628 nm. e) shows the electric field intensity distribution and f) magnetic field distribution for E-QGM1 at 835 nm.

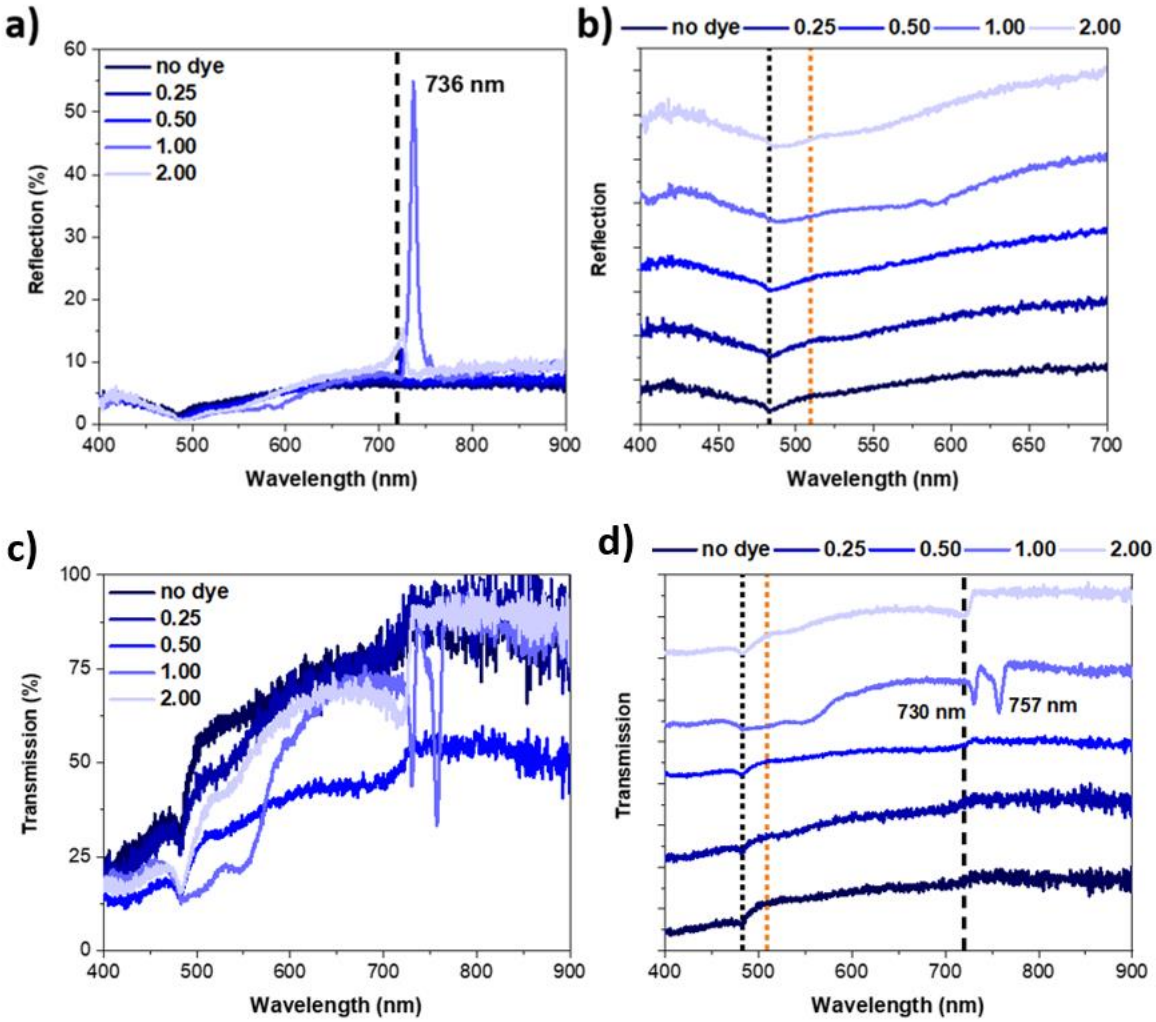

Figure 5-17 Two different views of the effect of increasing R6G concentration on the experimental zero-order reflection a,b) and transmission c,d) of the A480 array, (black short dashed line at $RA(1)_a$, orange short dashed line at $RA(1,1)_s$), black dashed line at $RA(1)_s$).

Figure 5-17 a,b show the experimental reflection spectra for the A480 array for different R6G concentrations. Like in the case of A550, no QGMs were observed for the lower concentrations. For the 1.00 mM concentration, one observes a sharp peak at 736 nm. From the analysis of the previous array by FDTD simulation, one can conclude that this is an electric QGM coupled to $RA(1)_s$ (E-QGM1). No QGM coupled to the $RA(1,1)_s$ are observed since the $RA(1,1)_s$ is at 509 nm, the coupled QGMs would be in a region of high R6G absorption and would not be able to exist in the layer. At 2.00 mM, one can observe what the spectra looks like before being able to support E-QGM1 as the R6G concentration is not as high. The transmission spectra for the A480 array is shown in **Figure 5-17 c,d** and similar to the case of the A550 array for the 1.00 mM, the transmission does not match with the reflection. In the transmission spectra one notices two dips: one at 730 nm and another at 757 nm. From the previous analysis on the transmission of the A550 with R6G and the work in the previous chapter, it is safe to attribute

the peak at 757 nm to the E-QGM1 and the peak at 730 nm to the M-QGM1 because the magnetic QGM always comes after the electric QGM, and because of their proximity to $RA(1)_s$ and their sharp Fano-shape. One can also appreciate the concentration of R6G on the A480 at 1.00 mM from the dip in transmission between 500-550 nm, which is a direct consequence of high R6G concentrations.

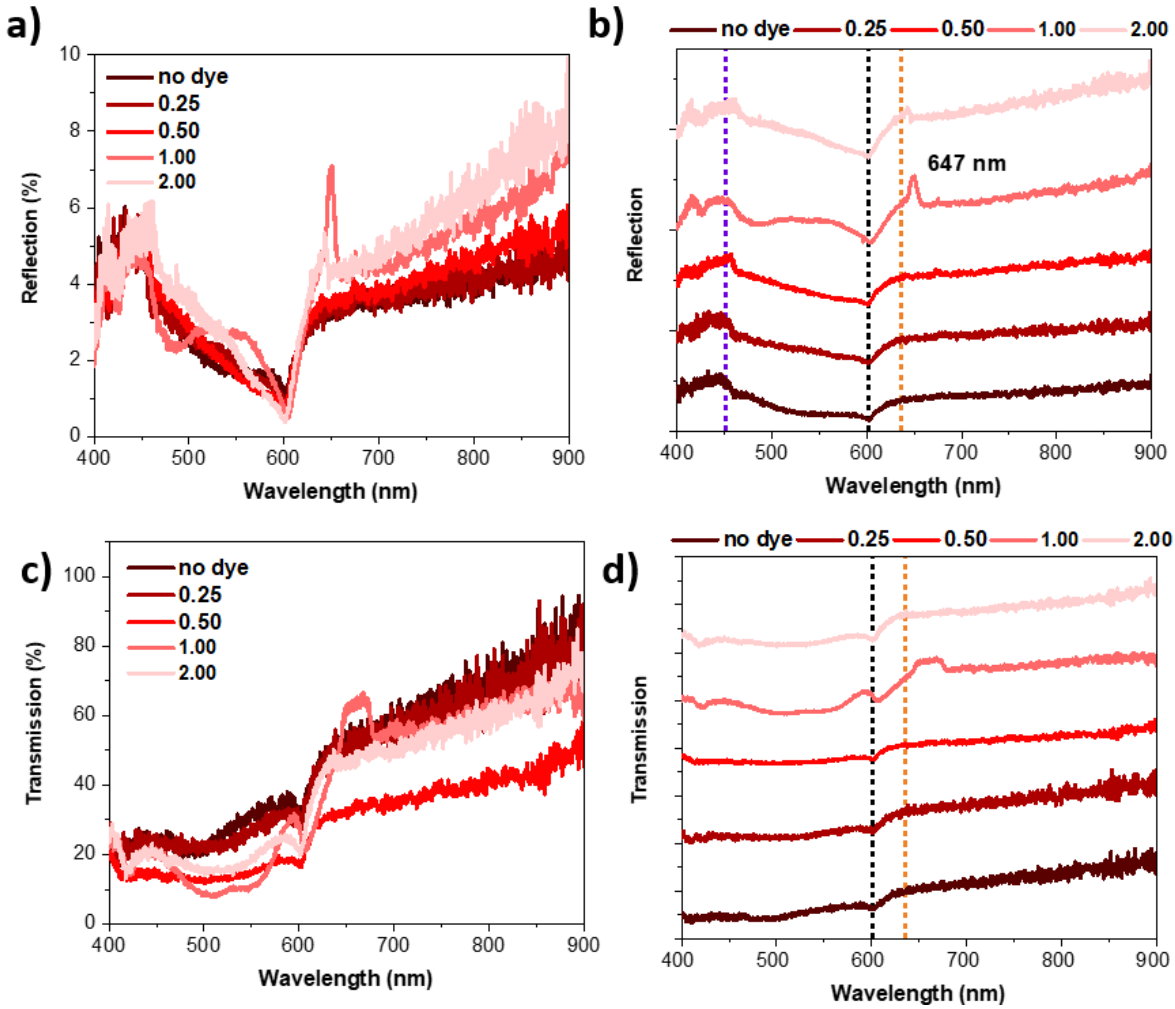

Figure 5-18 Two different views of the effect of increasing R6G concentration on the experimental zero-order reflection a,b) and c,d) and transmission spectra of the A600 array, (purple short dashed line at $RA(2)_s$, black short dashed line at $RA(1)_a$, orange short dashed line at $RA(1,1)_s$), black dashed line at $RA(1)_s$).

Figure 5-18 a,b shows the dependence of the A600 array reflection spectra on the R6G concentration. The experimental spectral range does not expand to wavelengths higher than 900 nm, therefore QGMs coupled to $RA(1)_s$ are not detectable. For 1.00 mM, there is a peak at 647 nm, which corresponds to the E-QGM2 and it is quite close to the RA at 636 nm. The refractive index of the layer is not high enough to support M-QGM2. For the same reasons as in the previous arrays, one does not observe any QGMs coupled to $RA(2)_s$. None of the other

concentrations show any QGMs. The transmission spectra for the A600 at 1.00 mM in **Figure 5-18 a,b** does no quite match with the reflection following the trend of the previous arrays at this concentration. Based on the plateau observed around 650 nm, it suggests at this concentration the A600 might be supporting E-QGM2 and M-QGM2, however it is not very clear as no clear dips are observed.

5.3 Effects R6G on the back scattering of light

Now the investigation centres on the effect of the varying R6G concentration on the back scattering spectra obtained with two different dark field microscope objectives, a 0.45 NA 20x objective and a 0.80 NA 50x objective, under dark field illumination. Differently from normal incidence, reflection and transmission spectra were collected only at the zero-order. The illumination on this set-up is at an angle of incidence greater than 26.7° for the 20x and 53.1° for the 50x objectives. With this set-up, one does not collect zero-order reflection, but rather the scattered light. Another difference in the behaviour of this measurements are the positions of the RA, which are obtained from diffraction orders by the grating equation[32]:

$$\vec{k}_{||d} = \vec{k}_{||i} + \vec{G}$$

where $\vec{k}_{||d}$ is the wave vector of the in-plane diffraction orders, $\vec{k}_{||i}$ is the in-plane projection of the incident wave vector, and $\vec{G}$ is the reciprocal lattice vector of the arrays. For normal incidence: $\vec{k}_{||d} = 0$, and at non-normal incidence: $\vec{k}_{||d} \neq 0$ and $\vec{k}_{||d}$ increases with incidence angle. Therefore, at non-normal incidence, all the RAs are wavelength dependent. Because of this, one expects to see significantly different spectra and features related to RA are expected to be less pronounced. The wavelength dependence of the RAs due to the in-plane projection incident light means that the 20x and 50x objectives will both have different RAs as they both have different illumination incidence angles. With the difference in illumination incident angle and NA between the objectives, it is expected they will have very different spectra from each other, especially due to the NA increase from the 50x allowing to collect scattered light at a larger angle range. The roles RA play and exactly what role R6G has on the shape of the scattering requires further understanding. However, significant colour change was observed in the scattering from the addition of R6G that was not due just to the absorption of R6G.

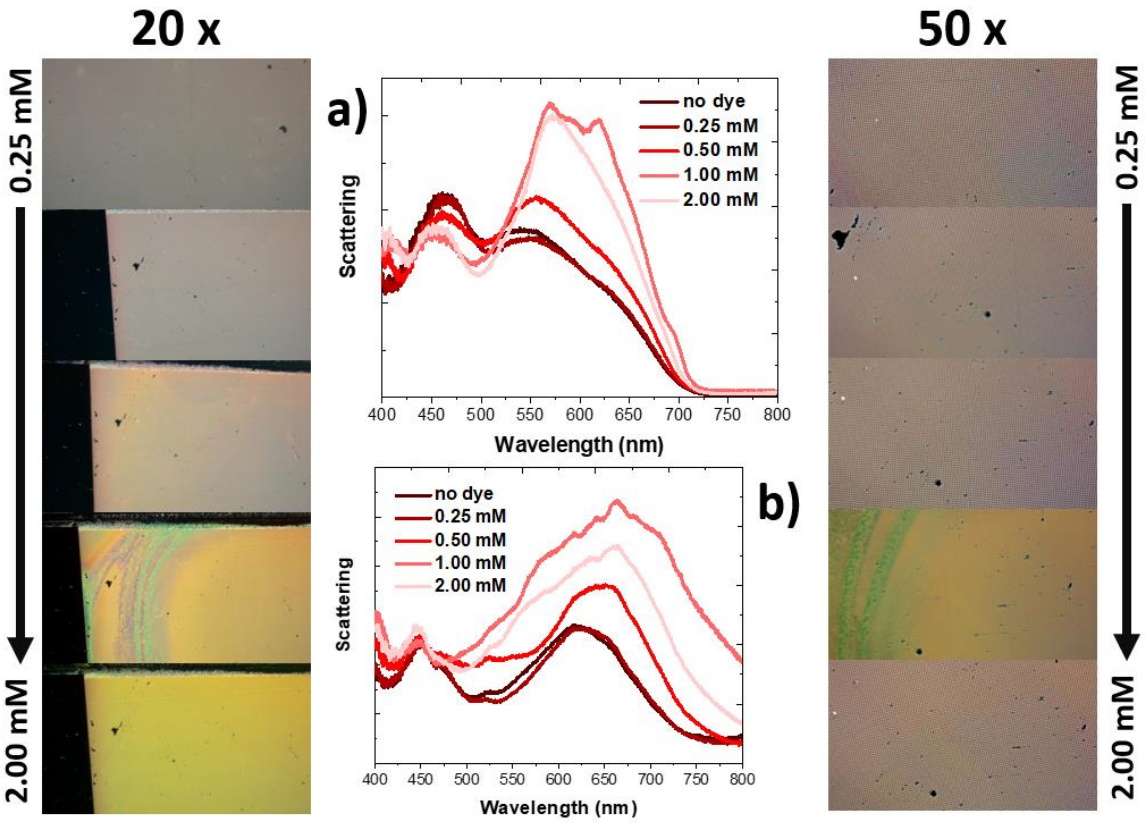

Figure 5-19 Darkfield scattering spectra of the A600 array with increasing R6G concentration for the a) 20x and b) 50x. Pictures on the left from top to bottom show the darkfield colour images obtained with the 20x objective with increasing R6G concentration (up to down) and on the left for the 50x objective.

Figure 5-19 a,b shows the effect of R6G on the back scattering spectra of the A600 array for the 20x and 50x objectives, respectively. The first thing to note is the significant difference between the 20x and 50x spectra. The first broad peak observed for the 20x objective with no dye is also of roughly the same shape and has the same position as for the 50x objective. For the 50x objective one observes a larger, redder second broad due to a larger numerical aperture being able to collect longer wavelengths of the non-zero grating orders. These features are a combination of the individual resonances (electric dipole, magnetic dipole, electric quadrupole etc.) of the pillar and grating orders. For the 20x objective, one notices a significant change in the scattering spectrum, as the addition of the dye produces an increase in intensity of the second peak and redshifts it slightly. For the highest concentration, one notices many emerging peaks for 1.00 mM concentration. The colour of the back-scattering image for the 20x goes from pale grey to a bright yellow and orange. In the scattering image for the 1.00 mM there are regions of very dense R6G which produce green and purple colours. The new emerging peaks in the scattering spectra are very likely due to RAs and QGMs as they become more prominent with increasing concentration. For the 50x objective, one observes small changes in

the first peak and a massive broadening of the second peak with increasing R6G concentration. When the concentration increases, one observes the emergence of many new peaks in the scattering spectra, very likely because of RAs.

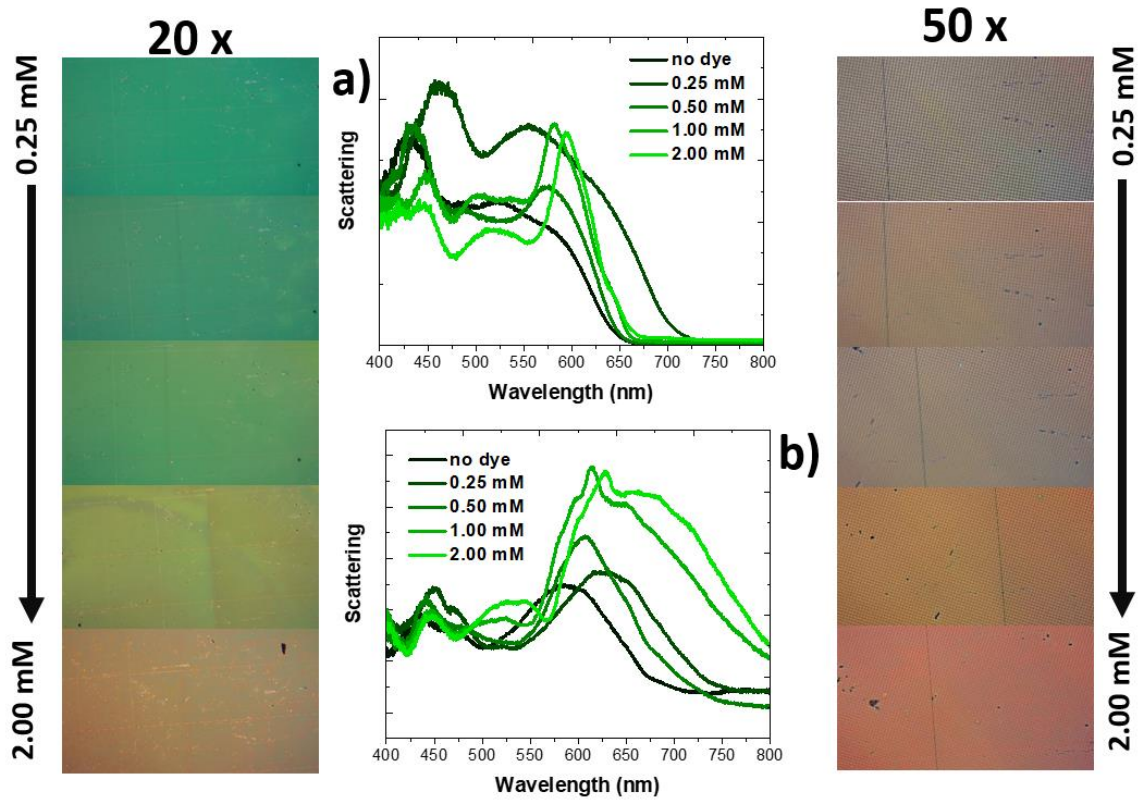

Figure 5-20 Dark-field scattering spectra of the A600 array with increasing R6G concentration for the a) 20x and b) 50x. Pictures on the left from top to bottom show the dark-field colour images obtained with the 20x objective and on the right for the 50x objective with increasing R6G concentration (top to bottom).

Figure 5-20 a,b shows the dark-field back scattering spectra for the 20x and 50x objective, respectively, for the A600 array. For the 20x objective one observes a splitting in both broad peaks with increasing R6G concentrations. A very similar behaviour in FDTD simulations was observed while experimenting on the effects that the few array periods have on the extinction spectra of the arrays. **Figure 5-21** shows the extinction spectrum at normal incidence for a 5x5 A600 array no substrate. One identifies a split in the first broad peak around the RA(1,1) and in the second peak around RA(1). The shape of the 20x scattering for 1.00 and 2.00 mM is very similar to the FDTD extinction spectra of the 5x5, indicating there may be some form of intermediate coupling between the RAs and the resonances of the pillar. This needs to be investigated more. For the 50x objective one observes again the increase and broadening of the second peak. One still observes the splitting at roughly the same position, and one observes a sharper feature emerge at around 650 nm for 1.00 mM and 2.00 mM that could

hint to some form of QGM. The behaviour of back scattering spectra for the A550 is significantly different that of the A600, which suggests a stronger interaction than that observed for the A600. With the increase of R6G concentration, the A550 array turns from a bright green colour to an orange, yellow colour for the 20x objective. For the 50x objective, the array turns from a pale greyish colour to a bright red and orange, due to the redshift and increasing dominance of the second peak.

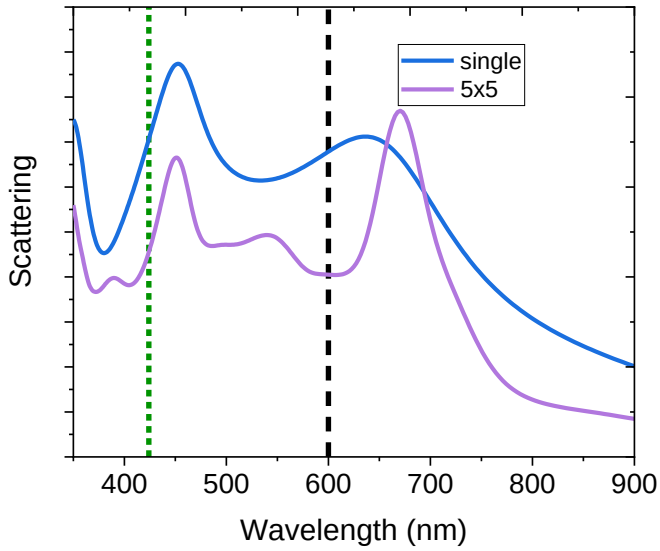

Figure 5-21 Extinction spectra for a single pillar of the A600 array and a 5x5 A600 array with no substrate (RA (1) at 600 nm marked by the black dashed line and RA(1,1) at 424 nm is marked by the short dashed green line).

The dark-field back scattering spectra for the A480 array is shown in **Figure 5-22 a,b** for the 20x and 50x objective, respectively. For the 20x spectra one does not observe a broadening of the spectra, but the dip in the spectrum redshifts from approximately 450 nm to 480 nm for the higher dye concentrations. This could be a similar feature to the splitting observed for the A550 array. One also observes some shoulders in the slope of the scattering spectra at higher concentration. From the images on the left in **Figure 5-22**, one can see that the colour of the A480 array with the 20x objective does not change a lot. With the 50x objective, the second peak for the A480 array is related almost entirely to high grating orders because the A480 pillar has its magnetic dipole at 446 nm. The second peak of the A480 array redshifts and broadens with increasing R6G concentration, changing the colour of the array from a bright green to orange.

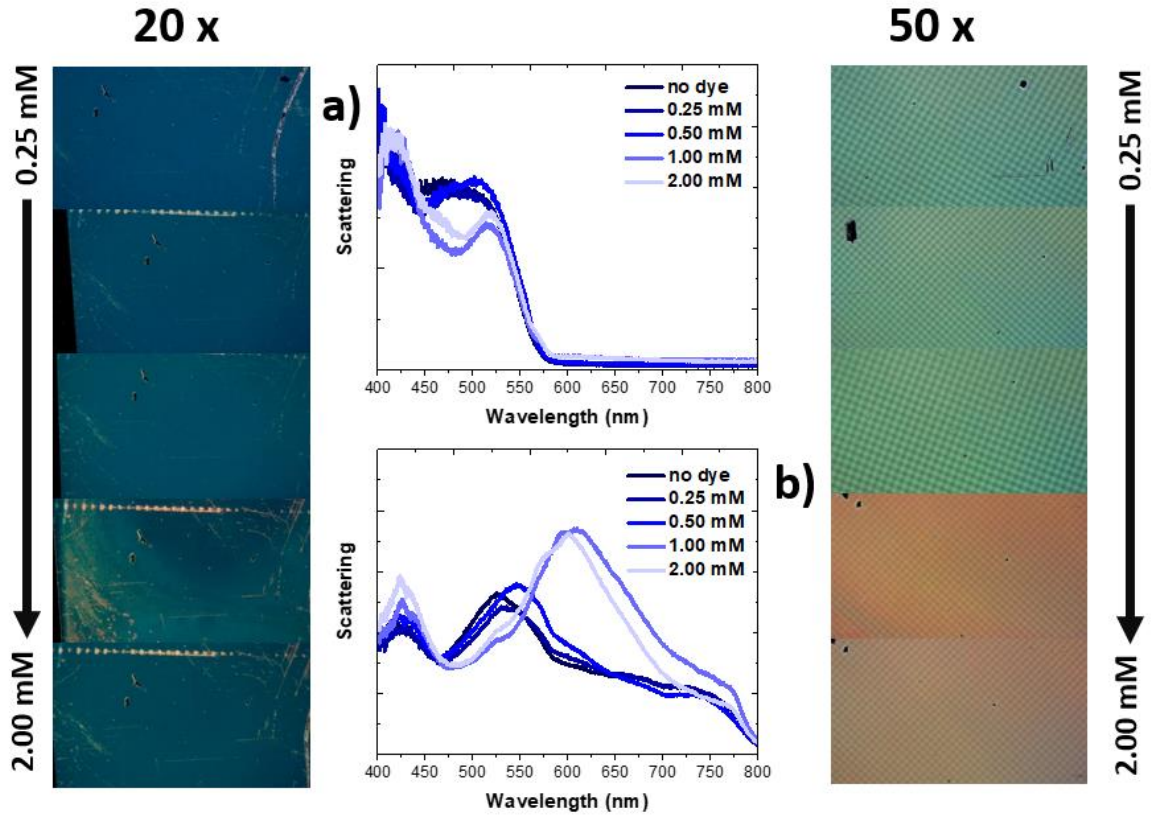

Figure 5-22 Dark-field scattering of the A600 array with increasing R6G concentration spectra for the a) 20x and b) 50x. Pictures on the left from top to bottom show the dark-field colour images obtained with the 20x objective and on the right for the 50x objective with increasing R6G concentration (top to bottom)

5.4 Conclusion

The A600, A550 and A480 arrays show no sharp peaks in reflection from QGMs. QGMs could couple into the arrays due to the roughness and porosity of the residual layer reducing its effective refractive index of the TiO_2 layer, which limits the capacity of the layer to support QGMs. The effects the gaps and roughness have on the reflection and transmission spectra were minimal, they affect the layer in a way that is equivalent to reducing the refractive index of the layer. Very good agreement was found between simulation and experiment by simulating a structure that has a 30% porosity pillar, 45 % porosity layer with 50 nm RMS. The region between 400-500 nm was as well reproduced by the FDTD simulations.

The addition of R6G to the arrays yielded very interesting results. E-QGM1, E-QGM2 and M-QGM2 are observed for the A550 array for high R6G concentrations and successfully

showed through simulation that the sharp peaks observed in experiment are directly related to the QGMs. For the A480 array at high concentrations of R6G, E-QGM1 and M-QGM1 were observed as sharp features in reflection and transmission. Lastly, in the case of the A600 array, only E-QGM2 was observed at high R6G concentrations. This is exciting as there have only been a few observations QGMs in titania-based structures[77,78]. Furthermore, the E-QGM1 mode observed for the A550 and A480 at high R6G concentrations had Q-factors of ~110 (FWHM ~ 8 nm) and ~80 (FWHM ~ 8 nm), respectively, and a reflection peak of roughly ~50%. The experimental Q-factors for the A550 arrays are considerably lower the values from the FDTD calculation using the "60% l.p" index for the layer, resulting in a Q-factor ~280 and reflection peak of ~80%. The difference between experiment and simulation is very likely due to unaccounted factors in the simulation, such as an increase in the refractive index of the pillar's due to the addition of R6G, irregularities in the residual layer's thickness or imperfections of the array. The calculated FDTD values are comparable to the Q-factors obtained from measurements of Shunsuke Murai *et al.* on SLRs in silicon rectangular arrays, they obtained Q-factor ~298 (FWHM ~2 nm) and high extinction 90% for arrays with smaller particles size[52]. The sharpness of the QGMs peaks in the arrays measured in this work, can be improved in these arrays by having pillars of smaller dimensions and by incorporating different materials with less losses into the layer to increase the index. Finally, significant colour changes were observed due to R6G has on the dark-field scattering spectra. Significant colour changes and effects arising from the RA were observed. The effects R6G has on the array are reversible by cleaning the arrays in acetic acid. However, the effects of R6G in layer were modelled as simply as flat layer mix of R6G and TiO_2, additional studies on the morphology of the layer by using AFM and modelling the effects of R6G on the pillars have on the spectra of the array still need to be considered in future work.

6 Influence of Rhodamine 6G emission by TiO_2 Arrays

The aim of this chapter is to study the potential of the TiO_2 arrays for application for photoluminescence modification of emitters. Since these array are fabricated via soft-NIL lithography and this method can be used to build such array on many surface and devices as the maximum temperature does not exceed 350 °C during fabrication[68,69], these arrays can could be used for the PL modification of LEDs, assist in colour-conversion devices, and as well in the photobleaching of dyes. Studying the interaction of theses arrays with rhodamine 6G (R6G) will being insights towards being used for such applications.

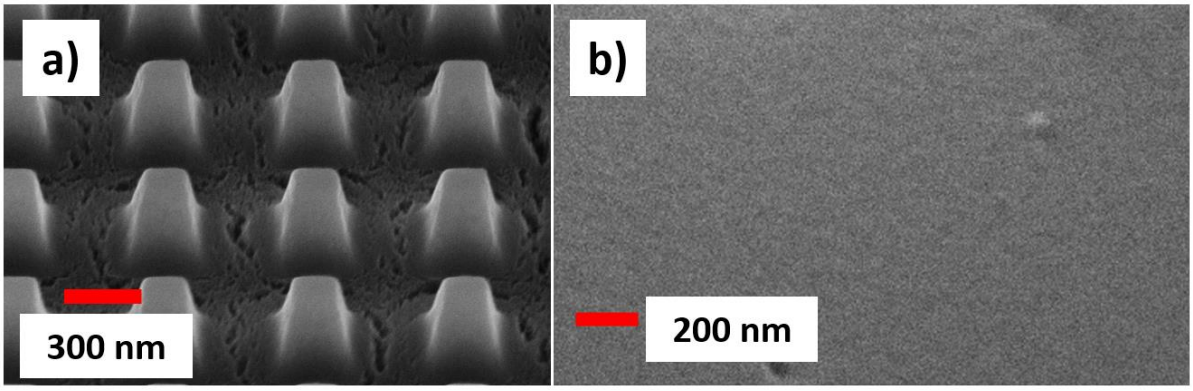

Figure 6-1 Scanning electron microscope images of the a) A600 array and b) TiO_2 layer.

This chapter uses the same TiO_2 arrays as in the previous chapter, however instead of focusing on the influence R6G has on the TiO_2 arrays, this chapter focuses on the influence the arrays have on R6G photoluminescence. The properties of the arrays are recapped in **Table 6-1**. In this chapter the photoluminescence of R6G is compared between the different arrays but also to the TiO_2 layer next to the arrays left over from the fabrication. The properties of the layer are quite different from the array. In **Figure 6-1 a** it can be seen that the arrays have a very rough porous region between the pillars, while **Figure 6-1 b** the TiO_2 layer off the arrays is much smoother and it is also thicker (170 nm) than the TiO_2 layer between the pillars (130 nm). The surface area on the arrays per unit cell is increased compared the TiO_2 by the pillar and more substantially by the rough and porous region between the pillars. This would increase the

concentration of R6G on the arrays compared to the TiO_2 layer and more R6G aggregates would form on the arrays[105,106].

Table 6-1 Dimensions of the three arrays

Array	Period	Base Length	Top Length	TiO_2 Layer Thickness	Height
A600	600 nm	320 nm	170 nm	~130 nm	260 nm
A550	550 nm	280 nm	150 nm	~130 nm	260 nm
A480	480 nm	185 nm	75 nm	~130 nm	280 nm

6.1 Photoluminescence of R6G on TiO_2 arrays

To investigate the ability of the TiO_2 arrays to modify the luminescence of R6G, a 0.35 mM solution of R6G in ethanol was spin coated on the arrays. The emission peak of R6G in solution was at 560 nm. Before spin coating the R6G solution, the arrays were cleaned in a bath of acetic acid for 10 minutes, then 5 minutes in acetone and finally rinsed with IPA. Pre-cleaning the arrays facilitated the spin coating the R6G molecules in solution uniformly across the arrays. Low concentrations of R6G were chosen in order to have little to-no effect on the optical properties of the arrays.

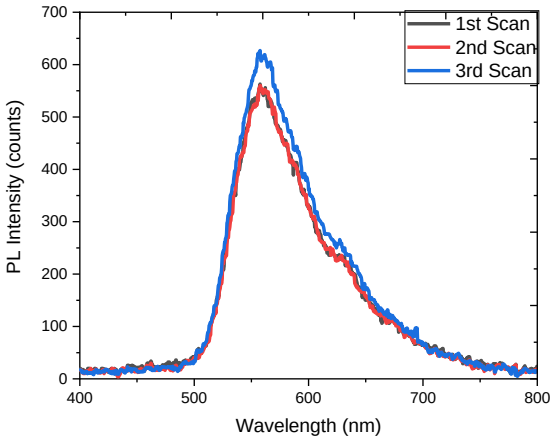

Figure 6-2 Photoluminescence of R6G after three consecutive measurement scans on the same area using an excitation wavelength of 375 nm at 20 μW, with spot size of ~1 μm and 10 MHz repetition rate.

The effects of the TiO_2 arrays on R6G emission were investigated in both frequency and time-domain. Three different pulsed lasers (with an instrument response function (IRF) with a lifetime of 150 ps) were used to excite the R6G molecules in reflection geometry, using a 40x objective with NA of 0.6. The excitation wavelengths were chosen to be 375 nm, 405 nm and 466 nm, all at 20 μW. The experimental set-up used is described in **section 3.4**. Under these measurement conditions the R6G photoluminescence behaviour was not affected by the measurements using the 375 nm laser. The 375 nm laser was used to test the reproducibility because at this wavelength TiO_2 is excited and this can lead to an increase in R6G photodegradation[64]. In **Figure 6-2** it is observed that two consecutive scans on the same area do not affect the PL of R6G, only after the third consecutive scan the PL increases by roughly 10%. We first turn our attention to the R6G PL. The detected PL from R6G on all the investigated arrays is significantly increased when compared to R6G on the TiO_2 layer.

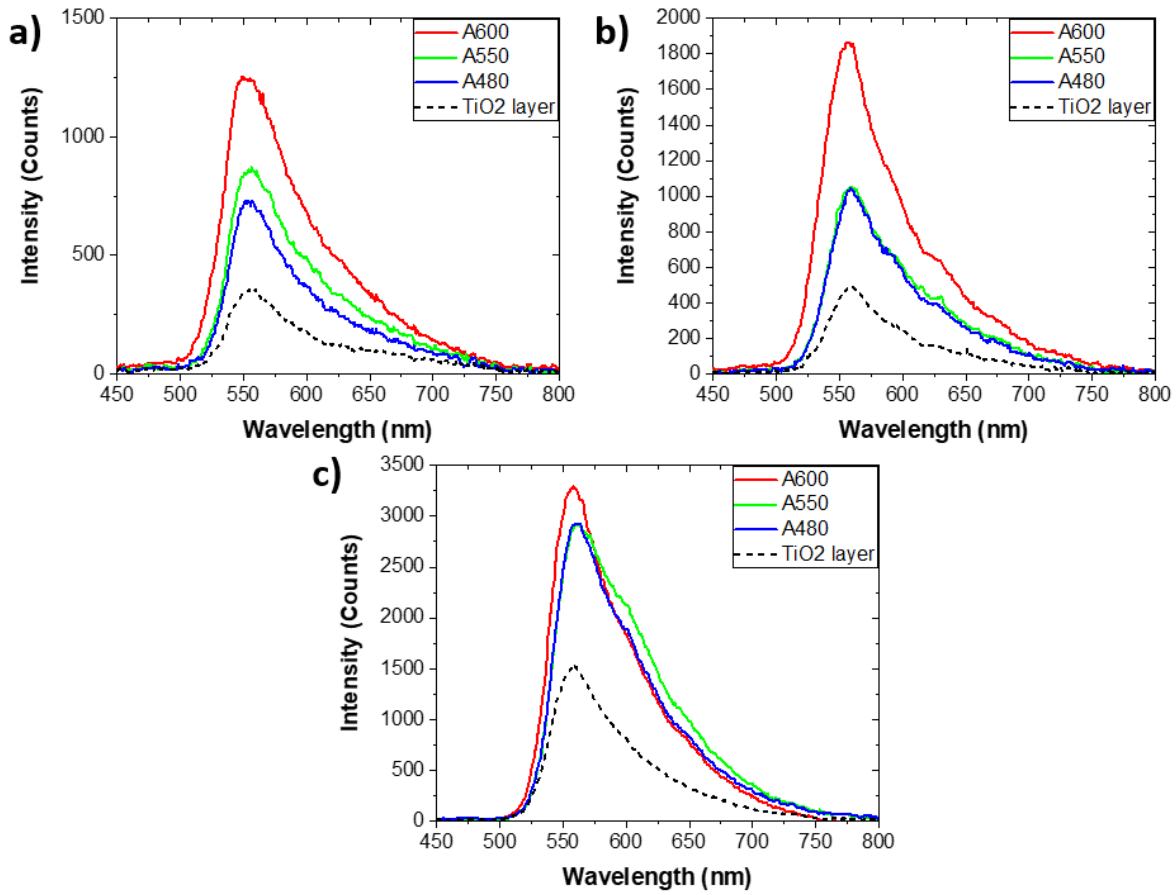

Figure 6-3 Photoluminescence spectra of theTiO2 arrays A600, A550, A480 and of the TiO2 layer coated with R6G molecules excited at a) 375nm, b) 405 nm, and c) 466 nm averaged over several different scan on different areas on the arrays.

For all samples, including the TiO2 layer, an increase of PL intensity is observed with increasing excitation wavelength of the lasers (375, 405. Ad 466 nm), this was expected because of the increasing absorption cross section of R6G with increasing excitation wavelength. However, the relative increase in number of detected photons, the ratio of the integrated PL from the arrays and from the TiO_2 layer excited at the same wavelength, varies with excitation wavelength. 3.6 times more photons are detected for the A600 sample as compared to the TiO_2 layer when excited at 375 nm (**Figure 6-3 a**), 4.2 times more photons when exited at 405 nm but only 2.2 times more photons when excited at 466 nm. The relative increase in number of detected photons for the A480 and A550 array does not vary substantially with excitation wavelength (**Table 6-2**).

Table 6-3 Relative increase in PL on the arrays, i.e. the ratio of the spectral integrated R6G PL from the arrays and from the TiO_2 layer off the arrays excited at the same wavelength.

Sample/Excitation	375 nm	405 nm	466 nm
A600	3.6	4.2	2.2
A550	2.4	2.4	2.3
A480	2.0	2.2	2.2

However, the observed increase in R6G PL on the arrays cannot be entirely attributed to an increase in emission of the R6G on the arrays. The arrays have larger surface area due to the lateral surface of the pillar. The estimated increase in surface area for A600, A550, and A480 were found to be 1.53, 1.58, and 1.52, respectively. The corrected values for the PL increase corrected for the increase in surface area are shown in **Table 6-4**. 2.7x increase is still observed after correction for the A600 array at 405 nm excitation. Even though we still see an increase in R6G PL on all the arrays after correcting for surface area there is still one big assumption we are making, that the R6G concentration is the same on the array and on the TiO_2 layer. By taking a closer look at the surface of the TiO_2 layer (**Figure 6-1 a**) and the surface of the area between the arrays (**Figure 6-1 b-d**) it is not difficult to observe that the area between the pillars is significantly rougher and more porous than the TiO_2 layer, as mentioned above. This increases the surface area on the arrays drastically and the R6G could also be absorbed into the layer between the pillars due to its porosity. Therefore, it cannot be concluded that PL enhancement of R6G on the arrays is observed. It is concluded from the measurements that the R6G emission can be significantly modified on the arrays depending on the excitation

wavelength of the laser and on the geometry of the arrays as there is significantly more PL from the A600 at 375 nm and 405 nm excitation relative to 466 nm excitation than the A550 and A480.

Table 6-4 Relative increase in number of detected photons (N), i.e., the ratio of the spectral integrated R6G PL from the arrays and from the TiO2 layer excited at the same wavelength.

Sample/Excitation	375 nm	405 nm	466 nm
A600	2.4	2.7	1.4
A550	1.5	1.5	1.5
A480	1.3	1.4	1.4

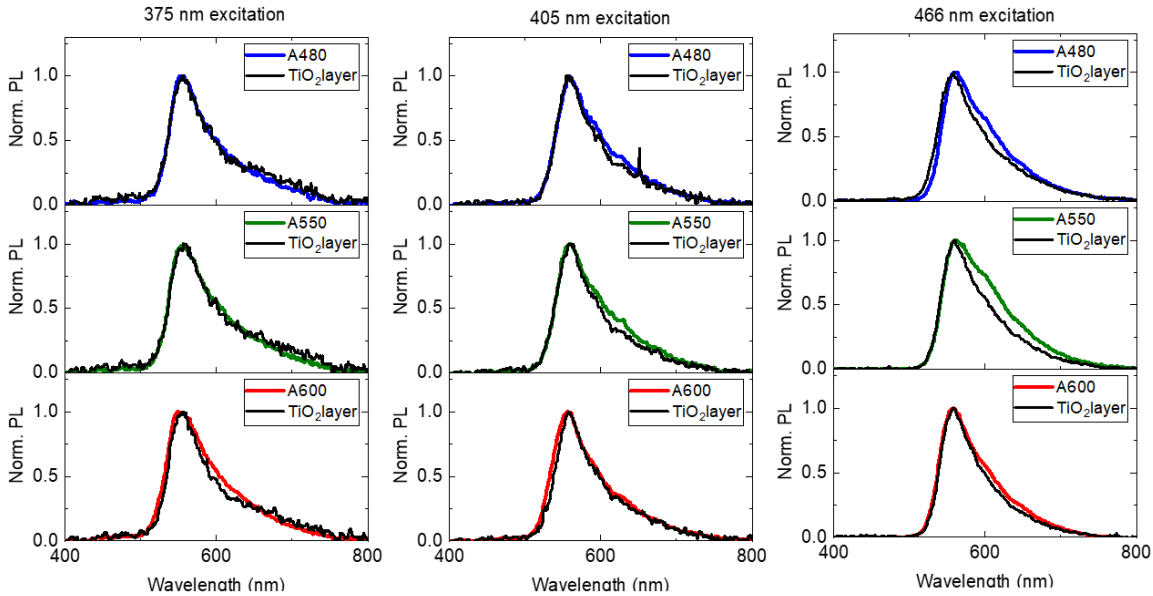

Figure 6-4 Normalized R6G PL, on array and off array (TiO_2 layer) comparison for three different excitation wavelengths 375 nm, 405 nm, 466 nm (left to right).

Virtually no spectral reshaping from the arrays can be observed when compared to the PL shape on the film at 375 nm excitation in **Figure 6-4 a**. For the 405 nm excitation a red shoulder is starting to form for the A550 and A480 arrays in **Figure 6-4 b**. This reshaping cannot be due to light redistribution due to the array since this would be independent of excitation wavelength. At high concentrations of R6G, R6G can aggregate into molecular dimers such as j-aggregates and h-aggregates. J-aggregates of R6G have a redshifted emission and absorption compared to the R6G monomer[105,106]. The shoulder seen in the PL could be due to the formation of j-aggregates. It is very likely the arrays have a higher concentration of R6G due to the increase in surface area and the porosity of the TiO_2 layer in the arrays, the increase in

concentration would create more j-aggregates as they tend to form with increasing concentration [105,106]. At 466 nm excitation in **Figure 6-4 c**, the red shoulder broadens possibly due to more efficient excitation of the j-aggregates. It is the mostly present on the A550 array and the A480, with only a slight shoulder on the A600, indicating that it is likely the A550 and A480 have slightly higher R6G concentrations, as such fast photoluminescence decay lifetimes for these arrays are expected.

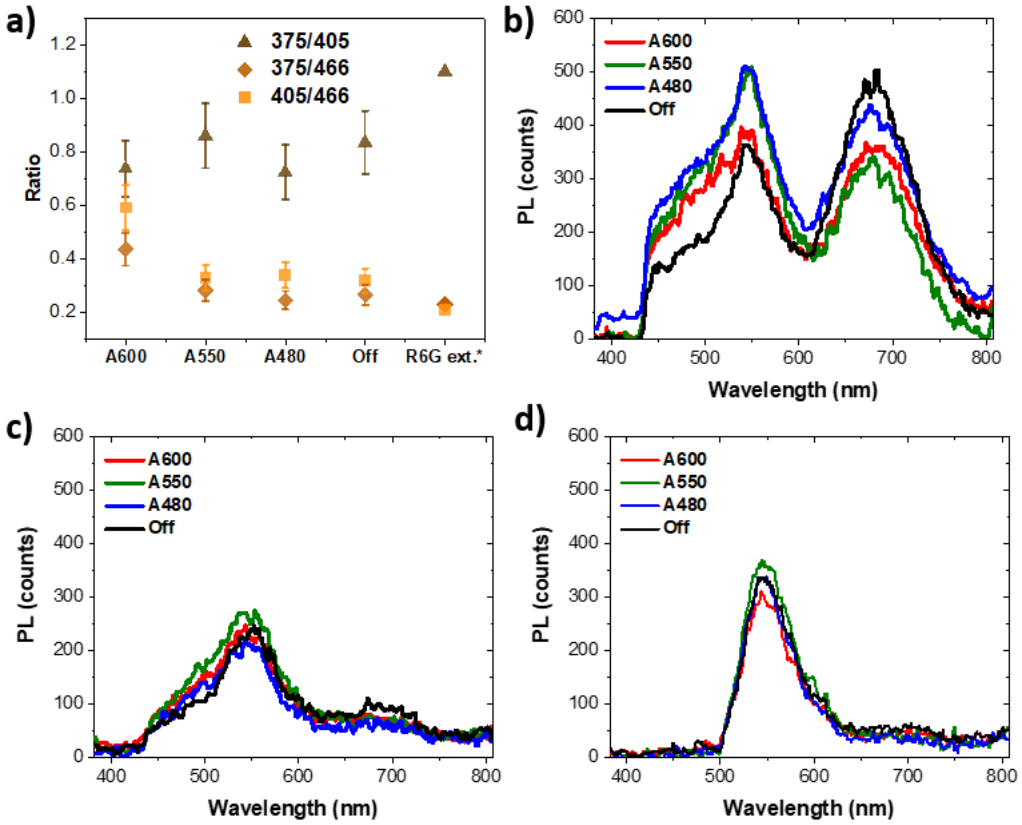

Figure 6-5 a) R6G emission ratios for different excitation wavelengths (375/405, 375/466, 405/466) to obtain the molar extinction values for R6G from reference [107], the A600, A550 and A480. TiO_2 emission of arrays and TiO_2 layer after removal of R6G using ~500x higher laser powers for 375 and 405 nm excitation and 450 long pass filter. b) 375 nm and c) 405 nm. d) TiO_2 emission of arrays and TiO_2 layer after removal of R6G using ~10x higher laser powers and 500 long pass filter. PL was collected over 5 minutes.

The R6G emission ratio between different excitation wavelengths are compared. The molar extinction values for R6G at 375nm, 405 nm and 466 nm are obtained from Ref[107], then the ratios between 375/405, 375/466, 405/466 are calculated. The calculated ratios were 1.10, 0.23, and 0.21 respectively. This gives us an approximation on what the ratios of R6G PL would be between the different laser excitations if only direct excitation from the laser is responsible. In **Figure 6-5 a,** the ratios of PL between different excitations are shown for the different arrays, the ratios of 375/466 and 405/466 for the A550, A480 and off the array on the

TiO_2 layer are very similar and very close to the ratios of the molar extinction of R6G[107]. The A600 375/466 and 405/466 ratios are much larger than other arrays and on the TiO_2 layer. The 375/405 ratio is very similar between all the arrays, which indicates that the process responsible for the increase in emission for the 375 nm and 405 nm excitation on the A600 is likely related to an increase in the excitation of R6G. In work done by S. A. Tomás et al[108] on the influence of R6G doping on TiO_2 sol-gel films, they found two new peaks in the R6G photoluminescence excitation spectra after incorporating R6G into the TiO_2 film. The first peak is centred at roughly 406 nm and it is attributed to defect states from the interaction of R6G with the TiO_2 surface or to the formation of $R6B^+$ radical, because adsorbed R6G gives one electron to the conduction band of TiO_2[108,109]. The second peak is centred roughly at 360 nm and it is much more efficient than the first PLE peak, they attributed this peak to be likely caused by highly efficient energy transfer between the TiO_2 conduction band and R6G excited states, 375 nm is at the edge of the peak. The interaction of R6G and TiO_2 should be the same no matter on which array they are or if they are on the TiO_2 film if the TiO_2 properties are the same. This is confirmed by looking at the PL of TiO_2 after the R6G was removed from the arrays. The PL from the bare TiO_2 arrays and film at 375 nm excitation in **Figure 6-5 b,** shows two peaks one centred around 466 nm and the other at 680 nm, these peaks correspond to two emission peaks of anatase TiO_2. In work done by Deborah K. Pallotti et al, two PL peaks of anatase TiO_2 were observed a green one centred between 510 and 530 nm and a red one centred around 650 nm[110]. The green peak corresponds is due to radiative recombination of free electrons with holes in defect states and the red peak is attributed to free holes and electrons that relax from conduction band and shallow sub gap states to deep defect states[110], UV and oxygen exposure can irreversibly alter the PL emission. The slight differences between the arrays does show slight differences in TiO_2 properties, however there is nothing outstanding about the A600 emission. For the 405 nm excitation in **Figure 6-5 c**, no significant differences are observed between the TiO_2 arrays and film, both peaks reduce in intensity due to lower PLE efficiencies[110]. Similarly, at 466 nm excitation in **Figure 6-5 d**, no significant differences are observed between them. There is no outstanding behaviour of the PL of TiO_2 on the A600 that would indicate the properties of the TiO2 are different from the other arrays and could account for the changes in PL observed.

6.2 Time Resolved Photoluminescence of R6G on TiO_2 arrays

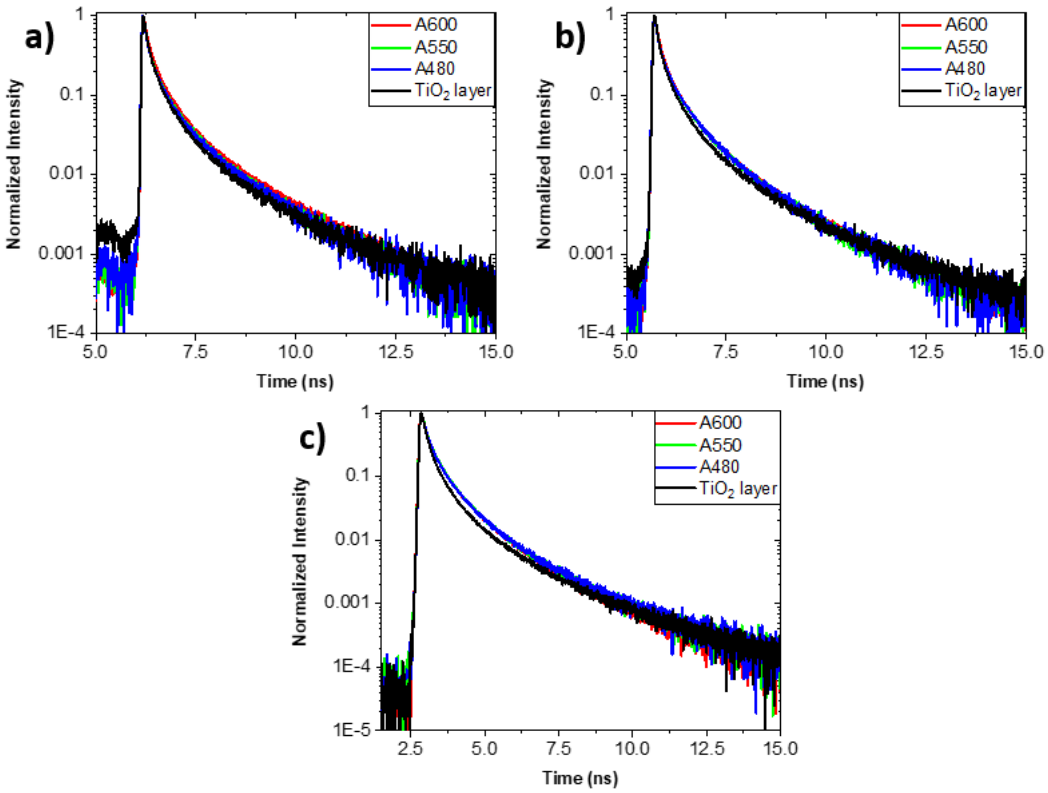

Figure 6-6 Time resolved photoluminescence measurements of R6G emission on TiO_2 arrays and film at a) 375 nm excitation, b) 405 nm excitation, c) 466 nm excitation.

The lifetime of R6G on the TiO_2 arrays at 375 nm excitation obtained from time resolve (TRPL) photoluminescence measurements are shown in **Figure 6-6 a**, the lifetimes on the arrays are slightly longer than off the array and are nearly indistinguishable from each other. The lifetimes were fitted as described in section 3.4. The calculated τ_{avg} off the array is 0.53 ns, 0.58 ns for the A600, 0.57 ns for the A550, and 0.57 ns for the A480. These lifetimes agree with reported values, such as in a study done by Lydia Bechger et al., where R6G PL decay on bare TiO_2 is found to have a multi exponential decay and an average lifetime of 0.58 ns[95]. The lifetime of R6G on the A600, A550 and A480 are nearly indistinguishable from each other. The short lifetime component (τ_1) is 100 ps for the arrays and 90 ps off the array, this component within the resolution of the system (IRF = 150 ps) and not much information can be extracted from this component. There is no considerable difference between any of the lifetime components to be able to explain the increase in emission for the A600 at 375 nm excitation.

405 nm excitation is where the largest increase in R6G emission is observed for the A600. Like the 375 nm excitation no considerable difference can be seen between the lifetime of the arrays in **Figure 6-6 b**. The results for the tri-exponential fits for 405 nm excitation are shown in **Table 6-6**, the calculated τ_{avg} off the array is 0.48 ns, 0.61 ns for the A600, 0.58 ns for the A550, and 0.57 ns for the A480. There is now a larger difference between the lifetimes off and on the arrays. There is also a larger difference between the lifetime of the A600 which is slightly longer than the A550 and A480, but the difference of 40 ps is within the fitting error and possible concentration differences. Like with 375 nm excitation, there is no significant difference between the lifetimes to explain why the A600 array has considerably larger emission. The lifetime of R6G on the TiO_2 arrays at 466 nm excitation are shown in **Figure 6-6 c** and the tri-exponential fit results in **Table 6-7**. The τ_{avg} of the A600 is 0.65 ns, A550 is 0.66 ns, A480 is 0.67 ns, and off the array is 0.61 ns. Like the other excitation powers, the lifetime on the arrays is slightly longer and the lifetime between the arrays is nearly the same.

The results from the TRPL do not point towards an enhancement of the radiative rate of R6G on the A600 array as the lifetime of the A600 is not significantly shorter than the A550 or A480 for the 375 and 405 nm excitation and that the lifetime on the arrays is slightly longer. However, this is not conclusive since in the detection system cannot resolve processes faster than 150 ps and the short component of the PL decay (~100 ps) of R6G has the largest amplitude of the three lifetime components. The lifetimes of R6G j-aggregates is very fast ~4 ps [111] in ethanol, it is not possible to resolve any changes to j-aggregate lifetime with our measurements.

Table 6-5 Lifetime components and amplitudes for the three arrays and TiO_2 layer for the 375 nm pulsed laser.

375 nm	**τ_{avg} (ns)**	**A_1**	**τ_1 (ns)**	**A_2**	**τ_2 (ns)**	**A_3**	**τ_3 (ns)**
Film	0.53	0.61	0.09	0.33	0.32	0.06	1.17
A600	0.58	0.56	0.10	0.36	0.33	0.08	1.18
A550	0.57	0.58	0.10	0.34	0.35	0.08	1.16
A480	0.57	0.58	0.10	0.33	0.34	0.09	1.10

Table 6-6 Lifetime components and amplitudes for the three arrays and TiO_2 layer for the 405 nm pulsed laser.

405 nm	τ_{avg} (ns)	A_1	τ_1 (ns)	A_2	τ_2 (ns)	A_3	τ_3 (ns)
Film	0.48	0.59	0.09	0.34	0.30	0.08	0.98
A600	0.61	0.54	0.10	0.39	0.34	0.08	1.24
A550	0.58	0.58	0.09	0.34	0.32	0.08	1.14
A480	0.57	0.56	0.09	0.35	0.31	0.09	1.10

Table 6-7 Lifetime components and amplitudes for the three arrays and TiO_2 layer for the 466 nm pulsed laser

466 nm	τ_{avg} (ns)	A_1	τ_1 (ns)	A_2	τ_2 (ns)	A_3	τ_3 (ns)
Film	0.61	0.70	0.17	0.26	0.51	0.04	1.64
A600	0.65	0.57	0.17	0.35	0.49	0.08	1.35
A550	0.66	0.54	0.17	0.38	0.48	0.08	1.37
A480	0.67	0.57	0.17	0.35	0.49	0.08	1.39

6.3 Power Dependence of Time Resolved Photoluminescence of R6G on the A600

The measurements in this section were done using the same setup and conditions as in the previous section. Three different areas on the A600 and on the layer were examined for each of the three excitation wavelengths (375, 405, 466 nm). The power dependence was done on the same area per excitation wavelength. **Figure 6-7 a, b, and c** show the laser power dependence on the maximum intensity of the TRPL decay (intensity at t=0) for the A600 array and on the TiO_2 layer for 375 nm, 405 nm, 466 nm. For 405 and 375 nm excitation there is a nearly linear dependence with the intensity at t=0 of the R6G emission at low powers, however at the higher power the dependence becomes sub linear. On the layer the power dependence remains linear throughout the entire range. The lifetime on the A600 for 375 and 405 nm excitation, shown in **Figure 6-8 a and c** respectively, starts increasing significantly at the higher powers, corresponding with the change observed in the intensity at t=0. For the layer, the lifetime at 375 and 405 nm excitation remains virtually the same, a slight increase observed at the highest power in **Figure 6-8 b and d**. Unfortunately, the laser at 466 nm could not reach

high enough powers, for the power range measured the intensity at t=0 has a linear behaviour throughout the range measured on the A600 and for the layer it has a sub linear dependence at the higher end of the range. Despite the behaviour at 466 being opposite from 375 and 405 nm, the power range is not enough to draw any conclusions from this data. These results point towards an increase in the excitation of R6G on the array, the sublinear laser power dependence of the intensity at t=0, show signs of emission saturation due to increase pumping or increase in photobleaching of R6G, this is further shown by the increase in lifetime of the R6G observed.

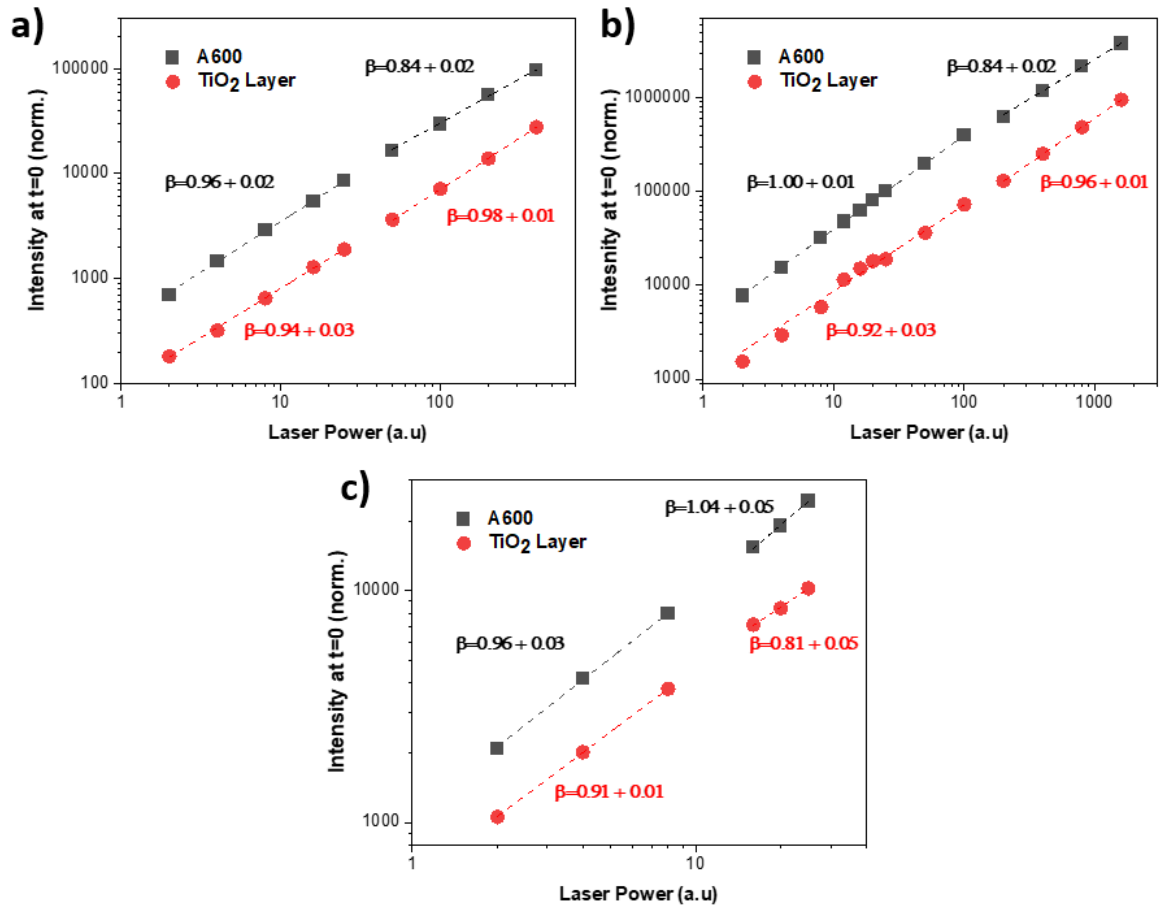

Figure 6-7 Intensity at t=0R6G PL dependence on laser power for a TiO_2 layer region close to the A600 and on the A600 array, for a) 375 nm, b) 405 nm and c) 466 nm excitation. The dependence was fitted by an allometric equation of the form $y = ax^{\beta}$. A fit was done on the low and high-power behaviours of the PL. Results for β are color-coded to their respective positions.

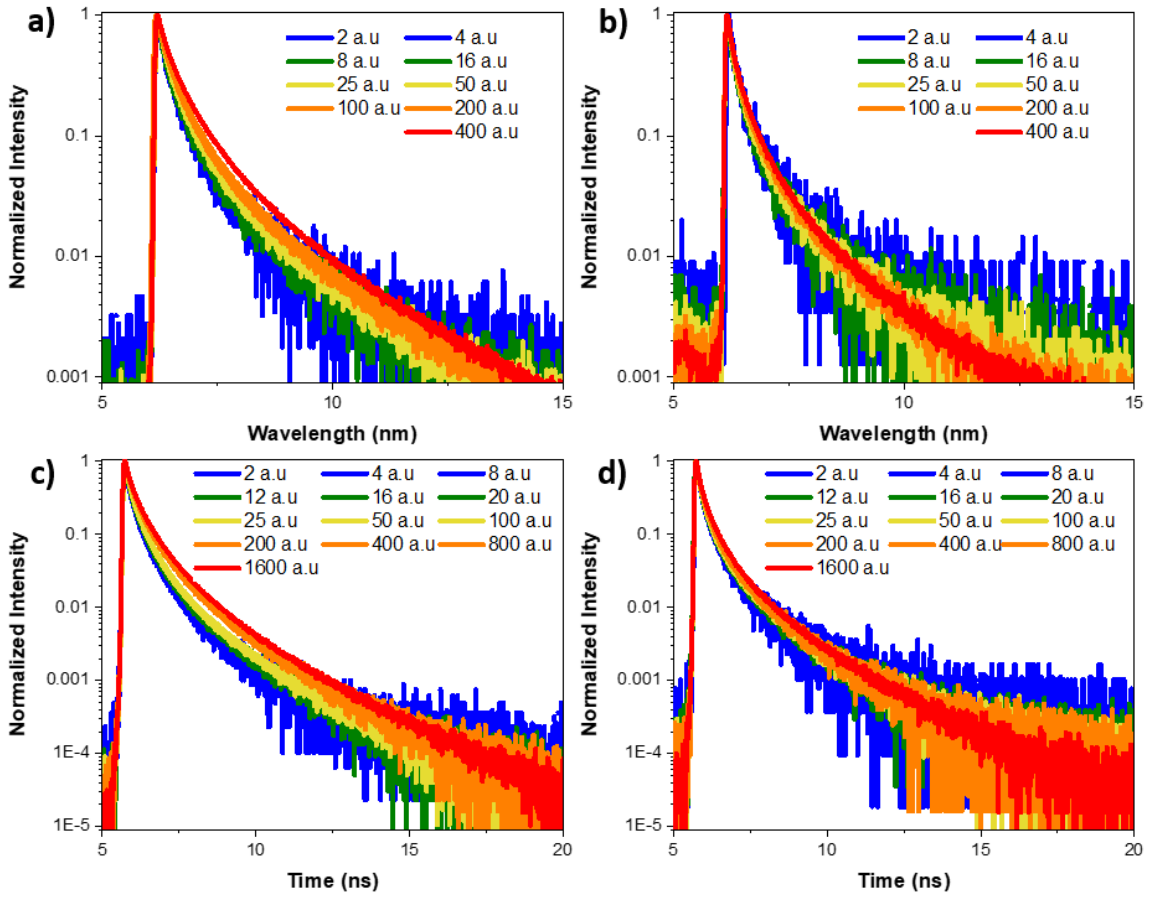

Figure 6-8 TRPL of R6G emission at 375 nm excitation for a) the A600 and b) TiO_2 layer. TRPL of R6G emission on at 405 nm excitation for c) the A600 and d) TiO_2 layer.

6.4 Photobleaching of R6G on TiO_2 arrays

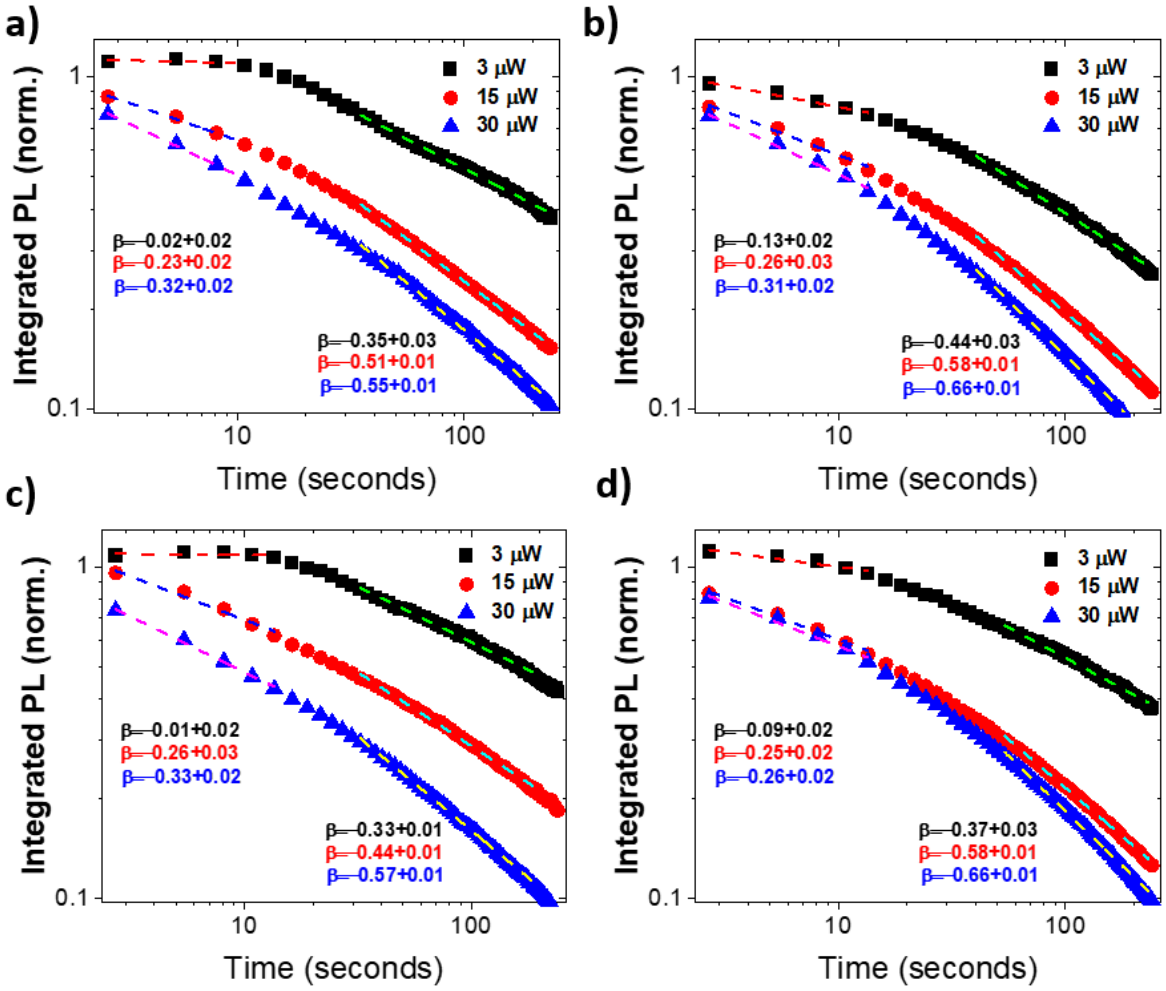

Figure 6-9 Integrated R6G PL dependence over time normalized to initial Integrated PL value, for different excitation powers for a 405 nm laser. a) a TiO_2 layer region close to the A600, b) on the A600 array, c) a TiO_2 layer region close to the A550, and d) on the A550 array at three different excitation powers for a 405 nm laser. The dependence was fitted by an allometric equation of the form $y = ax^{\beta}$. A fit was done on the initial and final photobleaching behaviours of the PL. Results for β are color-coded to their respective powers. Left values are from the initial fit and right values are from the later fits.

Now the photobleaching of R6G on the A550 and A600 arrays at 405 nm excitation is investigated. The photobleaching rate of R6G on TiO_2 increases with excitation power and concentration[62]. A higher photobleaching rate is expected on the arrays due to higher concentration of R6G, however similar concentrations of R6G are expected for the A550 and A600, since the A550 has 47.0% of its surface area as the rough region between pillars and 46.7% for the A600. In **Figure 6-9 a,b** the integrated PL of R6G over time is shown under constant focused (~1 μm^2 spot size) 405 nm laser irradiation on the TiO_2 layer next to the A600

array and on the A600 Array respectively for three different powers, 3 µW, 15 µW and 30 µW, on a log-log scale. The integrated PL photobleaching shows there are two different photobleaching behaviours, a slower initial photobleaching for roughly the first 10 seconds then followed by a faster photobleaching. The photobleaching curve for ~the initial 10 seconds and the final part for the quenching were fitted by an allometric fit of $y = ax^{\beta}$ to compare the different powers. The photobleaching rate (β) increases with increasing laser power for both the initial photobleaching and at later times. The quenching on and off the A600 array are displayed in **Figure 6-9 a,b**. At 3 µW the initial quenching rate is larger on the array than off while at 15 and 30 µW it the R6G PL photobleaching rate are the same (within error). For the latter part of the photobleaching decay, the rate is larger on the A600 than off the array. The increase in the PL photobleaching rate on the arrays is further shown by looking at the ratio between on and off the A600 in **Figure 6-10 a**. The ratio decreases fast initially and then slightly rises before continuing to decrease at a slower rate for 3 µW. For 15 µW there is a fast initial decrease followed by a slower decrease, for 30 uW there is a slight rise before a gradual decrease that slows as times goes on. R6G PL on the A600 is clearly bleaching at a faster rate than on the TiO_2 layer. R6G photocatalytic degradation can be enhanced on TiO_2 by an increase in porosity as this increases the contact area of the R6G with the TiO_2 surface[112]. There is an increase in surface area on the arrays due to the pillar structure and the increased porosity of the TiO_2 layer, which explains in part the increase in R6G photobleaching rate on the arrays. However, the A600 could also have increased localized electric fields due to the pillar resonances and RA which would increase the photobleaching rate, since higher laser powers increase the photobleaching rate. For the A550 the integrated PL of R6G over time for on the A550 array and a region off the A550 array respectively, is shown in **Figure 6-9 c,d**. Like the A600, there are two initial behaviours a slower initial quenching followed by a faster quenching and the quenching rate increases with increasing power. For the 3 µW the initial photobleaching rate on the A550 array is faster than off the array, however it is not clear if the later photobleaching rate is faster due to the errors of the fit. **Figure 6-10 b**, show the ratio between on and off the A550 array, for 3 µW the ratio decreases initially and afterwards it remains relatively constant. For 15 µW the behaviour is very similar to the A600 array, and at 30 µW a larger initial increase in the ratio is observed due to the slower initial photobleaching rate on the A550 to the off area.

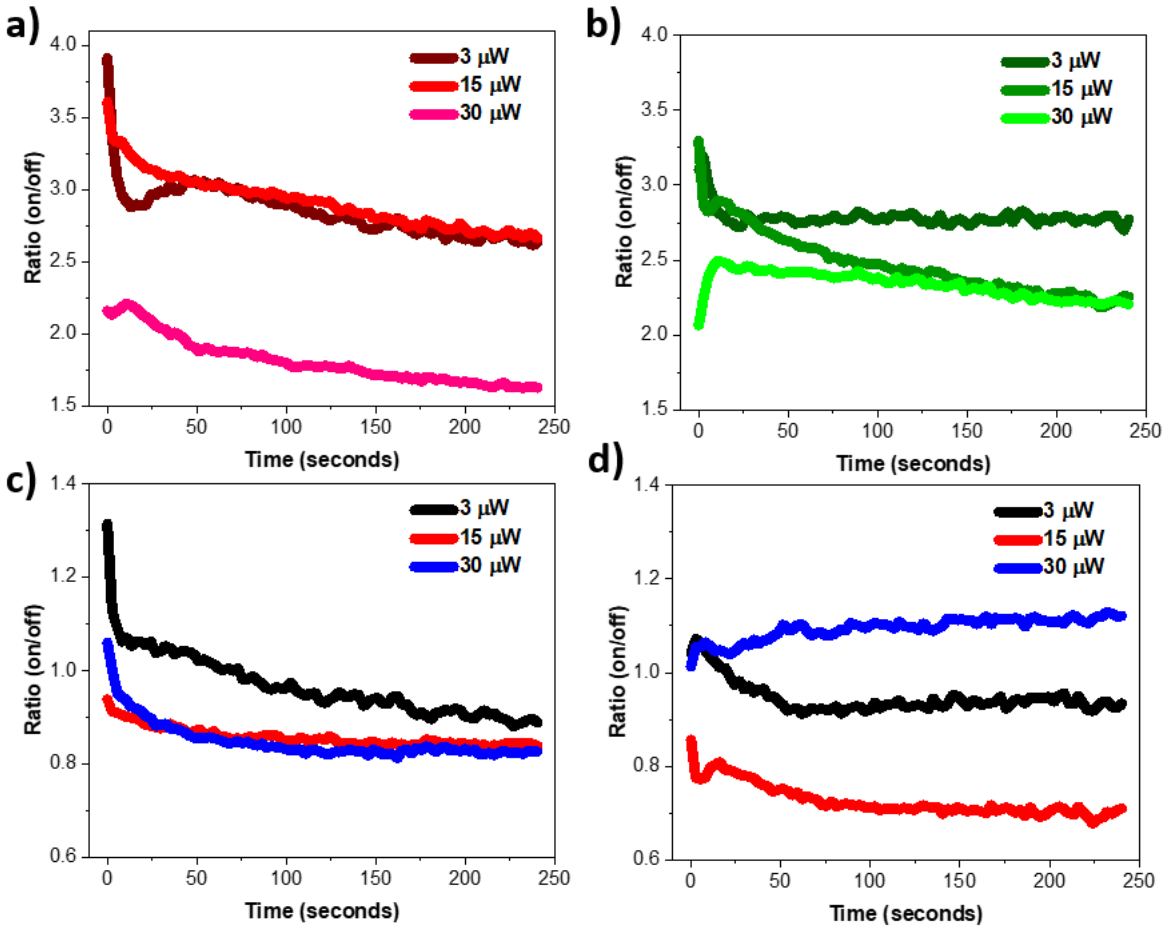

Figure 6-10 R6G emission ratios (array/TiO_2 layer) dependence over time for a) A600 and b) A550 at three different excitation powers for a 405 nm laser. R6G emission ratios (A600/A550) c) on array and d) off array on TiO_2 layer.

The photobleaching rates on the A600 at 3 µW are significantly faster than on the A550 array. This is visible in **Figure 6-10 c which shows** the ratio between the A600 and the A550 (A600/A550). A sharp initial decrease is observed followed a slower constant decrease. At 15 and 30 µw an initial decrease is observed, not as strong as at 3 µW, afterwards the ratio stabilizes, as indicated by the rates which are nearly identical at these powers. The A600 has higher photobleaching rates, this are most likely due to an increase in electric field intensity, however an increase in photobleaching rate can also be due to an increase in R6G concentration, this is unlikely since, as mentioned before, 46.7% of the A600 surface area is the rough layer between arrays, while for the A550 it is 47.0%. The R6G concentration should be similar on both samples. The ratio of the TiO_2 area next to the arrays needs to be compared to see if similar behaviours are observed as on the arrays, this is show in **Figure 6-10 d.** At 3 µW an initial decrease in the ratio is observed, however it is not nearly as strong, and it is a much longer decrease than on the arrays. The ratio on the TiO_2 layer does not continue to decrease at longer

times, it stabilizes. At 30 µW the sharp initial decrease is not observed on the TiO_2 layer ratio, and at 15 µW, the behaviour of the ratio is very similar to the arrays. The sharp decrease in the ratio of the arrays at 3 and 30 µW is not present at all on the TiO_2 layer ratio. The photobleaching of R6G on the arrays points towards an increase in incidence excitation, since the A600 initially photobleaching much faster than the A550 at 3 and 30 µW, the A600 and the A550 should have similar R6G concentration and the sharp initial decrease in the ratio is not observed on the TiO_2 layer.

6.5 FDTD study and Discussion on Array properties on the enhanced R6G emission observed on the A600 array at 375 and 405 nm.

This section will look at how the electric fields on the arrays for the 375 nm and 405 nm excitation differ from an excitation at 466 nm. Due to the higher emission of R6G on the A600 at 375 nm and 405 nm excitation relative to 466 nm, it is expected that the A600 will show a larger electric field intensity at 375 nm and 405 nm to relative to 466 nm excitation than for the A550 and A480 samples. The electric field intensities for three different geometries of the arrays will be investigated using a single pillar, 3x3 array and finally for the infinite array. In the experimental setup the spot size is approximately 1 μm^2, which corresponds to the excitation a single pillar or a single pillar and its immediate neighbours. The refractive indices used in this section for the TiO_2 setup for the pillar and layer are the same used for the previous section corresponding to the best fit to the experimental data, but there is no roughness on the layer. These conditions are TiO_2 with porosity of 30% for the pillar and 45% for the layer. The concentration of R6G used was very low, such that it does not have any considerable effect on the reflection and transmission spectra, so the effects of r6g are not considered in the FDTD simulations.,

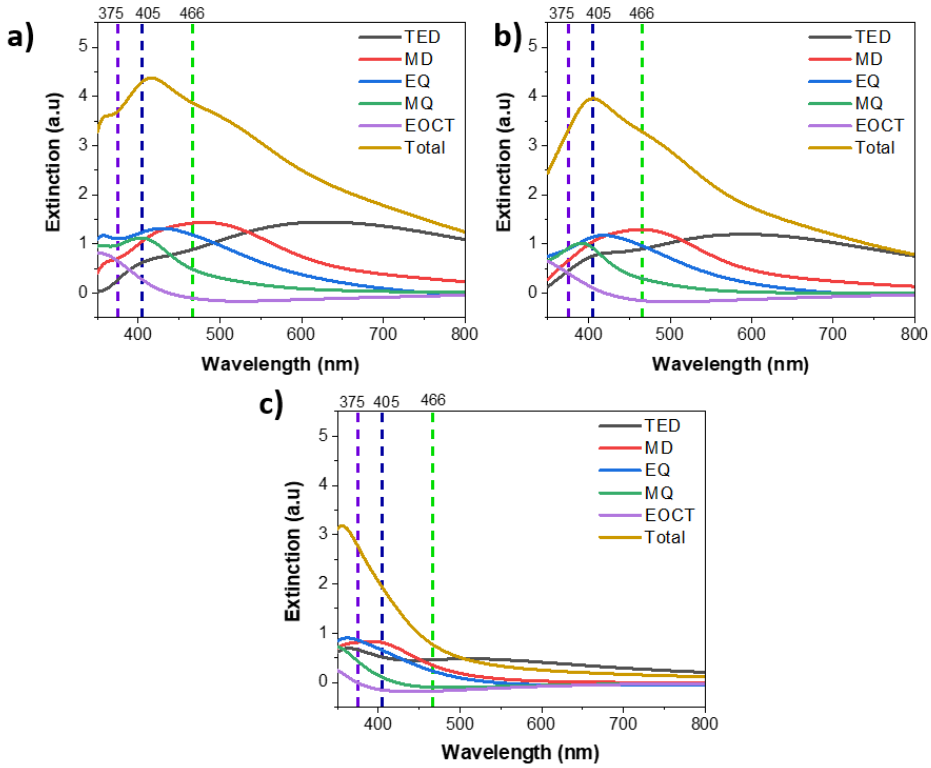

Figure 6-11 Multipole decomposition of the extinction spectra obtained from FDTD simulations on the a) A600, b) A550 and c) A480 for the single pillars.

To understand firstly, why there is an enhancement of the R6G emission only on the A600 array we begin by looking at the single pillar multipole decomposition of the arrays using the same methods described in the previous chapters, based on the method of Evlyukhin et al[76,100]. The multipole decomposition for the arrays is shown in **Figure 6-11 a, b, c**, for the A600, A550 and A480 respectively. The different laser excitations are marked by the dashed lines. The A600 and the A550 spectra are very similar to each other in terms of the positions of the multipole resonances, the A550 is slightly blue shifted due to the smaller dimensions. At 375 nm excitation there is an overlap in both the A600 and the A550 with the same resonances predominantly the electric and magnetic quadrupole (EQ and MQ). For the A480 at 375 nm the overlap with the MQ is not as strong and there is a better overlap with the magnetic dipole (MD). Similarly, at 405 nm excitation the A600 and A550 there is very similar overlap to the pillar's resonances. However, for the A480 pillar the 405 nm excitation does not overlap with the MQ and there is a better overlap with the MD. At 466 nm for both the A600 and the A550 overlaps with the MD and EQ and with the tail of the MQ. In the case of the A480 the 466 nm laser is at the tail of the MD, EQ, and MQ. The A600 resonances are too similar the A550 to explain why there was an increase in R6G PL on the A600 and not on the A550. The A480 array has the largest change in terms of overlap with the resonances going from 375 nm to 466

nm, The ED and MD electric field intensities are mostly in the centre of the of the pillar, whereas the higher resonances tend to be closer to the pillars surface. Looking at the single pillar resonances the 375 and 405 nm excitation overlap more with the MQ and EQ compared to 466 nm, this may contribute to the increase in PL from the A600. However, it could be expected that a similar behaviour should have been observed for the A550 the individual pillars as the spectra from these two cases are so similar.

For the infinite arrays, RAs that couple to quasi-guided modes (QGMs) in the TiO_2 layer cause a significant increase in electric field intensity in the TiO_2 layer and surface as seen in the previous chapters. The RAs for different arrays at normal incidence that couple to QGMs from the substrate side are found in **Table 5-1**, RAs. For the A600 $RA(2,1)_s$ at 402.5 nm, a RA coupled into QGMs around 405 nm would be expected and this would lead to an increase in R6G emission due to an increase in electric field intensity by the QGMs. At 375 nm no RA coupling to QGMs are expected for the A600 array, however the A550 has $RA(2,1)_s$ at 369 nm that could lead to a RA coupled to QGMs around 375 nm. The A480 has $RA(2,0)_s$ could also lead to QGMs around 375 nm. At 466 nm excitation the A600 has $RA(2,0)_s$ at 450 nm that could lead QGMs around 466 nm, however the refractive index of TiO_2 drops significantly from 405 nm to 466 nm which will hinder the capacity for the layer to hold a QGMs. If in the experimental set-up many pillars were illuminated, it might be expected that the A550 and A480 would show greater R6G emission compared under excitation at 375 nm relative to 466 nm or the A600 sample because of the proximity to RAs. However, it is not expected that RAs coupled to QGMs play a role in the experimental data because the spot size of the laser excites at most one pillar and its nearest neighbour. In order to observe behaviours of an infinite array, the arrays need to be 100 x100 pillars to converge to infinite array[74]. The next part will focus on comparing the electric fields at 375 and 405 nm with 466 nm for three different configurations, single pillar, 3x3 and array to see if the A600 shows a stronger relative field to 466 nm and compared to the other arrays, the same parameters as described before were used for these simulations.

Table 6-8 RA position of the three arrays

	$RA(1,0)_a$	**$RA(1,1)_a$**	**$RA(1,0)_s$**	**$RA(1,1)_s$**	**$RA(2,0)_s$**	**$RA(2,1)_s$**
A600	600	424.3	900	636.4	450	402.5
A550	550	388.9	825	583.4	412.5	369.0
A480	480	339.4	720	509.1	360	322.0

To investigate the increased emission relative to 466 nm observed for the A600 array, the electric field intensity distribution obtained from FDTD simulations for 375 and 405 nm is divided by the electric field intensity distribution at 466 nm. This is presented in three different views, z-normal at 20 nm below the pillar, y-normal at the origin and x-normal at the origin. This should give a clear picture of the electric field intensity distribution and will allow for the comparison between the arrays. Firstly, the single pillar visualizations of the relative field intensity distribution for the A600, A550 and A480 are shown in **Figure 6-12, Figure 6-13, Figure 6-14** respectively. Not surprisingly the relative fields for the A600 and A550 at 375 and 405 nm are very similar to each other, as expected from the multipole analysis discussed earlier. For these pillars most of the electric field intensity enhancement relative to the 466 nm case is surrounding the pillar at 375 and 405 nm and the fields at 375 nm are more intense. For the A480 at 375 and 405 nm, most of the field enhancement relative to 466 nm is inside the pillar, this is because the multipole resonances are far from 466 nm. The field outside the pillar is much weaker than the A600 and A500. Clearly the simulations do not suggest higher excitation for the A600 pillar, since the profiles are too similar.

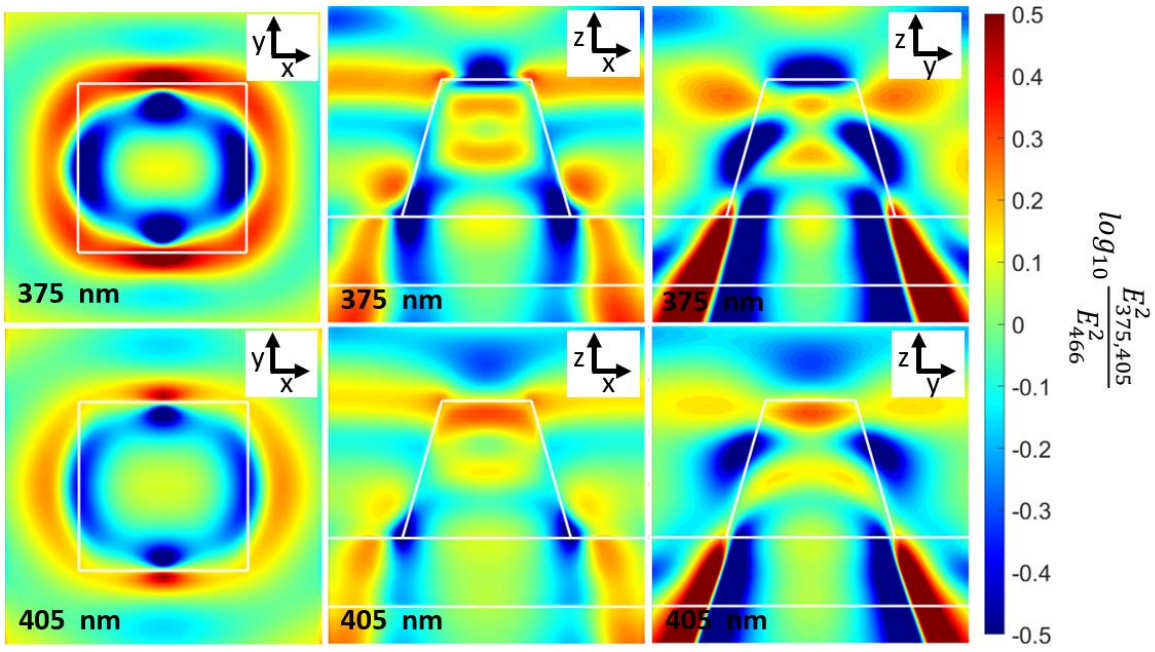

Figure 6-12 Relative electric field intensity of the A600 single pillar in three different views, z-normal at 20 nm below the pillar, y-normal at the origin and x-normal at the origin. At 375 nm (top row) and 405 nm (bottom row). The electric field profiles at 375 and 405 nm are divided by the electric field intensity profile at 466 nm.

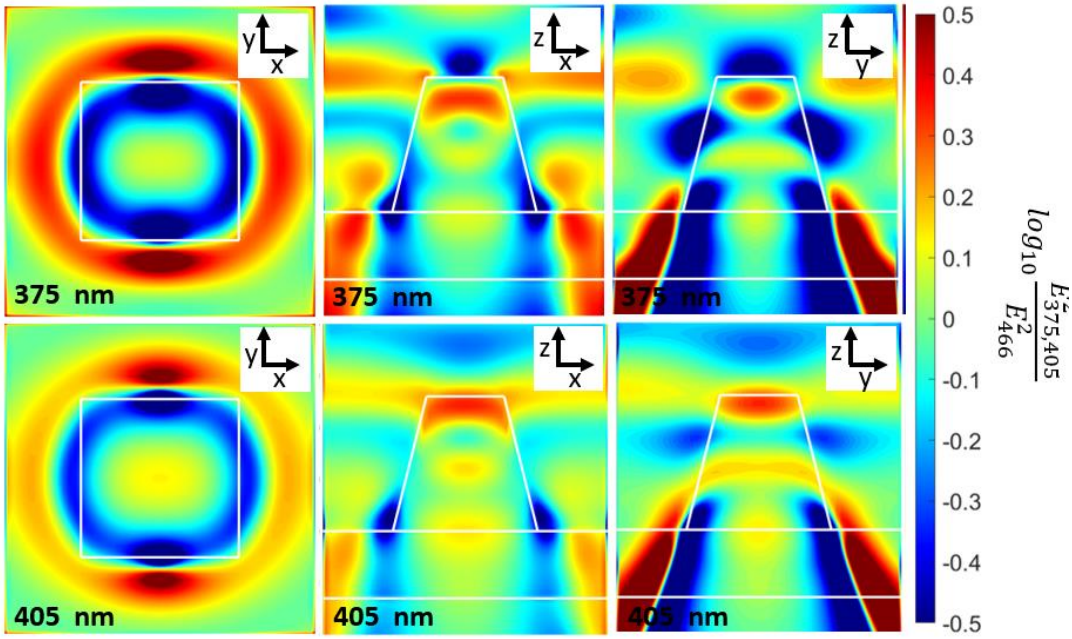

Figure 6-13 Relative electric field intensity of the A550 single pillar in three different views, z-normal at 20 nm below the pillar, y-normal at the origin and x-normal at the origin. At 375 nm (top row) and 405 nm (bottom row). The electric field profiles at 375 and 405 nm are divided by the electric field intensity profile at 466 nm.

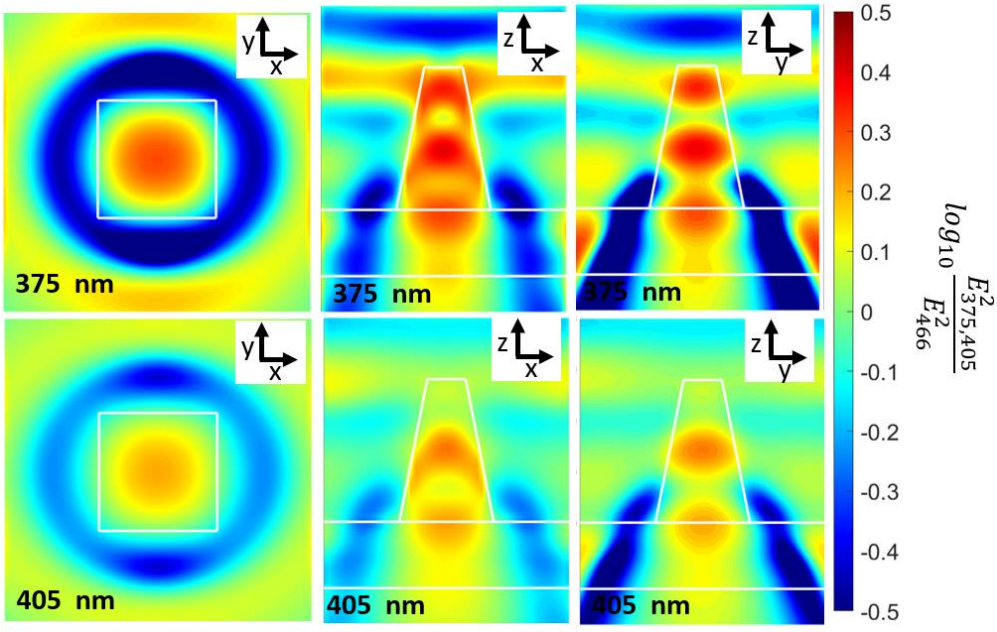

Figure 6-14 Relative electric field intensity of the A480 single pillar in three different views, z-normal at 20 nm below the pillar, y-normal at the origin and x-normal at the origin. At 375 nm (top row) and 405 nm (bottom row). The electric field profiles at 375 and 405 nm are divided by the electric field intensity profile at 466 nm.

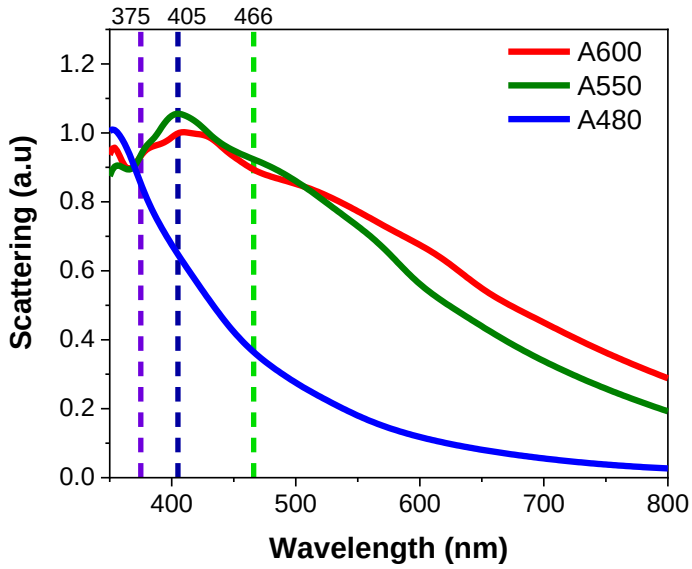

Figure 6-15 Scattering spectra of 3x3 the A600, A550 and A480 arrays obtained from FDTD simulations.

For the excitation of 3x3 arrays the scattering does not change drastically from a single pillar as seen in **Figure 6-15** as the arrays need to be roughly 100x100 to converge to infinite array[74]. The single pillar scattering spectra were shown above in Figure 0-11. The same analysis is now done as for the single pillar, **Figure 6-16, Figure 6-17 and Figure 6-18** show the relative electric field intensity distribution for the A600, A550 and A480, respectively. The relative field intensities are very similar with respect to the single pillar, however now the intensity field maps for the A600 and the A550 are significantly different. The A550 has stronger relative field intensities close to the pillar, however the A600 has significantly greater relative field intensities in the region between the pillars. Despite not seeing direct evidence of the excitation enhancement suggested by the experimental data the simulation shows that the fields even for a 3x3 array differ significantly from single particle allowing for the A600 and A550 to have different field intensity profiles which would affect the emission of R6G. The field of the A480 is significantly different than the A600 and A550. By varying different parameters in the array such as the layer thickness, layer index, roughness, pillar's index, and the R6G effects on the array, it would be possible to have relative field intensity profiles that would match the experimental observations. However, the simulations suggest that as the A550 and A600 arrays are so similar it may not be possible to account for the difference in observations based on the field maps.

.

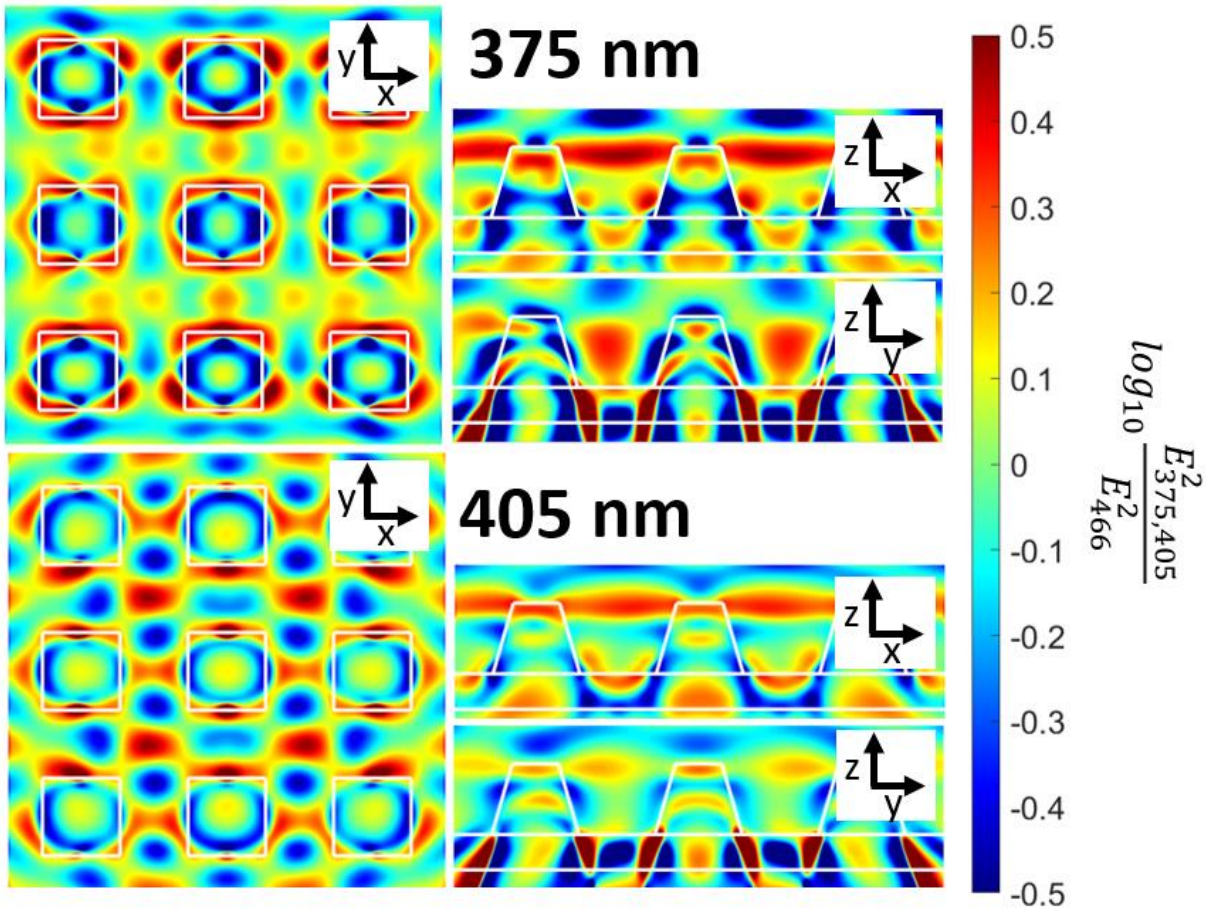

Figure 6-16 Relative electric field intensity of the 3x3 A600 in three different views, z-normal at 20 nm below the pillar, y-normal at the origin and x-normal at the origin. At 375 nm (top row) and 405 nm (bottom row). The electric field profiles at 375 and 405 nm are divided by the electric field intensity profile at 466 nm.

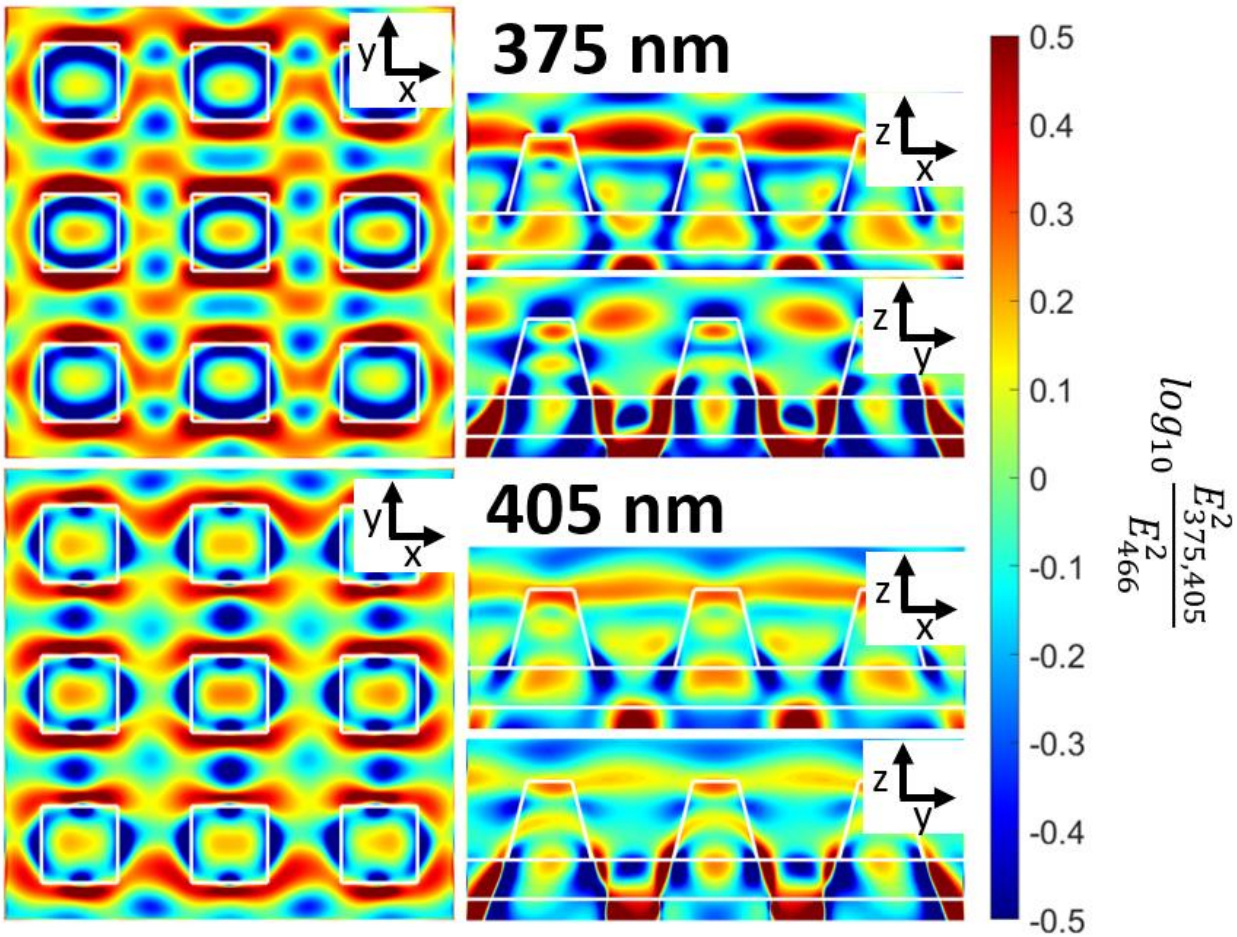

Figure 6-17 Relative electric field intensity of the 3x3 A550 in three different views, z-normal at 20 nm below the pillar, y-normal at the origin and x-normal at the origin. At 375 nm (top row) and 405 nm (bottom row). The electric field profiles at 375 and 405 nm are divided by the electric field intensity profile at 466 nm.

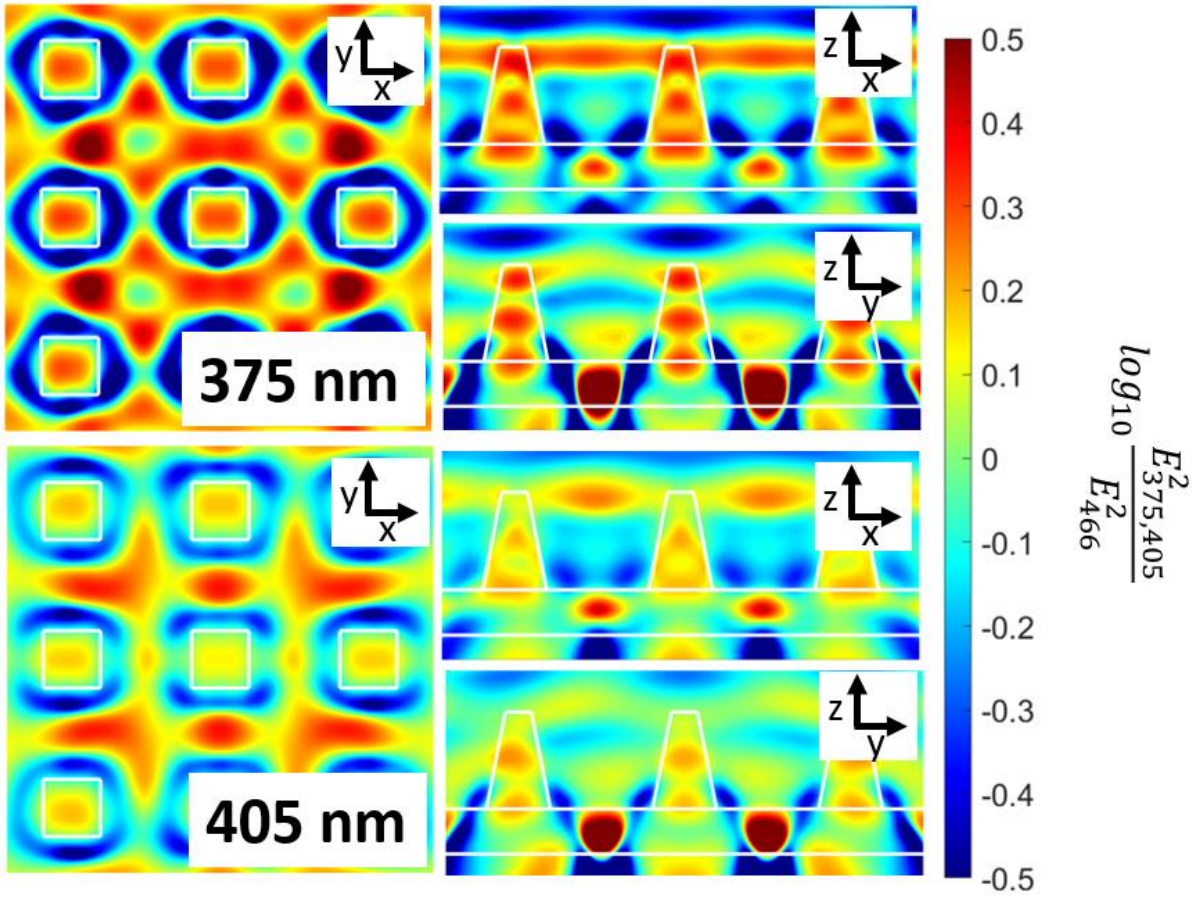

Figure 6-18 Relative electric field intensity of the 3x3 A480 in three different views, z-normal at 20 nm below the pillar, y-normal at the origin and x-normal at the origin. At 375 nm (top row) and 405 nm (bottom row). The electric field profiles at 375 and 405 nm are divided by the electric field intensity profile at 466 nm.

6.6 Conclusion

To conclude this chapter, The R6G photoluminescence manipulated by the geometry TiO_2 array geometry and excitation wavelength. The A600 had a much stronger R6G PL at 375 and 405 nm relative to 466 nm than the A550 and A480. The red shoulder appearing as the excitation wavelength increased on the arrays, suggests the formation of R6G j-aggregates and the data indicated that the A550 and A480 possibly have a higher R6G concentration since the number of aggregates increases with concentration. The reshaping is not caused by the arrays because there is no reshaping observed at 375 nm excitation. The lifetime on the arrays regardless of excitation is always slightly longer than on the TiO_2 layer. The A600 lifetime is

not significantly different than all the other lifetimes. The lifetime data did not provide any evidence of an increase in the radiative rate was responsible for the larger emission of R6G relative to 466 observed at 375 and 405 nm. The arrays did not modify the radiative rate as seen in the TRPL spectra where the lifetime decays of R6G were virtually the same on the arrays. The power dependence of the R6G emission on the A600 array is significantly different than on the TiO_2 layer, a sub linear behaviour emission dependence on laser power appears at the higher powers accompanied by a significant increase in lifetime not observed on the TiO_2 layer, this further suggests the increase in R6G emission is related to the excitation enhancement. There is also an observed increase in R6G photobleaching on the A600 and A550 array. The A600 array shows faster photobleaching times than the A550, further suggesting that there is higher excitation of R6G on the A600 array at 405 nm, however this could be caused by an increase in R6G concentration on the A600. Finally, simulations on the single pillar show that the A600 and A550 are too like each other to significantly vary the electric field intensity profiles, so no conclusive evidence of difference between the A550 and A600 enhanced excitation can be determined from the field maps. However, it is noted that in a 3x3 array the electric fields intensity profiles are significantly different for the A550 and A600 arrays, but the trends based on these simulations do not support higher excitation fields at 375 nm and 405 nm excitation for the A600 array compared with the A550 array. The mechanism of the observed emission enhancement has yet to be fully understood.

6.7 Conclusion and Future Work

In this thesis, the properties of TiO_2 nanopillar arrays fabricated via soft nanoimprint lithography are studied. The TiO_2 arrays were fabricated by the group of Marco Abbarchi. Firstly, the optical properties of TiO_2 nanopillar arrays are studied using a FDTD method. The impact of the residual TiO_2 layer on the properties of the collective resonances of the array has been demonstrated. If the refractive index of the residual layer is higher than the substrate and the layer is sufficiently thick, QGMs will be allowed to exist in the residual TiO_2 layer. The position of the RA can be tuned by changing the refractive index of the residual TiO_2 layer, the periodicity of the array in the x and y direction and the thickness of the TiO_2 layer. The electric QGMs are more susceptible to changes in the refractive index of the residual layer 130 nm thick, while the magnetic QGMs are more susceptible to changes in the substrate's index. The QGMs in these arrays lead to very sharp and strong reflection peaks that correlate to strong electric field enhancements near the surface of the array. The strongest enhancement and reflection peaks are from QGMs coupled to RA (1,0) and (0,1), the second strongest to RA(1,1) and the third strongest are observed for the higher order RA (2,0), (0,2) and (1,2).

The second chapter experimentally explores the properties of the A600, A550 and A480 arrays. The three arrays show no signs of QGMs despite the residual TiO_2 layer being 130 nm thick. This was due to the greater roughness and porosity present in the residual. The increase in porosity and roughness of the residual layer is due to the fabrication process. The effect of roughness on the residual layer's ability to support QGMs were studied computationally. A rough layer and a layer with gaps can still support QGMs, and it is seen that the effect of the roughness on the QGMs is almost equivalent to reducing the refractive index of the layer. Very good agreement was found between FDTD simulation of the arrays and the experimental normal reflection and transmission measurements. The most prominent feature of the three arrays was a sharp features in normal reflection and transmission at RA(1,0) on the air side. QGMs appeared for all three arrays when solution greater than 1.00 mM of R6G were added. This was due to the R6G increasing the effective refractive index of the residual layer to a value significantly greater than the glass substrate (>1.5). For the A550 array, E-QGM1, E-QGM2 and M-QGM2 were observed experimentally as large and narrow reflection peaks and transmission dips in the normal reflection and transmission measurements. For the A480 array, E-QGM1 and M-QGM1 were observed as sharp features in reflection and transmission. The A600 array only showed the E-QGM2 after the 1.0 mM R6G solution was added. FDTD

simulations confirmed that the peaks observed in the reflection spectrum were QGMs. Very good correlation between the experimental and simulation shapes of the QGMs is observed for the A550 array. The effect of R6G on the dark-field scattering spectra with a 20x and 50x objective was also discussed. Significant colour changes were observed and are likely arising due to some form of coupling to the RAs. All these changes observed in the arrays by the addition of R6G were reversed by the removal of the dye.

Lastly, the effect of the TiO_2 arrays on the R6G emission was studied by adding 0.35 mM solution of R6G on the arrays. The emission of R6G could be modified due to the resonances supported by the TiO_2 array's geometry and excitation wavelength. R6G on the A600 array had a much stronger photoluminescence at 375 nm and 405 nm excitation relative to the photoluminescence at 466 nm. There was a red shoulder on the PL spectrum that appeared on the arrays and became more prominent with increasing wavelength. The reshaping of the PL was not due to arrays as there was no visible red shoulder in the PL at 375 nm excitation. This indicated the formation of j-aggregates on the arrays, likely due to the increase of R6G concentration due to the high porosity and roughness of the TiO_2 residual layer. The A550 and A480 had larger red shoulders than the A600 possibly indicating that the A550 and A480 had higher R6G concentrations. The lifetime of the A600 array, however, showed no signs of emission enhancement, as the lifetimes of all the arrays were virtually the same. There was no modification of the radiative rate of R6G due to the array. The dependence of the R6G emission on the excitation power for the 375 and 405 nm excitation showed a different behaviour on the A600 array than on the TiO_2 layer off the array. A sublinear dependence on excitation power was observed for R6G photoluminescence in the A600 for both mentioned excitation wavelengths at the higher powers, while off the array the behaviour did not change across the range. An increase in photobleaching was also observed on the A600 and A550 array at 405 nm excitation compared to the photobleaching off the arrays. Although the A600 does show higher photobleaching rate than the A550, the difference is not sufficient to support any substantial claims. The increase in photobleaching observed on the arrays compared to off the arrays was due to the increase in surface area and R6G concentration due to the roughness of the TiO_2 layer between the pillars. FDTD simulation show that for the excitation of a single pillar, the field intensities at 375 nm and 405 nm relative to the fields at 466 nm for the A550 and A600 with single pillar excitation are too alike to account for the increase in the 375/466 and 405/466 emission ratios on the A600. However, the electric field intensity profiles of a 3x3 array for the A600 and the A550 array are significantly different from each other, but they still do not clearly

show that the A600 has greater relative field intensities at 405 and 375 nm. Despite most of the experimental evidence pointing towards excitation enhancement of R6G on the A600 array, these results are not conclusive, and the exact underlying mechanism still has to be understood.

The TiO_2 arrays fabricated via soft-NIL by the group of Marco Abbarchi are very large, they have an area of $1mm^2$ and are relatively easy to fabricate. This study looks at the impact of a residual TiO_2 layer and the conditions needed for these arrays to support QGMs, and how their positions can be manipulated. It has been shown experimentally that even if the residual layer is not optically thick enough to support QGMs due to its porosity, another material can be added to increase the effective index of the residual layer to support QGMs. First and second order electric and magnetic QGMs were observed and yielded sharp reflection peaks at normal incidence of roughly 50% and transmission dips of roughly 80%. Modification of dye emission on the periodic structures has also been observed. The large surface area of these arrays, the relatively cheap and fast fabrication method, and the residual layer of TiO_2 left behind during fabrication can help these arrays to support QGMs. QGMs are very sensitive to changes in refractive index, making them excellent candidates for a variety of applications, especially sensing.

For the future work, more studies need to be done on the mechanisms behind the R6G emission enhancement observed for the A600 array. Also check for emission modification of other dyes, quantum dots and quantum wells. The power dependence should be done for the three excitation wavelengths in the same power range. This will determine if the sublinear dependence of R6G emission for higher excitation powers is produced by the array or if it is due to emission enhancement and if the sublinear behaviour is also observed on the A600 array at 466 nm excitation. The R6G on the arrays was excited by a focused laser excitation. R6G PL dependence on both R6G concentration and excitation spot size could be interesting to explore. Fabrication of arrays with a tailored residual TiO_2 layer that supports the QGMs is an interesting follow-up for this work, with a view to sensing applications. A dye that has high absorption at the QGMs resonances could experience significant emission enhancement.

7 References

(1) Vohnsen, B. A Short History of Optics. *Physica Scripta* **2004**, *2004* (T109), 75.

(2) Michelson, A. A.; Morley, E. W. LVIII. On the Relative Motion of the Earth and the Luminiferous Æther. *The London, Edinburgh, and Dublin Philosophical Magazine and Journal of Science* **1887**, *24* (151), 449–463.

(3) Ritchie, R. H. Plasma Losses by Fast Electrons in Thin Films. *Physical Review* **1957**, *106* (5), 874.

(4) Barnes, W. L.; Dereux, A.; Ebbesen, T. W. Surface Plasmon Subwavelength Optics. *nature* **2003**, *424* (6950), 824–830.

(5) Fernández-Domínguez, A. I.; García-Vidal, F. J.; Martín-Moreno, L. Unrelenting Plasmons. *Nature Photonics* **2017**, *11* (1), 8–10.

(6) Moskovits, M. Surface-Enhanced Spectroscopy. *Reviews of Modern Physics* **1985**, *57* (3), 783.

(7) Kneipp, K.; Wang, Y.; Kneipp, H.; Perelman, L. T.; Itzkan, I.; Dasari, R. R.; Feld, M. S. Single Molecule Detection Using Surface-Enhanced Raman Scattering (SERS). *Physical Review Letters* **1997**, *78* (9), 1667.

(8) McNay, G.; Eustace, D.; Smith, W. E.; Faulds, K.; Graham, D. Surface-Enhanced Raman Scattering (SERS) and Surface-Enhanced Resonance Raman Scattering (SERRS): A Review of Applications. *Applied Spectroscopy* **2011**, *65* (8), 825–837.

(9) Ojha, A. K.; Donfack, P.; Materny, A. Complex Concentration Dependence of SERS and UV–Vis Absorption of Glycine/Ag-Substrates Because of Glycine-Mediated Ag-Nanostructure Modifications. *Journal of Raman Spectroscopy* **2012**, *43* (9), 1183–1190.

(10) Atwater, H. A.; Polman, A. Plasmonics for Improved Photovoltaic Devices. In *Materials For Sustainable Energy: A Collection of Peer-Reviewed Research and Review Articles from Nature Publishing Group*; World Scientific, 2011; pp 1–11.

(11) Clavero, C. Plasmon-Induced Hot-Electron Generation at Nanoparticle/Metal-Oxide Interfaces for Photovoltaic and Photocatalytic Devices. *Nature Photonics* **2014**, *8* (2), 95–103.

(12) Tvingstedt, K.; Persson, N.-K.; Inganäs, O.; Rahachou, A.; Zozoulenko, I. V. Surface Plasmon Increase Absorption in Polymer Photovoltaic Cells. *Applied Physics Letters* **2007**, *91* (11), 113514.

(13) Guzatov, D.; Gaponenko, S.; Demir, H. V. Plasmonic Enhancement of Electroluminescence. *AIP Advances* **2018**, *8* (1), 015324.

(14) Pryce, I. M.; Koleske, D. D.; Fischer, A. J.; Atwater, H. A. Plasmonic Nanoparticle Enhanced Photocurrent in GaN/InGaN/GaN Quantum Well Solar Cells. *Applied Physics Letters* **2010**, *96* (15), 153501.

(15) Higgins, L. J.; Marocico, C. A.; Karanikolas, V. D.; Bell, A. P.; Gough, J. J.; Murphy, G. P.; Parbrook, P. J.; Bradley, A. L. Influence of Plasmonic Array Geometry on Energy Transfer from a Quantum Well to a Quantum Dot Layer. *Nanoscale* **2016**, *8* (42), 18170–18179.

(16) Abbas, A.; Tian, L.; Morrissey, J. J.; Kharasch, E. D.; Singamaneni, S. Hot Spot-Localized Artificial Antibodies for Label-Free Plasmonic Biosensing. *Advanced Functional Materials* **2013**, *23* (14), 1789–1797.

(17) Knight, M. W.; King, N. S.; Liu, L.; Everitt, H. O.; Nordlander, P.; Halas, N. J. Aluminum for Plasmonics. *ACS Nano* **2014**, *8* (1), 834–840.

(18) Boltasseva, A.; Atwater, H. A. Low-Loss Plasmonic Metamaterials. *Science* **2011**, *331* (6015), 290–291.
(19) Gjerding, M. N.; Pandey, M.; Thygesen, K. S. Band Structure Engineered Layered Metals for Low-Loss Plasmonics. *Nature Communications* **2017**, *8* (1), 1–8.
(20) Wang, F.; Shen, Y. R. General Properties of Local Plasmons in Metal Nanostructures. *Physical Review Letters* **2006**, *97* (20), 206806.
(21) Kravets, V. G.; Kabashin, A. V.; Barnes, W. L.; Grigorenko, A. N. Plasmonic Surface Lattice Resonances: A Review of Properties and Applications. *Chemical Reviews* **2018**, *118* (12), 5912–5951.
(22) Kuznetsov, A. I.; Miroshnichenko, A. E.; Brongersma, M. L.; Kivshar, Y. S.; Luk'yanchuk, B. Optically Resonant Dielectric Nanostructures. *Science* **2016**, *354* (6314), aag2472.
(23) Baranov, D. G.; Zuev, D. A.; Lepeshov, S. I.; Kotov, O. V.; Krasnok, A. E.; Evlyukhin, A. B.; Chichkov, B. N. All-Dielectric Nanophotonics: The Quest for Better Materials and Fabrication Techniques. *Optica* **2017**, *4* (7), 814–825.
(24) Staude, I.; Schilling, J. Metamaterial-Inspired Silicon Nanophotonics. *Nature Photonics* **2017**, *11* (5), 274.
(25) Evlyukhin, A. B.; Novikov, S. M.; Zywietz, U.; Eriksen, R. L.; Reinhardt, C.; Bozhevolnyi, S. I.; Chichkov, B. N. Demonstration of Magnetic Dipole Resonances of Dielectric Nanospheres in the Visible Region. *Nano Letters* **2012**, *12* (7), 3749–3755.
(26) Van de Hulst, H. *Light Scattering by Small Particles*; Dover Publications, Inc., 1981.
(27) Evlyukhin, A. B.; Reinhardt, C.; Seidel, A.; Luk'yanchuk, B. S.; Chichkov, B. N. Optical Response Features of Si-Nanoparticle Arrays. *Physical Review B* **2010**, *82* (4), 045404.
(28) Kuznetsov, A. I.; Miroshnichenko, A. E.; Fu, Y. H.; Zhang, J.; Luk'Yanchuk, B. Magnetic Light. *Scientific reports* **2012**, *2*, 492.
(29) Meinzer, N.; Barnes, W. L.; Hooper, I. R. Plasmonic Meta-Atoms and Metasurfaces. *Nature Photonics* **2014**, *8* (12), 889.
(30) Shalaev, V. M. Optical Negative-Index Metamaterials. *Nature Photonics* **2007**, *1* (1), 41–48.
(31) Cai, W.; Chettiar, U. K.; Kildishev, A. V.; Shalaev, V. M. Optical Cloaking with Metamaterials. *Nature Photonics* **2007**, *1* (4), 224–227.
(32) Castellanos, G. W.; Bai, P.; Gómez Rivas, J. Lattice Resonances in Dielectric Metasurfaces. *Journal of Applied Physics* **2019**, *125* (21), 213105.
(33) Wood, R. W. XLII. On a Remarkable Case of Uneven Distribution of Light in a Diffraction Grating Spectrum. *The London, Edinburgh, and Dublin Philosophical Magazine and Journal of Science* **1902**, *4* (21), 396–402.
(34) Hessel, A.; Oliner, A. A New Theory of Wood's Anomalies on Optical Gratings. *Applied optics* **1965**, *4* (10), 1275–1297.
(35) Zou, S.; Schatz, G. C. Narrow Plasmonic/Photonic Extinction and Scattering Line Shapes for One and Two Dimensional Silver Nanoparticle Arrays. *The Journal of Chemical Physics* **2004**, *121* (24), 12606–12612.
(36) Kravets, V.; Schedin, F.; Grigorenko, A. Extremely Narrow Plasmon Resonances Based on Diffraction Coupling of Localized Plasmons in Arrays of Metallic Nanoparticles. *Physical Review Letters* **2008**, *101* (8), 087403.
(37) Kravets, V.; Schedin, F.; Kabashin, A.; Grigorenko, A. Sensitivity of Collective Plasmon Modes of Gold Nanoresonators to Local Environment. *Optics Letters* **2010**, *35* (7), 956–958.

(38) Giannini, V.; Vecchi, G.; Rivas, J. G. Lighting up Multipolar Surface Plasmon Polaritons by Collective Resonances in Arrays of Nanoantennas. *Physical Review Letters* **2010**, *105* (26), 266801.
(39) Vecchi, G.; Giannini, V.; Rivas, J. G. Shaping the Fluorescent Emission by Lattice Resonances in Plasmonic Crystals of Nanoantennas. *Physical Review Letters* **2009**, *102* (14), 146807.
(40) Lozano, G.; Grzela, G.; Verschuuren, M. A.; Ramezani, M.; Rivas, J. G. Tailor-Made Directional Emission in Nanoimprinted Plasmonic-Based Light-Emitting Devices. *Nanoscale* **2014**, *6* (15), 9223–9229.
(41) Czaplicki, R.; Kiviniemi, A.; Laukkanen, J.; Lehtolahti, J.; Kuittinen, M.; Kauranen, M. Surface Lattice Resonances in Second-Harmonic Generation from Metasurfaces. *Optics letters* **2016**, *41* (12), 2684–2687.
(42) Utikal, T.; Zentgraf, T.; Paul, T.; Rockstuhl, C.; Lederer, F.; Lippitz, M.; Giessen, H. Towards the Origin of the Nonlinear Response in Hybrid Plasmonic Systems. *Physical Review Letters* **2011**, *106* (13), 133901.
(43) Zhou, W.; Dridi, M.; Suh, J. Y.; Kim, C. H.; Co, D. T.; Wasielewski, M. R.; Schatz, G. C.; Odom, T. W.; others. Lasing Action in Strongly Coupled Plasmonic Nanocavity Arrays. *Nature Nanotechnology* **2013**, *8* (7), 506.
(44) Yang, A.; Hoang, T. B.; Dridi, M.; Deeb, C.; Mikkelsen, M. H.; Schatz, G. C.; Odom, T. W. Real-Time Tunable Lasing from Plasmonic Nanocavity Arrays. *Nature Communications* **2015**, *6* (1), 1–7.
(45) Zhang, X.; Ma, X.; Dou, F.; Zhao, P.; Liu, H. A Biosensor Based on Metallic Photonic Crystals for the Detection of Specific Bioreactions. *Advanced Functional Materials* **2011**, *21* (22), 4219–4227.
(46) Zhukovsky, S. V.; Babicheva, V. E.; Uskov, A. V.; Protsenko, I. E.; Lavrinenko, A. V. Enhanced Electron Photoemission by Collective Lattice Resonances in Plasmonic Nanoparticle-Array Photodetectors and Solar Cells. *Plasmonics* **2014**, *9* (2), 283–289.
(47) Zywietz, U.; Evlyukhin, A. B.; Reinhardt, C.; Chichkov, B. N. Laser Printing of Silicon Nanoparticles with Resonant Optical Electric and Magnetic Responses. *Nature Communications* **2014**, *5* (1), 1–7.
(48) Evlyukhin, A. B.; Matiushechkina, M.; Zenin, V. A.; Heurs, M.; Chichkov, B. N. Lightweight Metasurface Mirror of Silicon Nanospheres. *Optical Materials Express* **2020**, *10* (10), 2706–2716.
(49) Babicheva, V. E.; Evlyukhin, A. B. Resonant Lattice Kerker Effect in Metasurfaces with Electric and Magnetic Optical Responses. *Laser & Photonics Reviews* **2017**, *11* (6), 1700132.
(50) Ding, P.; He, J.; Wang, J.; Fan, C.; Liang, E. Electromagnetically Induced Transparency in All-Dielectric Metamaterial-Waveguide System. *Applied Optics* **2015**, *54* (12), 3708–3714.
(51) Ding, P.; Li, M.; He, J.; Wang, J.; Fan, C.; Zeng, F. Guided Mode Caused by Silicon Nanopillar Array for Light Emission Enhancement in Color-Converting LED. *Optics Express* **2015**, *23* (16), 21477–21489.
(52) Murai, S.; Castellanos, G. W.; Raziman, T.; Curto, A. G.; Rivas, J. G. Enhanced Light Emission by Magnetic and Electric Resonances in Dielectric Metasurfaces. *Advanced Optical Materials* **2020**, *8* (16), 1902024.
(53) Zhang, C.; Jing, J.; Wu, Y.; Fan, Y.; Yang, W.; Wang, S.; Song, Q.; Xiao, S. Stretchable All-Dielectric Metasurfaces with Polarization-Insensitive and Full-Spectrum Response. *ACS Nano* **2019**, *14* (2), 1418–1426.

(54) Gutruf, P.; Zou, C.; Withayachumnankul, W.; Bhaskaran, M.; Sriram, S.; Fumeaux, C. Mechanically Tunable Dielectric Resonator Metasurfaces at Visible Frequencies. *ACS Nano* **2016**, *10* (1), 133–141.
(55) Murai, S.; Verschuuren, M.; Lozano, G.; Pirruccio, G.; Rodriguez, S.; Rivas, J. G. Hybrid Plasmonic-Photonic Modes in Diffractive Arrays of Nanoparticles Coupled to Light-Emitting Optical Waveguides. *Optics Express* **2013**, *21* (4), 4250–4262.
(56) Green, M. A.; Keevers, M. J. Optical Properties of Intrinsic Silicon at 300 K. *Progress in Photovoltaics: Research and Applications* **1995**, *3* (3), 189–192.
(57) DeVore, J. R. Refractive Indices of Rutile and Sphalerite. *JOSA* **1951**, *41* (6), 416–419.
(58) Sarkar, S.; Gupta, V.; Kumar, M.; Schubert, J.; Probst, P. T.; Joseph, J.; König, T. A. Hybridized Guided-Mode Resonances via Colloidal Plasmonic Self-Assembled Grating. *ACS Applied Materials & Interfaces* **2019**, *11* (14), 13752–13760.
(59) Fujishima, A.; Rao, T. N.; Tryk, D. A. Titanium Dioxide Photocatalysis. *Journal of Photochemistry and Photobiology C: Photochemistry reviews* **2000**, *1* (1), 1–21.
(60) Wold, A. Photocatalytic Properties of Titanium Dioxide (TiO2). *Chemistry of Materials* **1993**, *5* (3), 280–283.
(61) Pelaez, M.; Nolan, N. T.; Pillai, S. C.; Seery, M. K.; Falaras, P.; Kontos, A. G.; Dunlop, P. S.; Hamilton, J. W.; Byrne, J. A.; O'shea, K.; others. A Review on the Visible Light Active Titanium Dioxide Photocatalysts for Environmental Applications. *Applied Catalysis B: Environmental* **2012**, *125*, 331–349.
(62) Mills, A.; Belghazi, A.; Davies, R. H.; Worsley, D.; Morris, S. A Kinetic Study of the Bleaching of Rhodamine 6G Photosensitized by Titanium Dioxide. *Journal of Photochemistry and Photobiology A: Chemistry* **1994**, *79* (1–2), 131–139.
(63) Lu, P.-J.; Huang, S.-C.; Chen, Y.-P.; Chiueh, L.-C.; Shih, D. Y.-C. Analysis of Titanium Dioxide and Zinc Oxide Nanoparticles in Cosmetics. *Journal of food and Drug Analysis* **2015**, *23* (3), 587–594.
(64) Asiri, A. M.; Al-Amoudi, M. S.; Al-Talhi, T. A.; Al-Talhi, A. D. Photodegradation of Rhodamine 6G and Phenol Red by Nanosized TiO2 under Solar Irradiation. *Journal of Saudi Chemical Society* **2011**, *15* (2), 121–128.
(65) De Witte, K.; Busuioc, A.; Meynen, V.; Mertens, M.; Bilba, N.; Van Tendeloo, G.; Cool, P.; Vansant, E. Influence of the Synthesis Parameters of TiO2–SBA-15 Materials on the Adsorption and Photodegradation of Rhodamine-6G. *Microporous and Mesoporous Materials* **2008**, *110* (1), 100–110.
(66) Ghorai, T. K.; Biswas, N. Photodegradation of Rhodamine 6G in Aqueous Solution via SrCrO4 and TiO2 Nano-Sphere Mixed Oxides. *Journal of Materials Research and Technology* **2013**, *2* (1), 10–17.
(67) Schilling, K.; Bradford, B.; Castelli, D.; Dufour, E.; Nash, J. F.; Pape, W.; Schulte, S.; Tooley, I.; van den Bosch, J.; Schellauf, F. Human Safety Review of "Nano" Titanium Dioxide and Zinc Oxide. *Photochemical & Photobiological Sciences* **2010**, *9* (4), 495–509.
(68) Bottein, T.; Wood, T.; David, T.; Claude, J. B.; Favre, L.; Berbézier, I.; Ronda, A.; Abbarchi, M.; Grosso, D. "Black" Titania Coatings Composed of Sol–Gel Imprinted Mie Resonators Arrays. *Advanced Functional Materials* **2017**, *27* (2), 1604924.
(69) Checcucci, S.; Bottein, T.; Gurioli, M.; Favre, L.; Grosso, D.; Abbarchi, M. Multifunctional Metasurfaces Based on Direct Nanoimprint of Titania Sol–Gel Coatings. *Advanced Optical Materials* **2019**, *7* (10), 1801406.
(70) Tsai, M. C.; Tsai, T. L.; Lin, C. T.; Chung, R. J.; Sheu, H. S.; Chiu, H. T.; Lee, C. Y. Tailor Made Mie Scattering Color Filters Made by Size-Tunable Titanium Dioxide Particles. *The Journal of Physical Chemistry C* **2008**, *112* (7), 2697–2702.

(71) Sun, S.; Zhou, Z.; Zhang, C.; Gao, Y.; Duan, Z.; Xiao, S.; Song, Q. All-Dielectric Full-Color Printing with TiO2 Metasurfaces. *ACS Nano* **2017**, *11* (5), 4445–4452.
(72) Checcucci, S.; Bottein, T.; Claude, J.-B.; Wood, T.; Putero, M.; Favre, L.; Gurioli, M.; Abbarchi, M.; Grosso, D. Titania-Based Spherical Mie Resonators Elaborated by High-Throughput Aerosol Spray: Single Object Investigation. *Advanced Functional Materials* **2018**, *28* (31), 1801958.
(73) Spinelli, P.; Macco, B.; Verschuuren, M.; Kessels, W.; Polman, A. Al2O3/TiO2 Nano-Pattern Antireflection Coating with Ultralow Surface Recombination. *Applied Physics Letters* **2013**, *102* (23), 233902.
(74) Zakomirnyi, V.; Ershov, A.; Gerasimov, V.; Karpov, S.; \AAgren, H.; Rasskazov, I. Collective Lattice Resonances in Arrays of Dielectric Nanoparticles: A Matter of Size. *Optics Letters* **2019**, *44* (23), 5743–5746.
(75) Zakomirnyi, V. I.; Karpov, S. V.; \AAgren, H.; Rasskazov, I. L. Collective Lattice Resonances in Disordered and Quasi-Random All-Dielectric Metasurfaces. *JOSA B* **2019**, *36* (7), E21–E29.
(76) Evlyukhin, A. B.; Fischer, T.; Reinhardt, C.; Chichkov, B. N. Optical Theorem and Multipole Scattering of Light by Arbitrarily Shaped Nanoparticles. *Physical Review B* **2016**, *94* (20), 205434.
(77) Hermannsson, P. G.; Vannahme, C.; Smith, C. L.; Sørensen, K. T.; Kristensen, A. Refractive Index Dispersion Sensing Using an Array of Photonic Crystal Resonant Reflectors. *Applied Physics Letters* **2015**, *107* (6), 061101.
(78) Maho, A.; Lobet, M.; Daem, N.; Piron, P.; Spronck, G.; Loicq, J.; Cloots, R.; Colson, P.; Henrist, C.; Dewalque, J. Photonic Structuration of Hybrid Inverse-Opal TiO2—Perovskite Layers for Enhanced Light Absorption in Solar Cells. *ACS Applied Energy Materials* **2021**, *4* (2), 1108–1119.
(79) Mie, G. Beiträge Zur Optik Trüber Medien, Speziell Kolloidaler Metallösungen. *Annalen der physik* **1908**, *330* (3), 377–445.
(80) Mätzler, C. MATLAB Functions for Mie Scattering and Absorption, Version 2. **2002**.
(81) Bohren, C. F.; Huffman, D. R. *Absorption and Scattering of Light by Small Particles*; John Wiley & Sons, 2008.
(82) Van de Groep, J.; Polman, A. Designing Dielectric Resonators on Substrates: Combining Magnetic and Electric Resonances. *Optics Express* **2013**, *21* (22), 26285–26302.
(83) Miroshnichenko, A. E.; Evlyukhin, A. B.; Yu, Y. F.; Bakker, R. M.; Chipouline, A.; Kuznetsov, A. I.; Luk'yanchuk, B.; Chichkov, B. N.; Kivshar, Y. S. Nonradiating Anapole Modes in Dielectric Nanoparticles. *Nature Communications* **2015**, *6* (1), 1–8.
(84) Novotny, L.; Hecht, B. *Principles of Nano-Optics*; Cambridge university press, 2012.
(85) Babicheva, V. E.; Evlyukhin, A. B. Multipole Lattice Effects in High Refractive Index Metasurfaces. *Journal of Applied Physics* **2021**, *129* (4), 040902.
(86) Shalaev, M. I.; Sun, J.; Tsukernik, A.; Pandey, A.; Nikolskiy, K.; Litchinitser, N. M. High-Efficiency All-Dielectric Metasurfaces for Ultracompact Beam Manipulation in Transmission Mode. *Nano Letters* **2015**, *15* (9), 6261–6266.
(87) Cho, E.-H.; Kim, H.-S.; Cheong, B.-H.; Oleg, P.; Xianyua, W.; Sohn, J.-S.; Ma, D.-J.; Choi, H.-Y.; Park, N.-C.; Park, Y.-P. Two-Dimensional Photonic Crystal Color Filter Development. *Optics Express* **2009**, *17* (10), 8621–8629.
(88) Zhang, J.-T.; Wang, L.; Luo, J.; Tikhonov, A.; Kornienko, N.; Asher, S. A. 2-D Array Photonic Crystal Sensing Motif. *Journal of the American Chemical Society* **2011**, *133* (24), 9152–9155.
(89) Baek, S.; Ha, S.-J.; Lee, H.; Kim, K.; Kim, D.; Moon, J. H. Monolithic Two-Dimensional Photonic Crystal Reflectors for the Fabrication of Highly Efficient and

Highly Transparent Dye-Sensitized Solar Cells. *ACS Applied Materials & Interfaces* **2017**, *9* (42), 37006–37012.
(90) McMahon, J. M.; Henzie, J.; Odom, T. W.; Schatz, G. C.; Gray, S. K. Tailoring the Sensing Capabilities of Nanohole Arrays in Gold Films with Rayleigh Anomaly-Surface Plasmon Polaritons. *Optics Express* **2007**, *15* (26), 18119–18129.
(91) Christ, A.; Tikhodeev, S.; Gippius, N.; Kuhl, J.; Giessen, H. Waveguide-Plasmon Polaritons: Strong Coupling of Photonic and Electronic Resonances in a Metallic Photonic Crystal Slab. *Physical review letters* **2003**, *91* (18), 183901.
(92) Lee, H.-S.; Kwak, J. Y.; Seong, T.-Y.; Hwang, G. W.; Kim, W. M.; Kim, I.; Lee, K.-S. Optimization of Tunable Guided-Mode Resonance Filter Based on Refractive Index Modulation of Graphene. *Scientific Reports* **2019**, *9* (1), 1–11.
(93) Rodriguez, S.; Murai, S.; Verschuuren, M.; Rivas, J. G. Light-Emitting Waveguide-Plasmon Polaritons. *Physical Review Letters* **2012**, *109* (16), 166803.
(94) Baranov, D. G.; Zuev, D. A.; Lepeshov, S. I.; Kotov, O. V.; Krasnok, A. E.; Evlyukhin, A. B.; Chichkov, B. N. All-Dielectric Nanophotonics: The Quest for Better Materials and Fabrication Techniques. *Optica* **2017**, *4* (7), 814–825.
(95) Bechger, L.; Koenderink, A. F.; Vos, W. L. Emission Spectra and Lifetimes of R6G Dye on Silica-Coated Titania Powder. *Langmuir* **2002**, *18* (6), 2444–2447.
(96) Elsherbeni, A. Z.; Demir, V. *The Finite-Difference Time-Domain Method for Electromagnetics with MATLAB Simulations*; The Institution of Engineering and Technology, 2016.
(97) Evlyukhin, A. B.; Reinhardt, C.; Chichkov, B. N. Multipole Light Scattering by Nonspherical Nanoparticles in the Discrete Dipole Approximation. *Physical Review B* **2011**, *84* (23), 235429.
(98) Radescu, E.; Vaman, G. Exact Calculation of the Angular Momentum Loss, Recoil Force, and Radiation Intensity for an Arbitrary Source in Terms of Electric, Magnetic, and Toroid Multipoles. *Physical Review E* **2002**, *65* (4), 046609.
(99) Chen, J.; Ng, J.; Lin, Z.; Chan, C. Optical Pulling Force (Supplementary). *Nature Photonics* **2011**, *5* (9), 531–534.
(100) Evlyukhin, A. B.; Reinhardt, C.; Evlyukhin, E.; Chichkov, B. N. Multipole Analysis of Light Scattering by Arbitrary-Shaped Nanoparticles on a Plane Surface. *JOSA B* **2013**, *30* (10), 2589–2598.
(101) Zhang, S.; Bao, K.; Halas, N. J.; Xu, H.; Nordlander, P. Substrate-Induced Fano Resonances of a Plasmonic Nanocube: A Route to Increased-Sensitivity Localized Surface Plasmon Resonance Sensors Revealed. *Nano letters* **2011**, *11* (4), 1657–1663.
(102) Knight, M. W.; Wu, Y.; Lassiter, J. B.; Nordlander, P.; Halas, N. J. Substrates Matter: Influence of an Adjacent Dielectric on an Individual Plasmonic Nanoparticle. *Nano Letters* **2009**, *9* (5), 2188–2192.
(103) Karasiński, P.; Gondek, E.; Drewniak, S.; Kajzer, A.; Waczyńska-Niemiec, N.; Basiaga, M.; Izydorczyk, W.; Kouari, Y. E. Porous Titania Films Fabricated via Sol Gel Rout–Optical and AFM Characterization. *Optical Materials* **2016**, *56*, 64–70.
(104) Djorovic, A.; Meyer, M.; Darby, B. L.; Le Ru, E. C. Accurate Modeling of the Polarizability of Dyes for Electromagnetic Calculations. *ACS omega* **2017**, *2* (5), 1804–1811.
(105) Vogel, R.; Meredith, P.; Harvey, M.; Rubinsztein-Dunlop, H. Absorption and Fluorescence Spectroscopy of Rhodamine 6G in Titanium Dioxide Nanocomposites. *Spectrochimica Acta Part A: Molecular and Biomolecular Spectroscopy* **2004**, *60* (1–2), 245–249.

(106) Bojarski, P.; Matczuk, A.; Bojarski, C.; Kawski, A.; Kukliński, B.; Zurkowska, G.; Diehl, H. Fluorescent Dimers of Rhodamine 6G in Concentrated Ethylene Glycol Solution. *Chemical Physics* **1996**, *210* (3), 485–499.
(107) Birge, R. R. Kodak Laser Dyes. *Kodak Publication* **1987**, *JJ-169*.
(108) Tomás, S.; Stolik, S.; Palomino, R.; Lozada, R.; Persson, C.; Pepe, I.; Da Silva, A. F. Influence of Rhodamine 6G Doping on the Optical Properties of TiO 2 Sol-Gel Films. *Journal of applied physics* **2005**, *98* (7), 073516.
(109) Itoh, K.; Chiyokawa, Y.; Nakao, M.; Honda, K. Fluorescence Quenching Processes of Rhodamine B on Oxide Semiconductors and Light-Harvesting Action of Its Dimers. *Journal of the American Chemical Society* **1984**, *106* (6), 1620–1627.
(110) Pallotti, D. K.; Passoni, L.; Maddalena, P.; Di Fonzo, F.; Lettieri, S. Photoluminescence Mechanisms in Anatase and Rutile TiO2. *The Journal of Physical Chemistry C* **2017**, *121* (16), 9011–9021.
(111) Penzkofer, A.; Leupacher, W. Fluorescence Behaviour of Highly Concentrated Rhodamine 6G Solutions. *Journal of Luminescence* **1987**, *37* (2), 61–72.
(112) Ghazzal, M.; Kebaili, H.; Joseph, M.; Debecker, D. P.; Eloy, P.; De Coninck, J.; Gaigneaux, E. M. Photocatalytic Degradation of Rhodamine 6G on Mesoporous Titania Films: Combined Effect of Texture and Dye Aggregation Forms. *Applied Catalysis B: Environmental* **2012**, *115*, 276–284.